

**Seismic Performance of Reinforced Masonry Shear Walls with Different Masonry  
Boundary Element Configurations**

Layane Hamzeh

A Thesis

In the Department of

Building, Civil and Environmental Engineering

Presented in Partial Fulfillment of the Requirements

For the Degree of

Doctor of Philosophy (Civil Engineering) at

Concordia University

Montréal, Québec, Canada

March 2021

© Layane Hamzeh, 2021

**CONCORDIA UNIVERSITY**  
**School of Graduate Studies**

This is to certify that the thesis prepared

By: Layane Hamzeh

Entitled: Seismic Performance of Reinforced Masonry Shear Walls with Different Masonry  
Boundary Element Configurations

and submitted in partial fulfillment of the requirements for the degree of

**Doctor of Philosophy (Civil Engineering)**

complies with the regulations of the University and meets the accepted standards with respect to  
originality and quality.

Signed by the final examining committee:

\_\_\_\_\_ Chair  
Dr. Hovhannes A. Harutyunyan

\_\_\_\_\_ External Examiner  
Dr. Maged Youssef

\_\_\_\_\_ External to Program  
Dr. Ramin Sedaghati

\_\_\_\_\_ Examiner  
Dr. Ashutosh Bagchi

\_\_\_\_\_ Examiner  
Dr. Emre Erkmen

\_\_\_\_\_ Thesis supervisor  
Dr. Khaled Galal

Approved by \_\_\_\_\_  
Dr. Michelle Nokken, Graduate Program Director

\_\_\_\_\_  
Dr. Mourad Debbabi Dean  
Gina Cody School of Engineering and Computer Science

Date of Defence: 2020-03-09

## **ABSTRACT**

### **Seismic Performance of Reinforced Masonry Shear Walls with Different Masonry Boundary Element Configurations**

**Layane Hamzeh, Ph.D.**

**Concordia University, 2021**

Reinforced masonry (RM) shear walls are commonly used as a seismic force-resisting system (SFERS) in low and mid-rise buildings. Considerable progress has been made on the seismic performance of reinforced masonry shear walls with masonry boundary elements (RMSW+BEs). The integration of masonry boundary elements at the wall end zones of RM shear walls showed an enhancement in the lateral performance and curvature ductility compared to that of rectangular RM shear walls. The addition of masonry boundary elements increases the stability of the compression zone and preserves the flexural strength of the wall. This further increases the ductility of the walls, which in turn, increases the ductility modification factor of the wall that reduces the earthquake design load and thus achieves more economical masonry buildings. The research work outlined herein contributes to the understanding of the seismic behaviour and enhance the overall structural performance and competitiveness of RMSW+BEs.

The main objective of this research study is to investigate the seismic behaviour of RMSW+BEs, highlight the ability of boundary elements to enhance the seismic performance of reinforced masonry buildings with RMSW+BEs, and hence, provide the necessary data to support the recent codification of this system in masonry design codes (TMS 402/602 and CSA S304). In this study, seventy full-scale fully grouted flexure dominated reinforced masonry shear walls with C-shaped boundary elements are numerically modelled under reversed cyclic quasi-static lateral loading and constant axial load. The key design detailing parameters used to investigate the seismic performance of the studied walls are the type of reinforcement (steel and GFRP), the boundary element length, and vertical reinforcement ratio in the boundary element, transverse hoop spacing, aspect ratio, and axial stress. The overall performance of each wall is examined in terms of hysteretic response, strength capacity, level of deformation, stiffness degradation, effective

stiffness, and response modification factor. Validated and calibrated macro-modelling approaches were developed and utilized to simulate the nonlinear in-plane response of the RMSW+BEs.

The obtained results demonstrated that decreasing the transverse hoop spacing in the masonry boundary element enhanced the wall's lateral load and displacement, indicating the effectiveness of confining the masonry boundary element core in delaying failure. Besides, increasing the masonry boundary element's length and vertical reinforcement ratio in the boundary element resulted in a significant increase in the lateral strength and displacement of the walls. Moreover, higher ductility related modification factor,  $R_d$ , values were suggested for steel-reinforced walls that could reduce the seismic demand on masonry buildings. The value  $R_d=3$  for ductile walls specified by the Canadian standard CSA S304 (2014) seems to be conservative if adopted for this wall type. In addition, fragility curves at different damage states were developed according to the FEMA P-58 methodology, which can be adopted in future performance-based seismic design approaches. Furthermore, this study analyzed the experimental results of previously tested forty-three fully grouted flexure-dominated rectangular RMSWs under quasi-static cyclic loading that are available in the literature. An equation for the modified section reduction factor for the effective stiffness for both the Canadian and the American masonry standards was proposed using linear regression, taking into consideration the effect of axial stress, vertical and horizontal reinforcement ratios. The force-based design parameters in terms of seismic force response modification factor and deflection amplification factor were assessed, and refined values were suggested to be implemented in future design codes. The numerical and analytical findings in this research are expected to facilitate the practical implementation of RM shear walls with masonry boundary elements as a practical and competitive SFRS in the future masonry design standards.

## **Dedications**

*To my parents; Ghada Choughary and Mohamad Hamzeh,*

*To my husband; Daniel Ghannoum,*

*To my sister; Nathalie.*

## **Acknowledgments**

I would like to express my deepest gratitude to my supervisor, Professor Khaled Galal, for his guidance and support throughout this research during my time at Concordia University. You have helped me understand the essential work of a researcher, which will help me through my scientific career path.

I would also like to thank my colleagues, Dr. Hamid Arabzadeh, Dr. Shadman Hosseinzadeh, Dr. Nader Aly, Dr. Ala' Obaidat, Dr. Khalid Al-Otaibi, for their support, discussions, hints, and motivation. Profound thanks are due to the postdoctoral fellows Dr. Ahmed Hassanein and Dr. Ahmed Ashour for their suggestions and guidance.

The support from the Natural Science and Engineering Research Council of Canada (NSERC), l'Association des Entrepreneurs en Maçonnerie du Québec (AEMQ), the Canadian Concrete Masonry Producers Association (CCMPA), and the Canadian Masonry Design Centre (CMDC) is much appreciated. Also, I would like to acknowledge the financial support from Concordia University.

Last but not least, I would like to say that no words could express my sincere gratitude to my parents for their patience, care, and support for everything they did and are still doing for me. Without their continuous support, love, prayers, and encouragement throughout my life, I would have never been the one I am now.

## Table of Contents

List of Figures .....	xi
List of Tables .....	xvi
Chapter 1 .....	1
1.1 Background.....	1
1.2 Research Significance and Motivation .....	5
1.3 Research Objectives.....	6
1.4 Thesis Layout.....	7
Chapter 2.....	9
2.1 Introduction.....	9
2.2 Performance of Rectangular RM Shear Walls.....	9
2.3 Performance of RM Shear Walls with End Confined Zones .....	14
2.4 Applications and Techniques for Confinement in Improving Seismic Performance .....	17
2.5 Numerical Analysis of RM Shear Walls.....	20
2.6 GFRP-reinforced Shear Walls .....	27
2.7 Summary and Concluding Remarks .....	30
Chapter 3.....	33
3.1 Introduction.....	33
3.2 Selection Criteria and Design of Walls.....	33
3.2.1 Phase I.....	34
3.2.2 Phase II.....	37
3.3 Loading Protocol.....	41
3.4 Nonlinear Numerical Models.....	42
3.4.1 SeismoStruct .....	42
3.4.1.1 Model overview .....	42
3.4.1.2 Constitutive material models .....	42
3.4.1.3 Element model .....	44
3.4.2 OpenSees.....	48
3.4.2.1 Model overview .....	48
3.4.2.2 Material models .....	48

3.4.2.2.1 Masonry .....	48
3.4.2.2.2 Steel reinforcement .....	50
3.4.2.2.3 GFRP reinforcement .....	51
3.4.2.3 Strain penetration effects .....	54
3.4.2.6 Element model .....	58
3.5 Numerical Model Validation .....	60
3.5.1 Validation of walls using SeismoStruct.....	60
3.5.2 Validation of walls using OpenSees .....	64
Chapter 4.....	68
4.1 Introduction.....	68
4.2 Numerical Program.....	68
4.3 Lateral Load-Displacement Response .....	68
4.4 Displacement Ductility .....	73
4.5 Influence of Different Parameters on the Lateral Response of Walls in Phase I.....	76
4.5.1 Effect of axial compressive stress.....	79
4.5.2 Effect of vertical reinforcement ratio in BE .....	79
4.5.3 Effect of aspect ratio .....	80
4.6 Influence of Different Parameters on Lateral Response of Walls in Phase II .....	81
4.6.1 Type of reinforcement (GFRP vs. Steel) .....	81
4.6.2 Confinement ratio of transverse reinforcement .....	83
4.6.3 Amount of vertical reinforcement in boundary element.....	86
4.6.4 Size of boundary element.....	88
4.6.5 Aspect ratio .....	89
4.7 Conclusions.....	91
Chapter 5.....	94
5.1 Introduction.....	94
5.2 Fragility Assessment.....	95
5.2.1 Development of fragility curves .....	95
5.2.2 Liliefors test .....	103
5.3 Force-based Design Parameters for Rectangular RMSWs .....	106
5.3.1 Database.....	106

5.3.2 Wall Classification According to CSA S304-14 and TMS 402/602-16 .....	108
5.3.3 Load- displacement idealization .....	109
5.3.4 Effective stiffness.....	112
5.3.4.1 Effect of design parameters .....	114
5.3.4.2 Proposed stiffness reduction factor $\alpha_w^{proposed}$ .....	114
5.3.5 Seismic Response Modification Factors .....	116
5.3.5.1 Seismic force modification factor .....	117
5.3.5.2 Overstrength related force modification factor.....	121
5.3.5.3 Deflection amplification factor .....	123
5.4 Force-based Design Parameters for RMSW+BEs .....	125
5.4.1 Ductility Related Modification Factor .....	125
5.4.2 Effective Stiffness for RMSW+BEs .....	128
5.4.3 Stiffness degradation.....	130
5.5 Conclusions.....	134
Chapter 6.....	137
6.1 Summary.....	137
6.2 Conclusions.....	139
6.2.1 Model validation .....	139
6.2.2 Effect of design parameters .....	139
6.2.3 Fragility and stiffness assessment.....	142
6.3 Recommendations for Future Research .....	144
References.....	145
Appendix A.....	153
A1. Sensitivity of the numerical model .....	153
A2. Limitations of the numerical model.....	162
A3. Analytical failure modes.....	162
Appendix B.....	164
Appendix C.....	176

## List of Figures

Figure 1.1 Cross-sections: (a) Rectangular RMSW; (b) RMSW+BEs.....	2
Figure 1.2 Type of masonry units in boundary elements: (a) standard stretcher blocks; (b) C-shaped blocks.....	4
Figure 2.1 Details of concrete masonry walls (Priestley 1986).....	11
Figure 2.2 Wall resistances at the onset of yield and ultimate capacities (Shedid et al. 2008)....	13
Figure 2.3 Effect of end configuration on a) Displacement ductility; b) Drift (Shedid et al. 2009).....	15
Figure 2.4 Visually observed damage states: (a) Spalling of the face shell and vertical cracking; (b) crushing of the masonry (Banting 2013).....	16
Figure 2.5 Bed joint confinement techniques (Hart et al.1988).....	18
Figure 2.6 Details of reinforced masonry boundary elements (Obaidat et al. 2017).....	20
Figure 2.7 MVLEM representation (Orakcal et. al 2004).....	22
Figure 2.8 Sensitivity of responses to the number of elements: (a) Lateral load-top displacement response, (b) Longitudinal strain in the MVLE (Orakcal et al. 2004).....	23
Figure 2.9 (a) Pushover curves (Archetype S13); (b) Collapse fragility curves (Archetype S13) (Ezzeldin et al. 2016).....	25
Figure 2.10 Proposed structural layout of Ductile (D) and Gravity (G) shear walls for RM buildings (Aly and Galal, 2020).....	27
Figure 2.11 Details of reinforcement configuration (Mohamed et al. 2014).....	28
Figure 2.12 Cross-section and reinforcement details of tested walls (Hassanein et al. 2019a)....	29
Figure 2.13 (a) Concrete compressive strain envelope; (b) Energy dissipation (Hassanein et al. 2019a).....	30
Figure 3.1 Cross-section of RMSW+BEs: (a) $\rho_{v(BE)}=0.79\%$ ; (b) $\rho_{v(BE)}=1.18\%$ ; (c) $\rho_{v(BE)}=1.58\%$ (i.e., all dimensions in mm).....	35

Figure 3.2 Cross-sections for RMSW+BE: (a) Square BE with 4 bars in BE; (b) Square BE with 8 bars in BE; (c) Rectangular BE with 8 bars in BE; (d) Rectangular BE with 16 bars in BE (i.e., all dimensions in mm).....	40
Figure 3.3 Sample of the loading protocol for Wall 1.....	41
Figure 3.4 Schematic diagram of wall used in the numerical model.....	46
Figure 3.5 Model discretization.....	47
Figure 3.6 Stress strain relationship of: (a) Concrete02 material (Mander et al. 1988); (b) Steel02 material (Menegotto and Pinto 1973); (c) GFRP (Elastic material).....	52
Figure 3.7 Bond-slip components used to consider strain penetration effects: (a) schematic; (b) fibre-based model for each core wall segment; (c) stress-displacement relationship developed by Zhao and Sritharan (2007).....	55
Figure 3.8 Pinching_4 material model used for modelling shear (McKenna et al. 2013) adapted from the OpenSees manual, 2012).....	57
Figure 3.9 Fibre distribution in the wall section.....	57
Figure 3.10 Schematic diagram of the element and node distribution of RMSW+BE.....	59
Figure 3.11 Cross-section of walls utilized for numerical validation (a) W2; (b) W3 and W6; (c) W1.....	61
Figure 3.12 Experimental versus numerical hysteresis loops: (a) W2 (adopted from Banting et al. 2014); (b) W3 (adopted from Shedid et al. 2010); (c) W6 (adopted from Shedid et al. 2010)...	63
Figure 3.13 Cross-section details of W1 and W11 (Banting and El-Dakhakhni (2012)), W3 (Shedid et al. (2010)) and GnoX (Hassanein et al. (2019a)).....	66
Figure 3.14 Experimental and numerical load-displacement response of W1 (Banting and El-Dakhakhni 2012), W11 (Banting and El-Dakhakhni 2012), W3 (Shedid et al. 2010) and GnoX (Hassanein et al. 2019a).....	66
Figure 4.1 Typical load-displacement hysteresis and envelope: (a) S6S4-0, (b) S12 S4-60, (c) S12G4-60.....	69

Figure 4.2 Load-displacement hysteresis' envelopes for RMSW+BEs.....	78
Figure 4.3 Displacement ductility for walls in Phase I.....	80
Figure 4.4 Effect of utilized type of reinforcement (steel vs.GFRP) on RMSWs.....	82
Figure 4.5 Recorded strain in the extreme fibre GFRP longitudinal reinforcement.....	82
Figure 4.6 Effect of Shoop on steel-reinforced walls.....	83
Figure 4.7 Effect of spacing on GFRP-reinforced walls: a) RMSW with square-shaped BE, b) RMSW with rectangular shaped BE.....	84
Figure 4.8 Idealized ductility for steel-reinforced walls: a) RMSW with square-shaped BE, b) RMSW with rectangular shaped BE.....	85
Figure 4.9 Effect of $\rho_{vBE}$ on steel-reinforced walls.....	86
Figure 4.10 Effect of $\rho_{vBE}$ on GFRP-reinforced walls: a) RMSW with square-shaped BE, b) RMSW with rectangular shaped BE.....	87
Figure 4.11 Effect of boundary element size on steel-reinforced walls.....	88
Figure 4.12 Effect of boundary element size on GFRP-reinforced walls: (a) RMSW with $\rho_{vBE}=0.79\%$ , (b) RMSW with $\rho_{vBE}=1.58\%$ .....	89
Figure 4.13 Effect of aspect ratio on (a) steel-reinforced walls, (b) GFRP-reinforced walls.....	90
Figure 5.1 Fragility curves for all set of walls.....	99
Figure 5.2 Fragility curves based on design parameters: (a) $\rho_{v}(BE)$ ;(b) Axial stress; (c) Aspect Ratio.....	103
Figure 5.3 Sample of the experimental load-displacement curve bilinear idealization. (Modified from Shedid et al. (2008)).....	110
Figure 5.4 Comparison between idealized yield stiffness and effective stiffness computed using: (a) Canadian standards [CSA S304 (2014)], (b) US standards [TMS 402/602 (2016)].....	113

Figure 5.5 Relationship between idealized yield stiffness gross stiffness ratio and design parameters: (a) aspect ratio, (b) normalized axial stress, (c) vertical reinforcement ratio, (d) horizontal reinforcement ratio.....	115
Figure 5.6 Effective stiffness computed according to CSA and TMS procedure using a new proposed section reduction factor and compared to the experimental idealized yield stiffness.....	117
Figure 5.7 Quasi-static experimental results ( $R_d$ and $R$ values computed from database): (a) $R_d$ values for walls with $T_n < 0.5s$ , (b) $R_d$ values for walls with $T_n > 0.5s$ , (c) $R$ values for walls with $T_n < 0.5s$ , (d) $R$ values for walls with $T_n > 0.5s$ .....	120
Figure 5.8 Comparison of $R_o$ values computed from quasi-static experimental results and code limits.....	122
Figure 5.9 Comparison of $C_d$ values computed from quasi-static experimental results and code limits.....	124
Figure 5.10 Determination of the equivalent linear elastic response for wall S12G4-60.....	127
Figure 5.11 Secant stiffness degradation for steel-reinforced walls.....	131
Figure 5.12 Secant stiffness degradation for steel-reinforced walls. (continued).....	132
Figure 5.13 Secant stiffness degradation for GFRP-reinforced walls.....	133
Figure A.1 Experimental and numerical hysteresis loops for wall W2 (Banting and El-Dakhakhni 2014) with varying number of fibres.....	154
Figure A.2 Experimental and numerical hysteresis loops for wall W2 (Banting and El-Dakhakhni 2014) with: (a) 4 elements and varying first element length; (b) varying number of elements and first element length= $2L_p$ .....	155
Figure A.3 Experimental and numerical hysteresis loops for wall W3 (Shedid et al. 2010) with: (a) 4 elements and varying first element length; (b) varying number of elements and first element length= $2L_p$ .....	157
Figure A.4 Experimental and numerical hysteresis loops with varying initial shape factor of the transition curve, $R$ .....	158

Figure A.5 Experimental and numerical hysteresis loops with varying calibrating coefficients (A1 and A2) of transition curve .....	159
Figure A.6 Experimental and numerical hysteresis loops for wall W3 (Shedid et al. 2010) with varying initial curvature parameter, R0 .....	160
Figure A.7 Experimental and numerical hysteresis loops for wall W3 (Shedid et al. 2010) with varying curvature degradation parameters (CR1 and CR2).....	161
Figure A.8 Reinforcing steel and masonry failure mode criteria: (a) steel rebar failure, (b) masonry crushing in confined region, (c) masonry crushing in unconfined region .....	163
Figure B. 1 Load-displacement hysteresis loops for 70 walls .....	175

## List of Tables

Table 3.1 Test Matrix and wall details (Phase I) .....	36
Table 3.2 Summary of wall details used in the parametric study (Phase II) .....	39
Table 3.3 Material Mechanical Properties Utilized in the Numerical Models in Phase I .....	44
Table 3.4 Plastic hinge lengths for walls in phase I .....	45
Table 3.5 Material mechanical properties utilized in the numerical models (Phase II) .....	54
Table 3.6 Plastic hinge lengths for walls in Phase II .....	59
Table 3.7 Summary of wall details used for the model validation .....	60
Table 3.8 Validation of model predictions with the experimental data .....	62
Table 3.9 Summary of wall details used for numerical model validation .....	65
Table 3.10 Comparison of numerical model predictions with the experimental data .....	67
Table 4.1 Summary of lateral load and displacement of RMSW+BEs in Phase I .....	71
Table 4.2 Lateral load and displacement for RMSW+BEs from Phase II .....	72
Table 4.3 Displacement ductility for RMSW+BEs from Phase I .....	75
Table 4.4 Displacement ductility for steel-reinforced RMSW+BEs from Phase II .....	76
Table 5.1 Damage state description for RMSW .....	96
Table 5.2 Top drifts associated with damage states .....	100
Table 5.3 Lilliefors test results for the total set of walls .....	104
Table 5.4 Lilliefors test results based on design parameters.....	105
Table 5.5 Collected database for flexural dominated RMSWs tested under quasi-static cyclic loading .....	107
Table 5.6 Elastic perfectly plastic idealized loads, displacements, and stiffness .....	111
Table 5.7 Displacement ductility and $R_d$ for steel-reinforced walls .....	126

Table 5.8 $R_d$ for GFRP-reinforced walls.....	127
Table 5.9 Effective stiffness .....	129
Table C.1 RMSW category description according to TMS 402/602 and ASCE-7 (2016)...	176
Table C.2 RMSW category description according to CSA S304 (2014) .....	177
Table C.3 RMSW's classifications according to CSA S304 (2014) and TMS 402/602 (2016).....	178

# Chapter 1

## Introduction

### 1.1 Background

Masonry is one of the oldest building materials that are still used to date in North America and worldwide. Reinforced masonry systems are a vital alternative for low- and mid-rise residential and commercial buildings. In general, the perception that masonry structures have a limited ductility and poor seismic performance may be due to the poor performance of *unreinforced* masonry structures during previous earthquake events. However, several studies have shown that *reinforced* masonry seismic force-resisting systems (SFRS) can survive extreme seismic events with minimal damage (e.g., Abrams 1986, Seible et al. 1994).

Shear walls are commonly used as the SFRS in RM structures to provide lateral strength, stiffness, and energy dissipation that is required to resist the lateral loads arising from wind or from earthquakes. Designing the reinforced masonry shear wall (RMSW) to behave elastically during severe ground motion is not economical and impractical. As such, reinforced masonry shear walls are expected to undergo inelastic deformation during severe ground motion. Hence, enhancing wall ductility is a key factor for enhancing the building's seismic performance.

Reinforced concrete (RC) shear walls usually accommodate more than one layer of vertical steel reinforcement that is commonly enclosed by horizontal reinforcement (i.e., hoops) at the wall toes, the wall's most stressed zone. However, a rectangular RMSW typically accommodates only one layer of vertical reinforcement bars. Consequently, this single bar per cell does not allow the placement of confinement hoops at the end zones of the wall, which are subjected to high inelastic strains during an earthquake. As such, incorporating boundary elements to reinforced masonry shear wall's toes can accommodate more than one layer of vertical bars to provide a reinforcing cage to confine the region subjected to the high compressive stresses at failure and delay the buckling of the vertical reinforcement in the boundary element. The confinement provided by the transverse reinforcement can also increase the maximum compressive strain and strength of masonry and thus result in a more ductile behaviour (see Figure 1.1). The behaviour of reinforced masonry shear walls with boundary

elements (RMSW+BEs) is characterized by a small compression zone, which decreases curvatures at the onset of the yield of the vertical reinforcement and increases curvatures at ultimate conditions. This dual-action increases the curvature ductility and subsequently enhances the displacement ductility; which in turn, increases the ductility modification factor of the wall, which reduces the earthquake design load and thus achieves more economical masonry buildings. Recent studies (Shedid et al. 2010, Banting et al. 2014, Ezzeldin et al. 2016, Aly and Galal 2019, 2020) have shown that adding boundary elements to reinforced masonry shear walls enhanced the lateral performance, and curvature ductility in comparison to rectangular reinforced masonry shear walls.

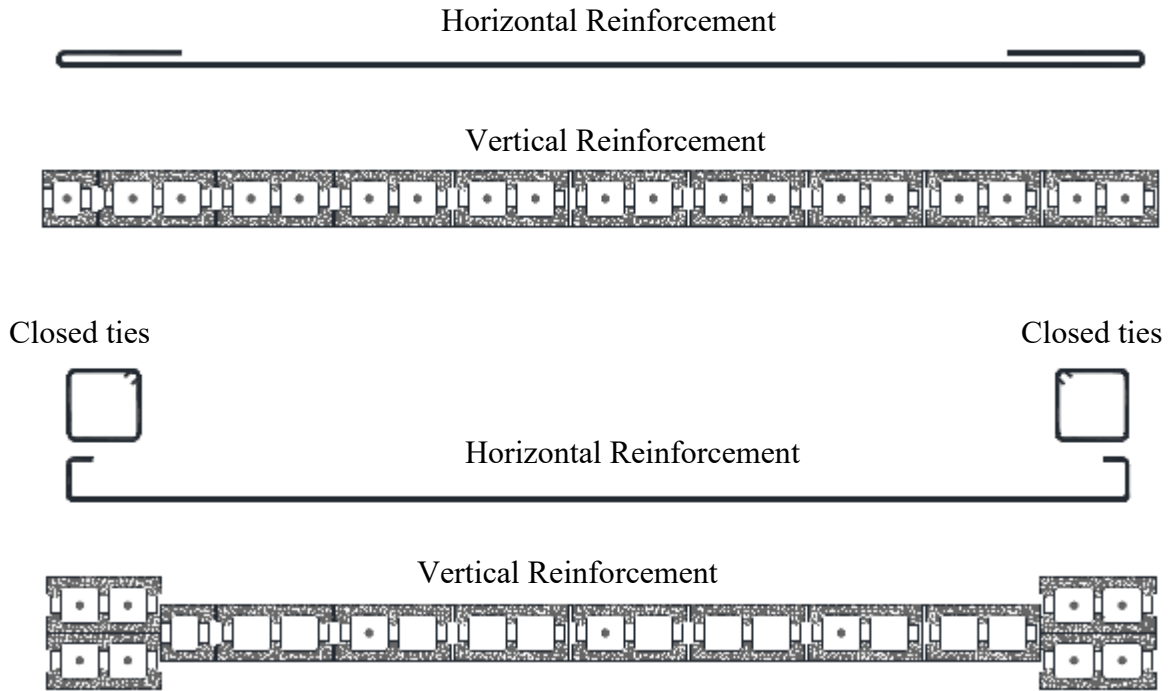


**Figure 1.1** Cross-sections: (a) Rectangular RMSW; (b) RMSW+BEs

The failure mechanism of RMSWs can be categorized into two main mechanisms, shear failure and flexural failure. Shear failure is sub categorized into sliding shear failure along the mortar bed joints, and formation of diagonal shear cracks. Shear failure mode is relatively brittle, and is usually accompanied with rapid strength and stiffness degradation. Flexure failure is characterized by the formation of cracks along the bed joints, and tensile yielding of the vertical reinforcement at the wall toes as well as the formation of a plastic hinge zone at the bottom of the wall. This is followed by compression crushing of the masonry and the grout in

the plastic hinge region, buckling, and fracture of vertical reinforcement under compression and tension, respectively. Flexural failure is the most preferred failure mode compared to shear failure since it has been shown to correspond with more ductile behaviour, and greater energy dissipation due to the tensile yielding of the vertical reinforcement.

Numerous experimental studies have been conducted on the performance of RMSW with rectangular cross-sections (e.g., Priestley and Elder 1982, Eikanas 2003, Shedid 2006, Shedid et al. 2010, Sherman 2011, Ahmadi 2012, Kapoi 2012, and Siyam 2015a). However, very little research has been carried out on the performance of RMSW+BEs under lateral load because early methods of confining masonry were focused on developing applications that are specifically tailored for walls with rectangular cross sections. More specifically, research was focused on introducing alternative materials that could be placed within concrete masonry units to provide confining effects.

Improving the ductility of masonry prisms by adding confinement was investigated in a number of studies in the literature (e.g., Priestley and Elder 1983, Hart et al. 1988, Shing et al. 1993, Dhanasekar and Shrive 2002, Malmquist 2004, and Abo El Ezz et al. 2015). For example, steel plates were placed on the mortar bed joints of the units to confine masonry (Priestley and Bridgeman 1974, Priestley and Elder 1982). This technique had the effect of increasing the ultimate compressive strain in the confined masonry and thus increasing the overall displacement ductility capacity of the wall. Hart et al. (1988) proposed different types of steel confinement reinforcement (e.g., closed wire mesh and seismic combs) to improve the post-peak behaviour of RM prisms. More recent work focused on confinement of unreinforced grouted concrete block using two types of welded wire mesh (Dhanasekar and Shrive 2002) to confine the grouted cells in unreinforced concrete block prisms. The wire mesh proved to be an effective means of increasing the peak compressive strength. The previous methods have the benefit of increasing the compressive strain capacity of the masonry, but they do not offer stability enhancement for a single row of vertical reinforcement. However, the introduction of masonry boundary elements detailed as confined masonry column pilasters not only minimizes the wall structural damage and instability, but also does not deviate from traditional masonry construction practice.

Experimental studies on the seismic performance of RMSW+BEs (Shedid et al. 2010, Banting and El-Dakhakhni 2012, Aly and Galal 2019, Aly and Galal 2020) concluded that the wall ductility and lateral response could be improved by integrating boundary elements at the wall's end zones. As such, the use of boundary elements presents an attractive opportunity for practical application and formalized prescriptive design code requirements. It should be noted that standard concrete block (see Figure 1.2a) was utilized in previous experimental studies (Shedid et al. 2010, and Banting and El-Dakhakhni 2012) to build the RMSW+BEs, which introduces some geometric limitations on the hoop spacing and placement of vertical reinforcement. Also, using stretcher blocks restricts the boundary elements shape to the square and restricts the number of vertical reinforcement bars. However, C-shaped blocks (see Figure 1.2 (b)) offer a larger single core where the mass of the block is lower compared to the standard hollow block, which makes the placement of reinforcement and grout easier. C-shaped boundary elements also allow designers to decrease the spacing between hoops in the boundary elements and eliminate the limitations associated with regular concrete blocks (i.e., stretchers) utilized in previous studies (Shedid et al. 2010, and Banting and El-Dakhakhni 2012). This study was conducted to investigate the capabilities of RM shear walls with boundary elements formed with C-shaped blocks to provide the required strength and ductility to resist earthquake events and to understand its nonlinear response. Subsequently, RMSW+BEs with C-shaped blocks can be considered as a potential competitive SFRS in moderate and high seismic hazard regions.

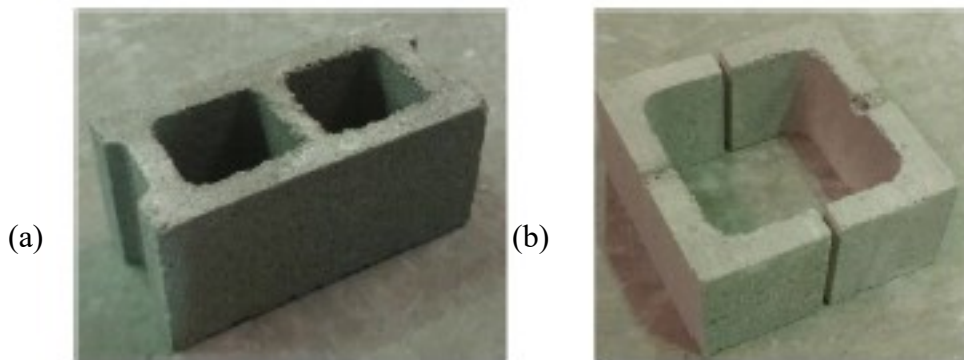


**Figure 1.2** Types of masonry units in boundary elements: (a) standard stretcher blocks; (b) C-shaped blocks (Aly and Galal 2019)

## 1.2 Research Significance and Motivation

With increasing environmental and economic concerns, there is a global drive to raise the efficiency of the building design process. Design optimization is required to promote higher building performance with less cost and less environmental impact. Design process enhancement could be achieved by optimizing the material utilization within the structural components. Reinforced masonry construction has known benefits of better fire protection, structural durability, energy efficiency and cost reduction. In recent decades, noticeable developments have been achieved in understanding the seismic response of reinforced masonry shear walls. This understanding is synchronous with the current uprising of performance-based seismic design. Performance-based design is an approach in which the structural design criteria are expressed in terms of achieving a set of performance objectives related to the level of damage (FEMA 445 2006).

Performance-based seismic design requires accurate damage/loss models for different seismic force-resisting systems. Fragility functions are considered one of the most common damage/loss models that link specific demand parameters i.e., drift ratio to the probability of exceedance of different damage states. Such damage state is primarily connected to a method of repair, which can be translated to the repair cost. The most recent FEMA P-58-1 (2018) guidelines provide fragility curves for evaluating the damageability of reinforced masonry shear walls with only a rectangular cross-section. In addition, few experimental studies are available to date focusing on the seismic response of RMSW+BEs. Consequently, limited data are available to generate fragility curves for RMSW+BEs.

The main motivation, presented in the current research, is to facilitate the adoption of RMSW+BEs as a new resilient SFRS in North American codes and standards. RMSW+BEs are considered as a newly proposed and innovative building system. However, there is still a big misconception that masonry structure cannot develop the required ductility to resist earthquake loads. Studies have shown that the addition of boundary elements at the wall's ends has the benefit of enhanced ductility by optimizing the materials used in wall construction. Nonetheless, previous studies utilized the standard stretcher blocks in forming the boundary elements that has some limitations. These limitations include not having a uniform concrete grout core and not allowing flexibility in the arrangement of vertical reinforcement

arrangements and the spacing of hoops. Hence, in this study utilizing C-shaped blocks in the boundary element instead of the standard stretcher blocks permits more flexibility in terms of the boundary element size, vertical reinforcement arrangement, and spacing of transverse reinforcement.

In addition, further numerical research is needed to investigate the overall response of RMSW+BEs considering the effect of different design parameters on the seismic response of RMSW+BEs. Although experimental tests provide comprehensive understanding on the lateral response and damage pattern of masonry walls and systems tested under simulated seismic loading. However, experiments are usually costly and require extensive facilities and resources. Accordingly, validated and reliable numerical modelling tools are more recently considered by many researchers and can be one of the effective solutions to investigate the performance of RMSW+BEs having various design parameters. Predicting the inelastic lateral response of RMSW+BEs is challenging and requires accurate numerical modelling tools that incorporate relevant material and geometric properties. Macro-models can be used as a key, not only to facilitate evaluating the overall response of the system, but also to help better understand the performance data in accordance with new seismic performance standards and assessment approaches. It can be inferred that the behaviour of RMSW+BEs constructed with C-shaped blocks is yet to be investigated. Therefore, there is a need to study full-scale RMSWs with C-shaped blocks, with differing configurations of boundary elements, to investigate the effect of changing specific parameters (i.e., size of BEs, arrangement and detailing of vertical reinforcement, type of reinforcement, transverse hoop spacing, aspect ratio, and axial load) on the wall response.

### **1.3 Research Objectives**

The main objective of this research are to facilitate the adoption of RMSW+BEs as a new resilient SFRS in North American codes and standards by quantifying the effectiveness of adding masonry boundary elements in enhancing the seismic performance of RM shear walls using numerical modelling. To achieve this objective, the following scope of work was defined:

1. To develop a reliable numerical modelling approach for RMSW+BEs, and calibrate and validate the developed numerical models using available experimental tests of RMSW+BEs from literature.

2. To investigate seventy full-scale fully grouted RMSW+BEs with different parameters, with boundary elements built using C-shaped blocks under quasi-static reversed cyclic loading in enhancing the seismic performance of RM.
3. To evaluate the effect of different design parameters on the lateral response of RMSW+BEs. The studied parameters are BE size, type of reinforcement (steel/GFRP), vertical reinforcement ratio in BE, aspect ratio, axial load, transverse hoop spacing.
4. To develop fragility curves at different damage states for seismic performance assessment that can be adopted in design approaches.
5. To evaluate the hysteretic response, effective stiffness, stiffness degradation, displacement ductility and seismic response modification factors for RMSW+BEs and recommend values to be adopted in the code.
6. To assess the force-based design parameters of rectangular RMSWs and propose a new stiffness reduction factor considering the effect of axial stress, vertical and horizontal reinforcement ratio.

#### **1.4 Thesis Layout**

The dissertation is comprised of six chapters (including the present one), a list of figures and tables, appendices, and references. The chapters present and discuss all the details of the performed numerical and analytical work. The content of the chapters are as follows:

- Chapter 1 presents the background; research significance and motivation; research objectives; and a description of the thesis layout.
- Chapter 2 provides a literature review of the previous experimental and numerical studies on seismic performance of RM shear walls; the applications and techniques of confinement in improving the seismic performance of RM boundary elements; and experimental studies on GFRP-reinforced shear walls. It also contains numerical modelling techniques for RM shear walls.
- Chapter 3 contains a description of the utilized numerical model including: the details of the employed software, the definition of constitutive materials, fibre discretization, details of element sizes and boundary conditions and meshes, loading protocol followed and the model validation for simulation of the RMSW+BEs behaviour. This chapter also presents the details of reinforced masonry shear walls used in Phases I and II.

- Chapter 4 presents the detailing design effects of on the inelastic response RMSW+BEs. This chapter focuses on the effect of BE size and detailing on the seismic response of full-scale flexure-dominated RMSW+BEs considering the effect of different design parameters such as transverse hoop spacing, type of reinforcement (steel/GFRP), amount of vertical reinforcement in BE, axial stress, and aspect ratio of the wall. This chapter documents the influence of the design parameters on wall's hysteretic response, and displacement ductility to evaluate the enhancement in seismic performance of RM buildings with RMSWs.
- Chapter 5 develops fragility curves at flexure damage states for seismic performance assessment of RMSW+BEs according to the FEMA P-58-1 (2018) methodology. Seismic response modification factors are also proposed for steel and GFRP reinforced masonry shear walls. In addition, this chapter also investigates the influence of design parameters on effective stiffness, and ductility-related response modification factors and compares the results with quasi-static cyclic loading of rectangular RMSWs.
- Chapter 6 presents a summary, the main conclusions of the dissertation, and recommendations for future research.

## **Chapter 2**

### **Literature Review**

#### **2.1 Introduction**

This chapter presents a brief literature review of the previous research performed on reinforced masonry (RM) shear walls. Section 2.2 focuses on the performance of rectangular RM shear walls, whereas section 2.3 focuses on the experimental studies on the performance of RM shear walls with end confinement zones. Section 2.4 discusses the applications and techniques for confinement in improving seismic performance. Section 2.5 summarizes the different available modelling techniques for simulating the nonlinear response of RM shear walls and the numerical studies investigating the performance of RM shear walls. Section 2.6 reviews the experimental studies on the performance of GFRP-reinforced shear walls. Finally, a summary of the literature review and some concluding remarks are presented in section 2.7.

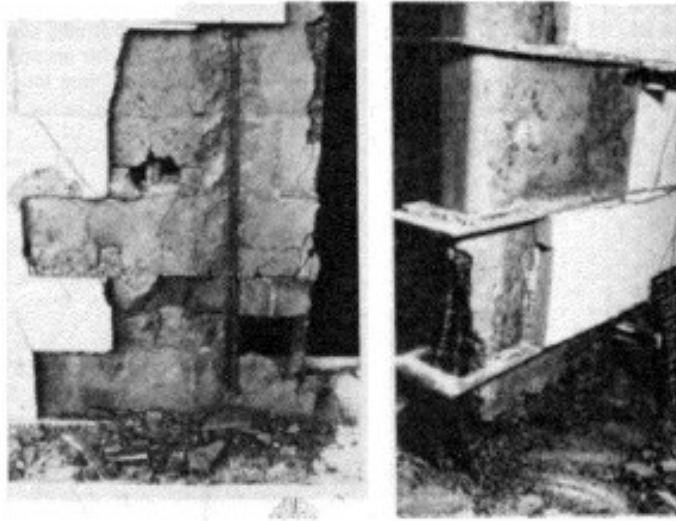
#### **2.2 Performance of Rectangular RM Shear Walls**

With the evolution of building codes and design standards, more demand was shifted towards RM structural systems; hence the use of unreinforced masonry walls became limited. The increased use of reinforced masonry shear wall systems has spurred numerous research investigations into the performance and failure modes of such systems. The failure modes of shear walls are categorized into either flexural or shear failure. Flexural failure is characterized by its favourable ductile behaviour due to the yielding of vertical reinforcement, the formation of the plastic hinge, and the crushing of masonry and grout. Shear failure is characterized by diagonal shear cracking and sliding of the bed joints (Shing et al. 1991). Most of the research has focused on the in-plane behaviour of masonry shear walls under cyclic lateral loading and different combinations of axial load and reinforcement (Priestley 1986, Shing et al. 1990, Ibrahim and Suter 1999, Eikanas 2003, Voon and Ingham 2006, Shedid et al. 2008). These studies showed that the flexure-dominated walls provide high levels of ductility and small strength degradation at large drift levels in comparison with shear-dominated walls. Multi-storey masonry buildings have been effectively utilized in regions with low seismic hazards, such as the 20-storey building in Brazil (Correa, 2016) and the 24-storey building in Winnipeg (Drysdale and Hamid 2005). However, the application in regions with moderate and high

seismicity is still limited due to the challenges involved with conventional types of masonry SFRS.

Priestley (1986) studied the seismic behaviour of concrete masonry structural walls under reversed cyclic loading. Priestley claimed that it was more realistic to recognize that the ultimate capacity of the masonry structure will be achieved and must design accordingly to ensure proper ductility without rapid strength degradation. Priestley (1986) conducted an experimental study on slender cantilever masonry shear walls measuring 6m in height and with an aspect ratio of 2.5. Two fully grouted concrete masonry walls were subjected to in-plane cyclic loading to investigate the influence of aspect ratio on ductility capacity, the use of confining plates in the plastic hinge region, and the potential for buckling of the compression end of the plastic hinge region. One of the walls was unconfined while the other had 600 mm long confining plates. Both walls were subjected to the same level of axial load and were loaded laterally with a single force at the top of the wall.

Results from the testing of the slender walls demonstrated that the confinement in the plastic hinge region improved both the strength and ductility of the walls. The walls without confinement also experienced higher levels of damage at the end of testing in comparison to the confined wall, as shown in Figure 2.1. The lapping of flexural reinforcement in the plastic hinge region resulted in bond failure and higher compression strains at an earlier stage of testing than anticipated. As a result, Priestley recommended that lap splices be avoided in potential plastic hinge zones. No lateral buckling was observed during testing even after the spalling of face shells. Research findings suggested that it is hard to assure adequate ductility capacity for shear walls of high aspect ratio. Therefore, it is necessary to add confining plates in the compression zones at each wall end in the plastic region to increase ductility capacity. The flexural capacity of RM shear walls was easily calculated with a reasonable degree of accuracy. However, the ductility and energy dissipation capabilities of such walls are not well quantified, despite being critical factors in predicting the structural performance under earthquake loading.



(a) Unconfined wall

(b) Confined wall

**Figure 2.1** Details of concrete masonry walls (Priestley 1986)

Shing et al. (1990) tested twenty-two masonry structural walls to enhance the knowledge of their strength and ductility. Each wall was subjected to cyclic, in-plane loading with a gradual increase of maximum displacement. Results showed that code specifications tend to overestimate the shear strength contributed by the horizontal reinforcement and neglect the influence of axial stress. Therefore, a new shear formula that takes into account the influence of axial stress and flexural reinforcement was proposed.

Ibrahim and Suter (1999) tested five fully grouted concrete masonry structural walls to investigate the effects of different parameters, including the applied axial stress, the amount of vertical reinforcement, and the aspect ratio on the lateral behaviour of concrete masonry shear walls. Walls 1-5 had nominal lengths of 56, 88, 120, 88, and 88 in., respectively. The height of all walls was 56 in. and 6 in. thick. Concrete blocks were attached at the base and top of the walls to produce a fixed-fixed condition and, therefore, effective wall aspect ratios of 0.23, 0.32, and 0.50. The vertical and horizontal reinforcement was uniformly distributed at 16 in. spacing. Four of the specimens were exposed to the same constant axial load, and the remaining specimen was exposed to a much larger constant axial load. Results showed that one wall failed by mixed flexural/shear behaviour, exhibiting flexural yielding of tensile reinforcement, diagonal cracking, and masonry compression toe crushing. However, the remaining four walls failed mainly by shear, exhibiting diagonal tensile cracking. Based on the test results, as the

wall aspect ratio decreased, the ductility was reduced, which is likely due to an increase in shear influence on failure behaviour. In addition, an increase in both the amount of flexural reinforcement and axial load tends to increase the ductility of the walls; this is mainly due to increasing confinement of the masonry from flexural reinforcement and the axial load causing an increase in the aggregate interlocks forces.

Eikanas (2003) studied the effects of varying wall aspect ratios on the wall's seismic response by testing seven cantilever walls. Test walls included aspect ratios of 0.72, 0.93, 1.5, and 2.1. Walls 1, 2, 3, and 7 had flexural reinforcement ratios that were approximately equal to the IBC (2000) maximum reinforcement ratio, whereas walls 4, 5, and 6 had flexural reinforcement ratios that were approximately twice the IBC (2000) maximum reinforcement ratio. All walls were tested under displacement control and subjected to fully reversed cyclic loading. Results from this study suggest that RM shear wall drift capacity is directly proportional to the aspect ratio. It was concluded that the aspect ratio of the wall has a substantial effect on the wall behaviour, where decreasing the aspect ratio led to an increase in the shear behaviour and a decrease in the drift capacity. As a result, the aspect ratio should be considered when developing code provisions for limiting flexural reinforcement. The current behavioural assumptions are based on flexural deformations. Hence squat walls should be excluded from these limitations, and a different design approach should be employed.

Voon and Ingham (2006) tested ten masonry structural walls to investigate the effects of the amount and distribution of horizontal reinforcement, the applied axial stress, and the aspect ratio had on the shear strength of such walls. It was found that masonry shear strength increases with the applied axial compressive stress and the amount of shear reinforcement, but it decreases inversely with an increase in wall aspect ratio. Furthermore, it was concluded that the post cracking performance of shear-dominated walls was substantially improved when the shear reinforcement is uniformly distributed along the height of the wall.

Shedid et al. (2008) tested six full-scale walls to failure under reversed cyclic lateral loading to investigate the effects of the amount and the distribution of vertical reinforcement and the level of axial load on inelastic behaviour and ductility. Results showed that yielding of the outermost vertical bars extended to a height equivalent to half the wall length. Moreover, the top wall displacement at the onset of yielding of the vertical reinforcement was highly

dependent on the amount of reinforcement, but only slightly affected by the level of axial stress as shown in Figure 2.2. However, at maximum loads, the displacements were less sensitive to the amount of vertical reinforcement and the level of axial stress. Correspondingly, the displacement ductility was found to be very sensitive to the amount of vertical reinforcement but was not dependent on the level of axial stress. In general, high levels of ductility and energy dissipation capabilities accompanied by relatively small strength degradation were observed for the test specimens.

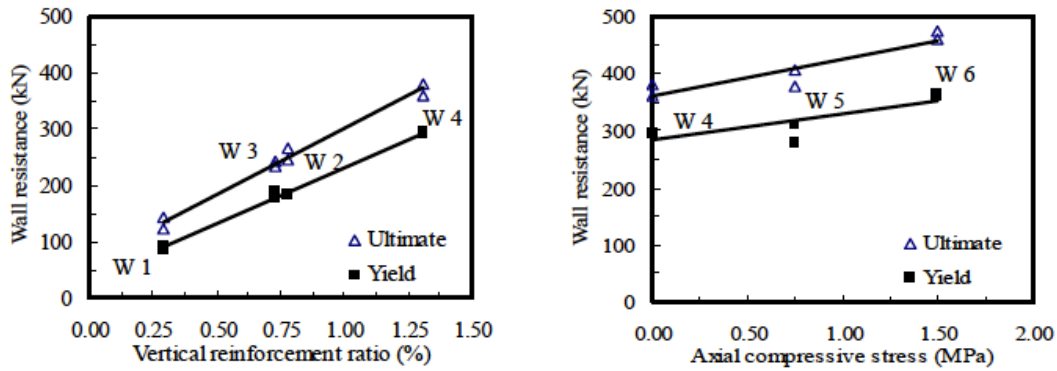


**Figure 2.2** Wall resistances at the onset of yield and ultimate capacities (Shedid et al. 2008)

Ahmadi et al. (2014) discussed the experimental results of thirty full-scale fully grouted RM shear walls tested under reversed quasi-static cyclic loading. Twelve out of the reported thirty RM shear walls were categorized as slender walls with aspect ratios 2, 3, and 4.5. The observed RM shear walls lateral strength was on average 24% higher than the calculated based on the MSJC (2011) provisions. The relationship between the nonlinear hysteretic response and key design parameters (aspect ratio, axial load, arrangement and amount of vertical reinforcement, and lap splices) was investigated. It was observed that the displacement corresponding to the peak strength decreases with the increase in vertical reinforcement ratio, and the axial stress has a slight effect on the wall's ductility. Test results showed that specimens tested with low vertical reinforcement ratios developed higher displacement ductility than those tested with high vertical reinforcement ratios. Moreover, specimens with low aspect ratios and lower axial load ratios had lower plastic hinge lengths. Lap splices in the vertical reinforcement caused a reduction in wall performance. In addition, walls with vertical reinforcement concentrated at jambs behaved similarly to walls with evenly distributed vertical reinforcement.

### **2.3 Performance of RM Shear Walls with End Confined Zones**

The ultimate strain enhancement by introducing transverse reinforcement in the compression zone was first reported by King (1946) for reinforced concrete columns. Since then, several research programs have been conducted to investigate this effect, and it became standard practice and detailing requirement to introduce transverse reinforcement to RC walls and columns to enhance both strength and deformation capacities. Similarly, such enhancement was realized in RM shear wall. Since the general responses of RM and RC elements are similar, similar performances of RM and RC walls with boundary elements would be expected.

Sajjad (1990) tested four masonry shear walls to study their behaviour while considering the effects of three confinements: hoop reinforcement (equivalent to the minimum confinement reinforcement required by UBC (1988), confinement reinforcement comb, and a spiral cage reinforcement. One of four walls did not have confinement, while the other three walls were confined with the aforementioned confinement techniques. All four masonry walls had the same dimensions, horizontal reinforcement ratio, vertical reinforcement ratio, and applied axial load. It was concluded that the confined reinforced walls had increased maximum loads by 6% to 14% compared to the unreinforced wall. Wherein, the maximum load exists when the strain of concrete masonry at the extreme compression fibre is equal to the usable strain. The results show that the drift at the maximum load increased by 58% to 64% compared to the unreinforced wall. Finally, adding confinement to the wall increased the maximum drift by up to 123% as compared to the unreinforced wall.

Recent research studies provided quantitative test data that led to the adoption of ductile RM shear walls with confined boundary elements in the Canadian design of masonry standard CSA S304-14 (CSA 2014). Shedid et al. (2009) introduced confinement to RM shear wall by adding flanges and boundary elements. Shedid et al. (2009) tested seven half scale, fully grouted masonry walls to investigate the cyclic flexure response of the reinforced concrete masonry rectangular walls, walls with flanges, and walls with boundary elements. The purpose of the test was to investigate the influence of adding flanges or boundary elements on the stability of the compression zone. The main goal of this study was to evaluate the effect of connecting flanges or boundary elements to the ends of the wall on the behaviour of the RM wall. All the walls had the same length; however, they had different end configurations and aspect ratios.

All of the walls were subjected to identical axial loading. It was concluded that the flanged and end-confined reinforced masonry walls exhibited an increase in ductility of at least 39 and 106% higher than that of the rectangular walls, respectively. The rectangular, flanged, and end-confined reinforced walls produced a drift at 20% strength of at least 1.0, 1.5, and 2.0%, respectively. The test's results showed that all the walls provided the same capacity and elastic stiffness, hence, saving more than 40% in the amount of vertical reinforcement for the end-confined reinforced walls. The measured displacement at yield in each phase did not differ significantly. However, significant differences were observed at maximum load and 20% strength degradation. Figure 2.3 shows that the ductility values calculated at 1% drift were similar in each phase for the tested walls; this is mainly due to the measured yield displacement being quite similar in each phase. However, the ductility at 20% strength degradation for end-confined walls was at least 50% higher than that of walls with rectangular cross-section indicating a significant effect on the seismic performance of end confined walls.

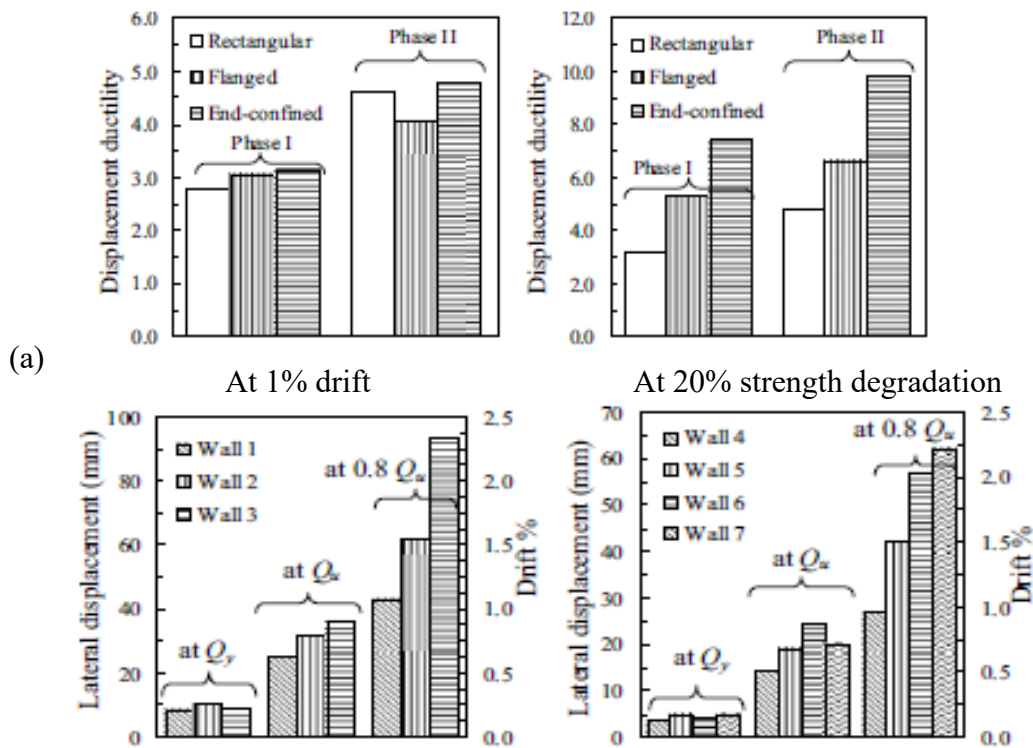


**Figure 2.3** Effect of end configuration on a) Displacement ductility; b) Drift (Shedid et al. 2009)

Banting (2013) tested nine half-scale, fully grouted masonry walls integrated with boundary elements. The objective of the study was to investigate the force-displacement behaviour and

performance-based seismic design consideration for the RM walls containing boundary elements. For comparison purposes, two walls from Shedid (2009) were included in this study. The parameters that were considered for comparison in this study included the wall height, the wall length, the height to length aspect ratio, the number of inter-story floor slabs, the discontinuity of confinement detailing above the plastic hinge, the axial load, and the vertical reinforcement ratio. Each wall had the same boundary element, which in turn produced differing relative wall to boundary element lengths. Banting (2013) also tested a series of four courses boundary element composed of two block units under uniaxial compression in order to investigate the compression stress-strain behaviour. These boundary elements were constructed with blocks and grout that were consistent with those used for the walls. It was concluded that adding boundary elements to the RM walls delayed the buckling of the vertical reinforcement and kept the inner core intact and stable, without a drop in resistance. It was observed that buckling of the vertical reinforcement, crushing of the grouted core, and eventually fracturing of the reinforcement were the main characteristics of the mode of failure (see Figure 2.4).



**Figure 2.4** Visually observed damage states: (a) Spalling of the face shell and vertical cracking; (b) crushing of the masonry (Banting 2013)

Aly and Galal (2019) investigated the inelastic cyclic response of RM walls subjected to high vertical forces from gravity loads (i.e., axial compressive stress that results in  $P/f'_m A_g$  higher than 10%). Three half-scale fully grouted walls were tested under in-plane fully reversed cyclic loading with constant axial load and top moment. The tested specimens represented typical walls in the plastic hinge region of a 12-story building. The boundary element's size and vertical reinforcement varied in the studied walls. The results demonstrated that the high

axial load increased the rate of stiffness degradation of the test specimens. Besides, enhancing the detailing in the end zones of the walls increased the ultimate masonry compressive strain and reduced the depth of the compression zone, resulting in an improvement in the section's ductility curvature ultimate capacity of the walls.

Aly and Galal (2019) reported the results of four tests on half-scale fully grouted RM shear walls with boundary elements under quasi-static reversed cyclic loading and constant axial load. The influence of the wall's shear span to depth ratio, type of masonry blocks in boundary element (stretcher or C-shaped), and lap splicing of vertical reinforcement in the plastic hinge region were quantified. Results showed that using C-shaped blocks instead of regular stretcher blocks in the boundary elements improved the construction process and time. In addition, the use of stretcher blocks limited the displacement capacity and resulted in a degrading post-peak response. The reduction in shear span to depth ratio increased the initial stiffness and lateral resistance but limited the ultimate capacity of the wall. Moreover, the lap splicing of vertical bars in the plastic hinge region increased the initial stiffness and resulted in a higher rate of stiffness and strength degradation. Besides, the premature tensile bond failure of extreme bars was prevented.

## **2.4 Applications and Techniques for Confinement in Improving Seismic Performance**

Understanding the material stress-strain behaviour is key for reliable structural analysis and design. The failure mechanism of unreinforced fully grouted masonry prisms tested under concentric compression axial loading is defined as a combined compression-tension failure. As the compression load increases, the lateral expansion of mortar and grout increases, leading to the tensile splitting of the block face shell and compression-tension failure of the unreinforced grout cores (Drysdale and Hamid 2005). However, when unconfined RM prisms fail, their vertical reinforcement buckles. Therefore, the failure mode of the unreinforced and the unconfined RM prisms is characterized by a brittle failure mechanism. Adding confinement reinforcement in masonry prisms prevents the brittle failure mechanism and provides a more ductile response to the tested prism.

Different techniques have been implemented in the literature to confine the masonry prisms. Early methods of confining masonry did not diverge from a conventional wall layout of a rectangular cross-section, with a single layer of vertical reinforcement. Instead, research was

focused on alternative materials that could be placed within the wall to provide confining effects (Priestley and Elder 1982; Hart et al. 1989). Figure 2.5 shows the different types of confinement that were proposed (e. g closed wire mesh, seismic combs, and steel plates) to improve the post-peak behaviour of RM prisms. For example, stainless steel plates were placed within the mortar bed on the face shell and web of the units for confinement (Priestley and Bridgeman 1974; Priestley and Elder 1982). This technique had the effect of increasing the ultimate compressive strain in the confined masonry and thus increasing the overall displacement ductility of the wall.

Another recent work on confinement of unreinforced grouted concrete block used two types of wire mesh proved to be an effective means of increasing the peak compressive strength (Dhanasekar and Shrive 2002). The previous methods provided the benefit of increasing the compressive strain capacity of the masonry, but they did not offer any enhancement of the stability for a single row of vertical reinforcement. The use of RM boundary elements detailed as confined columns present an opportunity for practical application and formalized prescriptive detailing requirements (Shedid et al. 2010; Banting and El- Dakhakhni 2012).

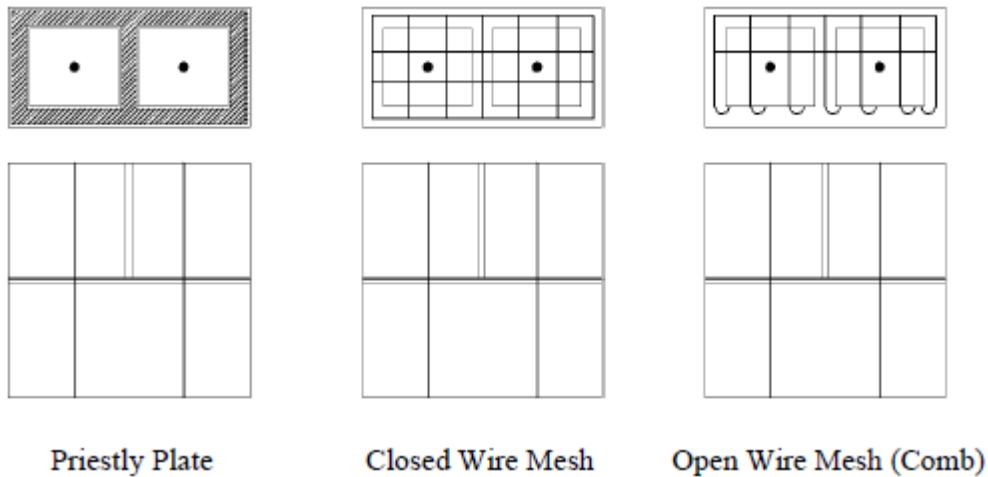


**Figure 2.5** Bed joint confinement technique (Hart et al.1988)

Evaluating the compression behaviour of the boundary elements is key for predicting the seismic response of the RM shear walls. Unlike reinforced concrete (RC), the experimental studies that focused on compressive stress-strain behaviour of reinforced masonry are scarce. Limited studies explored the behaviour of RM boundary elements, considering different confinement ratios. Abo El Ezz et al. (2015) tested seventeen full-scale, fully grouted concrete

masonry boundary elements using standard concrete blocks (i.e., double cell stretchers). It was concluded that the confining reinforcement enhances the strain ductility and has a noticeable effect on post-peak behaviour. In addition, a smeared compression stress-strain model was proposed for confined boundary elements capable of predicting the RM boundary element stress-strain response. However, using standard stretcher concrete blocks to build the RMBEs introduced limitations on the hoop spacing, as the hoops can be placed only at the mortar bed joint.

Therefore, Obaidat et al. (2017) introduced the use of C-shaped concrete masonry blocks in the RM boundary elements, which allows for having any hoop spacing, thus enhancing the confinement effect. Obaidat et al. (2017) tested sixteen full-scale fully grouted RM boundary elements to evaluate the compression stress-strain behaviour considering different confinement ratios of lateral reinforcement (i.e., different hoop spacing) as shown in Figure 2.6. The results showed that as the confinement ratio increases, the compression strain capacity increases, hence increasing the confined core area within the RM boundary element. Obaidat et al. (2018) investigated the compression stress-strain behaviour of reinforced C-shaped RMBEs considering the effects of various parameters including vertical reinforcement ratio, the volumetric ratio of transverse reinforcement, grout strength, and aspect ratio of boundary elements (height to thickness). Enhancement in both peak and post-peak stress-strain behaviour was observed by decreasing the hoop spacing, increasing the grout strength, decreasing the aspect ratio, and increasing the vertical reinforcement ratio. Apart from Obaidat et al. 2017, and 2018, there are limited studies conducted on the behaviour of RM boundary elements constructed with C-shaped blocks.

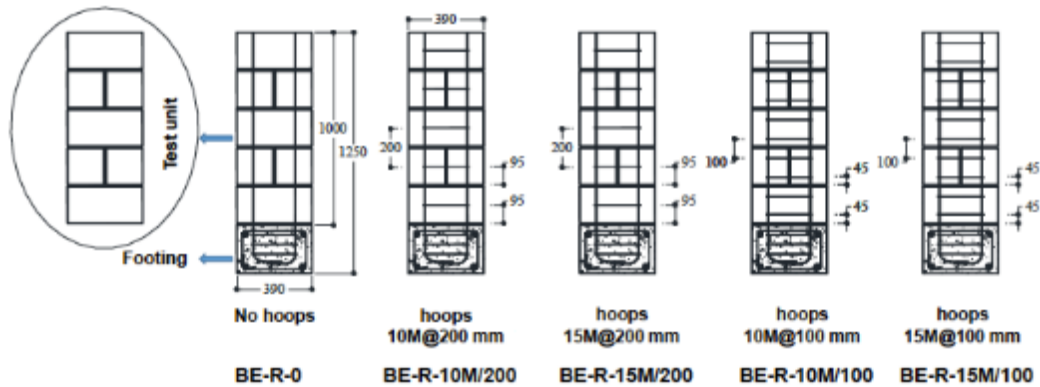


**Figure 2.6** Details of reinforced masonry boundary elements (Obaidat et al. 2017)

## 2.5 Numerical Analysis of RM Shear Walls

Extensive numerical studies were conducted to investigate the behaviour of RM shear walls under the lateral loads in order to enable the designers to predict their seismic response in a building when subjected to severe ground motion. Predicting the behaviour of RM walls under lateral loads requires enhanced numerical tools that are calibrated using controlled experimental tests. These tools should take into account most of the important factors that could affect the response of RM walls. Hence, modelling of RM walls involves several challenges in representing the combined effects of the moment, shear, and axial forces, in addition to bar slip, buckling, damping, boundary conditions, as well as rehabilitation method, if any. This section presents an overview of the different modelling techniques that have been used by researchers in the modelling of RM shear walls.

The two main approaches for simulating the nonlinear response of RM shear walls are micro-modelling and macro-modelling (Lourenço et al. 1998). Micro-modelling is based on the discretization of a structure into a finite number of small elements interconnected at a finite number of nodes. Micro-modelling utilizes solid elements, shell elements, or fibre shell elements to represent the shear walls. Macro-modelling is based on representing the overall structure with larger elements, each of which has properties that are equivalent to the sum of its components. Although micro-modelling has the ability to capture the local response of the structural member, it requires a fine level of mesh and detailing and is a complex approach that needs a high level of computational effort. However, macro-modelling does not require the same level of detailed discretization used for micro-modelling and has the ability to capture the

overall wall response. As a result, macro-modelling is considered as a preferred choice in simulating the response of large structures. Moreover, macro-modelling takes less processing time to study properties such as strength capacity, energy dissipation, and structure deformation.

The studies that have been conducted to develop nonlinear models for RM shear walls can be mainly categorized as (1) continuum finite element models, where the nonlinear behaviour of the masonry, longitudinal and shear reinforcement that comprise the shear wall are modelled explicitly; (2) distributed plasticity models, where numerical integration is used through the RM shear wall cross-section and along its length to distribute plasticity; and (3) concentrated plasticity models, where all the nonlinear effects of the RM shear walls are lumped into an inelastic spring idealized by a single-degree-of-freedom relationship.

The distributed plastic models are competent tools that are utilized for the simulations of the nonlinear response of RM shear walls due to their reasonable accuracy and numerical stability. In this approach, the entire member is modelled as an inelastic element; the source of inelasticity is being defined at the sectional level. Distributed inelasticity elements can be implemented with two main formulations: displacement-based (DB) and force-based (FB). The DB formulation is based on the stiffness of the element, whereas the FB formulation is based on the flexibility of the element. DB formulations assume linear curvature and constant average axial strain, while FB formulations assume linear moment and constant axial force along the element. Consequently, DB elements are sensitive to the structural members' discretization, whereas FB elements sometimes encounter convergence issues with strength degradation (Calabrese 2010).

Many studies developed and validated macro models for reinforced shear walls subjected to reversed cyclic loading. Orakcal et al. (2004) demonstrated the effectiveness of using multiple vertical line element (MVLEM) for modelling and simulating the inelastic response of RC structural walls. It was verified that the MVLEM model captures important response characteristics associated with cyclic behaviour RC structural walls governed by flexure. The sensitivity of analytically predicted global and local wall responses to changes in the model and material parameters were also investigated. The model was developed using a 2D MVLEM

wall element. A structural wall is modelled as a stack of  $m$  MVLEM elements, which are placed on one another, as shown in Figure 2.7.

The flexural response is simulated by a series of uniaxial elements connected to rigid beams at the top and bottom. The stiffness and force-deformation properties of the uniaxial elements are derived from uniaxial stress-strain material behaviour. The reinforcing steel stress-strain behaviour implemented in the wall model is the well-known nonlinear hysteretic model of Menegotto and Pinto (1973). The uniaxial hysteretic constitutive model for concrete developed by Chang and Mander (1994) is used as the basis for the material model implemented in this study. In this study, in order to assess the effect of tension stiffening on both steel and concrete of average stress-strain, concrete, and steel within each uniaxial element are subjected to the same average (smeared) strain.

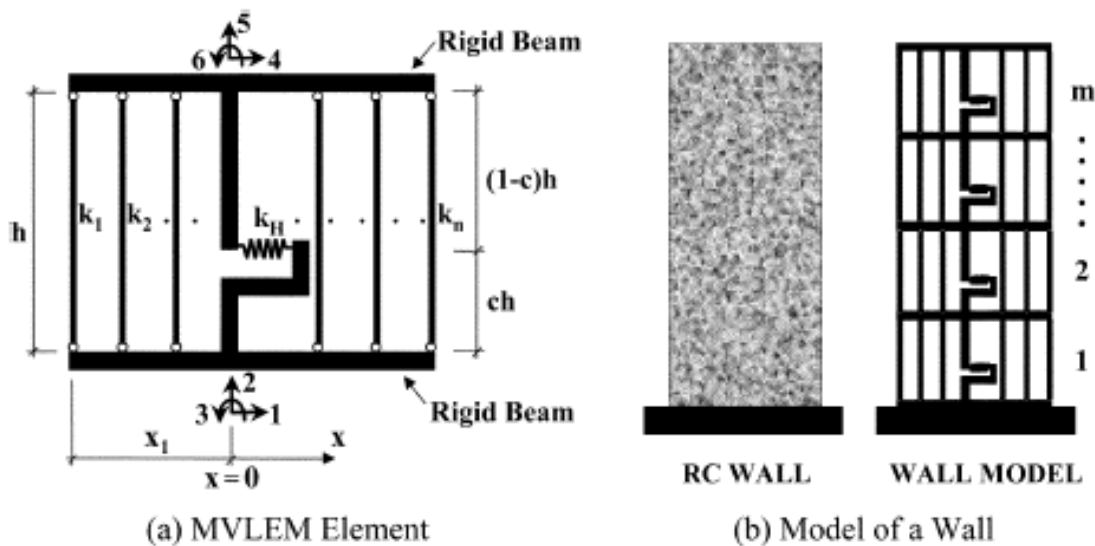


**Figure 2.7** MVLEM representation (Orakcal et. al 2004)

Based on analysis results, it is shown in Figure 2.8(a) that the number of MVLEM elements along the height of the wall and the number of vertical elements along the wall length does not affect the global response of the wall. Figure 2.8(b) shows a comparison of the average longitudinal strain histories predicted at the extreme concrete fibre and the centroid of the wall, in the MVLEM at the base of the two model configurations. It can be seen that the local prediction of strains is improved when using more MVLEM over the height of the wall. It was verified that the MVLEM captures important response characteristics associated with the cyclic

behaviour of slender reinforced concrete structural walls governed by flexure. Moreover, the characteristics of the cyclic response are captured in the analysis results.

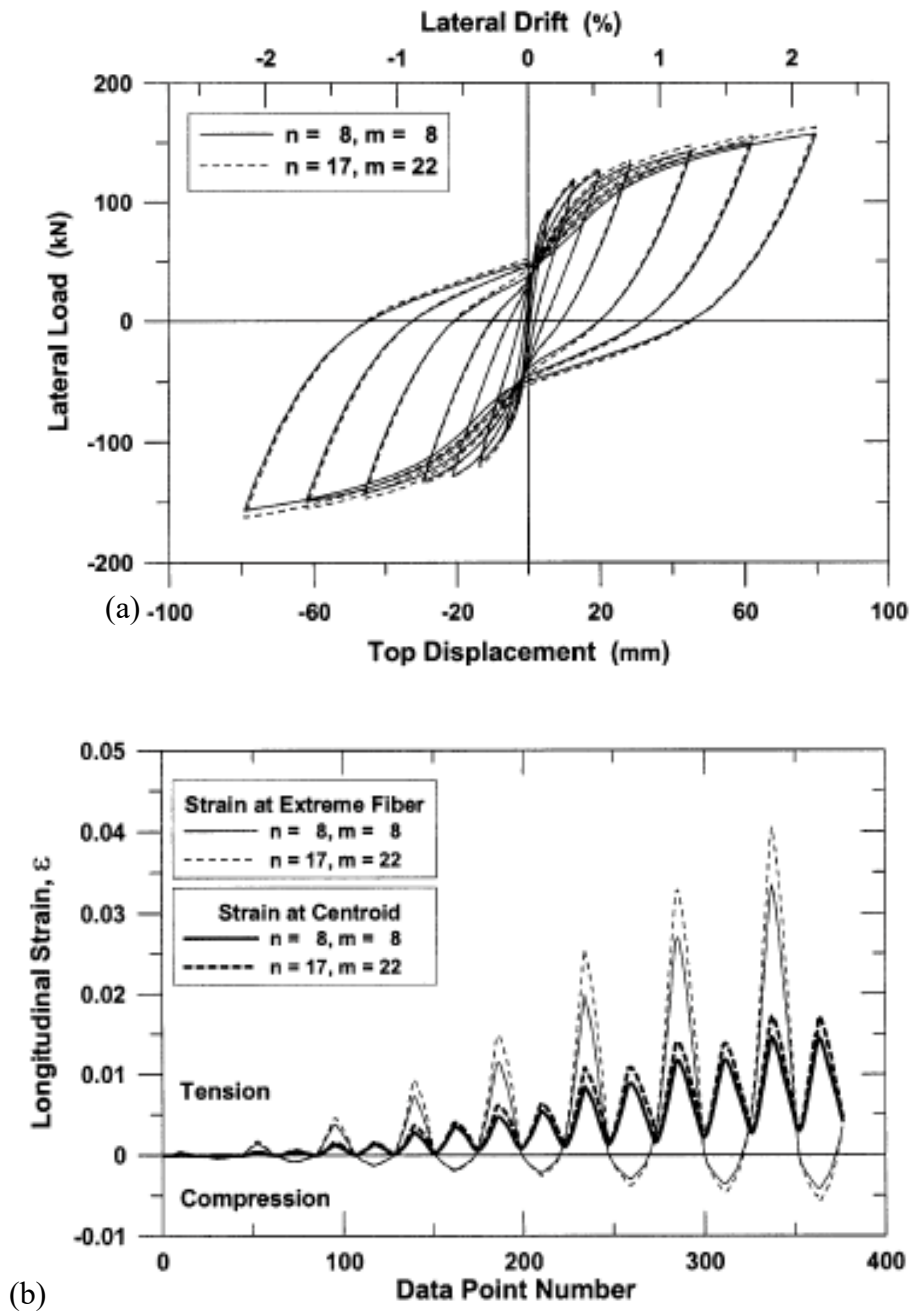


**Figure 2.8** Sensitivity of responses to the number of elements: (a) Lateral load-top displacement response, (b) Longitudinal strain in the MVLE (Orakcal et al. 2004)

It is important to note that the investigation conducted by Orakcal et al. (2004) on the model parameters demonstrated that the number of elements stacked on the top of each other along the height of the wall ( $m$ ), and the number of vertical elements within each wall element ( $n$ ) have a small effect in the global response. The MVLEM by Orakcal et al. (2004) is not capable of simulating the interaction between shear and flexural behaviours. Hence, the model can suitably simulate the compression and flexural failure only when the shear component is not essential. One of the major problems of this model is the difficulty of estimating the shear properties when experimental results are not available. For general simulations, when experimental information is not available, it is necessary to develop recommendations for estimating the shear behaviour of the wall sections. Therefore, further development and calibration of the shear component of these macro-models are needed to obtain more reliable and consistent results. It is worth mentioning that Kolozviari et al. (2015a) developed a modified MVLEM that takes into account the shear-flexure interaction. Ezzeldin et al. (2016) evaluated the seismic collapse risk of numerically modelled RM shear walls with boundary elements adopting the performance factors of rectangular RM shear walls using the FEMA P695 (2009) methodology. A 2D numerical macro model was developed using fibre-based beam-column elements to simulate the response of the walls. The analyses focused on evaluating the wall over-strength, period-based ductility, and seismic collapse margin ratios under the MCE. As shown in Figure 2.9(a), the stiffness curves up to yielding are almost identical for walls with and without boundary elements; however, the ultimate capacities increased by 80% for walls with boundary elements. It can also be seen from Figure 2.9(b), that wall with boundary element (S13-B) have a higher collapse spectral intensity,  $S_{CT}$  than the rectangular wall (S13). The study concluded that RM shear walls with boundary elements experienced an enhanced performance that is enough to meet the FEMA P695 (2009) acceptance criteria for the expected seismic collapse risk under the maximum considered earthquake (MCE) that the rectangular RM shear walls could not achieve. Results showed that integrating boundary elements enables low-rise walls to pass the methodology by reaching higher collapse margin ratios hence having a lower collapse risk in the event of an earthquake. The study also suggests that the response modification factor could be increased for RM shear walls with boundary elements.

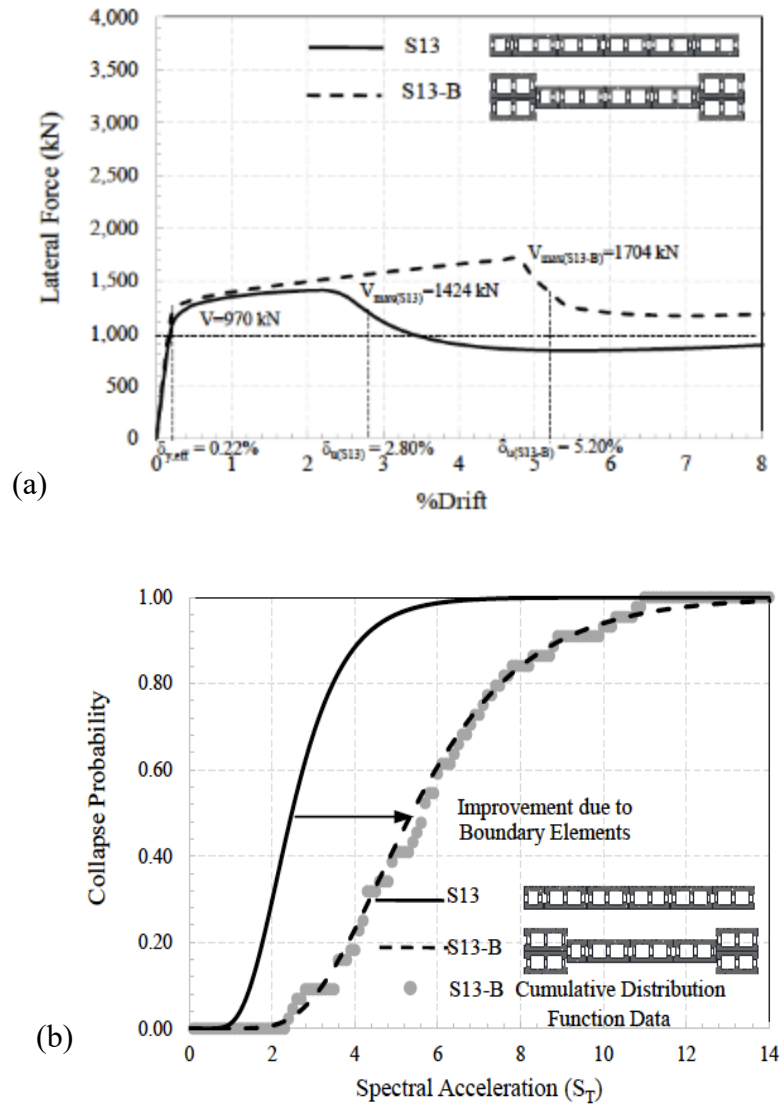


**Figure 2.9** (a) Pushover curves (Archetype S13); (b) Collapse fragility curves (Archetype S13) (Ezzeldin et al. 2016)

Furthermore, the enhancement of the wall response on the component level was observed at the system level by testing a third scale building consisting of RMSW+BEs walls by Ezzeldin et al. (2017a). Ezzeldin et al. (2017b) presented a methodology to generate system-level fragility curves for RMSW+BEs and applied it to a four-story building.

Aly and Galal (2019) assessed the seismic performance and collapse capacity of ductile RM buildings, having heights exceeding the code limits, built using ductile RM shear walls with boundary elements as the SFRS. A simplified numerical macro-model was developed for RM shear walls using SeismoStruct program (Seismosoft, 2016). Nonlinear static and dynamic analyses were executed to evaluate and quantify the collapse capacity of six archetype buildings according to FEMA P695 (2009) methodology. Height limits were proposed for ductile RM shear walls to ensure satisfactory seismic performance and low seismic collapse risk. Based on their findings, it was suggested that a height limit of 70 m for buildings in moderate seismicity regions and 50 m for buildings in regions with high seismic hazard.

More recently, Aly and Galal (2020) proposed a hybrid structural layout of ductile walls with boundary elements and gravity walls for RM shear wall buildings as shown in Figure 2.10 to enhance the structural performance at the system and component level. The influence of ductile shear wall ratios and cross-sectional configuration on the seismic behaviour of 12 RM shear wall buildings was quantified using a series of inelastic static and dynamic analyses. The structural layout of ductile and gravity walls substantially reduced the required ductile shear wall ratios to meet the requirements of the design code and standard, relative to the conventional load-bearing layout, and hence economized the design. Vertical extents were recommended for the boundary elements to optimize further the design of RCM buildings having shear walls with boundary elements. A gradual reduction of the boundary element's cross-sectional dimensions and reinforcement was suggested to avoid resulting in a vertical stiffness irregularity. It was demonstrated in this study that reducing the boundary element's length by increments of 200 mm every three floors until it was discontinued resulted in the most favorable structural response when an adequate ductile shear wall ratio is provided.

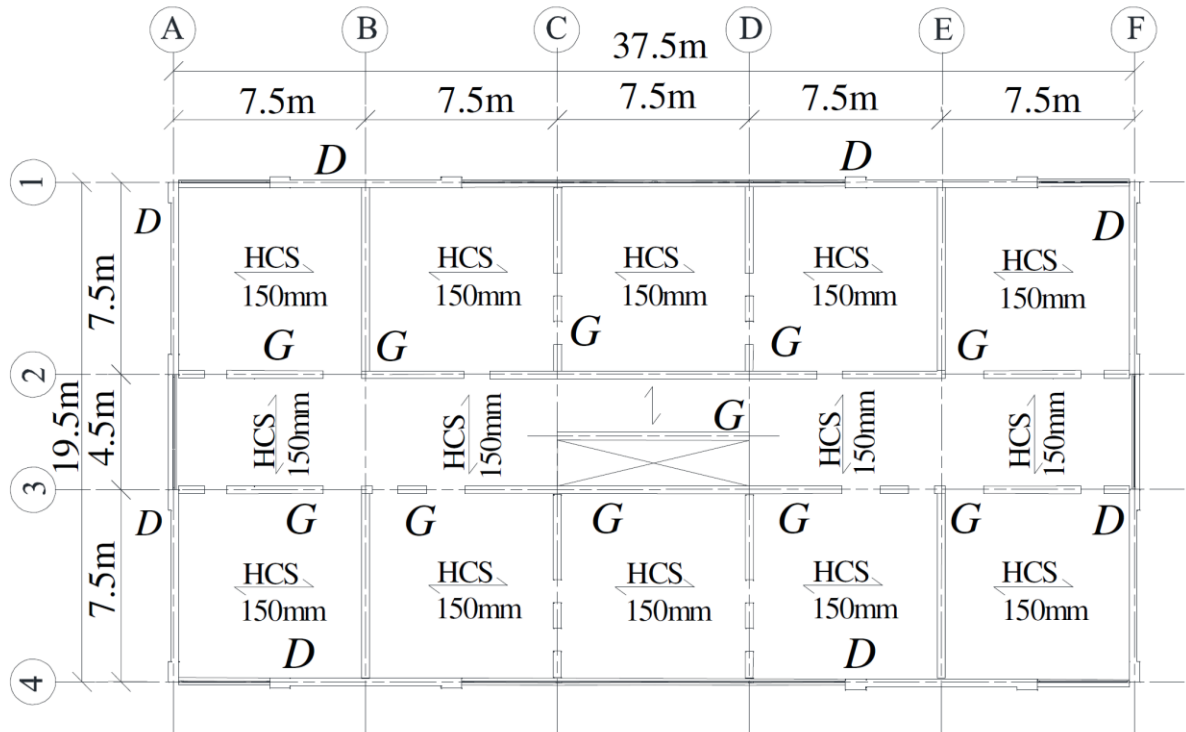


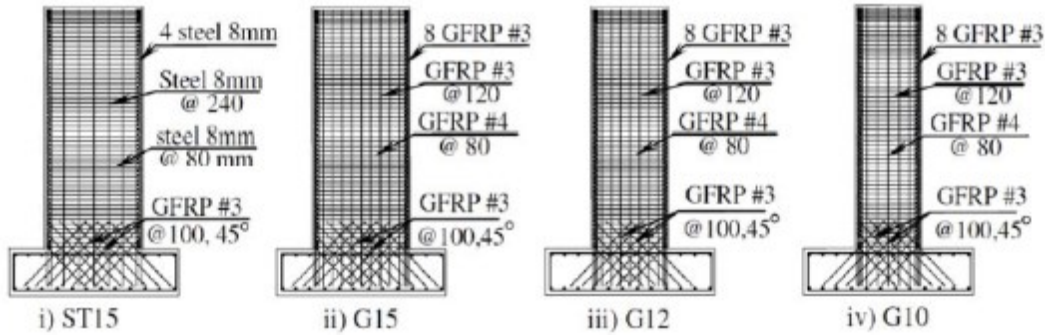
**Figure 2.10** Proposed structural layout of Ductile (D) and Gravity (G) shear walls for RM buildings (Aly and Galal, 2020)

## 2.6 GFRP-reinforced Shear Walls

Glass fibre-reinforced polymer (GFRP) bars have been innovatively used as reinforcement in structures due to their corrosion resistance in harsh climate conditions. Recent studies have investigated the seismic performance of GFRP-reinforced concrete shear walls. Results have shown that GFRP-reinforced shear walls demonstrated appropriate cyclic performance and good deformation capacity.

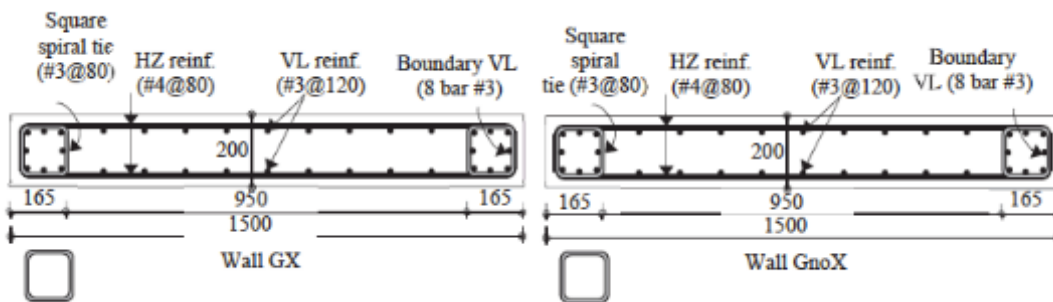
Mohamed et al. (2014) conducted a study that involved three concrete shear walls reinforced with GFRP bars with different aspect ratios and one steel-reinforced shear wall under combined reversed lateral and axial loading (see Figure 2.11). All the wall specimens were 3500 mm in height and 200 mm thick. ST15 and G15 were 1500 mm in length, whereas the length of the G12 and G10 was 1200 mm and 1000 mm, respectively. Results indicated that shear walls that were reinforced with GFRP-reinforced walls exhibited appropriate performance in resisting lateral loads associated with adequate strength and deformation capacity in comparison to the steel-reinforced wall. Crushing of concrete at one end associated with buckling of vertical

reinforcement for steel-reinforced walls and fracture of vertical reinforcement for GFRP-reinforced walls were among the observed failure modes. Moreover, there was no strength degradation and reasonable stability of stiffness in GFRP-reinforced walls. They also achieved a higher drift ratio of 3.1% as compared to the steel wall's 2.6%.



**Figure 2.11** Details of reinforcement configuration (Mohamed et al. 2014)

Hassanein et al. (2019) addressed the effect of the confinement level through testing six full-scale GFRP-reinforced shear walls under quasi-static cyclic loading with different confinement configurations. Two shear walls had boundaries reinforced with square GFRP spiral stirrups, while a third had boundaries reinforced with circular GFRP spiral stirrups. The remaining three shear walls had higher confinement of the boundary elements, consisting of a square GFRP spiral with two GFRP ties in the second, and two square spiral stirrups overlapped side by side in the third as shown in Figure 2.12.



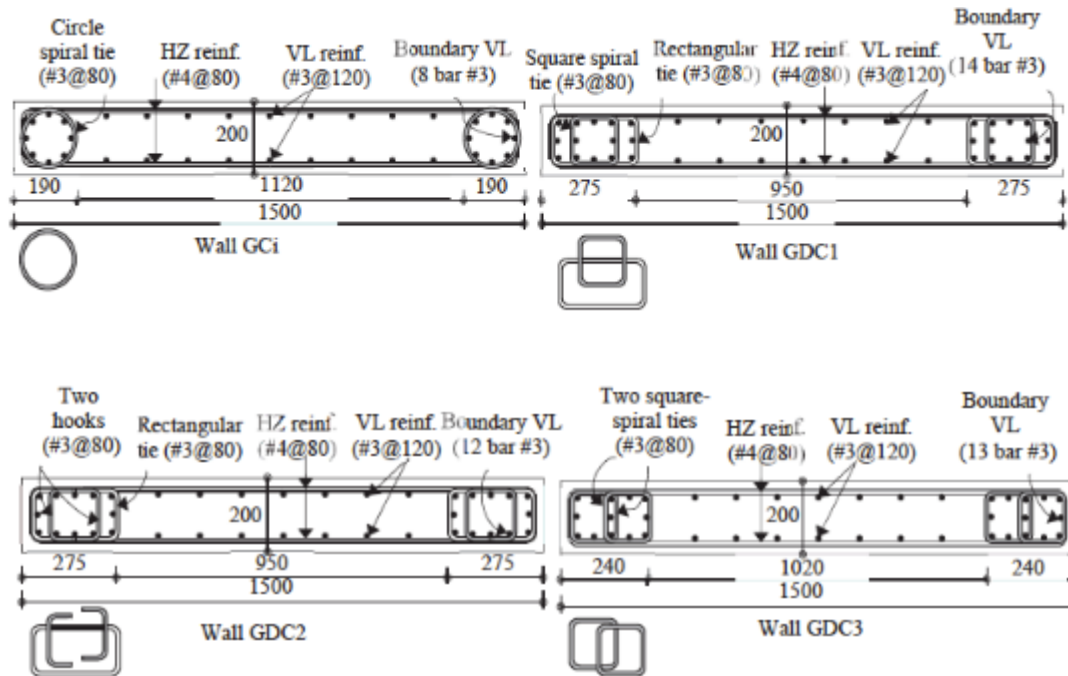


**Figure 2.12** Cross-section and reinforcement details of tested walls (Hassanein et al. 2019a)

A similar failure mechanism was observed in all specimens. The observation of damages indicated that flexural compression failure was the dominant failure mode. The failure occurred as follows: 1) fracture of vertical bars when ultimate capacity was achieved; 2) slight degradation in lateral and axial loads, increase in lateral displacement with constant lateral load; 3) fracture of all vertical bars and crushing of concrete in boundary element core. The obtained results also demonstrate that increasing the confinement level in GDC1, GDC2, and GDC3 enhanced the strength and deformability of the walls. This was mainly clear in delaying of concrete crushing by attaining high compressive strain of up to 0.016 (see Figure 2.13(a)). The concrete compressive strain achieved at failure for specimens (GDC1, GDC2, and GDC3) was 40% higher than that of walls with lower volumetric ratios (GX, GnoX, and GCi), which is mainly due to the higher confinement at the boundary elements. Furthermore, the energy dissipated up to 1% drift was almost similar for all walls. As shown in Figure 2.13 (b), walls having higher confinement in the boundary element dissipated more energy up to failure through a greater number of cycles due to higher displacement levels achieved.

Ductility is the ability of the wall to deform plastically without reduction in strength. The GFRP bars are elastic materials and do not exhibit yielding. However, the confining pressure is continuously increasing during the loading history due to the linear characteristics of the FRP

materials, allowing the concrete to reach a higher confined strain levels (Fam and Rizkalla, 2001). The yield deformation point for GFRP-reinforced walls corresponds to the point of concrete deterioration at the compressed end of the wall and the confinement mechanism starts. The ultimate displacement corresponds to the point at which the longitudinal reinforcement ruptures. As stated by Hassanein et al. (2019), the GFRP-reinforced walls had sufficient deformations through the confined concrete plastic deformations. As such, the concrete is the source of plasticity in GFRP-reinforced walls, and therefore increasing the confinement level enhances the shear wall's deformability by developing a higher level of concrete compressive strains.

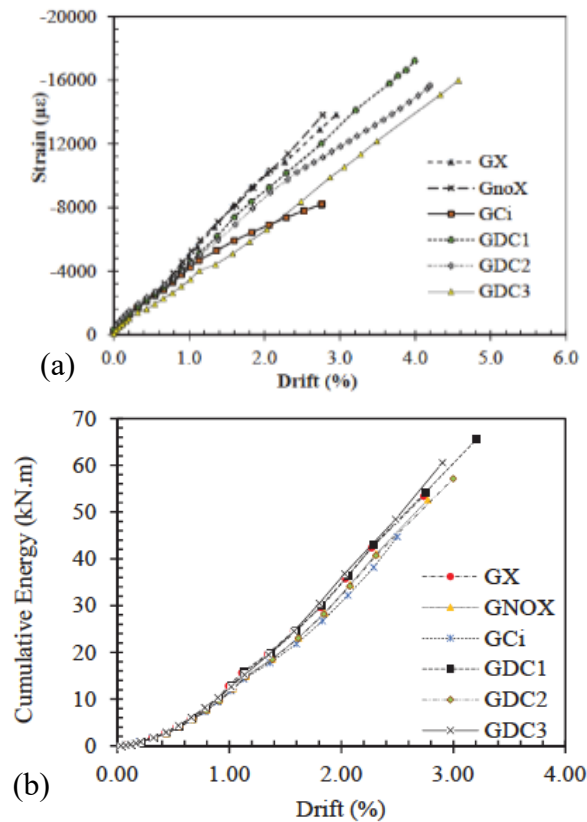


**Figure 2.13** (a) Concrete compressive strain envelope; (b) Energy dissipation (Hassanein et al. 2019a)

## 2.7 Summary and Concluding Remarks

RM shear walls with boundary elements present a potential seismic force-resisting system (SFERS) for mid-and high-rise buildings and have been proved to be able to provide the required

strength and ductility. Experimental studies on the seismic performance of RMSW+BEs concluded that integrating boundary elements at the wall's end zones could accommodate more than one layer of vertical bars to provide a reinforcing cage to confine the region subjected to the high compressive stresses at failure, this significantly enhanced the ductility and overall lateral response of the reinforced masonry shear walls. It was also concluded that adding boundary elements to the RM walls delayed the buckling of the vertical reinforcement and kept the inner core intact and stable, without a drop-in resistance. It was observed that buckling of the vertical reinforcement, crushing of the grouted core, and eventually fracturing of the reinforcement characterized the mode of failure.

It can also be inferred from the literature review that numerical studies showed a high seismic collapse capacity for RM shear walls with boundary elements. As a result, a higher seismic response modification factor could be assigned for RMSW+BEs. However, boundary elements utilized in previous research studies were typically constructed using regular stretcher blocks, which results in some limitations due to the geometry restrictions of the stretcher units. However, utilizing C-shaped boundary elements allows designers to decrease the spacing between hoops, increase the amount of vertical reinforcement, and flexibility in selecting the boundary element size. As such, the use of C-shaped boundary elements presents an attractive opportunity for practical application and formalized prescriptive design code requirements.

Different types of confinement were proposed (e. g closed wire mesh, seismic combs, and steel plates) to improve the post-peak behaviour of RM prisms. The previous methods provided the benefit of increasing the compressive strain capacity of the masonry, but they did not offer any enhancement of the stability for a single row of vertical reinforcement. Previous experimental results clearly showed that properly designed GFRP-reinforced concrete could attain their flexural capacities without strength degradation. In addition, the results also showed that the tested walls were able to achieve recoverable behaviour up to allowable drift limits before reaching moderate damage, and a maximum drift in comparison with steel-reinforced concrete shear walls. Therefore, recent advances in research for the applicability of GFRP-reinforced concrete shear walls have triggered the need to address its utilization in reinforced masonry shear walls. Therefore, there is a need to address the applicability of GFRP-reinforced masonry shear walls subjected to quasi-static cyclic loading as a new lateral resisting system.

Consequently, there is a need for more numerical research to investigate the overall response of RMSW+BEs considering the effect of different design parameters in order to facilitate the practical implementation of this new SFRS within the future masonry design codes.

## Chapter 3

### Numerical Investigation

#### 3.1 Introduction

This chapter presents the details of reinforced masonry (RM) shear walls used in the parametric study. The loading protocol and details of the utilized numerical model are described in this chapter, including a description of the developed model, the definition of constitutive materials, fibre discretization, details of element sizes and boundary conditions, and the model validation for simulation of the RMSW+BEs behaviour.

#### 3.2 Selection Criteria and Design of Walls

RM shear walls with boundary elements (BE) have been recently presented as a ductile alternative to RM rectangular shear walls. In addition, Glass Fibre-reinforced Polymer (GFRP) bars have been innovatively used as a durable and non-corrosive reinforcement in structures in harsh climate conditions. A total of seventy walls were used for the assessment of different parameters on the load-displacement response of reinforced masonry shear walls with boundary elements (RMSW+BEs) using numerical macro-models. The study is divided into two phases for the numerical modelling of full-scale, fully grouted RM shear walls with C-shaped boundary elements. Phase I consists of modelling thirty-six walls using *SeismoStruct* (Seismosoft, 2016) software. Phase II consists of modelling thirty-four walls using *OpenSees* (McKenna et al. 2013) software, taking into consideration the bond-slip and shear deformation effects. *SeismoStruct* (Seismosoft, 2016) was used in the first phase as it had the advantage of being very simple to create, and requires a short amount of time in terms of building the models and running the analyses. *OpenSees* (McKenna et al. 2013) software used in Phase II is an open source program for seismic response analysis of structural problems. It provides a wide range of uniaxial materials available for beam-columns, such as *Pinching4 material* for shear deformations, *MinMax material* for limiting strain capacity of steel/GFRP bars and *Bond SP01 material* for bond slip of the wall.

The walls were designed and detailed according to the CSA S304 (2014) requirements for ductile RM shear walls. The RMSW+BEs considered in the two phases were designed with a shear span-to-depth ratio greater than or equal to 1.5, and an adequate amount of reinforcement

and axial force to be flexure-dominated according to CSA S304 (2014) standard with a safe margin for the shear capacity to avoid undesirable shear failure. Therefore, the walls had shear capacities much larger than the shear forces corresponding to the predicted flexural strength (i.e. following capacity design concept). In addition, the configuration of the boundary element was selected in collaboration with the masonry industry in Canada to ensure its practicality for future manufacturing and use in the construction industry. The walls were modelled as cantilevers, and this was represented in the models by perfectly fixing the base degree of freedoms. The material properties for the walls were also based on the values recommended by CSA S304 (2014) design standards for masonry and steel and based on CSA S807 (2019) for GFRP bars.

### 3.2.1 Phase I

Thirty-six full-scale fully grouted RMSW+BEs were modelled using *SeismoStruct* software according to the details provided in Table 3.1. Numerical wall models are used for the assessment of different parameters on the load-displacement response of RMSW+BEs. The parameters under study are aspect ratio ( $AR$ ), axial compressive stress, and vertical reinforcement ratio in BE. The studied walls were 3990 mm in length, and varied in height (i.e., 6000 mm for  $AR=1.5$ , 9000 mm for  $AR=2.25$ , and 12000 mm for  $AR=3$ ).

Table 3.1 provides the dimensions and reinforcement details of the studied walls. As indicated in Table 3.1, different aspect ratios,  $H_w/L_w$ , have been considered in the current study varying from 1.5-3.75, where the aspect ratio is the height to length ratio of a wall. Three vertical reinforcement ratios in boundary element (BE),  $\rho_{v(BE)}$  (0.79, 1.18, and 1.58%) were also utilized to investigate their effect on the load-displacement response of RMSW+BEs. Moreover, three axial stress levels were applied to the RMSW+BEs to represent the range of compressive stresses found in practice. Figure 3.1 shows the cross-sectional configuration and reinforcement detailing of the walls under study. The RM shear walls had two C-shaped boundary elements at both sides, with a length of 390 mm and a thickness of 190 mm. All walls were detailed with the same vertical reinforcement in the web of four 20M bars [ $A_v=300 \text{ mm}^2$ ] and horizontal reinforcement of 10M bars [ $A_h=100 \text{ mm}^2$ ] spaced at 200 mm. The vertical reinforcement in the boundary element varied between four 20M bars, six 20M bars, and eight 20M bars for walls with  $\rho_{v(BE)}$  0.79, 1.18, and 1.58%, respectively. Each wall has an individual

designation as shown in Table 3.1, where the first letter, S denotes square-shaped BE, respectively. The number following the first letter represents the height of the wall,  $H_w$ , in m. The second letter S denotes the type of reinforcement as steel. The second number refers to the amount of vertical reinforcement in BE (i.e., 4 bars, 6 bars or 8 bars). The last number indicates the total axial stress applied on the wall in MPa.

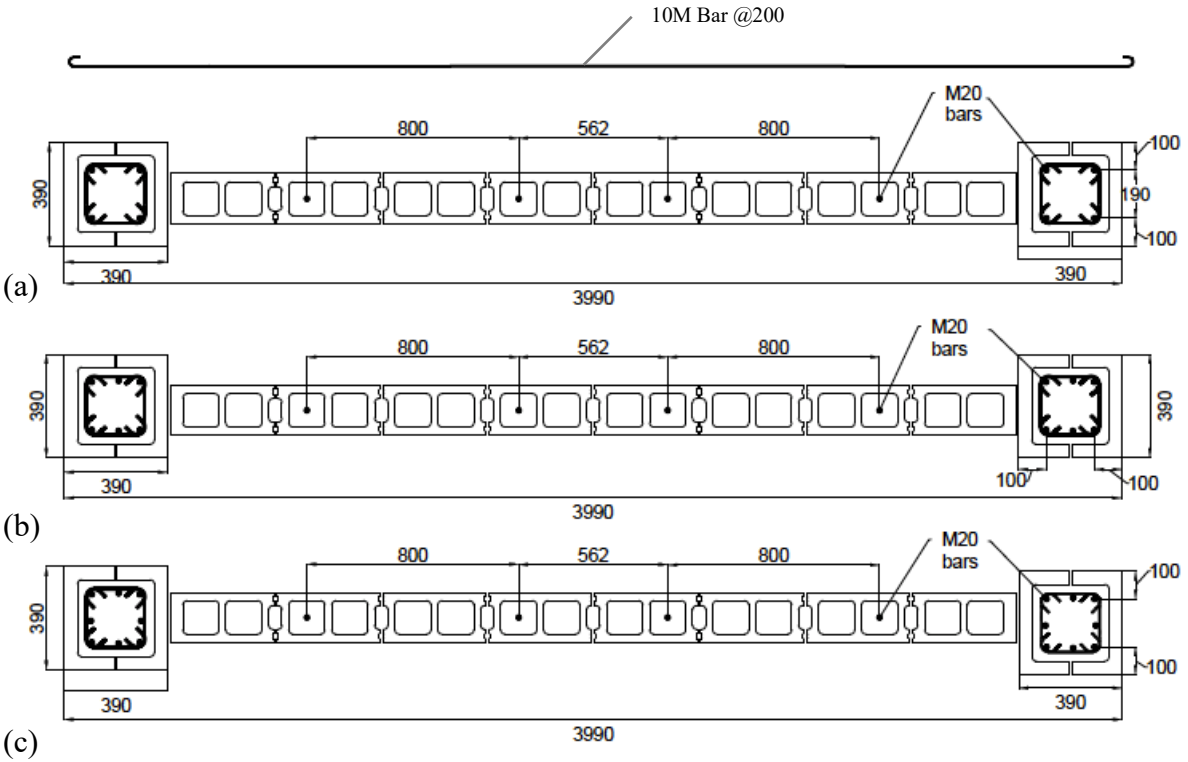


**Figure 3.1** Cross-section of RMSW+BEs: (a)  $\rho_{v(BE)}=0.79\%$ ; (b)  $\rho_{v(BE)}=1.18\%$ ; (c)  $\rho_{v(BE)}=1.58\%$  (i.e., all dimensions in mm)

**Table 3.1** Test Matrix and wall details (Phase I)

Wall #	Wall ID	$L_w$ (m)	$H_w$ (m)	$AR$	Vertical Reinforcement in BE		Axial compressive stress per story (MPa)	Total axial stress (MPa)
					No. & size	$\rho_{v(BE)}$ (%)		
1	S6S4-0	4	6	1.5	4-20M	0.79	0	0
2	S9S4-0	4	9	2.25	4-20M	0.79	0	0
3	S12S4-0	4	12	3	4-20M	0.79	0	0
4	S15S4-0	4	15	3.75	4-20M	0.79	0	0
5	S6S6-0	4	6	1.5	6-20M	1.18	0	0
6	S9S6-0	4	9	2.25	6-20M	1.18	0	0
7	S12S6-0	4	12	3	6-20M	1.18	0	0
8	S15S6-0	4	15	3.75	6-20M	1.18	0	0
9	S6S8-0	4	6	1.5	8-20M	1.58	0	0
10	S9S8-0	4	9	2.25	8-20M	1.58	0	0
11	S12S8-0	4	12	3	8-20M	1.58	0	0
12	S15S8-0	4	15	3.75	8-20M	1.58	0	0
13	S6S4-0.3	4	6	1.5	4-20M	0.79	0.15	0.3
14	S9S4-0.45	4	9	2.25	4-20M	0.79	0.15	0.45
15	S12S4-0.6	4	12	3	4-20M	0.79	0.15	0.6
16	S15S4-0.75	4	15	3.75	4-20M	0.79	0.15	0.75
17	S6S6-0.3	4	6	1.5	6-20M	1.18	0.15	0.3
18	S9S6-0.45	4	9	2.25	6-20M	1.18	0.15	0.45
19	S12S6-0.6	4	12	3	6-20M	1.18	0.15	0.6
20	S15S6-0.75	4	15	3.75	6-20M	1.18	0.15	0.75
21	S6S8-0.3	4	6	1.5	8-20M	1.58	0.15	0.3
22	S9S8-0.45	4	9	2.25	8-20M	1.58	0.15	0.45
23	S12S8-0.6	4	12	3	8-20M	1.58	0.15	0.6
24	S15S8-0.75	4	15	3.75	8-20M	1.58	0.15	0.75
25	S6S4-0.6	4	6	1.5	4-20M	0.79	0.3	0.6
26	S9S4-0.9	4	9	2.25	4-20M	0.79	0.3	0.9
27	S12S4-1.2	4	12	3	4-20M	0.79	0.3	1.2
28	S15S4-1.5	4	15	3.75	4-20M	0.79	0.3	1.5
29	S6S6-0.6	4	6	1.5	6-20M	1.18	0.3	0.6
30	S9S6-0.9	4	9	2.25	6-20M	1.18	0.3	0.9
31	S12S6-1.2	4	12	3	6-20M	1.18	0.3	1.2
32	S15S6-1.5	4	15	3.75	6-20M	1.18	0.3	1.5
33	S6S8-0.6	4	6	1.5	8-20M	1.58	0.3	0.6
34	S9S8-0.9	4	9	2.25	8-20M	1.58	0.3	0.9
35	S12S8-1.2	4	12	3	8-20M	1.58	0.3	1.2
36	S15S8-1.5	4	15	3.75	8-20M	1.58	0.3	1.5

### 3.2.2 Phase II

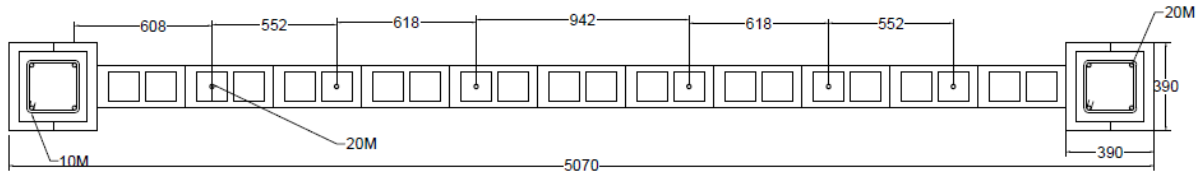
Thirty-four full-scale fully grouted RMSW+BEs were modelled using the DB beam-column elements nonlinear numerical modelling approach described earlier utilizing *OpenSees*. The numerical model was used to investigate the effect of different design parameters on the load-displacement response of RMSW+BEs under quasi-static cyclic loading. These parameters include the amount of vertical reinforcement ratio in the boundary element, size of boundary element, the spacing of transverse reinforcement in the boundary element, type of vertical and horizontal reinforcement (GFRP vs. steel), and aspect ratio of the wall. All the walls had the same length, and this was an important criterion to be able to determine the effect of the proposed wall end configuration on the overall response when walls with square-shaped BE were replaced with rectangular-shaped BE. In addition, the same vertical reinforcement ratio was utilized in both wall configurations (i.e., walls with square-shaped and rectangular-shaped BE) in order to allow for comparison between the walls in terms of the overall wall response.

Table 3.2 shows a summary of the wall details (i.e., dimensions and reinforcements) used in the parametric study. The wall's boundary elements constituted of full-scale two C-shaped masonry blocks facing each other to form the required square or rectangular dimensions. Boundary element length,  $L_{BE}$  and width  $B_{BE}$  have been selected to be 390 mm and 390 mm for square-shaped BEs, and 780 mm and 390 mm for rectangular-shaped BEs, respectively. Besides, a web length of 3510 mm, and a web thickness of 190 mm were utilized for all walls. Hence, the total length of all the walls,  $L_w$  was 5070 mm. The steel-reinforced walls were detailed with the same vertical reinforcement in the web of six 20M steel bars [ $A_v=300 \text{ mm}^2$ ] spaced at 800 mm and horizontal reinforcement of 20M steel bars [ $A_h=300 \text{ mm}^2$ ] spaced at 200 mm. In addition, the GFRP-reinforced walls were detailed with #6 (20M) vertical GFRP bars [ $A_v=284 \text{ mm}^2$ ], and #3 (10M) horizontal GFRP bars [ $A_h=71 \text{ mm}^2$ ]. The parametric study matrix includes two boundary element sizes; square BE 390 x 390 mm, and rectangular BE 780 x 390 mm. Two types of reinforcement were investigated, namely GFRP and steel bars. Two different spacing between transverse reinforcement were implemented in the boundary elements 60 mm, and 120 mm. In addition, two vertical reinforcement ratios in the boundary element were investigated: i.e., four 20M bars ( $\rho_{vBE} = 0.78\%$ ), and eight 20M bars ( $\rho_{vBE}=1.58 \%$ ). Furthermore, three  $AR$  were considered: 4 stories ( $AR=2.4$ ), 5 stories ( $AR=3$ ), and 6 stories

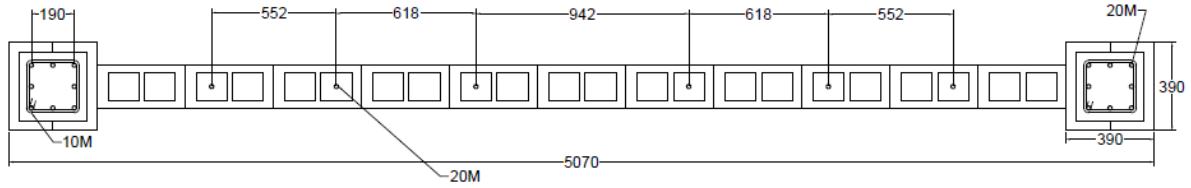
( $AR=3.5$ ). The axial stress was taken as 0.15 MPa per story for all walls resulting in 0.6, 0.75, and 0.9 MPa for 4, 5, and 6 stories walls, respectively. Each wall has an individual designation as shown in Table 3.2, where the first letter, S or R denotes square-shaped or rectangular-shaped BE, respectively. The number following the first letter represents the height of the wall,  $H_w$ , in m. The second letter S or G denotes the type of reinforcement as steel or GFRP. The second number refers to the amount of vertical reinforcement in BE (i.e., 4 bars or 8 bars). The last number indicates the spacing of the hoops (i.e., 60 mm or 120 mm). Figure 3.2 shows the cross-sections for RMSW+BEs with different boundary element detailing configurations.

**Table 3.2** Summary of wall details used in the parametric study (Phase II)

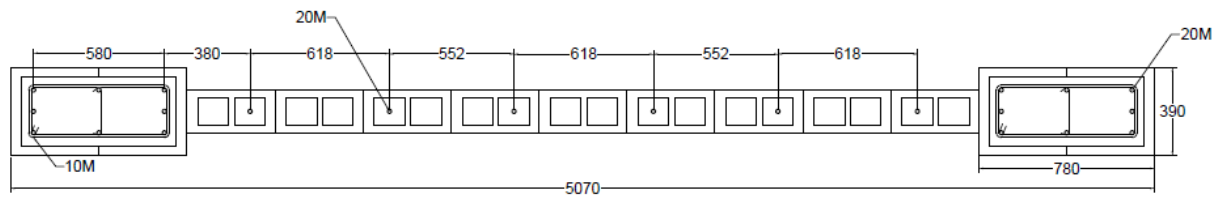
Wall #	Wall ID	$H_w$ (m)	$AR$	Boundary element				Web		Axial stress (MPa)
				$L_{BE}$ (m)	$B_{BE}$ (m)	Vertical bars No. & size	Hoops size @ spacing	Vertical bars No. and size	Horizontal bars size @ spacing	
1	S12S4-60	12	2.4	390	390	4-20M	10M@60	6-20M	20M@200	0.6
2	S15S4-60	15	3	390	390	4-20M	10M@60	6-20M	20M@200	0.75
3	S18S4-60	18	3.5	390	390	4-20M	10M@60	6-20M	20M@200	0.9
4	S12S8-60	12	2.4	390	390	8-20M	10M@60	6-20M	20M@200	0.6
5	S15S8-60	15	3	390	390	8-20M	10M@60	6-20M	20M@200	0.75
6	S18S8-60	18	3.5	390	390	8-20M	10M@60	6-20M	20M@200	0.9
7	S12S4-120	12	2.4	390	390	4-20M	10M@120	6-20M	20M@200	0.6
8	S15S4-120	15	3	390	390	4-20M	10M@120	6-20M	20M@200	0.75
9	S18S4-120	18	3.5	390	390	4-20M	10M@120	6-20M	20M@200	0.9
10	S12S8-120	12	2.4	390	390	8-20M	10M@120	6-20M	20M@200	0.6
11	S15S8-120	15	3	390	390	8-20M	10M@120	6-20M	20M@200	0.75
12	S18S8-120	18	3.5	390	390	8-20M	10M@120	6-20M	20M@200	0.9
13	R12S4-60	12	2.4	780	390	8-20M	10M@60	6-20M	20M@200	0.6
14	R15S4-60	15	3	780	390	8-20M	10M@60	6-20M	20M@200	0.75
15	R18S4-60	18	3.5	780	390	8-20M	10M@60	6-20M	20M@200	0.9
16	R12S8-60	12	2.4	780	390	16-20M	10M@60	6-20M	20M@200	0.6
17	R12S8-60	15	3.0	780	390	16-20M	10M@60	6-20M	20M@200	0.75
18	R15S8-60	18	3.5	780	390	16-20M	10M@60	6-20M	20M@200	0.9
19	R12S4-120	12	2.4	780	390	8-20M	10M@120	6-20M	20M@200	0.6
20	R15S4-120	15	3.0	780	390	8-20M	10M@120	6-20M	20M@200	0.75
21	R18S4-120	18	3.5	780	390	8-20M	10M@120	6-20M	20M@200	0.9
22	R12S8-120	12	2.4	780	390	16-20M	10M@120	6-20M	20M@200	0.6
23	R15S8-120	15	3	780	390	16-20M	10M@120	6-20M	20M@200	0.75
24	R18S8-120	18	3.5	780	390	16-20M	10M@120	6-20M	20M@200	0.9
25	S12G4-60	12	2.4	390	390	4-20M	10M@60	6-20M	20M@200	0.6
26	S15G4-60	15	3.0	390	390	4-20M	10M@60	6-20M	20M@200	0.75
27	S18G4-60	18	3.5	390	390	4-20M	10M@60	6-20M	20M@200	0.9
28	S12G8-60	12	2.4	390	390	8-20M	10M@60	6-20M	20M@200	0.6
29	S12G4-120	12	2.4	390	390	4-20M	10M@120	6-20M	20M@200	0.6
30	S12G8-120	12	2.4	390	390	8-20M	10M@120	6-20M	20M@200	0.6
31	R12G4-60	12	2.4	780	390	8-20M	10M@60	6-20M	20M@200	0.6
32	R12G8-60	12	2.4	780	390	16-20M	10M@60	6-20M	20M@200	0.6
33	R12G4-120	12	2.4	780	390	8-20M	10M@120	6-20M	20M@200	0.6
34	R12G8-120	12	2.4	780	390	16-20M	10M@120	6-20M	20M@200	0.6



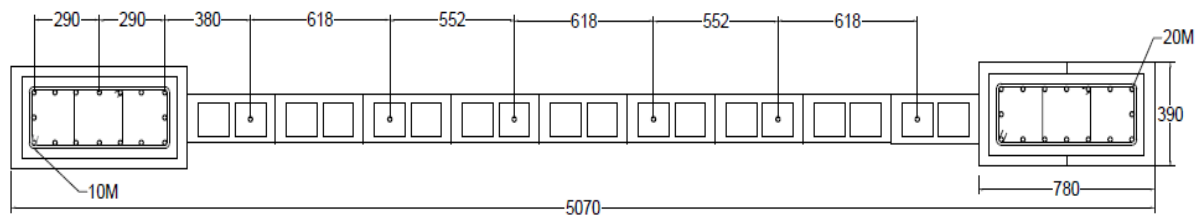
(a)



(b)



(c)



(d)

**Figure 3.2** Cross-sections for RMSW+BE: (a) Square BE with 4 bars in BE; (b) Square BE with 8 bars in BE; (c) Rectangular BE with 8 bars in BE; (d) Rectangular BE with 16 bars in BE (i.e., all dimensions in mm)

### 3.3 Loading Protocol

The lateral displacements loading history used in modelling the walls follows the fundamental requirements and recommendations of FEMA 461 (2007) and ASTM E2126-12. The loading was applied at a slow rate to allow ignoring the dynamic and strain rate effects. FEMA 461 (2007) recommends a loading protocol that is based on increments of a damaged state for structural components under quasi-static cyclic loading. The selected damage state in this study was the lateral displacement at the onset of the first yield in the outermost vertical reinforcement. The lateral displacement at yield,  $\Delta_y$  was predicted by plane sectional analysis based on actual material properties, strain compatibility, and internal force equilibrium. Lateral cyclic displacements were applied at the top of each wall twice at each displacement level at increasing multiples of  $\Delta_y$  until severe flexural damage state was reached. Severe flexural damage state was defined as the point where the lateral resistance of the wall reached 20% strength degradation from the peak resistance as recommended by FEMA P-58-1 (2018). All walls were subjected to the same loading protocol following displacement-controlled fully reversed loading history shown in Figure 3.3.

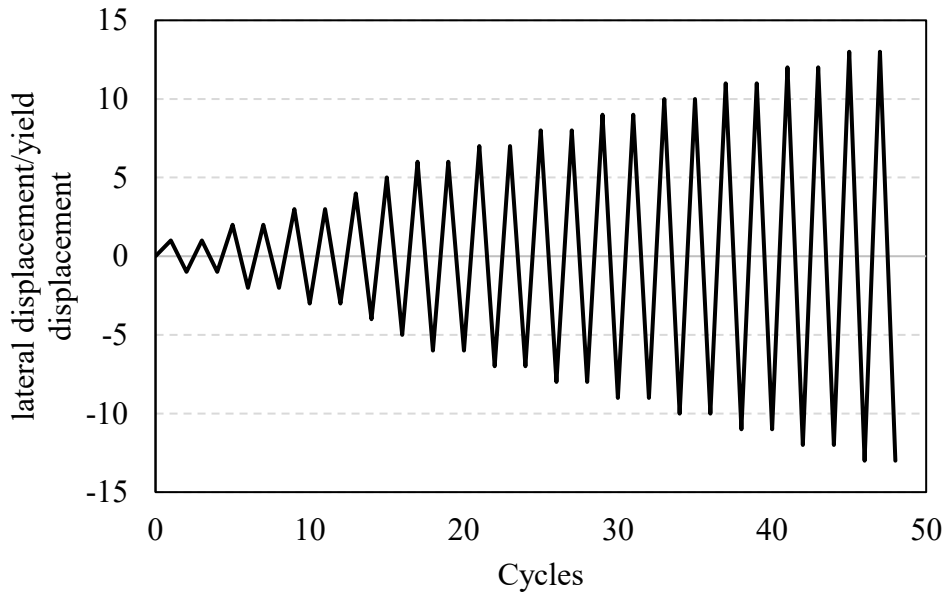


**Figure 3.3** Sample of the loading protocol for Wall 1

## **3.4 Nonlinear Numerical Models**

### **3.4.1 SeismoStruct**

#### **3.4.1.1 Model overview**

*SeismoStruct* (Seismosoft, 2016), a finite element package that uses fibre modelling approach, is used in Phase I of the current study to model the seismic response of thirty-six RMSW+BEs. The walls were modelled using displacement-based (DB), inelastic beam-column elements to simulate the inelastic flexural response of the RMSW+BEs under fully reversed cyclic loading. The DB beam-column elements are characterized by a constant axial deformation and linear curvature distribution along the element length for the estimation of the nonlinear response. Moreover, the element's stiffness is estimated through the integration of moment diagrams with linear curvature interpolation (Carvalho et al., 2013). The response is obtained by assuming a linear strain distribution across the wall's cross-section and calculating the stresses in each fibre using the material constitutive models. As such, from the nonlinear uniaxial stress-strain response of the individual fibres, the sectional moment-curvature state is obtained through the integration of the entire number of fibres (Rodrigues 2012). This is to fully account for the spread of inelasticity along the section length and across the depth. However, it should be noted that the fibre-based elements in *SeismoStruct* (Seismosoft, 2016) do not account for the shear deformations. Therefore, all the walls considered in the current study have a shear span-to-depth ratio greater than or equal to 1.5 and designed to fail in a flexural mode in order to minimize the shear deformation contribution to the overall RMSW+BEs response. The subsequent sections outline the utilized materials, element model, and fibre discretization.

#### **3.4.1.2 Constitutive material models**

The consideration of nonlinear material behaviour in the prediction of RMSW+BEs requires accurate modelling of the uniaxial material stress-strain cyclic response. The use of reliable material models is crucial in the utilized numerical modelling approach since it mainly depends on fibre discretization to capture the flexural response of the studied walls. Currently, there are no predefined constitutive models for the response of fully grouted concrete masonry in most of the available numerical modelling programs. There is limited research related to the axial and cyclic compressive stress-strain behaviour of fully grouted concrete masonry. It was demonstrated by previous research studies such as Banting and El-Dakhkhni (2014), Drysdale

and Khattab (1995) and Shing et al. (1990) that when concrete masonry is fully grouted and well detailed with horizontal and vertical reinforcement; the anisotropic characteristics of unreinforced masonry are substantially reduced. The masonry was modelled using Mander et al. (1988) nonlinear model for concrete (i.e., con\_ma in *SeismoStruct*). Among the available concrete constitutive models, Mander et al. (1988) model was capable of simulating the nonlinear response of fully grouted masonry, which has an overall response similar to that of concrete. This is also in line with the findings of other research studies such as Abdel-Latif et al (2015), Aly and Galal (2019), where the response of grouted masonry was also modelled using Mander et al. (1988) concrete model.

This is a uniaxial nonlinear constant confinement model that follows the constitutive relationship proposed by Mander et al. (1988) and the cyclic rules proposed by Martinez-Rueda and Elnashai (1997). The confinement effects provided by the lateral transverse reinforcement are incorporated through the rules suggested by Mander et al. (1988), whereby constant confining pressure is assumed throughout the entire stress-strain range. Therefore, the core area enclosed by the vertical bars and the transverse hoops were assigned a confined material property. The concrete material model was adjusted to take into consideration the effect of confinement of the closed ties by defining the confinement factor accordingly. However, the reinforced masonry shear wall web and the boundary element cover were assigned an unconfined material property. The input parameters of the model for the masonry are: the compressive strength,  $f'_m$ , the strain at peak strength,  $\varepsilon_m$ , the confinement factor,  $K$ , and the modulus of elasticity,  $E_m$ . The elastic modulus,  $E_m$ , was calculated according to CSA S304 (2014) code recommendation as  $850f'_m$ , where  $f'_m$  is the masonry compressive strength. Table 3.3 shows the mechanical material properties of steel and masonry used in the numerical modelling of the walls.

The steel reinforcement was modelled using Menegotto and Pinto (1973) nonlinear steel model (stl\_mp in *SeismoStruct*). This model is a uniaxial steel model proposed by Menegotto and Pinto (1973) coupled with the isotropic hardening rules proposed by Filippou et al. (1983). The input parameters are: the elastic Young modulus,  $E_s$ , the yield strength,  $f_y$ , the strain hardening ratio,  $r$ , and five coefficients representing the transition from elastic to plastic zone  $R, A_1, A_2, A_3$  and  $A_4$  (see Table 3.3). For the studied walls used in the numerical modelling, the

reinforcement yield strength,  $f_y$  and the modulus of elasticity,  $E_s$  are assumed to be 400 MPa and 200,000 MPa, respectively, as recommended by CSA S304 (2014). Buckling of longitudinal steel reinforcement in the walls was taken into consideration by taking the fracture/buckling strain as 0.1. The nonlinear modelling parameters of the reinforcing steel were influential on the simulated response of the walls. Hence, a sensitivity analysis was performed on the nonlinear modelling parameters of steel, in particular, the initial shape factor and the calibrating coefficients representing the transition curve (see Appendix A, Figures A.4 and A.5).

**Table 3.3** Material Mechanical Properties Utilized in the Numerical Models in Phase I

Parameter		Value	
Grouted masonry	Compressive strength, $f'_m$ (MPa)	17	
	Elasticity modulus of masonry, $E_m$ (MPa)	14850	
	Strain at peak strength, $\epsilon_c$	0.0015	
	Confinement factor, $K$	1.13	
Steel	Elasticity modulus of steel, $E_s$ (MPa)	200,000	
	Yield strength, $f_y$ (MPa)	400	
	Strain hardening parameter, $r$ (%)	0.005	
	Transition curve initial shape, $R$	18.8	
	Transition curve shape	$A_1$	18.5
		$A_2$	0.3
	Isotropic hardening	$A_3$	0
$A_4$		1	

### 3.4.1.3 Element model

Several formulae are available in the literature to estimate  $L_p$  of shear walls (Park and Paulay 1975, Paulay and Priestley, 1992; Priestley et al., 2007; Bohl and Adebar, 2011). The formula proposed by Bohl and Adebar (2011), which is based on nonlinear finite-element analysis results of twenty-two RC shear walls, was found to give the closest estimate of the plastic hinge length,  $L_p$ , for RMSW+BEs (Ezzeldin et al. 2016). In addition, it is one of the few formulas that account for the axial load effect on the inelastic displacement capacity of walls. Moreover, it results in plastic hinge lengths that are in good agreement with experimental results of RMSW+BEs (Aly and Galal 2019). Therefore, the  $L_p$  for the walls is estimated as proposed by

Bohl and Adebar (2011) as shown in Eq. (3.1), whereas, this equation gives a lower bound estimate of plastic hinge length (see Table 3.4).

$$L_p = (0.2l_w + 0.05z)\left(1 - \frac{1.5P}{f'_c A_g}\right) \leq 0.8l_w \quad (\text{Eq. 3.1})$$

where  $l_w$  is the wall length,  $z$  is the moment shear ratio,  $A_g$  is the gross area of the wall cross-section,  $f'_c$  is the concrete compressive strength (i.e.,  $f'_m$  will be used instead for masonry walls),  $P$  is the axial force on the section.

**Table 3.4** Plastic hinge lengths for walls in phase I

<b>Wall ID.</b>	<b><math>L_p</math> (mm)</b>	<b><math>L_w</math> (mm)</b>	<b><math>z</math> (mm)</b>	<b><math>P</math> (N)</b>	<b><math>f'_m</math> (MPa)</b>	<b><math>A_g</math> (mm<sup>2</sup>)</b>
W1, W5, W9	1008.0	3990	4200	0	17	914100
W2, W6, W10	1113.0	3990	6300	0	17	914100
W3, W7, W11	1218.0	3990	8400	0	17	914100
W4, W8, W12	981.3	3990	10500	0	17	914100
W13, W17, W21	1323.0	3990	4200	274230	17	914100
W14, W18, W22	1068.8	3990	6300	411345	17	914100
W15, W19, W23	1153.5	3990	8400	548460	17	914100
W16, W20, W24	1241.3	3990	10500	639870	17	914100
W25, W29, W33	954.6	3990	4200	548460	17	914100
W26, W30, W34	1024.6	3990	6300	822690	17	914100
W27, W31, W35	1089.0	3990	8400	1096920	17	914100
W28, W32, W36	1159.6	3990	10500	1279740	17	914100

The walls were modelled using displacement-based (DB), inelastic beam-column elements to simulate the inelastic flexural response of the reinforced masonry shear walls under fully reversed cyclic loading. To regularize the response of DB elements, it was also suggested by Calabrese et al. (2010) that localization of strain in the DB elements occurs in the most strained integration point, and not in a single element as typically used. Thus, to ensure the correct

regularization, the weight of the most strained integration point has to be equal to the plastic hinge length,  $L_p$ . The utilized DB elements have two integration points within each element at which the deformation is estimated. Hence, the regularized length of the first element should be twice  $L_p$ . This is also in line with another research study by Aly and Galal (2019) where the regularization technique was proven to be independent of the meshing size and resulted in the best agreement with experimental results. Figure 3.4 shows a schematic diagram of the developed wall model, including the distribution of nodes and elements. The wall was divided into four inelastic beam-column elements. It consists of the first element equal to twice the plastic hinge length,  $L_p$ , and three members of equal lengths. *SeismoStruct* user manual (Seismosoft, 2016) recommends 4 to 6 elements for each structural member. In addition, Calabrese et al. (2010) recommended that a good approximation to the response could be obtained with a mesh discretization of at least four elements. A sensitivity analysis was also performed to verify the validity of the proposed geometrical model for the RMSW+BEs (See Appendix A, Figure A.2).

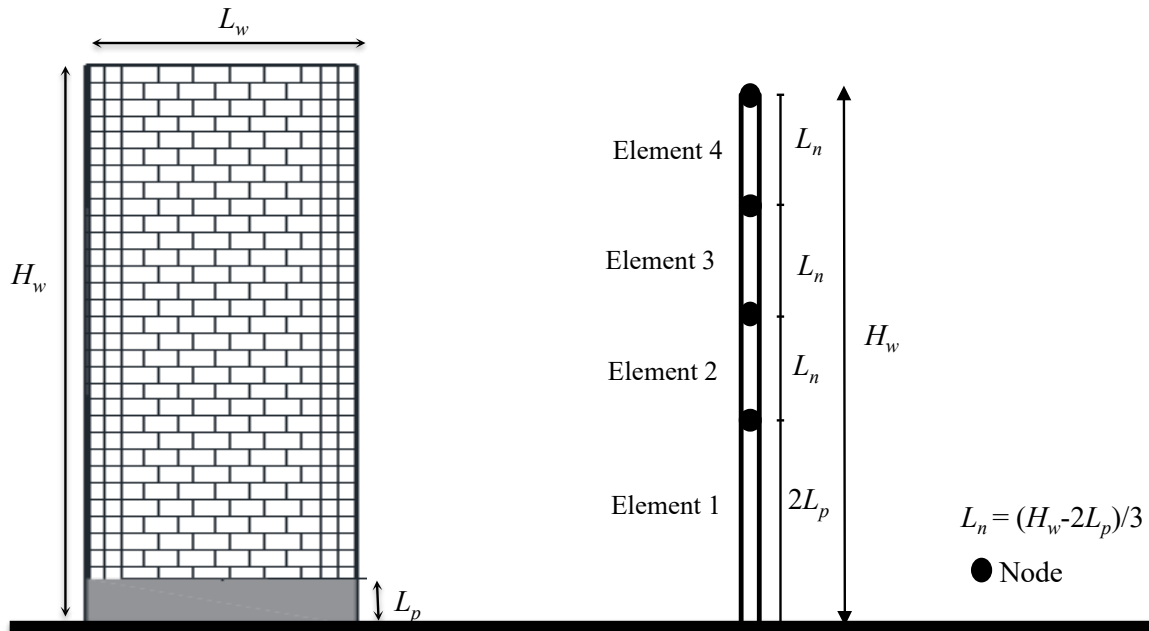


**Figure 3.4** Schematic diagram of wall used in the numerical model

In the utilized numerical modelling approach, the cross-section is divided into several fibres acting in parallel. Fibre discretization is adopted to represent the behaviour at the section level, where each fibre is associated with the corresponding uniaxial stress-strain relationships, as defined in the previous subsection for masonry and reinforcement (see Figure 3.5). The fibres in the boundary elements are divided into the region inside the confining hoops (confined) and the region outside the confining hoops (unconfined) of the cross-section. Therefore, the effect of confinement on the stress-strain response is solely taken into consideration for the confined grout core in the boundary elements. For each element, the resultant internal forces at the section are obtained by numerical integration. To ensure proper replication stress-strain relationship of the section, an adequate number of section fibres should be utilized. This mainly depends on the cross-section shape, material properties, and the expected degree of nonlinearity.

According to *SeismoStruct* user's manual (Seismosoft, 2016), 100 fibres for cross-sections composed of a single material and 200 for more complex cross-sections are recommended. Additionally, a sufficient number, around 150 to 350 fibres can lead to good estimates of the load-displacement hysteresis response according to (Boulangier et al. 2013). Consequently, a sensitivity analysis was performed to predict the optimum number of fibres required to properly simulate the flexural response of the walls (see Appendix A, Figure A.1). Based on the sensitivity analysis results, 300 fibres were used in the utilized model to ensure the accurate simulation of the stress-strain relationship and post-peak response of the walls.

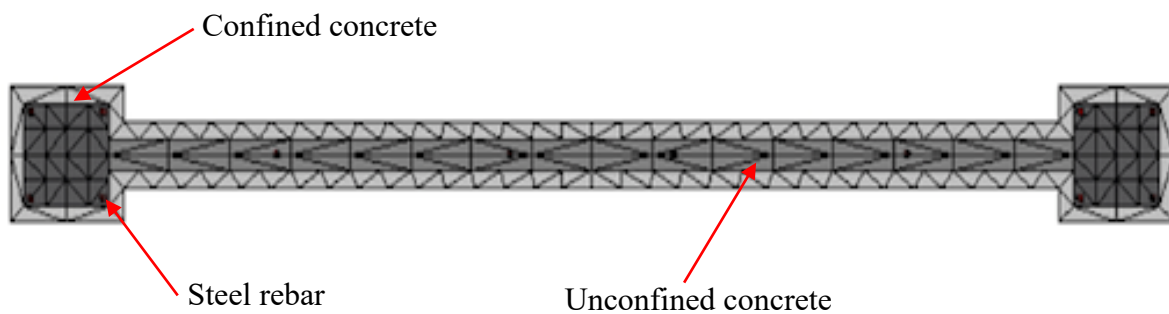


**Figure 3.5** Model discretization

## 3.4.2 OpenSees

### 3.4.2.1 Model overview

In this study, *OpenSees* (McKenna et al., 2013) modelling software is used to create macro models of the in-plane response of RMSW+BEs. The proposed model uses displacement-based (DB) beam-column elements, which assume a linear curvature distribution and a constant axial strain to determine the nonlinear response of the wall. A DB beam-column element with a fibre cross-section was used in order to model the shear wall components. The DB beam-column element was based on a displacement formulation that allows for distributed plasticity modelling, which would allow yielding to occur at any location along the element (Taucer et al. 1991). The nonlinear response of the element is therefore derived from the nonlinear stress-strain relationships for each fibre (masonry and steel). The formulation of the fibre DB beam-column element is based on sectional analysis; therefore, it does not consider bond-slip effects and neglects the effect of shear deformations. As such, additional behavioural features were included in the model to account for these aspects.

### 3.4.2.2 Material models

The utilized modelling approach primarily depends on fibre's discretization to capture the flexural response of the structural members. The analysis of RM structures requires the accurate constitutive relationships of masonry and reinforcing steel, especially for the fibre elements approach where uniaxial constitutive relationships of both constituent materials should be assigned to each element fibre. Thus, the use of reliable material models is very crucial.

#### 3.4.2.2.1 Masonry

There are no pre-defined constitutive material models developed for the simulation of the response of grouted concrete masonry in most of the available numerical modelling programs such as *OpenSees*. Previous research studies demonstrated that the anisotropic characteristics of unreinforced masonry are substantially reduced when concrete masonry is fully grouted and well detailed with horizontal and vertical reinforcement [Banting and El-Dakhkhni 2014, Drysdale and Khattab 1995, Shing et al. 1990]. Consequently, the nonlinear cyclic response of masonry is modelled using the uniaxial concrete model (*Concrete02 material*) proposed by Mander et al. (1988). *Concrete02 material* model in *OpenSees* is based on the uniaxial Kent-

Scott-Park concrete material with degraded linear unloading/reloading stiffness according to the work of Karsan-Jirsa (1969) and linear tension softening behaviour and uses the cyclic response rules developed by Martinez-Rueda and Elnashai (1997). These rules define the inelastic strain and account for the increase in stiffness deterioration and strength degradation with the increase in strain levels (i.e., it considers the accumulation of damage). Consequently, it provides an unconditionally numerically stable concrete constitutive relationship with strength and stiffness degradation at any strain level. The behavioural differences between concrete and fully grouted concrete masonry are accounted for by the proper definition of the material properties; this is also verified by comparing the simulated global response against the experimental results from the testing of fully grouted RM shear walls.

Its stress-strain relationship is presented in Figure 3.6(a). Among the available concrete models, this model was capable of simulating the nonlinear response of fully grouted masonry, which has a similar overall response to concrete. The model is calibrated by the following parameters, namely compressive strength,  $f'_m$ ; strain at max compressive strength,  $\epsilon_m$ ; crushing strength,  $f_{mu}$ ; strain at crushing strength,  $\epsilon_{mu}$ ; tensile strength,  $f_t$ ; tension softening stiffness,  $E_{ts}$ ; and  $\lambda$  which is the ratio between the unloading slope at  $\epsilon_{mu}$  and initial slope. The cyclic response rules used in Concrete02 material model define the inelastic strain “tension/compression” and account for the increase in stiffness deterioration and strength degradation with the increase in strain levels (i.e., it considers the accumulation of damage). Table 3.5 presents the compressive strength, elasticity modulus, and ultimate strain values used in the current study.

Confinement effects on masonry behaviour were also taken into account by assuming a constant confining pressure over the range of the stress-strain. The stress-strain curve assigned to the confined portions is multiplied by the confinement factor,  $K$ , as proposed by Mander et al. (1988), which is defined as the ratio between confined and unconfined concrete compressive strengths. The stress-strain relationship of confined concrete is presented in Eqs. (3.2-3.4); where  $f'_{mo}$ , and  $\epsilon'_{mo}$  are the unconfined masonry compressive strength, and the corresponding strain, respectively.  $f'_{mc}$  and  $\epsilon'_{mc}$  are confined masonry compressive strength and its corresponding strain, respectively.  $f'_l$  is the effective confining stress due to the lateral confinement reinforcement and can be determined based on the volumetric ratio and yield stress of the confinement reinforcement.

$$f'_{mc} = Kf'_{mo} \quad \text{Eq. (3.2)}$$

$$K = -1.254 + 2.254 \sqrt{1 + \frac{7.94f'_l}{f'_{co}} - 2\frac{f'_l}{f'_{co}}} \quad \text{Eq. (3.3)}$$

$$\varepsilon_{mc} = \varepsilon_{mo} \left[ 1 + 5 \left( \frac{f'_{mc}}{f'_{mo}} - 1 \right) \right] \quad \text{Eq. (3.4)}$$

### 3.4.2.2.2 Steel reinforcement

The uniaxial stress-strain model derived by Menegotto and Pinto (1973) was adopted to represent the nonlinear cyclic response of steel reinforcement. This model defined in *OpenSees* as (*Steel02 material*) incorporates the isotropic strain hardening rules defined by Filippou et al. (1983) and accounts for Baushinger effects, and pinching response in the hysteretic loops. The parameters in (*Steel 02 material*) include the modulus of elasticity,  $E_s$ , yield strength,  $f_y$ , the strain hardening coefficient,  $h$ , and other coefficients representing the transition from elastic to plastic zone  $R_0$ ,  $cR_1$ , and  $cR_2$ . Its stress-strain relationship can be seen in Figure 3.6 (b). It should be noted that buckling of vertical bars could not be simulated directly using *Steel02 material* in *OpenSees*. Therefore, the fracture strain of the steel bars was taken as 0.05 using the *MinMax material* option in *OpenSees* was used to limit the strain capacity of steel bars. Table 3.4 presents the mechanical properties of steel bars used in the numerical model. The nonlinear modelling parameters of the reinforcement were more influential than the masonry modelling parameters, in particular in terms of the initial curvature parameter,  $R_0$ , and the curvature degradation parameters ( $CR1$  and  $CR2$ ) of the transition curve. The mechanical properties of steel were chosen based on a sensitivity analysis (see Appendix A, Figures A.6 and A.7)

### 3.4.2.2.3 GFRP reinforcement

The GFRP bars are characterized by its elastic linear response under both tension and compression loading. Many studies (Deitz et al. 2003, Mallick 2008, De Luca et al. 2009) have investigated the compression behaviour of GFRP bars, and it was observed that the compressive strengths of GFRP bars are relatively low compared to the tensile strengths. Based on these studies, the compressive strength of GFRP bars was found to be between 50-80% of the tensile strength. In another study, the effect of the unbraced length-to-bar diameter ratio,  $L_u/d_b$ , on the compressive strength of the GFRP bars was investigated by AlAjarmeh et al. (2019). They concluded that bars with  $L_u/d_b$  ratio up to 4 failed by crushing, higher than a ratio of 8 failed by buckling, and those within a ratio of 4-8 failed by a combination of crushing and buckling. Also, the smaller #3 diameter bars provided almost similar ultimate compressive strength to their ultimate tensile strength, whereas the #5 and #6 bars failed at a compressive stress of only 65% of their tensile strength. They also noted that the slenderness ratio had no significant influence on the compressive modulus of elasticity. Moreover, the compressive strength capacity is not affected by  $L_u/d_b$  of 2-8, while it starts to decrease significantly after this ratio up to 55% decrease at  $L_u/d_b = 16$ . The results of these studies were considered when simulating the compression response of GFRP bars in the boundary elements. The contribution of GFRP bars in compression was considered by assuming the ultimate compressive strength capacity equal to 50% of the ultimate tensile strength capacity, while the elastic modulus of the compression curve was assumed the same as the tensile modulus, as shown in Fig. 3.6 (c). The GFRP bars were modelled using uniaxial *Elastic material* in *OpenSees* using the mechanical properties shown in Table 3.5. The Elastic Material was combined with *MinMax material* taking into consideration the ultimate strain capacity of GFRP bars.

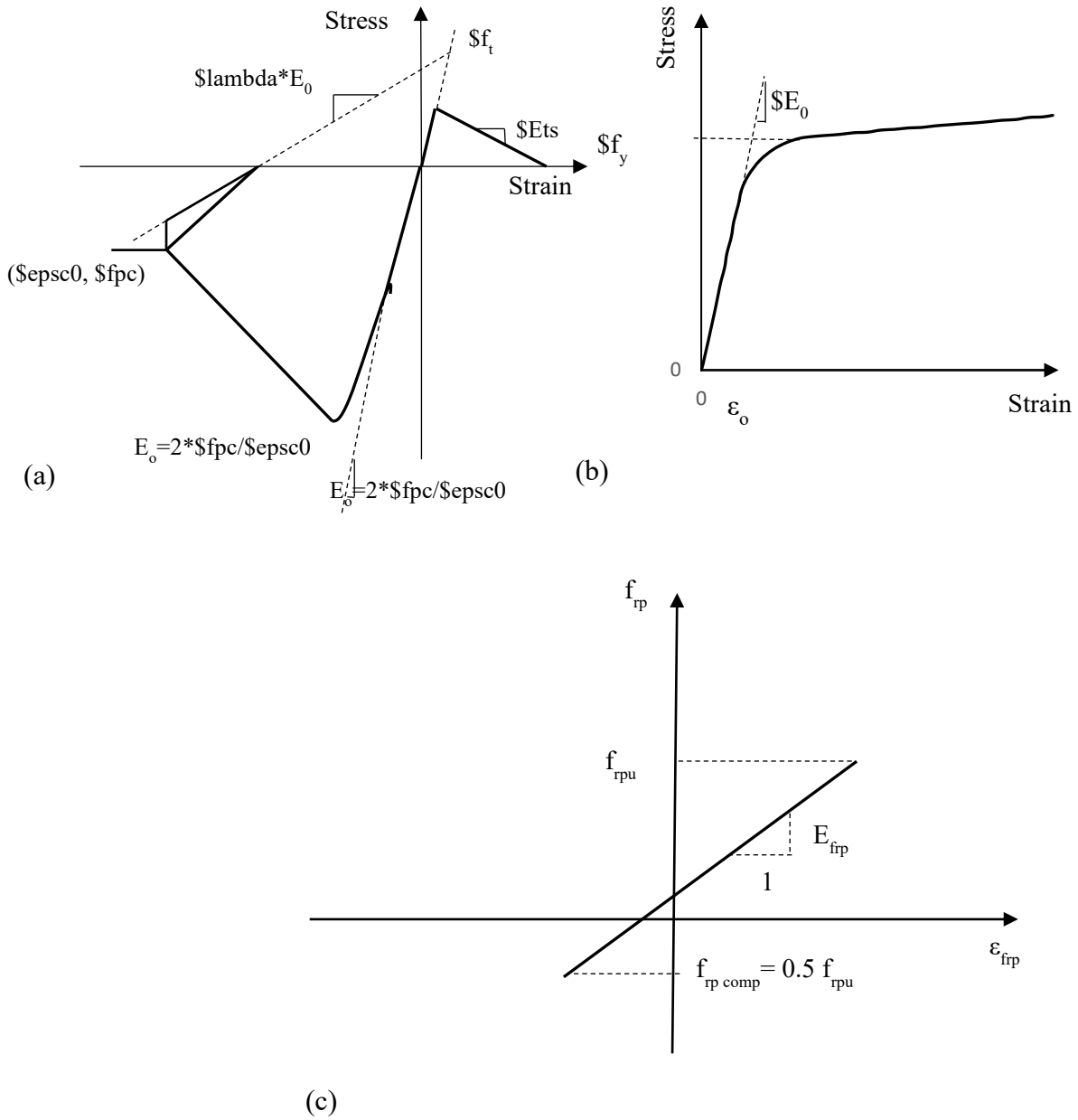


**Figure 3.6** Stress strain relationship of: (a) *Concrete02 material* (Mander et al. 1988); (b) *Steel02 material* (Menegotto and Pinto 1973); (c) *GFRP (Elastic material)*

#### 3.4.2.2.4 Confined masonry

The FRP confined masonry was simulated using the model developed by Lam and Teng (2003) intended for FRP external strengthening with some modifications. This model accounts for the unique characteristic of continuously increasing the confining pressure during the loading history due to the linear characteristics of the FRP material. The maximum compressive

strength,  $f_{cmu}$ , and the maximum compressive strain,  $\varepsilon_{cmu}$  in the FRP confined masonry, were calculated using Eq. (3.5) and Eq. (3.6), respectively.  $\varepsilon'_m$  is the maximum strain of unconfined masonry,  $f'_m$  is the unconfined masonry strength,  $k_{s1}$  is a shape factor for strength enhancement, and  $k_{s2}$  is a shape factor for strain enhancement, that both depend on the effectively confined area, and the aspect ratio.  $f_l$  is the maximum confining pressure due to the FRP confinement given by Eq. (3.7).

$$\varepsilon_{cmu} = \varepsilon'_m (1.75 + 12k_{s2} \frac{f_l}{f'_m} (\frac{\varepsilon_{fe}}{\varepsilon'_m})^{0.45}) \quad \text{Eq. (3.5)}$$

$$f'_{cm} = f'_m (1 + 3.3k_{s1} \frac{f_l}{f'_m}) \quad \text{Eq. (3.6)}$$

$$f_l = \frac{2E_f \varepsilon_{fe} (\eta t_f)}{D} \quad \text{Eq. (3.7)}$$

Where  $E_f$  is the tensile modulus of elasticity of GFRP reinforcement, the term  $\eta t_f$  represents the thickness of the confinement layer this term was replaced by the spiral tie bar diameter,  $d_f$ , and  $D$  is the diagonal of the cross-section for non-circular cross-sections,  $\varepsilon_{fe}$  is the effective strain level in GFRP reinforcement attained at failure given by Eq. (3.8):

$$\varepsilon_{fe} = k_e \varepsilon_{fu} \quad \text{Eq. (3.8)}$$

Where  $\varepsilon_{fu}$  is the ultimate tensile strain of the GFRP material,  $k_e$  is the GFRP strain efficiency factor accounts for the premature failure of the GFRP stirrups due to lower strength of the bend portion, a value of 0.26 suggested by Hassanein et al. (2019b) was used. Table 3.5 shows the mechanical material properties of steel, GFRP, and masonry used in the numerical modelling of RMSW+BEs.

**Table 3.5** Material mechanical properties utilized in the numerical models (Phase II)

Parameter		Value
Grouted Masonry	Compressive strength, $f'_{mo}$ (MPa)	17
	Elasticity modulus of masonry $E_m$ (MPa)	14850
	Strain at peak strength, $\varepsilon_{mo}$	0.0015
Steel	Elasticity modulus of steel, $E_s$ (MPa)	200,000
	Yield strength, $f_y$ (MPa)	400
	Strain hardening parameter, $h$ (%)	0.005
	Transition curve initial shape, $R$	10
	Transition curve shape	$CR1$
$CR2$		1.0
GFRP	Elasticity modulus of GFRP bars, $E_f$ (MPa)	50,000
	Ultimate strength of GFRP bars, $f_{fu}$ (MPa)	1100

### 3.4.2.3 Strain penetration effects

The strain penetration effect was considered in the modelling of RMSWs to avoid overestimating the wall's stiffness. If strain penetration is neglected, it will lead to underestimating the overall lateral drift of the wall. Kowalski et al. (1999) found that this effect makes a relatively considerable contribution to the total lateral deformation of flexural members. Hence, in the current study, the strain penetration effect was considered by using a zero-length element at the base of the wall segments. The stress-slip model proposed by Zhao and Sritharan (2007) was used to take into account the strain penetration effects in wall-footing intersections. Strain penetration represents the gradual transfer of vertical reinforcement forces to the surrounding concrete in the connecting member. The loaded end of the anchored bar exhibits slip at the connection interface resulting from the accumulative strain difference between the bar and the concrete within the connecting member. The bar embedment length was determined to be equal to or greater than the minimum anchorage length ( $l_{a,min}$ ) specified by Eq. (3.9) according to Zhao and Sritharan (2007), which was determined to be 278.6 mm.

A rotational spring at the base of the wall was used to model the bond-slip of the wall using (*Bond SP01 material*) available in the *OpenSees* platform to represent the vertical reinforcements. This model considers the total bar slip caused by strain penetration as a function

of a certain level of stress in the bar (Zhao and Sritharan 2007). Figure 3.7 shows the schematic location of a zero-length element at the base of the fibre-based model of the wall.

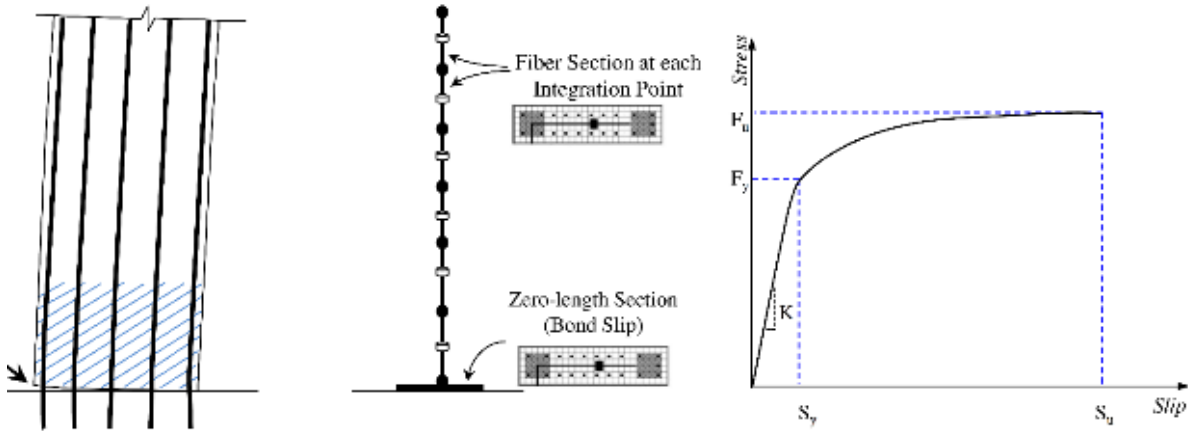


**Figure 3.7** Bond-slip components used to consider strain penetration effects: (a) schematic; (b) fibre-based model for each core wall segment; (c) stress-displacement relationship developed by Zhao and Sritharan (2007)

The parameters in (*Bond SP01 material*) include the diameter of the steel bar,  $d_b$ , yield and ultimate strengths of steel reinforcement,  $f_y$  and  $f_u$ , respectively. The material also includes the rebar slip at member interface under yield stress,  $S_y$ , the compressive strength of the adjoining connection member,  $f'_m$ , the rebar slip at the loaded end at the bar fracture strength,  $S_u$ . The parameters  $S_y$  and  $S_u$  can be calculated as given in Eq. (3.10) and Eq. (3.11), respectively. The parameter  $\alpha$  used in the local bond slip reaction was taken as 0.4, and the pinching factor for the cyclic slip vs. bar response,  $R$  was taken as 0.6. The initial hardening ratio in the monotonic slip vs. bar stress response,  $b$  was taken as 0.4.

$$l_{a,\min} = \frac{1}{7} \frac{f_y}{\sqrt{f'_m}} d_b \quad \text{Eq. (3.9)}$$

$$S_y = 2.5 \left( \frac{d_b}{8437} \frac{f_y}{\sqrt{f'_m}} (2\alpha + 1) \right)^{1/\alpha} \quad \text{Eq. (3.10)}$$

$$S_u = 35S_y \quad \text{Eq. (3.11)}$$

#### 3.4.2.4 Shear deformations

Most fibre elements do not account for the effect of shear deformations that occur due to lateral load, although experimental research shows that the flexure and shear displacements are coupled for most of the walls, even for walls with a relatively high aspect ratio (Massone and Wallace 2004). Subsequently, it was necessary to account for shear deformations in the adopted model. Therefore, the shear deformations in the walls were aggregated using a uniaxial material model available in the *OpenSees* platform (*Pinching4 material*) to facilitate accurate predictions of wall displacements.

*Pinching4* is a one-dimensional hysteretic load-deformation response model that involves a response envelope, an unload-reload path, and three damage rules that control the evolution of these paths (Lowe et al. 2013). Global material response parameters describing the walls' load-displacement envelopes are estimated and used as input for the *Pinching4* material. The forces global parameters indicated in Figure 3.8 as  $ePf1$ ,  $ePf2$ ,  $ePf3$ , and  $ePf4$  were estimated using mechanics based flexural analysis of shear walls, including the self-weight of the walls. On the other hand, the displacements illustrated in Figure 3.8 as  $ePd1$ ,  $ePd2$ ,  $ePd3$ , and  $ePd4$  were estimated using deflection calculation of cantilever walls with top load application taking into account flexural and shear displacements when calculating the gross stiffness of the walls. In this respect, three points were defined for the *Pinching4* material model as recommended by Waugh and Sritharan (2010). To define the first point, the lateral force corresponding to the first flexural cracking and the uncracked shear stiffness were used. The uncracked shear stiffness was obtained following the recommendations of Park and Paulay (1975) for uncracked rectangular beam. The second point was determined using the lateral force that was expected to cause flexural yielding of the vertical reinforcement and the effective shear stiffness (20% of the uncracked stiffness). The third point was defined using the ultimate lateral force and the post-yield shear stiffness (1% of the effective shear stiffness).

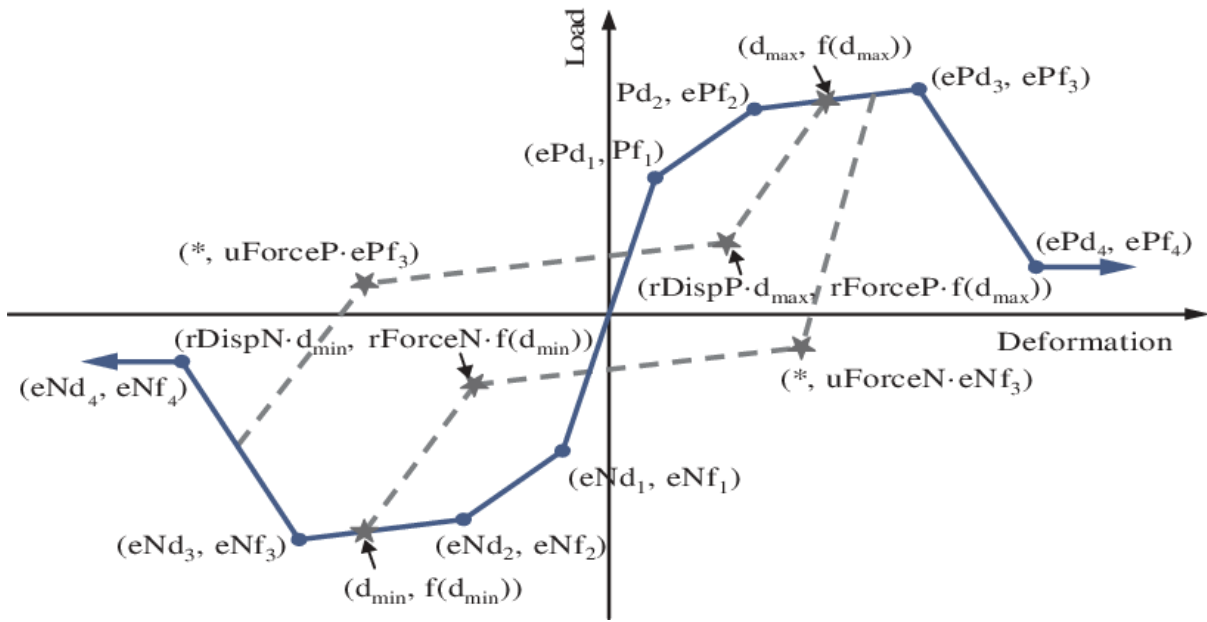


**Figure 3.8** Pinching\_4 material model used for modelling shear (McKenna et al. 2013)  
adapted from the *OpenSees* manual, 2012)

### 3.4.2.5 Section model

As discussed earlier, the cross-section is subdivided into several individual fibres acting in parallel to simulate the response of RM shear walls (see Figure 3.9). For masonry and steel reinforcement, the uniaxial stress-strain relationships are assigned to the corresponding section fibres. The strain or stress distribution over each section is then obtained through the integration of the nonlinear uniaxial stress-strain response of the individual fibres according to number of fibres per section. The confinement effect was taken into consideration in the model by assigning different material properties to the masonry region confined by stirrups within the boundary element.

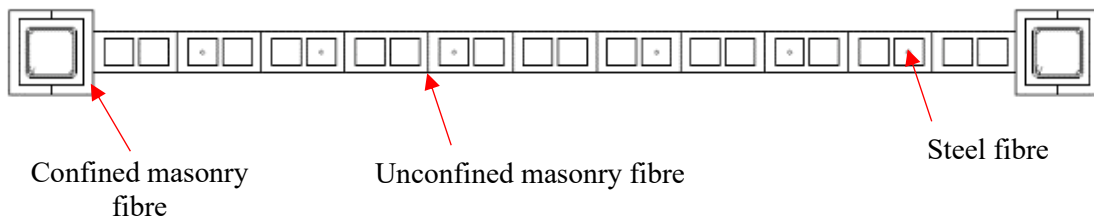


**Figure 3.9** Fibre distribution in the wall section

### 3.4.2.6 Element model

A schematic of the numerical model of the wall is illustrated in Figure 3.10, including the configuration of nodes and elements. It consists of an extreme member (1<sup>st</sup> element) with length equal to twice the plastic hinge and three members with equal lengths. All walls were assumed to have perfect base fixity, and soil-structure interaction was neglected as per the NIST study (2010). The choice of element length is essential when displacement-based beam-column elements are used with distributed plasticity and strain-softening material definitions (Ezzeldin et al. 2014). In RM structural walls, the strain localization will be concentrated in the first element above the wall base. Therefore, it was highlighted by several researchers (Légeron et al. 2005, Calabrese et al. 2010, Ezzeldin et al. 2016) that the use of  $L_p$  for the first element above the wall base, produces accurate and objective results. However, Calabrese et al. (2010) highlighted that localization and strain concentrations occur in the extreme integration point and not the extreme element. Therefore, the length of the extreme member could be twice the plastic hinge length ( $2*L_p$ ) in the typical case of two integration sections per element. This regularization technique achieves an objective global response in cases where softening sectional behaviour is present. The sensitivity of the utilized response regularization technique was assessed for RM shear walls modelled in *OpensSees* (See Appendix A, Figure A.3). It was observed that the overall simulated hysteresis response was not affected by the choice of the total number of elements. Thus, this regularization technique (i.e., first element length equal to  $2L_p$ ), was proven to reduce the dependency of the hysteresis response results on the number of utilized elements; hence, increasing the objectivity of the response predictions and scatter of results. As mentioned earlier, Bohl and Adebar (2011) given in Eq. (3.1) was deemed to be appropriate to be utilized for the calculation of  $L_p$ . Table 3.6 shows the plastic hinge lengths for 34 walls in Phase II.

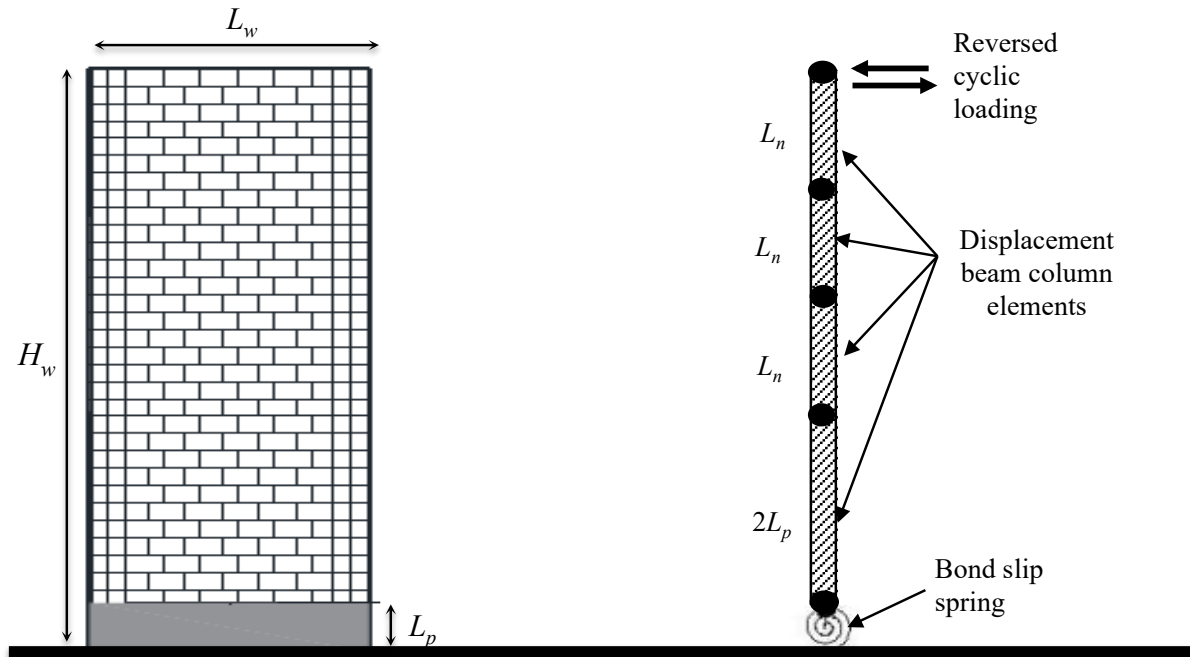


**Figure 3.10** Schematic diagram of the element and node distribution of RMSW+BE

**Table 3.6** Plastic hinge lengths for walls in Phase II

Wall Type	$H_w$ (mm)	$P$ (N)	$L_p$ (mm)
4- storey	12000	671580	1358.0
5- storey	15000	839475	1437.2
6- storey	18000	1007370	1513.4

### 3.5 Numerical Model Validation

#### 3.5.1 Validation of walls using SeismoStruct

The model predictions of the proposed modelling approach were validated against experimental tests data of RM shear walls from literature prior to the parametric study assessment. Four RM shear wall specimens experimentally tested under fully reversed displacement controlled quasi-static cyclic were used for the numerical model validation. All the walls were subjected to the same loading protocol as their corresponding experimental tests. The validation of the numerical modelling approach included walls that are rectangular and end-confined. Validating the numerical model against walls with different cross-sectional configurations, aspect ratios, and axial stress levels ensures the accuracy, reliability, and robustness of the utilized modelling approach. Table 3.7 summarizes the various design aspects of the four RM shear walls. Figure 3.11 shows the cross-section of walls utilized for the model validation, showing the wall dimensions, axial stress level, vertical and horizontal reinforcement details. The vertical,  $\rho_v$ , and horizontal reinforcement ratios,  $\rho_h$ , are defined as ratios of the areas of reinforcing bars to gross area of the horizontal or vertical masonry cross section, respectively.

**Table 3.7** Summary of wall details used for the model validation

Wall ID.	$L_w$ (mm)	$H_w$ (mm)	Vertical reinforcement		Horizontal reinforcement		AR	Axial stress (MPa)	Configuration
			No. & Size	$\rho_v$ (%)	No. & spacing (mm)	$\rho_h$ (%)			
W2 <sup>a</sup>	1235	3990	10-10M	0.69	1- D4 @ 95	0.3	3.2 3	0.89	End confined
W3 <sup>b</sup>	1802	3990	11-10M	0.55	1- D4 @ 95	0.3	2.2 1	0.89	End confined
W6 <sup>c</sup>	1802	2660	11-10M	0.55	2-D4 @ 95	0.6	1.4 8	0.89	End confined
W1 <sup>d</sup>	1802	3990	19-10M	1.17	1- D4 @ 95	0.3	2.2	1.09	Rectangular

<sup>a</sup> adopted from Banting and El-Dakhkhni (2014),

<sup>b</sup> adopted from Shedid et al. (2010),

<sup>c</sup> adopted from Shedid et al. (2010),

<sup>d</sup> adopted from Shedid et al. (2010).

The selected walls have different aspect ratios, ranging from 1.48 to 3.23. W2 adopted from Banting and El-Dakhkhni (2014) had a length of 1235 mm, height of 3990 mm,  $\rho_v$  of 0.69%, and  $\rho_h$  of 0.3 %. W1 adopted from Shedid et al. (2010) with a rectangular cross-section was 1802 mm in length, 90 mm in thickness, and 3990 mm in height. W3 and W6 adopted from Shedid et al.

(2010) had a length of 1802 mm were each detailed with  $\rho_v$  of 0.55%, but varied by  $\rho_h$  of 0.3% and 0.6% and a height of 3990 and 2660 mm respectively. The material mechanical properties reported by Banting and El-Dakhakhni (2014), and Shedid et al. (2010) were used in the model validation. The average compressive strength of the masonry prisms based on the experimental results was reported as 15 MPa for W2 and 16.4 MPa for W3, W6, and W1. The vertical steel reinforcement consisted of 10M bars [ $A_v=100 \text{ mm}^2$ ,  $d_b=11\text{mm}$ ] with yield strength of 496 MPa and Young's modulus of 200.6 GPa is utilized for all the walls. The horizontal reinforcement and stirrups were comprised of deformed wire, D4, [ $A_h=25.4 \text{ mm}^2$ ,  $d_b=5.7 \text{ mm}$ ] with a proof yield strength of 582.5 MPa for W2 and 534 MPa for W3, W6, and W1. As discussed earlier, the steel reinforcement was modelled using Menegotto and Pinto (1973) nonlinear steel model, and the confined and unconfined masonry was modelled using Mander et al. (1988) stress-strain model.

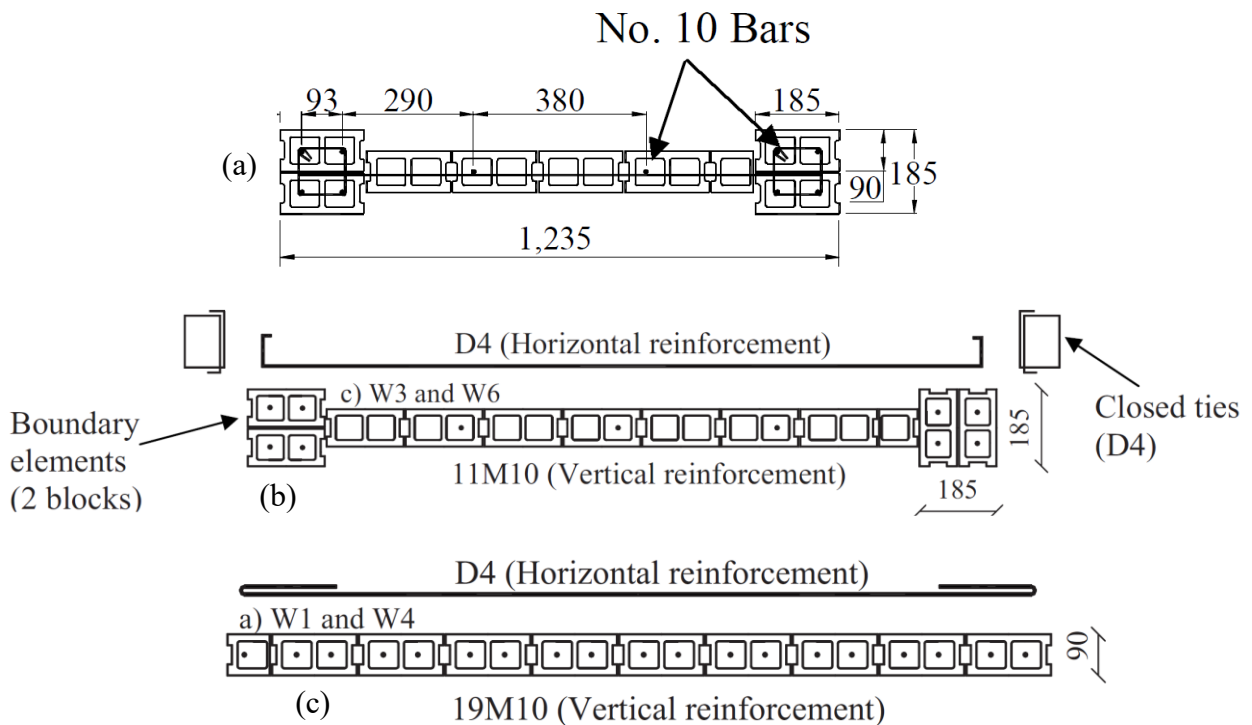


**Figure 3.11** Cross-section of walls utilized for numerical validation (a) W2; (b) W3 and W6; (c) W1

The computed load-displacement hysteresis of the four RM shear walls was validated against the experimental results reported by Banting and El-Dakhakhni (2014), and Shedid et al. (2010).

Figure 3.12 shows a good agreement between the experimental hysteresis loops and the corresponding computed numerical loops. The model was able to simulate the most relevant characteristics of the cyclic response, including the initial stiffness, peak load, stiffness degradation, and strength degradation at different drift levels. A summary of the strengths and displacement ductility computed from the experimental and numerical results is provided in Table 3.8. The key parameters of the walls include the yield load,  $Q_y$ , peak lateral load,  $Q_u$ , lateral load corresponding to 20% strength degradation,  $Q_{0.8u}$ , and displacement ductility at peak,  $\mu_{\Delta u}$  ( $\mu_{\Delta u} = \Delta_u / \Delta_y$ ). It can be observed from Table 3.8 that the model was able to compute the RMSW+BEs lateral capacity with a maximum error of 13%. The displacement ductility of the four walls is represented well by the numerical model, with a maximum error within 10%. Overall, it can be concluded that a good agreement between the experimental and numerical results was achieved considering the natural variation in reinforced masonry shear wall properties.

**Table 3.8** Validation of model predictions with the experimental data

Wall ID.	Load dir.	Experimental				Numerical				% Error			
		$Q_y$ (kN)	$Q_u$ (kN)	$Q_{0.8u}$ (kN)	$\mu_{\Delta u}$	$Q_y$ (kN)	$Q_u$ (kN)	$Q_{0.8u}$ (kN)	$\mu_{\Delta u}$	$Q_y$ (%)	$Q_u$ (%)	$Q_{0.8u}$ (%)	$\mu_{\Delta u}$ (%)
W2	(+) ve	76.4	94.1	76.0	3.0	81.3	93.3	74.6	2.9	7.7	0.9	1.8	3.3
	(-) ve	70.9	88.0	70.4	2.7	78.0	92.1	73.7	2.9	10.0	4.7	4.7	7.4
W3	(+) ve	112.0	151.0	123.0	4.3	120.9	154.0	123.2	4.0	7.9	2.0	0.2	7.0
	(-) ve	109.0	147.0	121.0	4.0	115.5	151.0	120.8	3.8	5.5	2.7	0.2	5.0
W6	(+) ve	174.0	247.0	194.0	5.9	195.0	245.5	196.4	5.7	12.7	0.6	1.2	3.4
	(-) ve	170.0	232.0	190.0	6.2	190.0	243.9	195.1	5.9	12.4	5.1	2.7	4.8
W1	(+) ve	101.0	177.0	142.0	5.6	110.0	185.0	148.0	5.1	8.2	4.5	4.2	8.9
	(-) ve	110.0	180.0	145.0	5.3	115.0	183.7	147.0	4.8	4.5	2.1	1.4	9.4

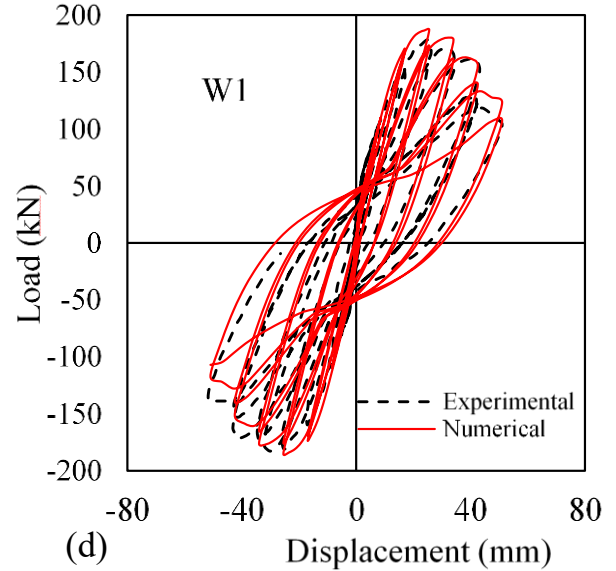
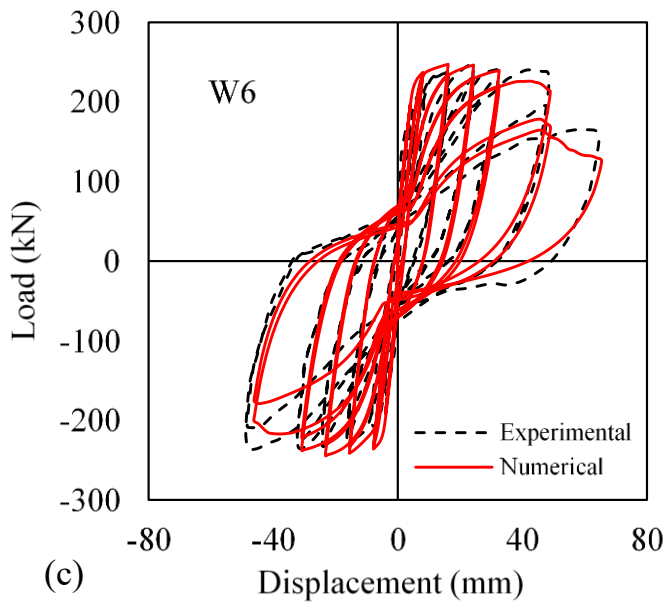
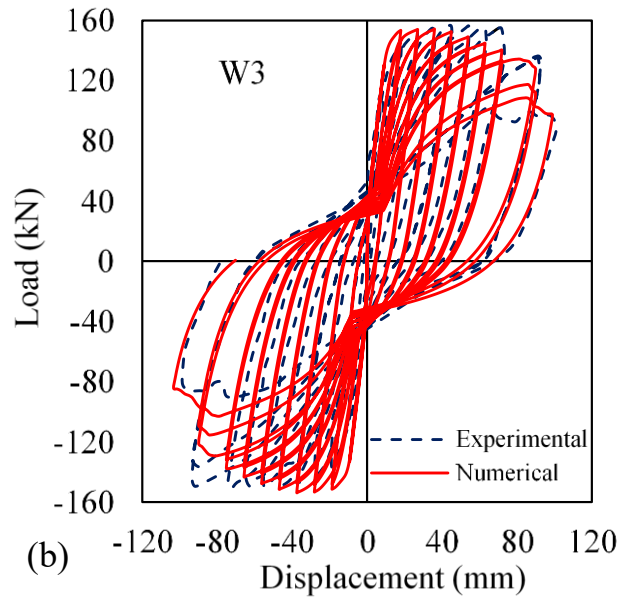
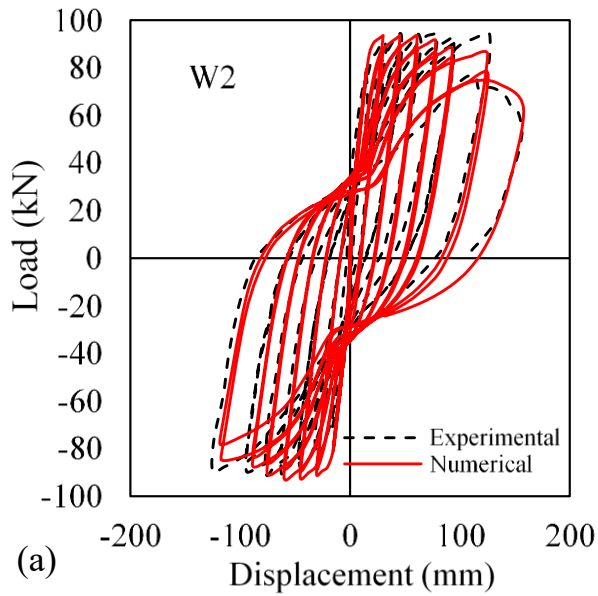


**Figure 3.12** Experimental versus numerical hysteresis loops: (a) W2 (adopted from Banting et al. 2014); (b) W3 (adopted from Shedid et al. 2010); (c) W6 (adopted from Shedid et al. 2010); and (d) W1 (adopted from Shedid et al. 2010)

### 3.5.2 Validation of walls using OpenSees

The proposed nonlinear modelling approach, along with the calibrated material modelling parameters implemented in this study were validated against two sets of experimental tests provided in the literature: Group-A for RMSW+BEs reinforced with steel rebars, and Group-B for RMSW+BEs reinforced with GFRP bars. It should be noted that there were no tests found in the literature for masonry shear walls reinforced with GFRP bars. Hence the authors calibrated the numerical model with concrete shear walls reinforced with GFRP bars since the behaviour is expected to be similar to that of RMSW. In order to validate the modelling approach and the assumed failure criteria for Group-A, three RM wall specimens were selected from Shedid et al. (2010), and Banting and El-Dakhakhni (2012) and were modelled using the numerical modelling approach detailed in the previous sections. As for Group-B, one reinforced concrete wall was modelled from Hassanein et al. (2019a), this wall was selected as it has similar reinforcement, wall dimensions, and boundary element detailing to the walls under study.

Validating the numerical model against walls with different aspect ratios, axial stress levels, and vertical reinforcement ratios ensures the accuracy, reliability, and robustness of the utilized modelling approach. Table 3.9 shows a summary of the walls' details used in numerical model validation. The cross-sections of the validated walls are shown in Figure 3.13. The same loading protocol used in the experimental tests was used in order to compare the numerical model and experimental test results. In addition, the values of masonry and steel material model parameters were based on material tests reported in the corresponding experimental studies (Shedid et al. 2010, Banting and El-Dakhakhni 2012, and Hassanein et al. 2019a). The selected walls have different aspect ratios, ranging from 1.5 to 2.3. W1 adopted from Shedid et al. (2010) had a length of 1802 mm, height of 3990 mm,  $\rho_v$  of 0.55%, and  $\rho_h$  of 0.3 %. W1 adopted from Banting and El-Dakhakhni (2012) had a length of 1235 mm, and a height of 1900 was detailed with  $\rho_v$  of 0.55%, and  $\rho_h$  of 0.6%. W11 adopted from Banting and El-Dakhakhni (2012) was 2665 mm in length, and 3990 mm in height with  $\rho_v$  of 0.51%, and  $\rho_h$  of 0.3%. WGnoX, an RC shear wall reinforced with GFRP bars, adopted from Hassanein et al. (2019a), was 1500 mm in length, 3500 mm in height, and detailed with  $\rho_v$  of 0.55%, and  $\rho_h$  of 1.6%.

**Table 3.9** Summary of wall details used for numerical model validation

Wall ID.	$L_w$ (mm)	$H_w$ (mm)	$AR$	Vertical reinforcement		Horizontal reinforcement		Axial stress (MPa)
				No. and size	$\rho_v$ (%)	Size @ spacing (mm)	$\rho_h$ (%)	
W3 <sup>a</sup>	1802	3990	2.2	11 No.10	0.55	D4@95	0.3	0.89
W1 <sup>b</sup>	1235	1900	1.5	10 No.10	0.69	D4@95	0.6	0.89
W11 <sup>c</sup>	2665	3990	1.5	14 No.10	0.51	D4@95	0.3	0.89
GnoX <sup>d</sup>	1500	3500	2.3	18 #3 GFRP	0.55	#4 GFRP @80	1.6	4.43

<sup>a</sup>adopted from Shedid et al. (2010),

<sup>b</sup> adopted from Banting et al. (2012),

<sup>c</sup> adopted from Banting et al. (2012),

<sup>d</sup> adopted from Hassanein et al. (20109a)

For the model validation, the material mechanical properties reported by Banting et al. (2012), Shedid et al. (2010), and Hassanein et al. (2019a) were used. The average compressive strength of the masonry prisms based on the experimental results was reported as 16.4 MPa for W3 and 15.0 MPa for W1, and W11. The vertical steel reinforcement consisted of 10M bars [ $A_v=100 \text{ mm}^2$ ,  $d_b=11 \text{ mm}$ ] with yield strength of 496 MPa, and Young's modulus of 200.6 GPa is utilized for all the walls. The horizontal reinforcement and stirrups were comprised of deformed wire, D4, [ $A_h=25.4 \text{ mm}^2$ ,  $d_b=5.7 \text{ mm}$ ] with yield strength of 534 MPa for W3; and 582.5 MPa for W1, and W11. For GnoX, the vertical web reinforcement consisted of two layers of #3 GFRP [ $E_f= 62.5 \text{ GPa}$ ,  $d_b=9.5 \text{ mm}$ ,  $f_{fu}=1303 \text{ MPa}$ ] bars spaced at 120 mm, and the horizontal reinforcement consists of two layers of #4 GFRP bars [ $E_f= 61.3 \text{ GPa}$ ,  $d_b= 12.7 \text{ mm}$ ,  $f_{fu}= 1346 \text{ MPa}$ ], spaced at 80 mm. As described earlier, the steel reinforcement was modelled using Menegotto and Pinto (1973) nonlinear steel model, and the confined and unconfined masonry was modelled using Mander et al. (1988) stress-strain model. The GFRP bars for GnoX were modelled using the uniaxial *Elastic material* model. Figure 3.14 shows a comparison between the experimental and the numerical load-displacement response of the walls. It can be seen that the numerical model is in good agreement with the hysteretic responses of the experimental test results. The numerical model is capable of simulating the initial stiffness, yield, and ultimate strengths, displacements, loading, and unloading of the post-peak branches.

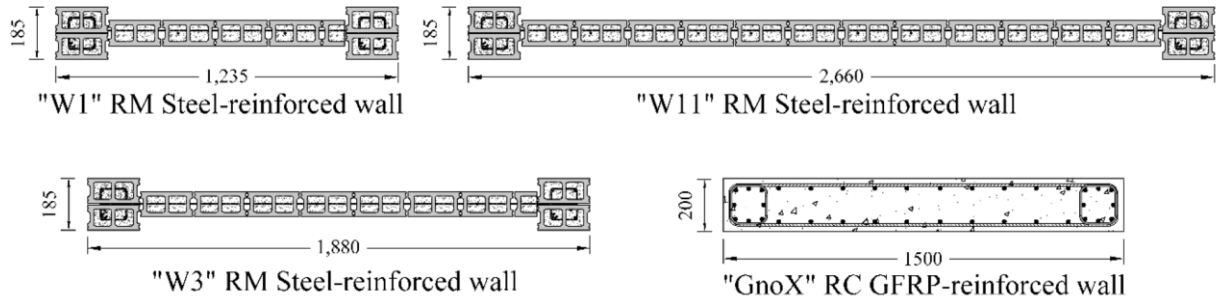


**Figure 3.13** Cross-section details of W1 and W11 (Banting and El-Dakhakhni 2012), W3 (Shedid et al. 2010) and GnoX (Hassanein et al. 2019a)

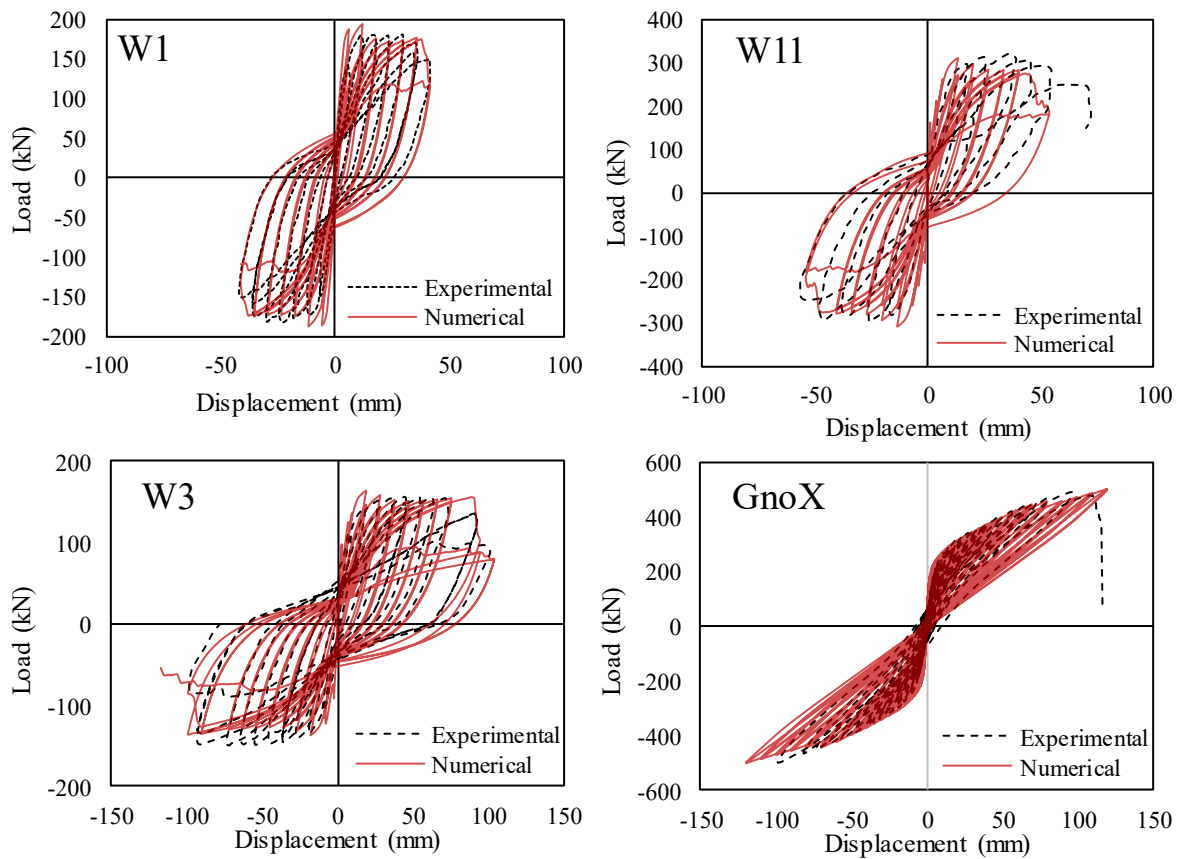


**Figure 3.14** Experimental and numerical load-displacement response of W1 (Banting and El-Dakhakhni 2012), W11 (Banting and El-Dakhakhni 2012), W3 (Shedid et al. 2010) and GnoX (Hassanein et al. 2019a)

Table 3.10 compares the numerical model key parameters, including strength and displacement predictions, with the corresponding experimental values. The key parameters of the walls include the yield strength,  $Q_y$ , ultimate strength,  $Q_u$ , strength corresponding to 20% strength degradation,  $Q_{0.8u}$ , and displacement ductility at the peak,  $\mu_{\Delta u}$ . It can be observed from Table 3.10 that the model was able to compute the RMSW+BEs lateral capacity with high accuracy. Also, the numerical model, with a maximum error of 7.0%, captured the key parameters of the behaviour. Overall, it can be concluded that the proposed numerical model can simulate the nonlinear response of RMSW+BEs with acceptable accuracy.

**Table 3.10** Comparison of numerical model predictions with the experimental data

Wall ID.	Experimental				Numerical				% Difference			
	$Q_y$ (kN)	$Q_u$ (kN)	$Q_{0.8u}$ (kN)	$\mu_{\Delta u}$	$Q_y$ (kN)	$Q_u$ (kN)	$Q_{0.8u}$ (kN)	$\mu_{\Delta u}$	$Q_y$ (%)	$Q_u$ (%)	$Q_{0.8u}$ (%)	$\mu_{\Delta u}$ (%)
W3	114.0	152.0	123.0	4.0	121.2	161.0	129.2	4.2	6.3	5.9	5.0	5.0
W1	150.0	177.4	141.9	4.9	157.0	181.9	151.1	5.0	4.7	2.5	6.5	2.0
W11	247.9	314.3	251.4	7.4	236.8	292.4	233.9	6.9	4.5	7.0	7.0	6.8
GnoX	-	488.4	-	-	-	501.1	-	-	-	2.6	-	-

## Chapter 4

### Effect of Design Parameters on the Inelastic Response of RMSW+BEs

#### 4.1 Introduction

Chapter 4 focuses on the seismic response of full-scale flexure-dominated RM shear walls with C-shaped boundary elements considering the effect of different design parameters such as transverse hoop spacing, size of boundary element, type of reinforcement (steel vs. GFRP), amount of vertical reinforcement in the boundary element, axial stress, and aspect ratio of the wall. This chapter documents the influence of the design parameters on the wall's hysteretic response, and displacement ductility to evaluate the enhancement in seismic performance of RM shear walls.

#### 4.2 Numerical Program

Numerical models were developed to assess the influence of different parameters on the lateral response of seventy RM shear walls with C-shaped boundary elements (RMSW+BEs). All walls were subjected to fully reversed displacement controlled quasi-static cyclic loading and were cycled up to 20% strength degradation. As mentioned earlier, the study is divided into two phases for the numerical modelling of full-scale, fully grouted RMSW+BEs. These parameters include the amount of vertical reinforcement ratio in boundary element, boundary element size, spacing of transverse reinforcement in boundary element, type of vertical and horizontal reinforcement (GFRP vs steel), and aspect ratio of the wall. The following sections provide results on the influence of the studied design parameters on the seismic response of RMSW+BEs.

#### 4.3 Lateral Load-Displacement Response

Figure 4.1 shows the typical hysteretic response for walls (S6S4-0, S12S4-60, and S12G4-60) from Phase I, and II. It can be seen that the steel-reinforced walls (S6S4-0, S12S4-60) had approximately a linear elastic response until the onset of the first yield in the outermost vertical reinforcement. The linear response was accompanied by thin hysteresis loops indicating a low level of energy dissipation. The response of the walls started to become nonlinear at higher lateral displacements after yielding of vertical reinforcement. Wider hysteresis loops were then observed, signifying the increase in the energy dissipated by the walls through the yielding of reinforcement and level of damage of masonry.

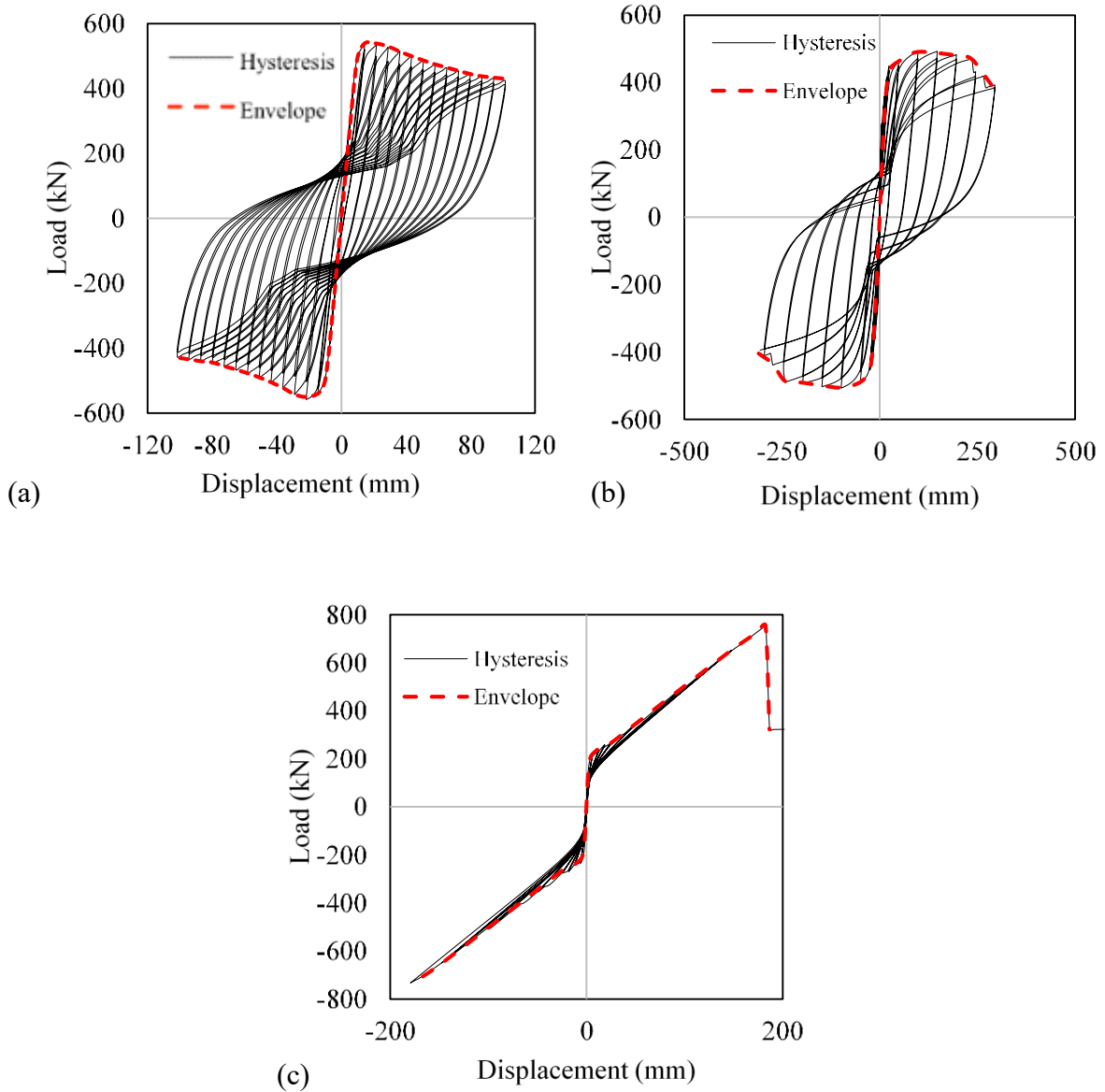


**Figure 4.1** Typical load-displacement hysteresis and envelope: (a) S6S4-0, (b) S12 S4-60, (c) S12G4-60

As depicted in Figure 4.1, the steel-reinforced walls (S6S4-0, S12S4-60) displayed a ductile hysteretic response that is nearly symmetric in both push and pull direction. The steel-reinforced walls in this study had similar behaviour in both directions with a symmetric lateral resistance and wide-open cycles. On the other hand, the hysteretic behaviour of the GFRP-reinforced walls (see Figure 4.1c) showed pinched hysteresis loops with symmetric lateral load-displacement relationship for loading in both the (+ve) and (-ve) direction until failure occurred at one end. The cycles in

the case of GFRP-reinforced walls had a minimal residual force, which is similar to the walls tested by Hassanein et al. (2019a). The GFRP-reinforced walls reached the ultimate strength and no strength degradation up to the peak point. The unloading and reloading curves showed linearity due to the GFRP elastic behaviour. The envelope of the load-displacement hysteretic curves for each wall was also generated using the peak of the hysteresis loop corresponding to each lateral displacement. Similarly, the envelopes of the load-displacement relationships were computed from the numerical models for the seventy walls in both Phases I and II. The load-displacement hysteresis of the seventy-modelled walls in Phases I and II can be seen in Appendix B, Figure B.1.

The lateral load and corresponding displacements of each of the modelled walls were obtained from the generated envelopes of the walls. In addition, analytical calculations using first principles (i.e., equilibrium and compatibility) were carried out using CSA S304 (2014) to predict the wall's yield strength,  $Q_{y(pred)}$ , and peak flexural strength,  $Q_{u(pred)}$  to further validate the numerical model calculations. Force equilibrium and plane section strain compatibility were used to determine  $Q_{y(pred)}$ , and  $Q_{u(pred)}$ . The theoretical yield strength was determined by assuming elastic strength in the masonry,  $f'_m = \epsilon_m \times E_m$ , and the extreme reinforcement at its average yield strain ( $\epsilon_u = 0.0025$ ) employed in CSA S304 (2014). The theoretical peak flexural strength,  $Q_{u(pred)}$ , was determined assuming an equivalent stress block of strength  $0.85f'_m$  over a compression block of strength  $0.85f'_m$  over a compression block depth of  $0.8c$  with a limiting strain of  $\epsilon_{mu} = 0.003$  as prescribed in the CSA S304 (2014). The predicted analytical and numerical lateral capacities at yield and the peak of all walls are listed in Table 4.1 and Table 4.2. For all walls, the ratio between the analytical and the numerical strength ranged between 1.0 and 1.2, and between 0.8 and 1.1 for the yield and ultimate load calculations, respectively. Consequently, a good agreement between the analytical and numerical predictions is achieved. The numerical yield load,  $Q_y$ , maximum load,  $Q_u$ , ultimate load  $Q_{0.8u}$ , and their corresponding yield displacement,  $\Delta_y$  (at the onset of the yield of vertical reinforcement), maximum displacement,  $\Delta_u$  (at maximum load), and ultimate displacement,  $\Delta_{0.8u}$  (at 20% strength degradation) of the walls are also shown in Tables 4.1 and 4.2, from Phase I, and II, respectively.

**Table 4.1** Summary of lateral load and displacement of RMSW+BEs in Phase I

Wall ID.	$Q_y$	$\Delta_y$	$Q_u$	$\Delta_u$	$Q_{0.8u}$	$\Delta_{0.8u}$	$Q_{y(pred)}$	$Q_{u(pred)}$	$Q_u / Q_{u(pred)}$	$Q_y / Q_{y(pred)}$
	(kN)	(mm)	(kN)	(mm)	(kN)	(mm)	(kN)	(kN)		
	Avg	Avg	Avg	Avg	Avg	Avg	Avg	Avg		
S6S4-0	385.8	7.3	545.0	21.8	436.0	100.0	348.5	612.0	0.89	1.11
S9S4-0	266.1	16.3	360.2	49.0	288.2	174.5	232.3	408.1	0.88	1.15
S12S4-0	190.0	29.1	274.0	82.6	219.2	270.75	174.2	306.1	0.90	1.09
S15S4-0	155.0	45.4	224.9	131.3	179.9	381.6	139.4	244.8	0.92	1.11
S6S6-0	518.9	7.5	720.0	22.4	576.0	92.5	483.0	791.9	0.91	1.07
S9S6-0	354.1	16.8	469.8	48.5	94.0	159.0	321.7	535.2	0.88	1.10
S12S6-0	272.1	29.8	355.6	89.4	284.5	238.4	241.3	401.4	0.89	1.13
S15S6-0	223.3	46.6	290.7	137.5	232.6	349.5	193.0	321.1	0.91	1.16
S6S8-0	651.6	7.6	893.0	22.6	714.4	87.5	616.5	808.0	1.11	1.06
S9S8-0	441.8	17.2	575.0	51.5	460.0	151.5	411.0	665.5	0.86	1.07
S12S8-0	337.1	30.5	434.0	88.2	347.2	228.8	308.3	401.4	1.08	1.09
S15S8-0	275.0	47.7	352.1	137.6	281.7	333.2	246.6	399.3	0.88	1.12
S6S4-0.3	491.0	7.5	635.4	21.8	508.3	95.0	425.0	721.8	0.88	1.16
S9S4-0.45	355.0	17.2	450.4	51.3	360.3	162.6	308.0	517.5	0.87	1.15
S12S4-0.6	287.0	31.1	361.7	93.3	289.4	247.5	249.5	415.3	0.87	1.15
S15S4-0.75	240.0	49.1	301.0	142.0	240.8	343.8	209.0	351.3	0.86	1.15
S6S6-0.3	621.2	7.7	811.0	22.3	648.8	86.0	558.0	912.8	0.89	1.11
S9S6-0.45	454.8	17.6	557.2	50.7	445.8	147.8	396.5	644.6	0.86	1.15
S12S6-0.6	364.0	31.7	441.5	95.1	353.2	236.8	316.0	510.6	0.86	1.15
S15S6-0.75	288.0	50.1	361.3	147.5	289.0	322.5	262.4	415.3	0.87	1.10
S6S8-0.3	751.3	7.9	983.9	23.6	787.1	82.5	692.4	1106.9	0.89	1.09
S9S8-0.45	540.6	17.9	665.9	51.9	532.7	141.5	485.1	774.0	0.86	1.11
S12S8-0.6	432.8	32.3	522.5	95.0	418.0	207.5	382.1	615.2	0.85	1.13
S15S8-0.75	362.0	50.9	424.8	152.7	339.8	310.0	315.3	463.6	0.92	1.15
S6S4-0.6	577.0	7.8	729.0	22.1	583.2	88.5	497.3	827.7	0.88	1.16
S9S4-0.9	440.0	18.0	551.0	53.0	440.8	144.6	381.5	625.2	0.88	1.15
S12S4-1.2	352.8	32.9	442.5	148.4	354.0	220.0	322.2	507.5	0.87	1.09
S15S4-1.5	297.2	52.4	376.0	102.7	300.8	250.0	276.8	403.1	0.93	1.07
S6S6-0.6	720.5	7.9	902.5	36.2	722.0	77.0	634.6	1021.3	0.88	1.14
S9S6-0.9	548.2	18.4	667.5	55.0	534.0	128.4	472.5	752.0	0.89	1.16
S12S6-1.2	416.0	33.5	521.0	100.4	416.8	187.5	388.0	507.5	1.03	1.07
S15S6-1.5	347.2	53.2	437.0	104.0	349.6	215.0	329.3	402.1	1.09	1.05
S6S8-0.6	848.0	8.1	1074.0	24.2	859.2	72.5	767.2	1214.9	0.88	1.11
S9S8-0.9	630.6	18.6	760.0	54.8	608.0	122.0	557.6	881.2	0.86	1.13
S12S8-1.2	519.5	33.9	600.0	101.8	480.0	180.0	453.8	660.0	0.91	1.14
S15S8-1.5	443.0	53.8	499.0	100.7	399.2	204.0	381.9	570.5	0.87	1.16

**Table 4.2** Lateral load and displacement for RMSW+BEs from Phase II

Wall ID.	$Q_y$ (kN)	$\Delta_y$ (mm)	$Q_u$ (kN)	$\Delta_u$ (mm)	$Q_{0.8u}$ (kN)	$\Delta_{0.8u}$ (mm)	$Q_{y(pred)}$ (kN)	$Q_{u(pred)}$ (kN)	$\frac{Q_u}{Q_{u(pred)}}$	$Q_y / Q_{y(pred)}$
	Avg	Avg	Avg	Avg	Avg	Avg	Avg	Avg		
S12S4-60	440.6	24.4	498.4	97.7	398.7	297.8	375.1	459.9	1.08	1.17
S15S4-60	376.5	38.7	412.8	115.2	330.2	410.7	322.8	394.0	1.05	1.17
S18S4-60	337.3	55.5	363.4	256.8	290.7	527.6	287.7	350.0	1.04	1.17
S12S8-60	622.2	24.6	702.4	152.3	561.9	351.9	548.7	647.5	1.08	1.13
S15S8-60	526.7	39.8	576.0	241.2	461.0	463.8	461.4	544.0	1.06	1.14
S18S8-60	440.2	58.4	507.3	345.4	405.8	599.3	403.0	475.0	1.07	1.09
S12S4-120	422.1	24.6	487.7	96.9	390.2	273.8	375.1	459.9	1.06	1.13
S15S4-120	362.8	38.8	422.6	230.3	338.0	370.4	322.8	394.0	1.07	1.12
S18S4-120	325.7	56.5	371.8	336.6	297.5	479.1	287.7	350.0	1.06	1.13
S12S8-120	594.2	25.4	708.5	149.5	566.8	307.2	548.7	647.5	1.09	1.08
S15S8-120	503.3	40.2	588.4	238.7	470.7	379.2	461.4	544.0	1.08	1.09
S18S8-120	435.4	58.3	501.4	171.3	401.1	545.6	403.0	475.0	1.06	1.08
R12S4-60	595.2	23.7	684.5	98.8	547.6	398.3	526.3	621.8	1.10	1.13
R15S4-60	511.1	39.0	573.2	237.0	458.45	464.8	446.5	524.1	1.09	1.14
R18S4-60	436.8	58.4	498.8	342.4	399.05	614.5	393.2	459.0	1.09	1.11
R12S8-60	877.4	25.3	1060	156.0	848.05	361.1	834.6	972.5	1.09	1.05
R12S8-60	743.2	40.6	870.9	329.0	696.75	487.3	692.6	803.9	1.08	1.07
R15S8-60	635.0	57.8	744.4	347.9	595.5	629.4	597.8	691.6	1.08	1.06
R12S4-120	562.6	24.6	692.8	162.0	554.24	314.3	526.3	621.8	1.11	1.07
R15S4-120	478.7	39.5	580.9	234.8	464.77	392.3	446.5	524.1	1.11	1.07
R18S4-120	429.1	57.0	493.6	313.7	394.85	510.2	393.2	459.0	1.08	1.09
R12S8-120	878.7	24.6	1059	152.0	847.5	296.6	834.6	972.5	1.09	1.05
R15S8-120	746.1	40.8	867.1	326.0	693.4	398.6	692.6	803.9	1.08	1.08
R18S8-120	647.5	59.6	745.9	353.3	596.7	531.9	597.8	691.6	1.08	1.08
S12G4-60	-	-	754.8	182.6	-	-	-	-	-	-
S15G4-60	-	-	586.9	262.5	-	-	-	-	-	-
S18G4-60	-	-	492.9	342.3	-	-	-	-	-	-
S12G8-60	-	-	1078.6	186.9	-	-	-	-	-	-
S12G4-120	-	-	757.5	183.0	-	-	-	-	-	-
S12G8-120	-	-	1039.8	181.5	-	-	-	-	-	-
R12G4-60	-	-	1014.4	190.7	-	-	-	-	-	-
R12G8-60	-	-	1617.5	208.2	-	-	-	-	-	-
R12G4-120	-	-	1026.5	188.2	-	-	-	-	-	-
R12G8-120	-	-	1562.4	189.9	-	-	-	-	-	-

#### 4.4 Displacement Ductility

Displacement ductility quantification is an essential tool to evaluate the RM walls' inelastic deformation capacities and to facilitate predicting the drift and damage levels under different levels of seismic demand. The displacement ductility is a measure of the ability of the member to deform after yielding of the tension reinforcement. To date, there has been no consensus amongst researchers in terms of identifying RM and RC walls' yield displacement point [Park and Paulay 1975; Paulay and Priestley 1992; Priestley and Kowalsky 2007; Shedid et al. 2010; and Banting and El-Dakhakhni 2012]. As can be observed from Figure 4.1, none of the walls had a well-defined yield plateau that can be used to calculate the displacement ductility. As such, idealizations of the load-displacement relationships for each of the studied RM shear walls were conducted, according to Tomažević (1999).

The load-displacement envelope curve was subsequently idealized to bilinear elastic-perfect plastic, using the approach suggested by Tomažević (1999). As such, the elastic line intersects the ascending curve in the experimental yield point. Then the perfect plastic line was adjusted such that the area under the bilinear idealization curve equals the area under the experimental load-displacement envelope up to failure point. The ultimate displacement,  $\Delta_{0.8u}$  was identified as the failure point based on Priestley et al. (1986), and Priestley et al. (2007) recommendation at 20% strength degradation on the post-peak descending curve. The displacement ductility,  $\mu_{\Delta}$  of the walls considered in this study is defined as the ratio of the ultimate wall displacement,  $\Delta_{0.8u}$  to the corresponding idealized yield displacement,  $\Delta_y^{id}$ .

According to Tomažević (1999), the load-displacement envelope can be idealized with an elastic-plastic relationship, then the idealized elastic-plastic resistance,  $F_{ep}$  can be evaluated by equating the energy under the load-displacement envelope to that under the idealized elastic-plastic relationship as shown in Eq. (4.1).

$$F_{ep} = K_e \left( \Delta_{0.8u} - \sqrt{\Delta_{0.8u}^2 - \frac{2A_{env}}{K_e}} \right) \quad \text{Eq. (4.1)}$$

where  $A_{env}$  is the area under the load-displacement envelope up to  $\Delta_{0.8u}$ ,  $\Delta_{0.8u}$  is the lateral displacement at 20% strength degradation, and  $K_e$  is the effective stiffness. The idealized yield displacement,  $\Delta_y^{id}$ , and ultimate displacement,  $\Delta_{0.8u}$  for both loading directions, are presented in

Tables 4.3 and 4.4. The idealized displacement ductility,  $\mu_{\Delta}$  values for steel-reinforced walls from Phase I are presented in Table 4.3. Similarly, the displacement ductility for steel-reinforced walls from Phase II was obtained, according to Tomažević (1999), as seen in Table 4.4. It can be observed that a high level of displacement ductility was achieved, reflecting the benefit of adding boundary elements to RM shear walls. This result indicates a significant effect on the seismic performance that should influence the seismic response modification factor of RMSW+BEs to be discussed in Chapter 5.

**Table 4.3** Displacement ductility for RMSW+BEs from Phase I

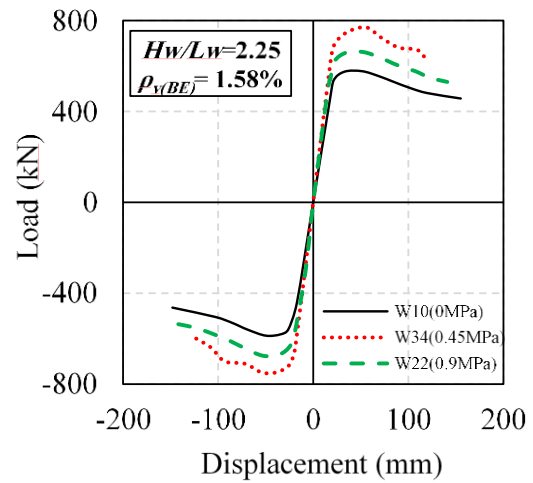
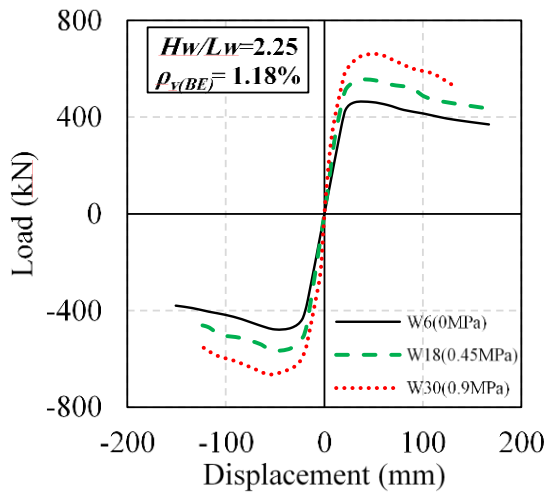
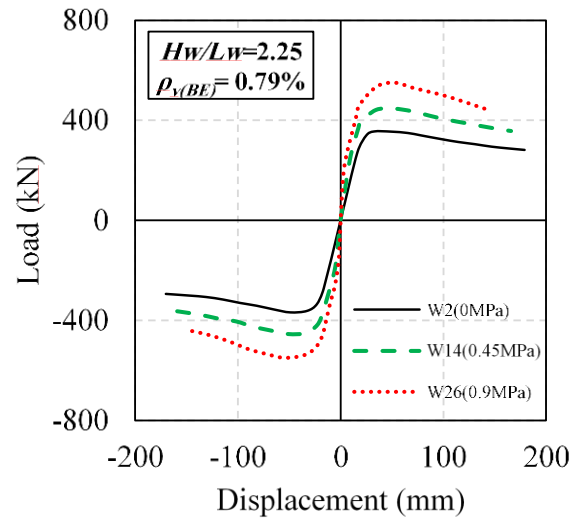
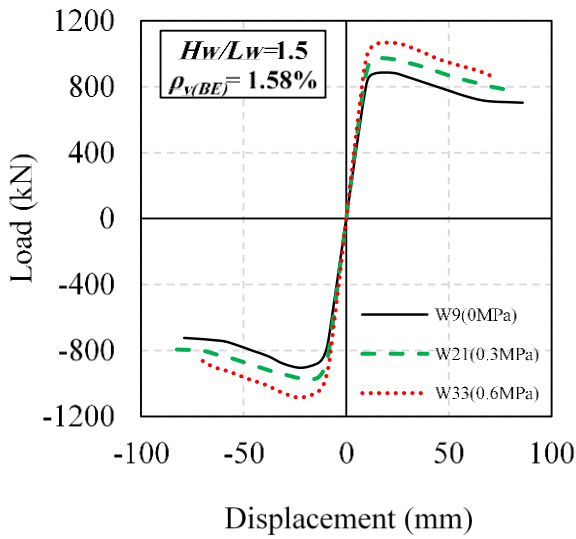
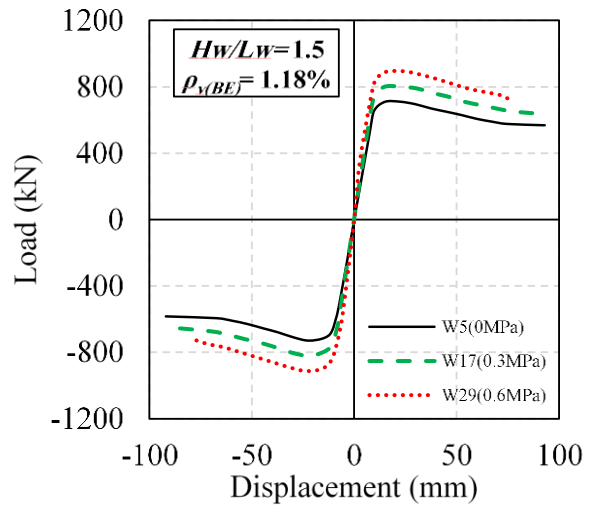
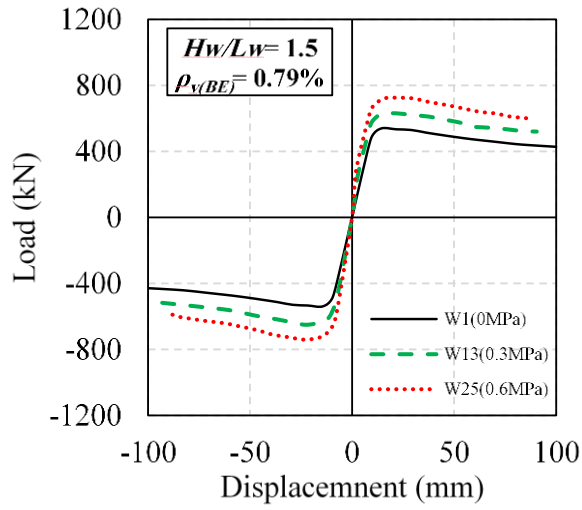
Wall ID.	$\Delta_y^{id}$ (mm)		$\Delta_{0.8u}$ (mm)		$\mu_{\Delta}$		
	(+ve)	(-ve)	(+ve)	(-ve)	(+ve)	(-ve)	Average
S6S4-0	9.1	9.1	100.0	100.0	11.0	11.0	11.0
S9S4-0	19.8	20.3	179.0	170.0	9.1	8.4	8.7
S12S4-0	34.8	35.6	280.0	261.5	8.1	7.3	7.7
S15S4-0	53.9	55.3	400.0	363.2	7.4	6.6	7.0
S6S6-0	9.1	9.3	93.0	92.0	10.2	9.9	10.1
S9S6-0	19.9	20.5	167.0	151.0	8.4	7.4	7.9
S12S6-0	35.3	35.5	238.4	238.4	6.7	6.7	6.7
S15S6-0	55.6	55.0	326.2	372.8	5.9	6.8	6.3
S6S8-0	9.2	9.3	86.0	89.0	9.3	9.5	9.4
S9S8-0	20.2	20.5	155.0	148.0	7.7	7.2	7.4
S12S8-0	35.5	36.4	244.0	213.5	6.9	5.9	6.4
S15S8-0	55.4	56.1	333.2	333.2	6.0	10.9	6.0
S6S4-0.3	8.9	8.9	93.0	97.0	10.5	8.2	10.7
S9S4-0.45	19.2	19.5	166.0	159.1	8.6	7.4	8.4
S12S4-0.6	33.7	33.8	245.0	250.0	7.3	6.5	7.3
S15S4-0.75	52.8	53.1	343.8	343.8	6.5	9.3	6.5
S6S6-0.3	9.0	9.1	87.0	85.0	9.7	6.8	9.5
S9S6-0.45	19.5	19.9	160.0	136.0	8.2	5.3	7.5
S12S6-0.6	34.6	41.3	253.6	220.0	7.3	6.0	6.3
S15S6-0.75	54.3	54.4	320.0	325.0	5.9	9.0	5.9
S6S8-0.3	9.2	9.2	82.5	82.5	9.0	7.0	9.0
S9S8-0.45	20.2	20.4	141.0	142.0	7.0	5.8	7.0
S12S8-0.6	36.3	36.2	205.0	210.0	5.7	5.5	5.7
S15S8-0.75	55.5	55.9	310.0	310.0	5.6	9.9	5.6
S6S4-0.6	8.9	8.9	89.0	88.0	10.0	7.2	10.0
S9S4-0.9	20.2	20.2	144.6	144.6	7.2	6.2	7.2
S12S4-1.2	35.4	35.6	220.0	220.0	6.2	4.4	6.2
S15S4-1.5	57.1	57.5	250.0	250.0	4.4	8.4	4.4
S6S6-0.6	9.2	9.2	77.0	77.0	8.4	6.1	8.4
S9S6-0.9	20.9	21.0	128.7	128.0	6.2	5.2	6.1
S12S6-1.2	36.6	36.6	185.0	190.0	5.1	3.6	5.1
S15S6-1.5	58.7	58.3	220.0	210.0	3.8	7.7	3.7
S6S8-0.6	9.3	9.4	73.0	72.0	7.8	6.0	7.7
S9S8-0.9	21.0	20.6	121.0	123.0	5.8	6.0	5.9
S12S8-1.2	37.3	37.5	180.0	180.0	4.8	4.8	4.8
S15S8-1.5	58.9	58.9	198.0	210.0	3.4	3.6	3.5

**Table 4.4** Displacement ductility for steel-reinforced RMSW+BEs from Phase II

Wall ID.	$\Delta_y^{id}$ (mm)		$\Delta_{0.8u}$ (mm)		$\mu_{\Delta}$		
	(+ve)	(-ve)	(+ve)	(-ve)	(+ve)	(-ve)	Average
S12S4-60	26.0	26.0	286.1	309.4	11.0	11.9	11.5
S15S4-60	41.2	39.9	391.9	429.5	9.5	10.8	10.1
S18S4-60	54.1	57.3	502.4	552.7	9.3	9.6	9.5
S12S8-60	25.6	26.7	344.4	359.4	13.5	13.4	13.5
S15S8-60	42.1	42.0	463.2	464.4	11.0	11.1	11.0
S18S8-60	65.2	61.3	591.7	606.9	9.1	9.9	9.5
S12S4-120	27.6	27.6	273.1	274.4	9.9	9.9	9.9
S15S4-120	43.1	43.6	359.3	381.5	8.3	8.7	8.5
S18S4-120	61.4	63.7	470.2	487.9	7.7	7.7	7.7
S12S8-120	28.5	29.4	306.1	308.3	10.7	10.5	10.6
S15S8-120	44.1	45.5	378.2	380.1	8.6	8.4	8.5
S18S8-120	66.3	62.7	529.9	561.2	8.0	8.9	8.5
R12S4-60	25.3	26.5	396.5	400.1	15.7	15.1	15.4
R15S4-60	42.1	42.1	462.4	467.2	10.9	11.1	11.0
R18S4-60	67.3	61.1	609.4	619.6	9.1	10.2	9.6
R12S8-60	29.9	29.1	361.2	360.9	12.1	12.4	12.3
R12S8-60	45.9	46.2	490.4	484.2	10.7	10.5	10.6
R15S8-60	65.0	66.6	624.7	634.0	9.6	9.5	9.6
R12S4-120	29.2	29.6	311.3	317.2	10.7	10.7	10.7
R15S4-120	48.8	44.9	398.8	385.7	8.2	8.6	8.4
R18S4-120	60.9	65.2	501.9	518.5	8.2	8.0	8.1
R12S8-120	28.5	28.4	302.4	290.7	10.6	10.2	10.4
R15S8-120	46.8	45.3	399.3	397.9	8.5	8.8	8.7
R18S8-120	67.2	65.3	543.9	520.0	8.1	7.9	8.0

#### 4.5 Influence of Different Parameters on the Lateral Response of Walls in Phase I

Thirty-six fully grouted RM shear walls with C-shaped boundary elements were modelled using the macro-modelling approach using fibre-based beam-column elements described earlier in Section 3.4.1 utilizing *SeismoStruct* (Seismosoft, 2016). The numerical model was used to evaluate the influence of variable design parameters on the in-plane lateral response of RMSW+BEs under quasi-static cyclic loading. The envelopes of the load-displacement relationships for the thirty-six modelled walls are presented in Figure 4.2. Based on the results of the numerical modelling, the effect of the studied parameters is discussed below.



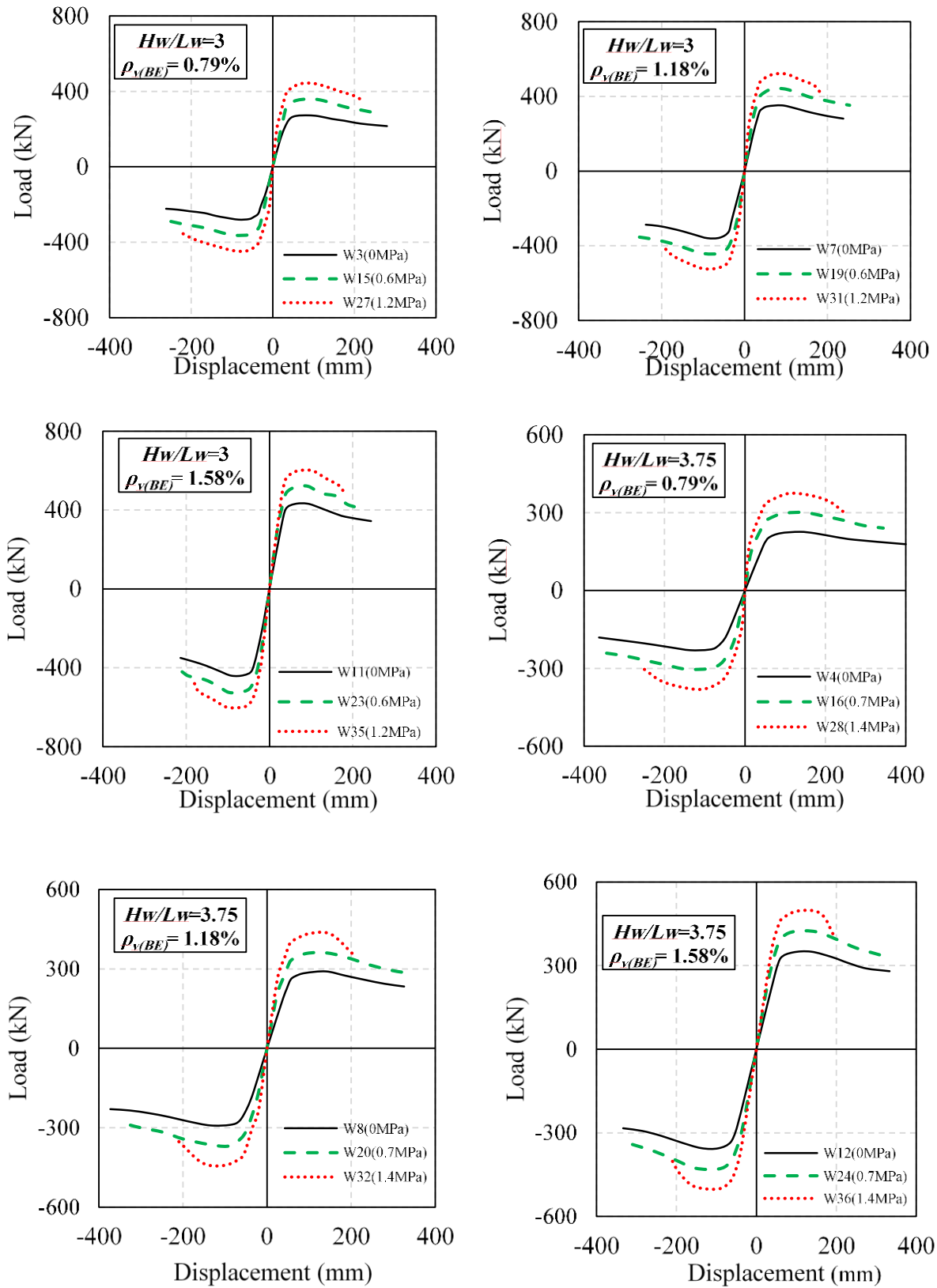


**Figure 4.2** Load-displacement hysteresis' envelopes for RMSW+Bes

#### 4.5.1 Effect of axial compressive stress

The effect of changing the axial compressive stress on the load-displacement behaviour is assessed. As shown in Figure 4.2, the RMSW+BEs ultimate strength increased with a higher level of axial stresses. For walls with  $\rho_{v(BE)}=0.79\%$ , as the level of axial stress increased from 0 to 0.3 MPa per story,  $Q_u$  increased by 34%, and 67% for walls having an aspect ratio of 1.5, and 3.75, respectively. Also, for walls with  $\rho_{v(BE)}=1.58\%$ , as the level of axial stress increased from 0 to 0.3 MPa per story,  $Q_u$  increased by 20%, and 42% for walls having an aspect ratio of 1.5, and 3.75, respectively. Moreover, it can be inferred that walls with a higher level of axial stress experienced more rapid strength and stiffness degradation. In addition, it can be observed that walls with a lower level of axial stress have higher displacements at failure (i.e., at 20% strength degradation).

In addition, it can be observed from Figure 4.4 that the walls' displacement ductility decreased with the increased axial stress, which is in agreement with the vast majority of experimental studies on RMSW (e.g., Shedid et al. 2008, and Banting and El-Dakhakhni 2012). That is mainly attributed to the increase in the yield displacement with the increase of axial load, whereas the ultimate displacements were almost similar. For walls with  $\rho_{v(BE)}=0.79\%$ ,  $\mu_{\Delta 0.8u}$  decreased by 10%, and 37% for walls having an aspect ratio of 1.5, and 3.75, respectively, with the increase of the level of axial stress. Moreover, for walls with  $\rho_{v(BE)}=1.58\%$ ,  $\mu_{\Delta 0.8u}$  decreased by 18%, and 42% for walls having an aspect ratio of 1.5, and 3.75, respectively, with the increase in the level of axial stress from 0 to 0.3 MPa/ story.

#### 4.5.2 Effect of vertical reinforcement ratio in BE

Figure 4.2 shows that the ultimate strength of walls increased as the vertical reinforcement ratio in BE increased. For walls with no axial stress, as  $\rho_{v(BE)}$  increased from 0.79% to 1.58%,  $Q_u$  increased by 64%, and 57% for walls having an aspect ratio of 1.5, and 3.75, respectively. Likewise, for walls with the level of axial stress 0.3 MPa/story, as  $\rho_{v(BE)}$  increased from 0.79% to 1.58%,  $Q_u$  increased by 47%, and 33% for walls having an aspect ratio of 1.5, and 3.75, respectively. The displacement ductility was dependent on the amount of vertical reinforcement. The results plotted in Figure 4.3 show that walls with low vertical reinforcement ratios in the boundary developed higher displacement ductility than those tested with high vertical reinforcement ratios. For walls with zero level of axial stress, as  $\rho_{v(BE)}$  increased from 0.79% to 1.58%,  $\mu_{\Delta 0.8u}$  decreased by 14% for walls having an aspect ratio of 1.5, and 3.75. Similarly, for

walls with a high level of axial stress, as  $\rho_{v(BE)}$  increased from 0.79% to 1.58%,  $\mu_{\Delta 0.8u}$  decreased by 21% for walls having an aspect ratio of 1.5, and 3.75. This was explained based on the fact that the yield displacements were almost similar for the walls, while the displacement at failure decreased slightly as the vertical reinforcement ratio increased.

#### 4.5.3 Effect of aspect ratio

The relationship between the wall aspect ratio and load-displacement behaviour is evaluated for four different aspect ratios (1.5, 2.25, 3, and 3.75). Figure 4.2 shows that the lateral resistance of masonry walls increases as the height to length ratio decreases. For walls having  $\rho_{v(BE)}=0.79\%$ , as aspect ratio increased from 1.5 to 3.75,  $Q_u$  decreased by 59%, and 48% for walls with a level of axial stress of 0 to 0.3 MPa/story, respectively. For walls having  $\rho_{v(BE)}=1.58\%$ , as aspect ratio increased from 1.5 to 3.75,  $Q_u$  decreased by 60%, and 54% for walls with a level of axial stress 0 to 0.3 MPa/story, respectively. Similar observations were also reported by Shedid et al. (2010), and Banting and El-Dakhkhni (2014). As shown in Figure 4.2, walls with  $AR=1.5$  and 2.25 experienced more rapid strength degradation than did walls with  $AR=3$  and 3.75. Moreover, the lateral displacement at failure increased with a higher aspect ratio.

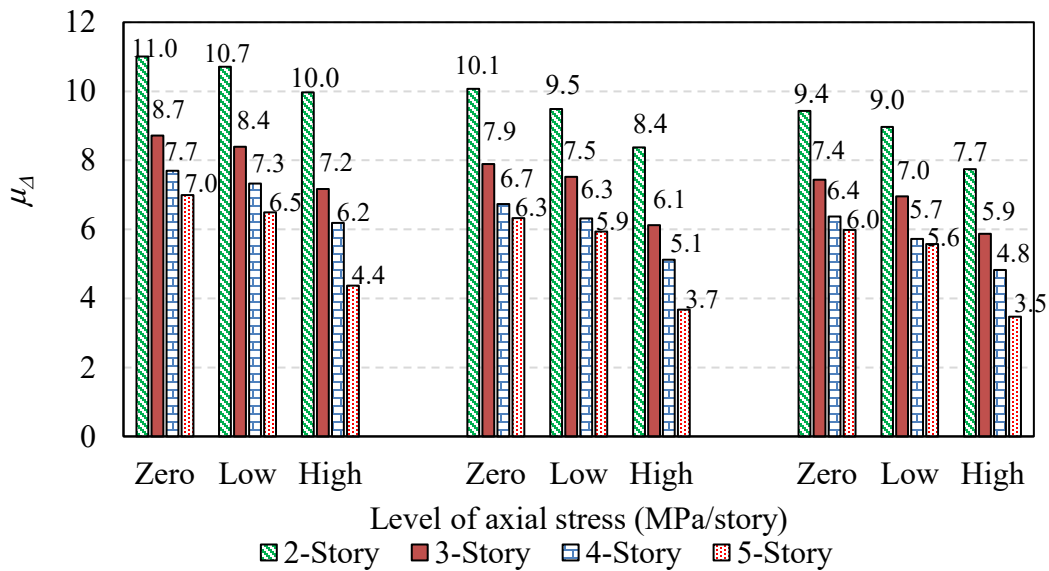


Figure 4.3 Displacement ductility for walls in Phase I

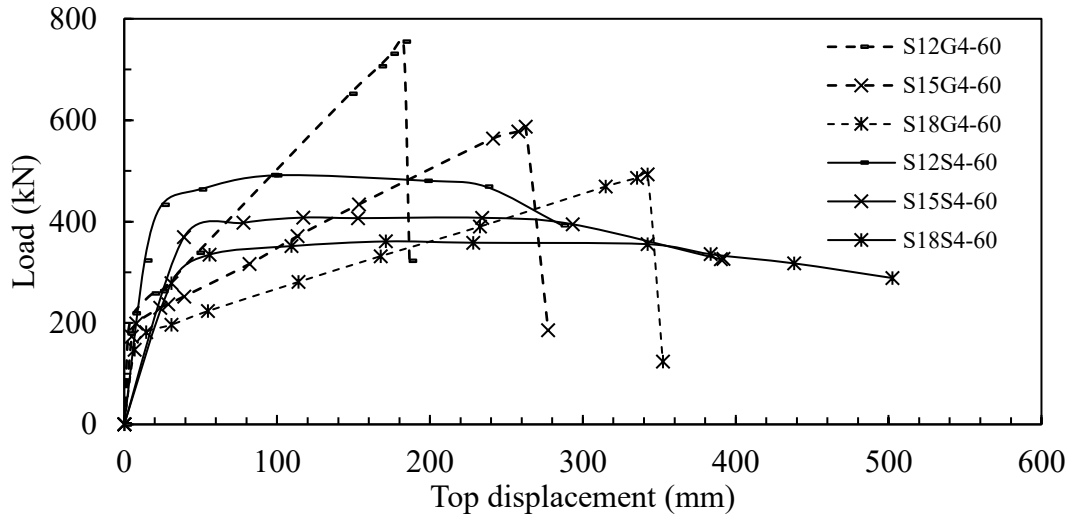
Results showed that the idealized displacement ductility decreased as aspect ratio increased, given that the walls had the same length, vertical reinforcement ratio, and axial stress. As aspect ratio increased from 1.5 to 3.75,  $\mu_{\Delta 0.8u}$  decreased by 37%, and 56% for walls with zero and high level of axial stress, respectively. The inversely proportional aspect ratio-ductility relationship is mainly attributed to the increase in the yield displacement value, as the aspect ratio increases, which was not offset by the increase in the ultimate displacement.

#### **4.6 Influence of Different Parameters on Lateral Response of Walls in Phase II**

Thirty-four fully grouted RM shear walls with C-shaped boundary elements were modelled using the DB beam-column elements nonlinear numerical modelling approach described earlier in section utilizing *OpenSees* (McKenna et al. 2013). The numerical model was used to investigate the effect of different design parameters on the load-displacement response of RMSW+BEs under quasi-static cyclic loading up to at least 20% lateral strength degradation of the post-peak response. Based on the results of the numerical modelling, the influence of the key parameters is discussed below.

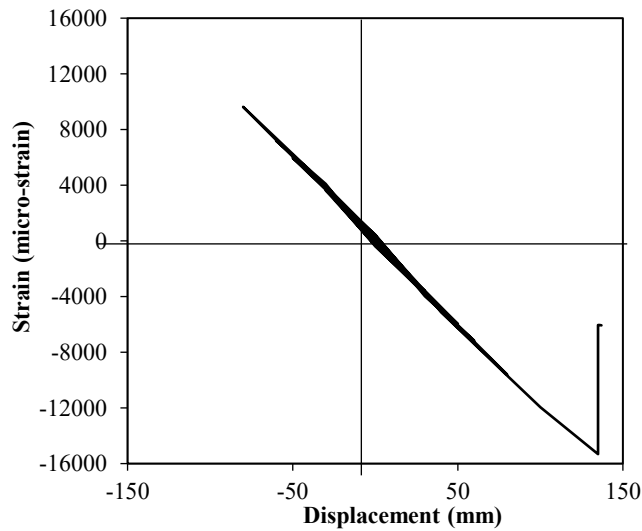
##### **4.6.1 Type of reinforcement (GFRP vs. Steel)**

Figure 4.4 shows the envelope curves for steel-reinforced walls and their counterpart GFRP-reinforced walls. GFRP-reinforced walls achieved a higher ultimate lateral load than steel-reinforced walls. The ultimate lateral loads attained for GFRP-reinforced walls were 754.8 kN, 586.9 kN, and 492.9 kN, corresponding to displacements of 182.6 mm, 262.5 mm, and 342.3 mm, for walls S12G4-60, S15G4-60, S18G4-60, respectively. However, for steel-reinforced walls with similar reinforcement ratio, the ultimate lateral loads were 498.4 kN, 412.8 kN, and 363.4 kN corresponding to displacements of 97.7 mm, 115.2 mm, and 256.8 mm, for walls S12S4-60, S15S4-60, and S18S4-60, respectively. That is mainly due to the higher initial softening response of GFRP-reinforced walls. After that point, the GFRP walls kept increasing almost linearly to failure.



**Figure 4.4** Effect of utilized type of reinforcement (GFRP vs. steel) on RMSWs

As reported by Hassanein et al. (2019a), the GFRP-reinforced walls did not encounter post-peak behaviour due to the linear elastic nature of GFRP bars up to rupture. The failure developed in GFRP-reinforced walls when the strain in the longitudinal bars at the extreme fibre reached its ultimate capacity. Figure 4.5 shows the recorded strain behaviour in that bar; this failure mechanism is similar to the failure reported by Hassanein et al. (2019) for GFRP-RC walls.



**Figure 4.5** Recorded strain in the extreme fibre GFRP longitudinal reinforcement  
“ Wall S12G4-60”

#### 4.6.2 Confinement ratio of transverse reinforcement

The presence of more confinement in the BEs by decreasing  $S_{hoop}$  from 120 mm to 60 mm enhanced the lateral load and displacement of the steel-reinforced walls (see Figure 4.6). For GFRP-reinforced walls, an increase in the confinement level at the boundary element also significantly enhanced both the lateral strength and top displacement (Figures 4.8). For example, for walls with square-shaped BEs, the ultimate lateral load increased from 1562 kN to 1617.5 kN, and the corresponding displacement from 181.5 mm to 186.9 mm.

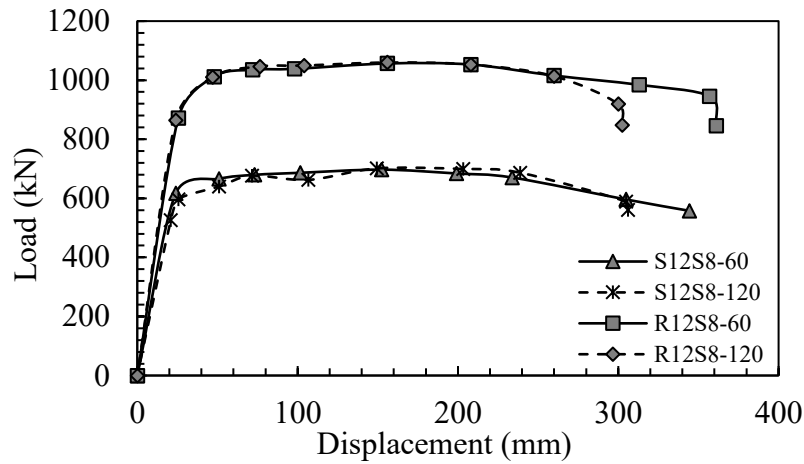


**Figure 4.6** Effect of  $S_{hoop}$  on steel-reinforced walls

Similar observations were also found for walls with rectangular shaped BE. As the confinement decreased (i.e.,  $S_{hoop} = 60$  mm to 120 mm),  $\mu_A$  decreased by 18%, and 20% for steel-reinforced walls with square-shaped BEs for  $\rho_{vBE} = 0.79\%$  and  $\rho_{vBE} = 1.58\%$ , respectively. Similarly,  $\mu_A$  decreased by 19%, and 23% for steel-reinforced walls with  $\rho_{vBE} = 0.79\%$  and 1.58%, respectively, as the  $S_{hoop}$  decreased for walls with rectangular-shaped BEs (see Figure 4.8). This indicates the effectiveness of the transverse reinforcement in confining the masonry core and delaying failure.

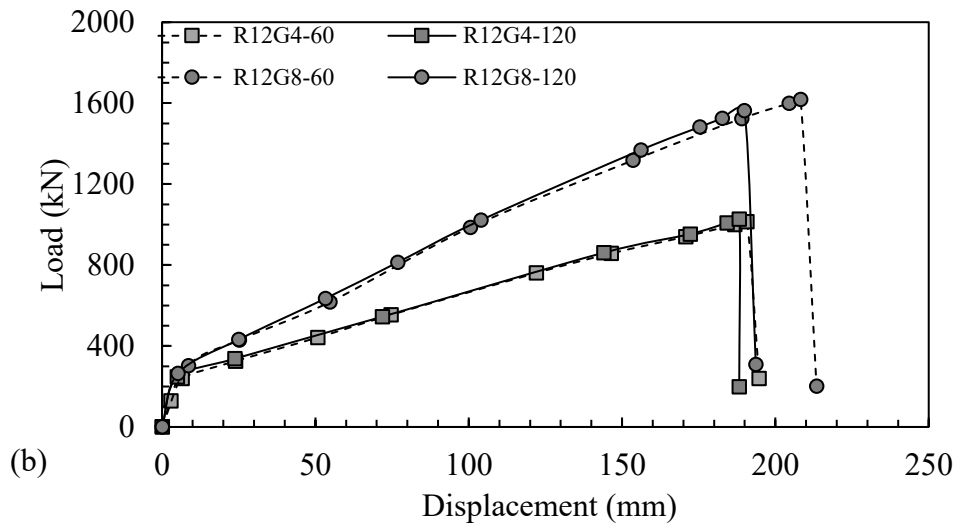
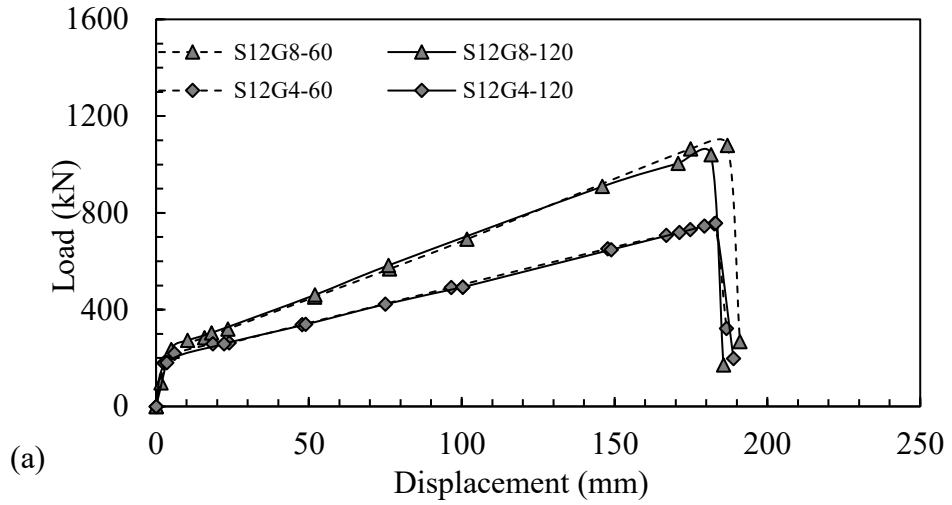


**Figure 4.7** Effect of spacing on GFRP-reinforced walls: a) RMSW with square-shaped BE, b) RMSW with rectangular shaped BE

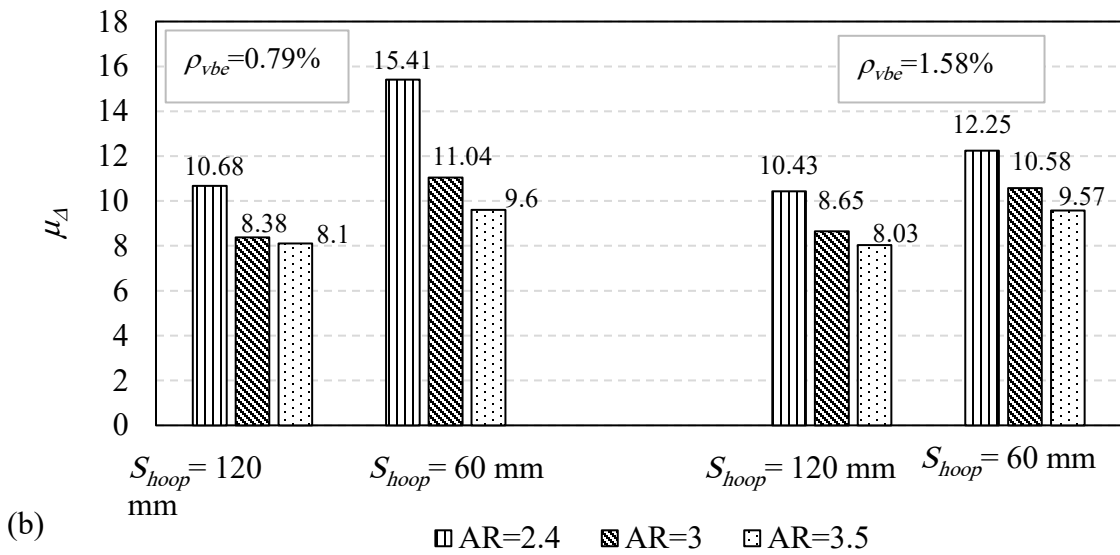
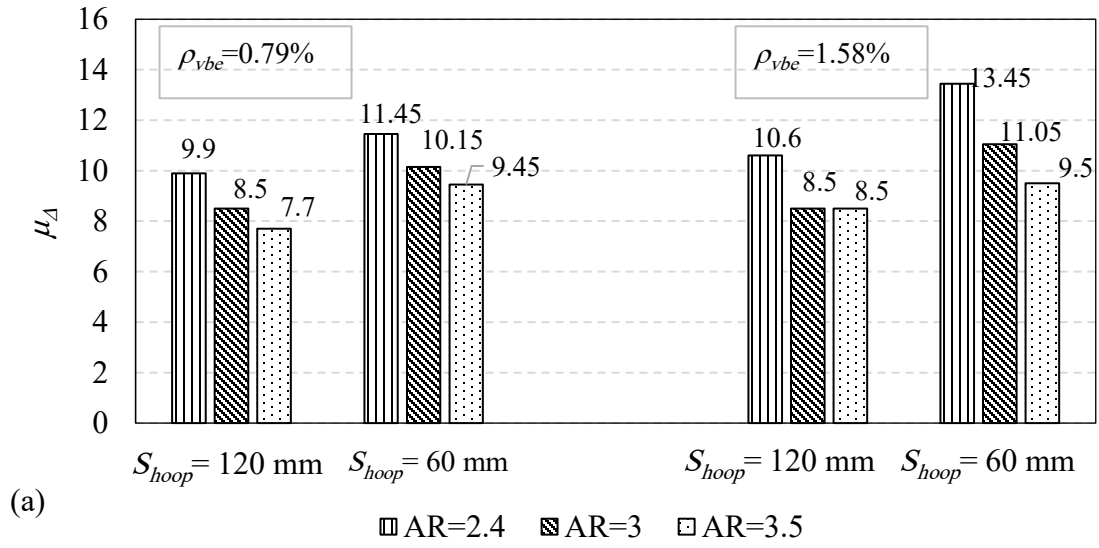


**Figure 4.8** Idealized ductility for steel-reinforced walls: (a) RMSW with square-shaped BE, (b) RMSW with rectangular-shaped BE

### 4.6.3 Amount of vertical reinforcement in boundary element

The effect of the vertical reinforcement ratio in the boundary element (BE) on the behaviour of the walls is evaluated in this section. As  $\rho_{vBE}$  increased, it can be seen from Figure 4.9 that there was an increase in the yield strength and ultimate strength of the wall. The effect of the amount of vertical reinforcement in BE on the load-displacement relationship was also studied for GFRP-reinforced walls. As shown in Figure 4.10a, for walls with square-shaped BE, the lateral load increased by 43% and 37% for  $S_{hoop} = 60$  mm and 120 mm, respectively. A similar trend was also observed for walls with rectangular shaped BE where the lateral load increased by 60% and 52% for  $S_{hoop} = 60$  mm and 120mm, respectively (see Figure 4.10b).

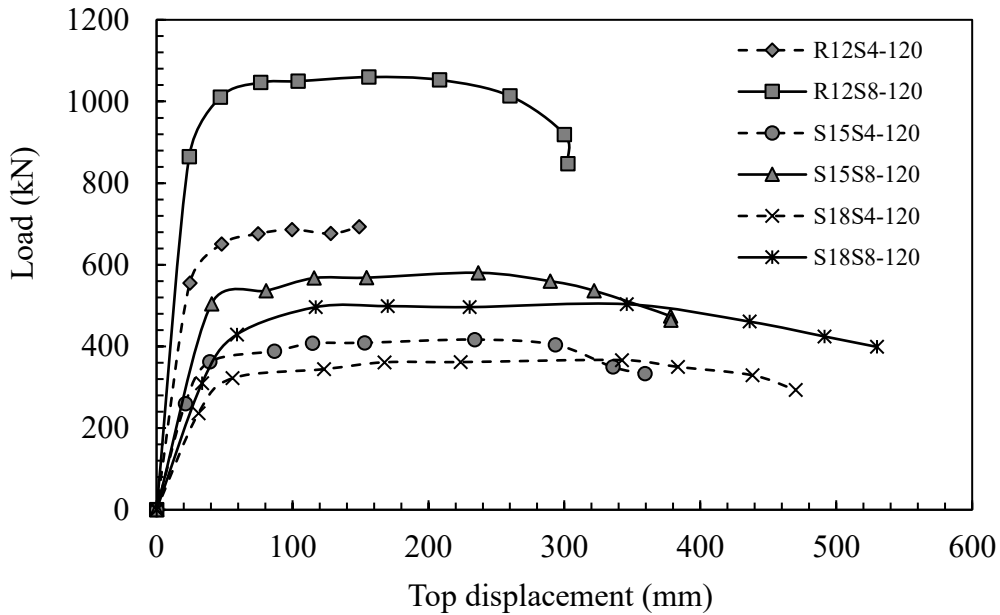


**Figure 4.9** Effect of  $\rho_{vBE}$  on steel-reinforced walls

In addition, as shown in Figure 4.8, walls with higher  $\rho_{vBE}$  developed higher displacement ductility on steel-reinforced walls. This is mainly due to the increase in the ultimate compressive strain sustained by the masonry extreme fibres, and the reduction in the depth of the compression zone, which lead to an improvement in the ultimate displacement capacity due to the increase in plastic deformations. For square-shaped BEs walls with  $AR = 2.4$ , as  $\rho_{vBE}$  increased from 0.79% to 1.58%,  $\mu_d$  increased from 11.5 to 13.5 by 16% for walls with high confinement ratio and increased by 6.8% from 9.9 to 10.6 for walls with low confinement ratios. For  $AR = 3$ , as  $\rho_{vBE}$  increased,  $\mu_d$  increased from 10.1 to 11.1 by 16% and remained the same ( $\mu_d = 8.5$ ) for walls with high, and low

confinement ratio, respectively. For  $AR = 3.5$ , as  $\rho_{vBE}$  increased,  $\mu_A$  remained 9.5 and increased by 9.8% from 7.7 to 8.5 for walls with high and low confinement ratio, respectively. For walls with rectangular-shaped BEs, for  $AR = 2.4$ , as  $\rho_{vBE}$  increased from 0.79% to 1.58%,  $\mu_A$  increased from 15.4 to 12.3 by 20% and did not have a noticeable effect for walls with high, and low confinement ratio, respectively. For  $AR = 3$ , as  $\rho_{vBE}$  increased,  $\mu_A$  increased from 11.0 to 10.6 by 3.6% and did not have a noticeable effect for walls with high and low confinement ratio, respectively. For  $AR = 3.5$ , as  $\rho_{vBE}$  increased,  $\mu_A$  remained 9.6, and 8.0, for walls with high and low confinement ratio, respectively.

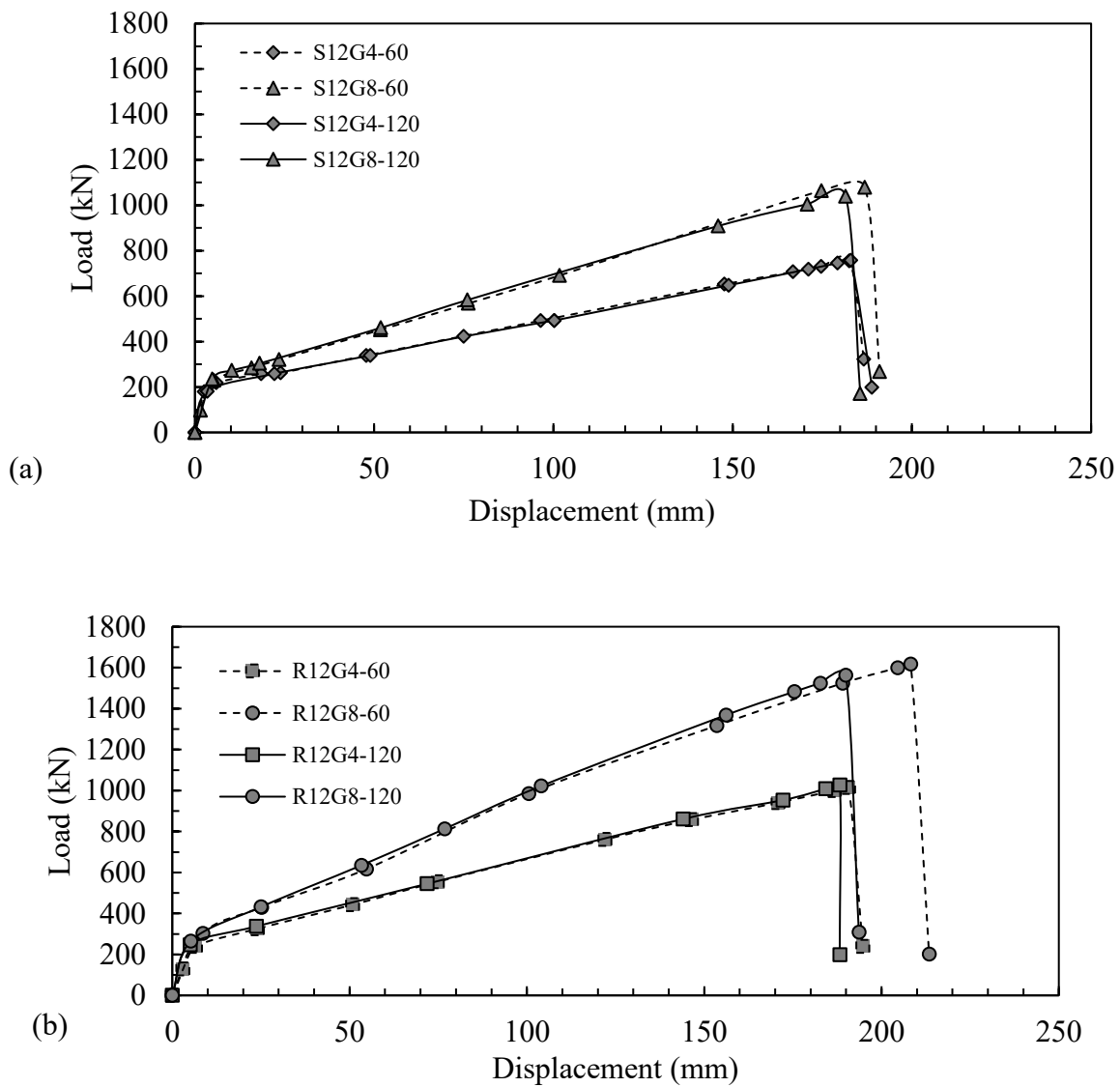


**Figure 4.10** Effect of  $\rho_{vBE}$  on GFRP-reinforced walls: a) RMSW with square-shaped BE, b) RMSW with rectangular shaped BE

#### 4.6.4 Size of boundary element

In this section, the effect of changing the size of BE on the load-displacement behaviour is evaluated. Based on the results from Table 4.2, the yield and maximum lateral load increased for walls with  $AR = 2.4, 3,$  and  $3.5$  by changing the length of BE from 390 mm to 780 mm. Moreover, results show that increasing the size of BE resulted in a slight improvement in the ultimate displacement of steel-reinforced walls (see Figure 4.11) and GFRP-reinforced walls (see Figures 4.13a and b). It was observed that there is an increase in the lateral load of 50% and 35% for walls with rectangular shaped BE for walls, and having  $\rho_{vBE} = 1.58\%$  and  $0.79\%$ , respectively. In addition, increasing the BE size had a minor effect on the displacement ductility for most of the steel-reinforced walls. However, it can be shown from Table 4.2 that for W4 ( $\mu_{\Delta} = 13.5$ ), and W13 ( $\mu_{\Delta} = 15.4$ ), that the wall can reach a higher ductility when the BE length is increased for walls with  $AR = 2.4$ . This increase in ductility could be explained as a result of an increase in the compressive strain in the long boundary element wall, which reduces the compression zone depth to the wall-length ratio leading to a more ductile section.

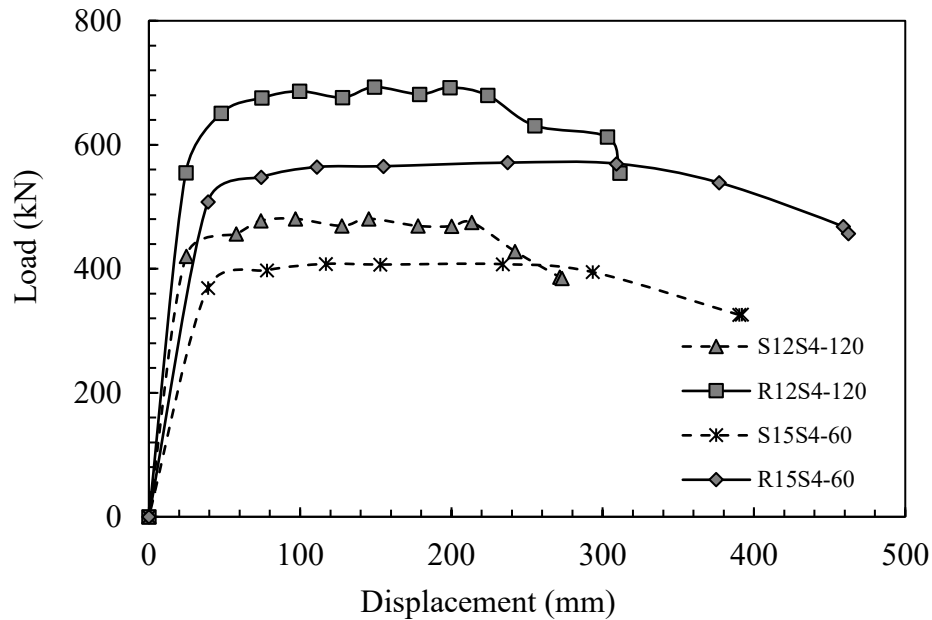


**Figure 4.11** Effect of boundary element size on steel-reinforced walls

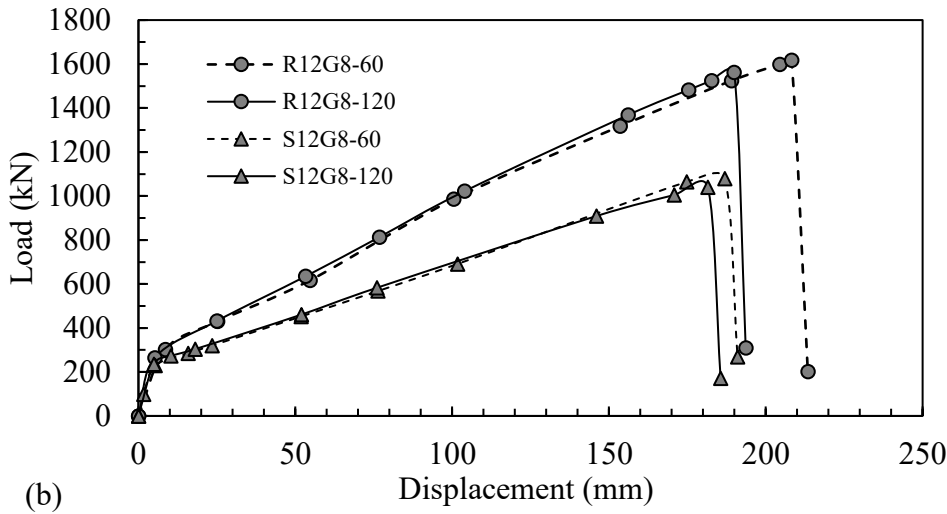
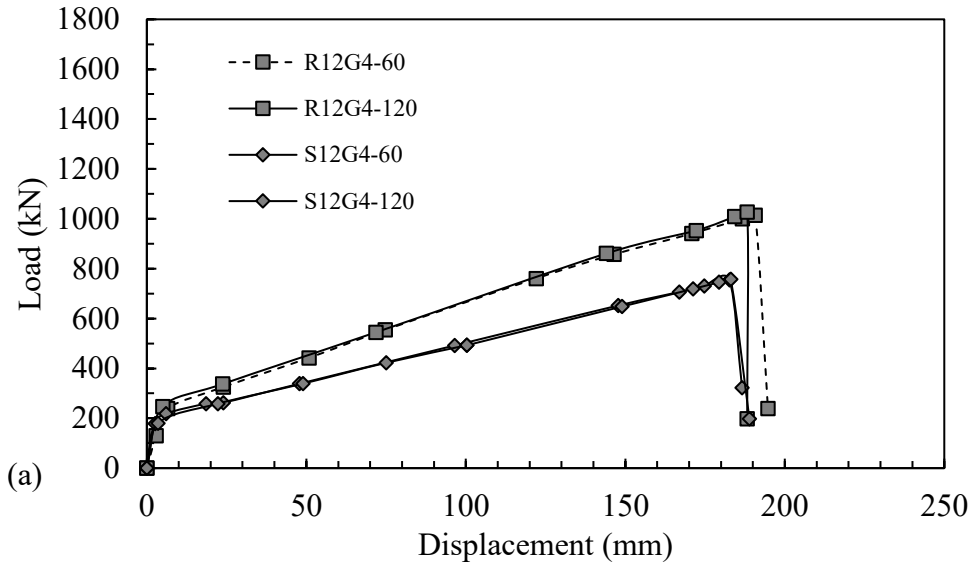


**Figure 4.12** Effect of boundary element size on GFRP-reinforced walls: (a) RMSW with  $\rho_{vBE}=0.79\%$ , (b) RMSW with  $\rho_{vBE}=1.58\%$

#### 4.6.5 Aspect ratio

The relationship between the wall's aspect ratio and load-displacement behaviour is evaluated for three different aspect ratios. Results in Table 4.2 show that increasing  $AR$  from 2.4 to 3.5, the yield strength, and the peak strength of the wall decreased for all walls. As shown in Figure 4.13a, steel-reinforced walls with lower  $AR$  experienced more rapid strength degradation than did walls with higher  $AR$ , and the displacement at ultimate loads increased as the  $AR$  increased. Furthermore, three GFRP-reinforced walls were considered with different aspect ratios to illustrate their

applicability covering the range of aspect ratios for medium-rise shear walls aspect ratio (typically between 2 and 4). As shown in Figure 4.13b, the three walls (S12G4-60, S15G4-60, S18G4-60) were able to achieve their flexural capacity with no strength degradation. Wall S18G4-60 with  $AR=3.5$  had lower  $Q_u=492.9$  kN in comparison to wall S12G4-60 with  $AR=2.4$  and  $Q_u=754.8$  kN. However, wall S18G4-60 achieved higher deformations in comparison to walls S15G4-60 and S18G4-60, as shown in Table 4.2.

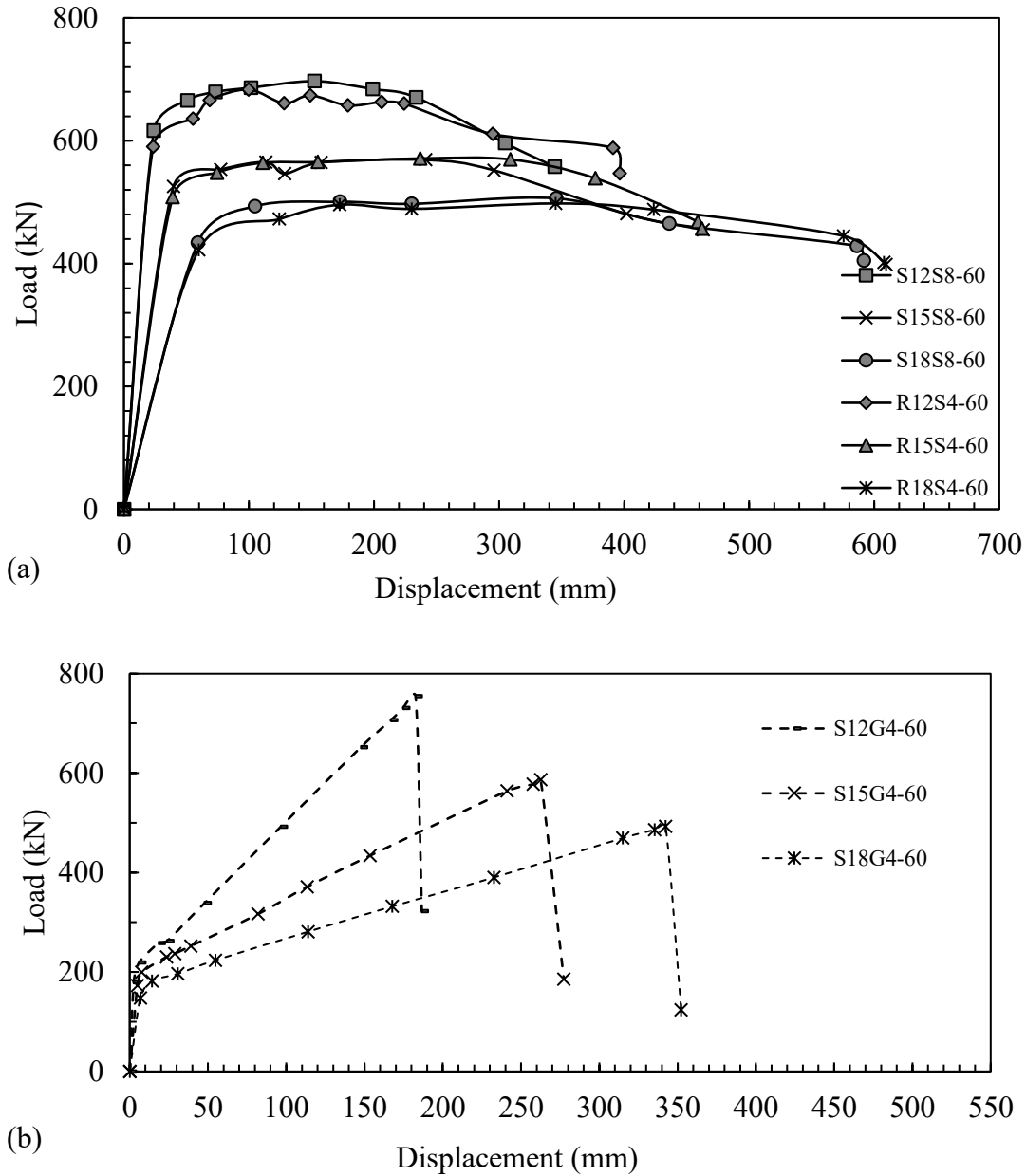


**Figure 4.13** Effect of aspect ratio on (a) steel-reinforced walls, (b) GFRP-reinforced walls

For walls with square-shaped BE, and low confinement (i.e.,  $S_{hoop} = 60$  mm), as the  $AR$  increased from 2.4 to 3.5,  $\mu_{\Delta}$  decreased by 6% from 9.9 to 7.7 for  $\rho_{vBE} = 0.79\%$  and decreased by 5% from 10.5 to 8.5 for  $\rho_{vbe} = 1.58\%$ . In addition, for walls with square-shaped BE with high confinement (i.e.,  $S_{hoop} = 120$  mm),  $\mu_{\Delta}$  decreased by 19% from 11.5 to 9.5 for walls with  $\rho_{vBE} = 0.79\%$  and decreased by 35% from 13.5 to 9.5 for walls with  $\rho_{vBE} = 1.58\%$ . Moreover, for walls with rectangular-shaped BE, and low confinement (i.e.,  $S_{hoop} = 60$  mm),  $\mu_{\Delta}$  decreased by 24% from 10.7 to 8.1 for walls with  $\rho_{vBE} = 0.79\%$ , and by 23% from 10.4 to 8.0 for  $\rho_{vBE} = 1.58\%$ , as  $AR$  increased. Similarly, as  $AR$  increased for walls with rectangular-shaped BE, high confinement (i.e.,  $S_{hoop} = 120$  mm),  $\mu_{\Delta}$  decreased by 37% from 15.4 to 9.6 for walls with  $\rho_{vBE} = 0.79\%$ , and by 21.9% from 12.3 to 9.6 for walls with  $\rho_{vBE} = 1.58\%$ . The inversely proportional aspect ratio-ductility relationship is due to the increase in the yield displacement as the aspect ratio increases, which was not offset by the increase in the displacement at maximum loads.

#### 4.7 Conclusions

In this chapter, the results of the parametric study were presented of a numerical study that was conducted on seventy full-scale fully grouted flexure-dominated RM shear walls with C-shaped boundary elements. Several design parameters were considered to understand the nonlinear response and investigate the seismic capabilities of RM shear walls with boundary elements formed with C-shaped blocks to provide the required strength and ductility to resist earthquake events. The present study also addressed the applicability of reinforcing masonry shear walls with GFRP bars to attain reasonable strength and drift. GFRP-RM shear walls are a corrosion-free lateral resisting system that is transparent to magnetic fields and radio frequencies and nonconductive thermally and electrically. The influence of parameters such as transverse hoop spacing, size of boundary elements, amount of vertical reinforcement, type of reinforcement (GFRP vs steel), axial stress, and aspect ratio on the wall's nonlinear response were investigated under quasi-static fully reversed cyclic loading. All walls were subjected to fully reversed displacement controlled quasi-static cyclic loading and were cycled up to 20% strength degradation. The following can be concluded from Phase I of the current study:

The variation of vertical reinforcement in BE had a noticeable effect on the RMSW+BEs peak strength. Results shows that walls with higher vertical reinforcement ratio in the BE ( $\rho_{v(BE)} = 1.58\%$ ) achieved a higher peak strength than those with lower vertical reinforcement ratios in

BE ( $\rho_{v(BE)}=0.79\%$ ). In addition, increasing the level of axial stress from zero to (0.3 MPa per story) resulted in increasing  $Q_{u(num)}$  by 26% for walls with ( $H_w/L_w = 1.5$ ), 42% for walls with ( $H_w/L_w = 2.25$ ), 48% for walls with ( $H_w/L_w = 3$ ), and 53% for walls with ( $H_w/L_w = 3.75$ ). However, the displacement ductility decreased with increasing axial stress, which is mainly attributed to an increase in yield displacement with increased axial stress. It was found that there was a decrease in  $\mu_{\Delta 0.8u}$  by 15% for walls with ( $H_w/L_w = 1.5$ ), 20% for walls with ( $H_w/L_w = 2.25$ ), 23% for walls with ( $H_w/L_w = 3$ ), and 40% for walls with ( $H_w/L_w = 3.75$ ). Results on the effect of varying the aspect ratio ( $H_w/L_w = 1.5, 2.25, 3, \text{ and } 3.75$ ) showed that the maximum lateral resistance of the walls increased as the height to length ratio decreased. Results obtained from the numerical mode indicated that walls with lower aspect ratio developed higher displacement ductility than those with higher aspect ratios. As  $H_w/L_w$  increased from 1.5 to 3.75,  $\mu_{\Delta 0.8u}$  dropped by 37%, 39%, and 55% for walls with zero, low and high axial stress, respectively. The inversely proportional aspect ratio-ductility relationship is due to the increase in the yield displacement as the aspect ratio increases, which was not offset by the increase in the displacement at maximum loads.

The following can be concluded from Phase II of the current study:

The steel-reinforced walls displayed a ductile behaviour, which approximately had a linear elastic response until the onset of the first yield in the outermost vertical reinforcement accompanied by thin hysteresis loops signifying a low level of energy dissipation; then, wider hysteresis loops signifying the increase in the energy dissipated by the walls were observed as the response of the walls started to become nonlinear at higher lateral displacements. On the other hand, the GFRP-reinforced walls reached the ultimate strength with no strength degradation up to the peak point due to the linear elastic nature of GFRP bars up to rupture. Decreasing the transverse hoop spacing from 120 mm to 60 mm significantly enhanced the lateral strength and displacement of steel-reinforced and GFRP-reinforced walls. This indicates the effectiveness of confining the masonry core by decreasing the hoop spacing in delaying failure. In addition, an increase in the vertical reinforcement ratio in the boundary element resulted in an increase in the yield and ultimate strength of the walls with square-shaped and rectangular-shaped BEs. Moreover, increasing the length of boundary element from 390 mm to 780 mm resulted in a slight improvement in the ultimate displacement of steel-reinforced and GFRP-reinforced walls.

However, a significant increase in the lateral load around 50% was observed for walls with rectangular-shaped BEs. Steel-reinforced and GFRP-reinforced walls with lower  $AR$  experienced more rapid strength degradation than did walls with higher  $AR$ , and the displacement at ultimate loads increased as the  $AR$  increased. The displacement ductility of the studied RMSW+BEs ranged from 7.7 to 15.4. Increasing the boundary element length results in increasing the ductility and increasing the yield and ultimate displacement of the wall. Moreover, increasing the vertical reinforcement in boundary elements increased the lateral strength, and the yield and ultimate displacement, but it had a minor effect on the ductility. In addition, increasing the confinement by decreasing the spacing between hoops had a noticeable effect on the displacement ductility for both walls with square-shaped and rectangular-shaped BEs.

## Chapter 5

### Development of Fragility Curves and Assessment of Force-based Design Parameters for RMSWs

#### 5.1 Introduction

Performance-based seismic design requires accurate damage models for different seismic force-resisting systems. Fragility functions are considered one of the most common damage models that link a specific demand parameter (i.e., story drift) to the probability of exceedance of different damage states. Recently, reinforced masonry shear walls with confined boundary elements showed enhanced lateral performance and curvature ductility compared to that of rectangular walls. However, limited data are available from literature to generate fragility curves for RMSW+BEs. In this chapter, the fragility curves for reinforced masonry shear walls with C-shaped boundary elements (RMSW+BE) were developed, adopting the guidelines set out by FEMA P-58-1 (2018). Results from the numerical models of thirty-six fully grouted walls (Phase I) described in Chapter 4 were used to generate fragility curves to assess the damageability of RMSW+BEs subjected to simulated seismic loads.

The wall effective elastic stiffness, displacement ductility, and seismic force modification factors are important force-based design (FBD) seismic design parameters for reinforced masonry (RM) shear walls. The effective stiffness,  $k_e$  of reinforced masonry shear walls (RMSW), is crucial in computing the natural period and, thus, the elastic forces, and essential also in computing the displacements corresponding to the seismic design forces. This study also analyzes previously reported test results of forty-three flexure-dominated fully-grouted rectangular RMSWs subjected to quasi-static cyclic load to evaluate the FBD parameters adopted by Canadian and US standards. In this study, based on the experimental results of forty-three tested walls, a new stiffness reduction factor is proposed considering the effect of axial stress, vertical reinforcement ratio, and horizontal reinforcement ratio. Moreover, the seismic force modification factors are compared to the Canadian and American codes. The present chapter also addresses the applicability of reinforced masonry shear walls with glass fibre-reinforced polymer (GFRP) bars to attain reasonable strength and drift. GFRP-RM shear walls are a corrosion-free lateral resisting system that is transparent to magnetic fields and radio frequencies and nonconductive thermally and electrically. Utilizing GFRP instead of steel bars has also many practical advantages since its much lighter than steel and

easy to be carried by masons hence resulting in higher productivity and efficiency. Numerical models of thirty-four flexure-dominated shear walls (Phase II) described in Chapter 4 were used to evaluate the influence of different design parameters on the hysteretic response, stiffness degradation, effective stiffness, and ductility related response modification factor was investigated to evaluate the enhancement in seismic performance of RM buildings with RMSW+BE.

## **5.2 Fragility Assessment**

### **5.2.1 Development of fragility curves**

Fragility curves are considered as an essential tool to mitigate structural losses from earthquakes and manage risk through seismic risk assessment. Fragility curves are developed to contribute towards a growing seismic performance database regarding the behaviour of RMSW+BEs. Fragility curves were introduced in the late 80s (Hwang 1987) where a specific engineering demand is related to the probability of exceedance of specific damage state (Hwang and Jaw 1990), such that the damage state is connected to the method of repair, which can be translated to repair cost.

In this study, the seismic performance of RMSW+BEs is assessed based on the guidelines and procedures provided in FEMA P-58-1 (2018) to evaluate the damageability of structural components using fragility functions. This methodology relates to the occurrence of specific damage states to the functionality or remediation costs when a structure is subjected to different levels of seismic events. To develop fragility curves, distinct damage states that are associated with different levels of repair, restoration efforts, and costs are identified. Damage states (DS) define the level of damage sustained by structural components under earthquake loading. In general, damage states are characterized by direct indicators of damage such as initiation of cracking, residual concrete crack width, the extent of concrete crushing, sliding shear displacement, reinforcement yielding, buckling, and fracture. Each of these damage states is linked with a method of repair, as shown in Table 5.1. In this study, the occurrence of damage states is identified for RMSW+BEs as it represents a new categorization of masonry structural walls in the Canadian design.

**Table 5.1** Damage state description for RMSW

<b>Damage state</b>	<b>Description</b>	<b>Repair measure</b>
DS1	<ol style="list-style-type: none"> <li>1. Few flexural and shear cracks with hardly noticeable residual crack widths.</li> <li>2. Slight yielding of extreme vertical reinforcement.</li> <li>3. No spalling.</li> <li>4. No fracture or buckling of vertical reinforcement.</li> <li>5. No significant structural damage.</li> </ol>	<ol style="list-style-type: none"> <li>1. Cosmetic repair.</li> <li>2. Patch cracks and paint each side.</li> </ol>
DS2	<ol style="list-style-type: none"> <li>1. Numerous flexural and diagonal cracks.</li> <li>2. Mild toe crushing with vertical cracks or light spalling at wall toes.</li> <li>3. No fracture or buckling of reinforcement.</li> <li>4. Small residual deformation.</li> </ol>	<ol style="list-style-type: none"> <li>1. Epoxy injection to repair cracks.</li> <li>2. Remove loose masonry.</li> <li>3. Patch spalls with nonshrink grout.</li> <li>4. Paint each side.</li> </ol>
DS3	<ol style="list-style-type: none"> <li>1. Severe flexural cracks.</li> <li>2. Severe toe crushing and spalling.</li> <li>3. Fracture or buckling of vertical reinforcement.</li> <li>4. Significant residual deformation.</li> </ol>	<ol style="list-style-type: none"> <li>1. Shore.</li> <li>2. Demolish the existing wall.</li> <li>3. Construct a new wall.</li> </ol>

Based on experimental observations (Shing et al., 1991), the failure modes of RMSW's are classified into three main types: (a) flexure, (b) diagonal shear, and (c) sliding shear. In this study, the fragility functions are limited to the flexure failure mode. Following the FEMA P-58-1 (2018) recommendations, flexure failure damage states can be further categorized into: slight (DS1), moderate (DS2), and severe damage state (DS3).

Using guidelines from FEMA P-58-1 (2018), damage state DS1 represents slight flexural damage and corresponds to a state at which the wall has been loaded to 80% of its peak resistance. Damage state DS2 represents moderate flexural damage and corresponds to a state at which the wall has reached its maximum flexural strength. Damage state DS3 represents severe flexural damage and associates to a state at which the wall has been loaded beyond its peak strength and exhibited a load drop of 20% from the peak.

Fragility functions relate the probability of exceedance of a damaged state to a demand parameter such as story drift ratio or floor acceleration. Component fragility functions provide a conditional probability that a particular damage state will occur in a component for a given demand value. The top drift,  $\Delta_i$  of each wall resulting from the occurrence of the first damage state associated with a specific method of repair, is selected as the demand parameter for use in fragility function generation. A lognormal probability distribution function is used to generate fragility curves. The lognormal probability distribution,  $F$  for any level of top drift,  $\Delta_i$  is given in Eq. (5.1) (FEMA P695 2009).

$$F(\Delta_i) = \varphi\left(\frac{\ln(\Delta_i / \theta_i)}{\beta_i}\right) \quad \text{Eq. (5.1)}$$

$$\theta_i = e^{\left(\frac{1}{M} \sum_{i=1}^M \ln \Delta_i\right)} \quad \text{Eq. (5.2)}$$

$$\beta = \sqrt{\beta_r^2 + \beta_u^2} \quad \text{Eq. (5.3)}$$

$$\beta_r = \sqrt{\left(\frac{1}{M-1}\right) \left(\sum_{i=1}^M \left(\ln\left(\frac{\Delta_i}{\theta_i}\right)\right)^2\right)} \quad \text{Eq. (5.4)}$$

where:

- $\theta_i$  = Median drift for each damage state given in Eq. (5.2),
- $\beta_i$  = Logarithmic standard deviation (dispersion) given in Eq. (5.3),
- $\varphi$  = Standard normal (Gaussian) cumulative distribution function,
- $F(\Delta_i)$  = Conditional probability that a component will have a damage state  $i$  when the value of the demand parameter is  $\Delta_i$ .
- $M$  = Number of specimens,
- $\Delta_i$  = Value of the demand parameter at which the damage state was identified,
- $\beta_r$  = Dispersion parameter given in Eq. (5.4),
- $\beta_u$  = Dispersion parameter accounts for uncertainty taken as 0.25 or 0.1,

The dispersion parameter  $\beta$  consists of two parts. The dispersion parameter,  $\beta_r$  accounts for the random variability of the data is calculated according to Eq. (5.4). The dispersion parameter  $\beta_u$  accounts for the uncertainty that the data represent the actual conditions in a real building. As stated by FEMA P-58-1 (2018),  $\beta_u$  is assumed to be 0.25 for the Class A fragility functions, while it is assumed to be 0.10 for Class B, based on the fact that the use of the normalized demand parameters in the Class B fragility functions better reflects the different design and loading conditions that might occur in real buildings. Therefore,  $\beta_u$  was taken as 0.1 in this study. For each damage state, the limiting level of top drift associated with the first occurrence of any damage state for a particular wall is also presented in Table 5.2. The total number of wall specimens is given as  $M$ , and the calculated values of  $\theta_i$  and  $\beta$  are listed in Table 5.3. The fragility functions are represented by a smoothed curve fit to the occurrence of each damage state in each wall. Figure 5.1 shows the fragility curves for each damage state (DS1, DS2, and DS3) for the studied 36 walls. It can be seen in Table 5.3 that the median drift  $\theta$  decreased from 0.22% at DS1 to 1.71% at DS3.

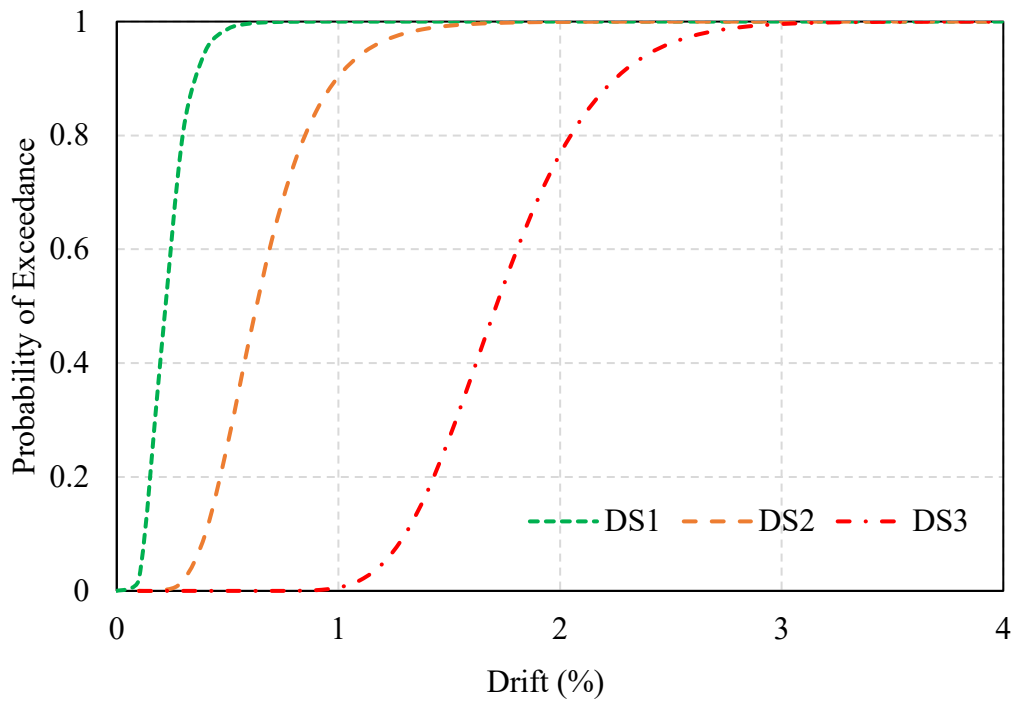


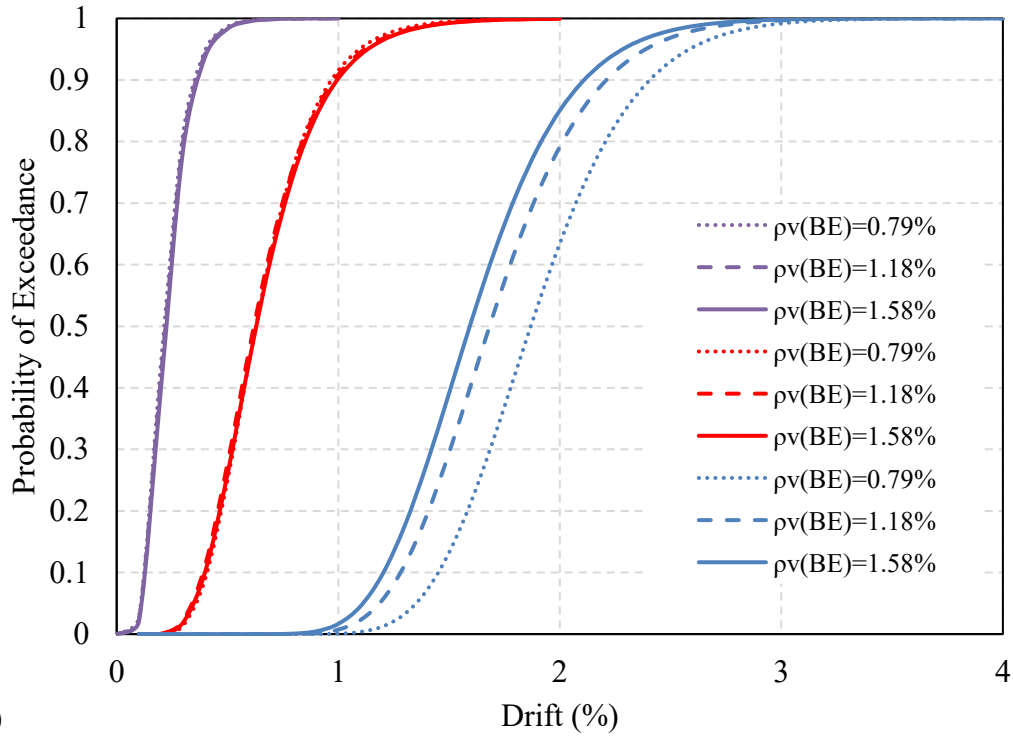
**Figure 5.1** Fragility curves for all set of walls

**Table 5.2** Top drifts associated with damage states

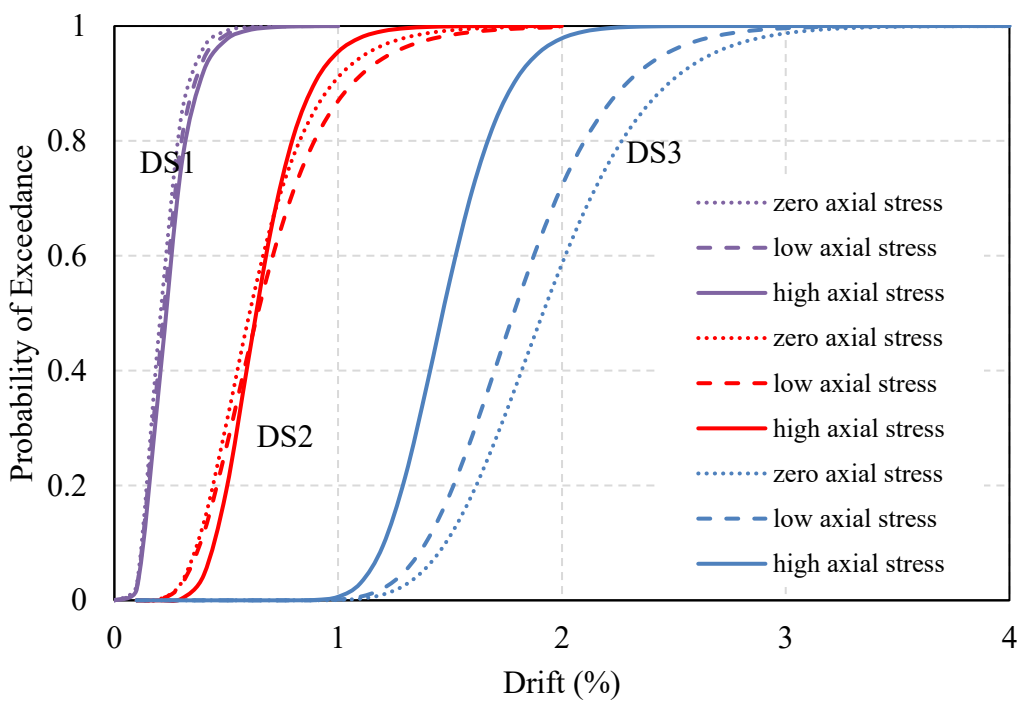
Wall ID	Top drift (%)		
	DS1	DS2	DS3
S6S4-0	0.12	0.36	1.67
S9S4-0	0.18	0.54	1.94
S12S4-0	0.24	0.69	2.26
S15S4-0	0.30	0.88	2.54
S6S6-0	0.12	0.37	1.54
S9S6-0	0.19	0.54	1.77
S12S6-0	0.25	0.75	1.99
S15S6-0	0.31	0.92	2.33
S6S8-0	0.13	0.38	1.46
S9S8-0	0.19	0.57	1.68
S12S8-0	0.25	0.73	1.91
S15S8-0	0.32	0.92	2.22
S6S4-0.3	0.13	0.36	1.58
S9S4-0.45	0.19	0.57	1.81
S12S4-0.6	0.26	0.78	2.06
S15S4-0.75	0.33	0.95	2.29
S6S6-0.3	0.13	0.37	1.43
S9S6-0.45	0.20	0.56	1.64
S12S6-0.6	0.26	0.79	1.97
S15S6-0.75	0.33	0.98	2.15
S6S8-0.3	0.13	0.39	1.38
S9S8-0.45	0.20	0.58	1.57
S12S8-0.6	0.27	0.79	1.73
S15S8-0.75	0.34	1.02	2.07
S6S4-0.6	0.13	0.37	1.48
S9S4-0.9	0.20	0.59	1.61
S12S4-1.2	0.27	1.24	1.83
S15S4-1.5	0.35	0.68	1.67
S6S6-0.6	0.13	0.60	1.28
S9S6-0.9	0.20	0.61	1.43
S12S6-1.2	0.28	0.84	1.56
S15S6-1.5	0.35	0.69	1.43
S6S8-0.6	0.13	0.40	1.21
S9S8-0.9	0.21	0.61	1.36
S12S8-1.2	0.28	0.85	1.50
S15S8-1.5	0.36	0.67	1.36

A set of fragility functions for each damage state (DS1, DS2, and DS3) depending on the design parameters is presented in Figure 5.2. As shown in Figure 5.2 (a), the reinforcement ratio,  $\rho_{v(BE)}$ , had minimal influence on the fragility curves for damage states DS1 and DS2. However, at DS3,  $\theta$  decreased by 18% for walls having a high reinforcement ratio in the BE (i.e.,  $\rho_{v(BE)}= 1.58\%$ ) when compared to walls having low vertical reinforcement ratio in BE (i.e.,  $\rho_{v(BE)}= 0.79\%$ ). In addition, the drifts for 80% probability of achieving DS3 are 2.25%, 2.05%, 1.95% for walls having  $\rho_{v(BE)}$  of 0.79%, 1.18%, and 1.58%, respectively. Figure 5.2 (b) shows that the axial load had a noticeable effect on the developed fragility curves for DS3, but a slight effect on damage states DS1 and DS2. For DS3,  $\theta$  decreased by 23% for walls under a high level of axial stress when compared to walls under zero level of axial stress. Furthermore, the drifts corresponding to 80% probability decreased from 2.3% to 1.7% for walls with a high level of axial stress when compared to walls with zero level of axial stress.

It can also be seen in Figure 5.2 (c) that the median drift  $\theta$  increased as aspect ratio increased for all damage states (DS1, DS2, and DS3). For DS1,  $\theta$  increased from 0.13% to 0.33%, for walls having  $H_w/L_w=1.5$  and  $H_w/L_w=3.75$ , respectively. For DS2,  $\theta$  increased from 0.38% to 0.86%, for walls having  $H_w/L_w=1.5$  and  $H_w/L_w=3.75$  respectively. For DS3,  $\theta$  increased from 1.44% to 1.96%, for walls having  $H_w/L_w=1.5$  and  $H_w/L_w=3.75$  respectively. It can also be inferred from Figure 5.2 (c) that the drifts associated with 80% probability for all damage states are lower for walls having a low aspect ratio (i.e.,  $H_w/L_w=1.5$ ) in comparison to walls with higher aspect ratios (i.e.,  $H_w/L_w=3.75$ ). For walls with  $H_w/L_w=3.75$ , the drifts corresponding to 80% probability of exceedance varied from 0.14%, 0.42%, 1.65% for DS1, DS2, DS3, respectively. For walls with  $H_w/L_w=1.5$ , the drifts at 80% probability of exceedance varied from 0.37%, 1.02%, 2.40% for DS1, DS2, DS3, respectively.



(a)



(b)

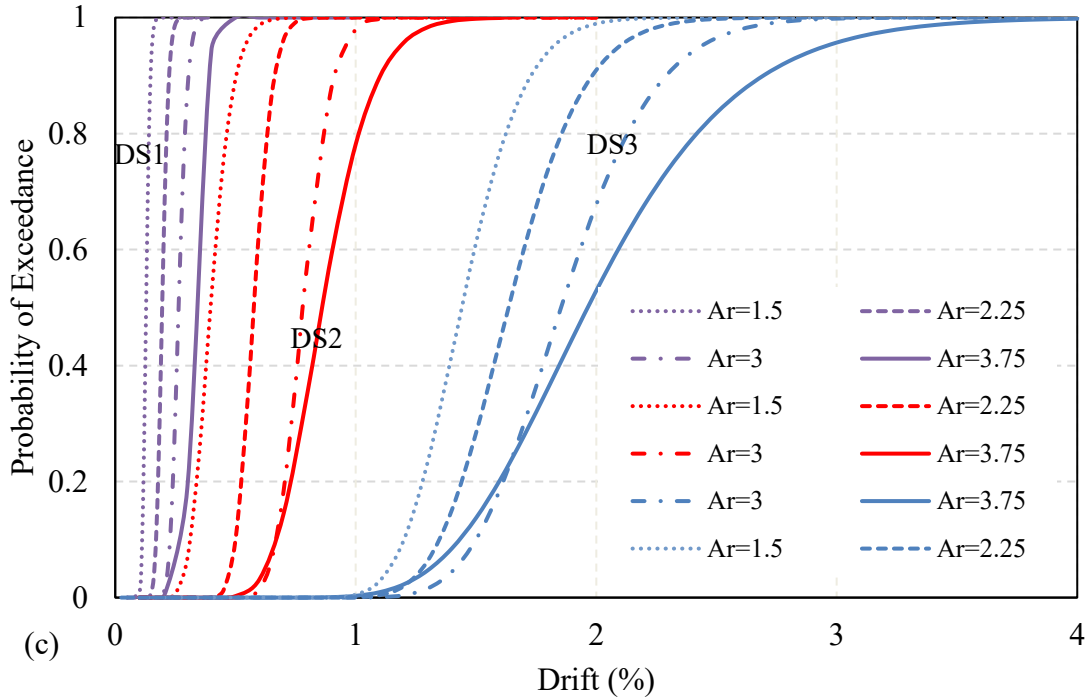


**Figure 5.2** Fragility curves based on design parameters: (a)  $\rho_{v(BE)}$ ; (b) Axial stress; (c) Aspect Ratio

### 5.2.2 Lilliefors test

Lilliefors test is used to quantify the goodness of fit of the fragility functions for all thirty-six walls (Lilliefors 1967). This test is carried out to assess the acceptability of the lognormal distribution for a 95% confidence level as required by FEMA P-58-1 (2018). The results for the Lilliefors test for all walls are presented in Table 5.3. The  $D$  statistic is the Kolmogorov-Smirnov test parameter and corresponds to the maximum of the absolute value of the differences between the empirical and theoretical cumulative distribution function. The null hypothesis,  $H_0$ , for the test, is the decision on whether to accept or reject the hypothesis (A=Accept, R=Reject). The null hypothesis is accepted if  $D$  is less than or equal to the Lilliefors test parameter  $D_{crit}$  at a 5% significance level.

The developed fragility functions passed the Lilliefors test for damage states (DS1, DS2, DS3) of the thirty-six walls. FEMA P-58-1 (2018) quantifies the fragility functions as high quality if the fragility functions pass the Lilliefors test and have logarithmic standard deviations,  $\beta$  less than 0.6. The results indicate that the developed set of fragility functions for the in-plane response of RMSW+BEs corresponding to flexure-dominated damage states (DS1, DS2, and DS3) are

considered high-quality fragility functions, which can be adopted in the performance-based seismic design framework. Furthermore, the results obtained from the fragility assessment support the inclusion of Special RM shear walls with confined boundary elements within future masonry design codes as well within the development of future performance-based seismic design codes.

**Table 5.3** Lilliefors test results for the total set of walls

<b>Damage state</b>	<b>Logarithmic distribution</b>		<b>Lilliefors test</b>		
	$\theta$	$\beta$	$D$	$D_{crit}$	$H_0$
DS1	0.22	0.38	0.144	0.146	A
DS2	0.63	0.36	0.116	0.146	A
DS3	1.71	0.23	0.086	0.146	A

**Table 5.4** Lilliefors test results based on design parameters

Damage state	Design Parameters	Logarithmic distribution		Lilliefors test		
		$\theta$	$\beta$	$D$	$D_{crit}$	$H_0$
DS1	$\rho_{v(BE)}=0.79\%$	0.212	0.39	0.146	0.243	A
	$\rho_{v(BE)}=1.18\%$	0.216	0.39	0.149	0.243	A
	$\rho_{v(BE)}=1.58\%$	0.220	0.39	0.148	0.243	A
DS2	$\rho_{v(BE)}=0.79\%$	0.607	0.365	0.139	0.243	A
	$\rho_{v(BE)}=1.18\%$	0.619	0.360	0.142	0.243	A
	$\rho_{v(BE)}=1.58\%$	0.630	0.357	0.146	0.243	A
DS3	$\rho_{v(BE)}=0.79\%$	1.87	0.197	0.137	0.243	A
	$\rho_{v(BE)}=1.18\%$	1.68	0.213	0.138	0.243	A
	$\rho_{v(BE)}=1.58\%$	1.59	0.219	0.150	0.243	A
DS1	$AR=1.5$	0.128	0.105	0.264	0.274	A
	$AR=2.25$	0.195	0.109	0.256	0.274	A
	$AR=3$	0.263	0.113	0.261	0.274	A
	$AR=3.75$	0.332	0.116	0.251	0.274	A
DS2	$AR=1.5$	0.378	0.111	0.270	0.274	A
	$AR=2.25$	0.576	0.110	0.266	0.274	A
	$AR=3$	0.781	0.121	0.258	0.274	A
	$AR=3.75$	0.860	0.194	0.190	0.274	A
DS3	$AR=1.5$	1.441	0.142	0.154	0.274	A
	$AR=2.25$	1.635	0.151	0.168	0.274	A
	$AR=3$	1.854	0.165	0.180	0.274	A
	$AR=3.75$	1.964	0.247	0.252	0.274	A
DS1	Zero axial stress	0.205	0.372	0.173	0.243	A
	Low axial stress	0.217	0.386	0.177	0.243	A
	High axial stress	0.227	0.398	0.184	0.243	A
DS2	Zero axial stress	0.604	0.375	0.155	0.243	A
	Low axial stress	0.641	0.396	0.187	0.243	A
	High axial stress	0.633	0.269	0.227	0.243	A
DS3	Zero axial stress	1.915	0.201	0.107	0.243	A
	Low axial stress	1.785	0.194	0.119	0.243	A
	High axial stress	1.467	0.153	0.131	0.243	A

## 5.3 Force-based Design Parameters for Rectangular RMSWs

### 5.3.1 Database

In this study, the data from previously tested fully grouted RMSW under quasi-static cyclic loading was analyzed following the FBD philosophies adopted by both ASCE 7-16 (2016) and the NBCC (2015). Forty-three rectangular flexural dominated RMSWs are considered in this study collected from literature [Priestley, and Elder (1982), Eikanas (2003), Shedid (2006), Shedid et al. (2008), Sherman (2011), Ahmadi (2012), Kapoi (2012), Siyam (2015)]. As shown in Table 5.5, the walls covered a wide range of design parameters where the axial compressive stress ranges from 0.05 to 3.6 MPa, the wall height to length ( $h_w/l_w$ ) aspect ratio ranges from 0.7 to 4.6, the vertical and horizontal reinforcement ratio ( $p_v, p_h$ ) varies from 0.3 to 1.3 and 0.1 to 0.4, respectively. Moreover, the average compressive strength,  $f'_m$  of tested prisms for the considered walls ranges from 11.2 MPa to 30 MPa. Although most of the considered walls were constructed as a full scale, seven scaled walls, having a scale of 0.7, 0.5, and 0.3, are considered in the database, as shown in Table 5.5. Scaled walls were built using scaled masonry blocks, rebars, and in some studies, the aggregate gradation of the mortar and the grout was also scaled to use finer aggregates.

It should be noted that the axial stress reported in Table 5.5 is computed based on the imposed axial load, the wall's own weight, and the loading beam's weight. Table 5.5 reports the height from the top of the footing to the point of application of load,  $h_{top}$ , and the wall's height,  $h_w$ . In addition, the average compressive strength of the tested prisms is reported in MPa, and  $f'_m$  is extracted from CSA S304 (2014), and TMS 402/602 (2016) based on block strength is also reported. To avoid any deviation in the prism testing method between each study, this study utilizes the  $f'_m$  values based on the block strength rather than the average tested prism strength (see Table 5.5). Walls W39, and W40 tested by Kapoi (2012) had two layers of vertical reinforcement concentrated toward the wall ends (i.e., jambs). The vertical reinforcement of Wall W14 tested by Shedid (2006) had high yield strength of 629 MPa. Walls W34 and W35 had a lap splice in the vertical rebars.

**Table 5.5** Collected database for flexural dominated RMSWs tested under quasi-static cyclic loading

Ref.	Wall ID#	Specimen label in the reference	Axial load (P)					AR	Scale	Shear span to depth ratio M/Vdv	Vertical reinforcement								Horizontal reinforcement					Block Strength Mpa	$f'_m$		Average experimental prism strength		$T_e$ (sec)		
			N	mm	mm	mm	mm				No. of bars	$A_s$ mm <sup>2</sup>	$S_v$ mm	$\rho_v$ %	$f_{yv}$ MPa	$f_{sv}$ MPa	Cover 1 mm	Cover 2 mm	No. of bars	$A_h$ mm <sup>2</sup>	$S_h$ mm	$\rho_h$ %	$f_{yh}$ MPa		$f_{sh}$ MPa	MPa	MPa	MPa		MPa	
																															mm
			CSA Table 4	TMS Table 2	CSA (4blocks)	MSJC (2blocks)																									
Priestley & Elder (1982)	1	Wall 1	640000	2400	6000	6000	140	2300	2.5	0.7	3.1	12	201	200.0	0.72	434	727	100	100	27	113.1	200.0	0.3635	322	455	40.0	13.5	20.7	25.00	25	0.45
	2	Wall 3	250000	2400	6000	6000	140	2300	2.5	0.7	3.1	12	201	200.0	0.72	434	727	100	100	27	113.1	200.0	0.3635	322	455	40.0	13.5	20.7	25.00	25	0.31
Eikanas (2003)	3	Wall 1	61729	1413	1321	1829	194	1311	1.3	1.0	1.2	4	200	406.4	0.29	455	-	101.6	101.6	5	129.0	406.4	0.18	444	-	21.2	10.4	14.8	9.0	11.2	0.07
	4	Wall 2	66525	1413	2134	2642	194	1311	1.9	1.0	1.9	4	200	406.4	0.29	455	-	101.6	101.6	7	129.0	406.4	0.18	444	-	21.2	10.4	14.8	9.0	11.2	0.16
	5	Wall 4	61729	1413	1321	1829	194	1311	1.3	1.0	1.2	7	200	203.2	0.51	455	-	101.6	101.6	5	129.0	406.4	0.18	444	-	21.2	10.4	14.8	9.0	11.2	0.08
	6	Wall 5	66525	1413	2134	2642	194	1311	1.9	1.0	1.9	7	200	203.2	0.51	455	-	101.6	101.6	7	129.0	406.4	0.18	444	-	21.2	10.4	14.8	9.0	11.2	0.13
	7	Wall 6	47389	1006	2134	2642	194	905	2.6	1.0	2.6	5	200	203.2	0.51	455	-	101.6	101.6	7	129.0	406.4	0.18	444	-	21.2	10.4	14.8	9.0	11.2	0.13
	8	Wall 7	79485	1819	1321	1829	194	1718	1.0	1.0	0.9	5	200	406.4	0.28	455	-	101.6	101.6	5	129.0	406.4	0.18	444	-	21.2	10.4	14.8	9.0	11.2	0.06
	9	Wall 2	29485	1800	3600	3600	190	1700	2.0	1.0	2.5	9	500	200.0	1.32	503	704	100.0	100.0	18	100.0	200.0	0.2632	491	786	22.7	10.9	15.5	14.9	17.1	0.08
	10	Wall 3	29485	1800	3600	3600	190	1700	2.0	1.0	2.5	5	500	400.0	0.73	503	704	100.0	100.0	9	100.0	400.0	0.1316	491	786	22.7	10.9	15.5	14.9	17.1	0.09
Shedid (2006)	11	Wall 4	29485	1800	3600	3600	190	1700	2.0	1.0	2.5	9	300	200.0	0.79	504	706	100.0	100.0	9	100.0	400.0	0.1316	491	786	22.7	10.9	15.5	14.9	17.1	0.08
	12	Wall 5	29485	1800	3600	3600	190	1700	2.0	1.0	2.5	5	200	400.0	0.29	499	699	100.0	100.0	6	100.0	600.0	0.0877	491	786	22.7	10.9	15.5	14.9	17.1	0.10
	13	Wall 6	284940	1800	3600	3600	190	1700	2.0	1.0	2.5	9	500	200.0	1.32	503	704	100.0	100.0	18	100.0	200.0	0.2632	491	786	22.7	10.9	15.5	14.9	17.1	0.24
	14	Wall 7	541940	1800	3600	3600	190	1700	2.0	1.0	2.5	9	500	200.0	1.32	629	880	100.0	100.0	18	100.0	200.0	0.2632	491	786	22.7	10.9	15.5	14.9	17.1	0.29
Shedid (2009)	15	Wall 1	176776	1802	3990	3990	90	1757	2.2	0.5	2.8	19	100	90.0	1.17	495	600	45.0	45.0	39	25.4	95.0	0.2759	534	600	27.2	12.5	17.9	16.0	18.4	0.24
	16	Wall 4	176776	1802	2660	2660	90	1757	1.5	0.5	1.8	19	100	90.0	1.17	495	600	45.0	45.0	26	25.4	95.0	0.2759	534	600	27.2	12.5	17.9	16.0	18.4	0.12
Sherman (2011)	17	WSU-Wall 1A	220739	1006	2013	1829	194	905	1.8	1.0	2.5	5	284	203.2	0.7285	451	722	101.6	101.6	9	129.0	203.2	0.33	456	730	24.0	11.4	16.3	16.0	20.0	0.23
	18	WSU-Wall 1B	220739	1006	2013	1829	194	905	1.8	1.0	2.5	5	284	203.2	0.7285	446	714	101.6	101.6	9	129.0	203.2	0.33	456	730	24.0	11.4	16.3	16.0	20.0	0.21
	19	WSU-Wall 2A	431746	1006	2013	1829	194	905	1.8	1.0	2.5	5	129	203.2	0.3309	451	722	101.6	101.6	9	129.0	203.2	0.33	456	730	24.0	11.4	16.3	16.0	20.0	0.27
	20	WSU-Wall 2B	431746	1006	2013	1829	194	905	1.8	1.0	2.5	5	129	203.2	0.3309	450	720	101.6	101.6	9	129.0	203.2	0.33	450	720	24.0	11.4	16.3	16.0	20.0	0.26
	21	WSU-Wall 3	18208	1819	1819	1626	194	1718	0.9	1.0	1.3	9	129	203.2	0.3295	450	720	101.6	101.6	3	129.0	609.6	0.12	450	720	24.0	11.4	16.3	16.0	20.0	0.04
	22	WSU-Wall 4	397186	1819	1819	1626	194	1718	0.9	1.0	1.3	9	129	203.2	0.3295	450	720	101.6	101.6	8	129.0	203.2	0.33	450	720	24.0	11.4	16.3	16.0	20.0	0.12
	23	WSU-Wall 5	15120	1819	1413	1219	194	1718	0.7	1.0	1.0	9	129	203.2	0.3295	450	720	101.6	101.6	6	129.0	203.2	0.33	450	720	24.0	11.4	16.3	16.0	20.0	0.02
	24	WSU-Wall 6	394099	1819	1413	1219	194	1718	0.7	1.0	1.0	9	129	203.2	0.3295	450	720	101.6	101.6	6	129.0	203.2	0.33	450	720	24.0	11.4	16.3	16.0	20.0	0.10
Ahmadi (2012)	25	UT-W-13	385301	1219	3886	3658	194	1118	3.0	1.0	4.0	6	284	203.2	0.72	421	703	101.6	101.6	9	129.0	406.4	0.16	448	705	24.0	11.4	16.3	24.0	30.0	0.40
	26	UT-W-14	574204	1219	3886	3658	194	1118	3.0	1.0	4.0	6	129	203.2	0.33	448	705	101.6	101.6	9	129.0	406.4	0.16	448	705	24.0	11.4	16.3	18.4	23.0	0.62
	27	UT-W-15	574204	1219	3886	3658	194	1118	3.0	1.0	4.0	6	284	203.2	0.72	421	703	101.6	101.6	9	129.0	406.4	0.16	448	705	24.0	11.4	16.3	18.4	23.0	0.59
	28	UT-W-16	845752	1219	3886	3658	194	1118	3.0	1.0	4.0	6	129	203.2	0.33	448	705	101.6	101.6	9	129.0	406.4	0.16	448	705	24.0	11.4	16.3	18.4	23.0	0.64
	29	UT-W-17	250384	812.8	3886	3658	194	711	4.5	1.0	6.0	4	284	203.2	0.72	421	703	101.6	101.6	18	129.0	203.2	0.33	448	705	24.0	11.4	16.3	23.2	29.0	0.67
	30	UT-W-18	478642	812.8	3886	3658	194	711	4.5	1.0	6.0	4	129	203.2	0.33	448	705	101.6	101.6	18	129.0	203.2	0.33	448	705	24.0	11.4	16.3	23.2	29.0	0.80
	31	UT-W-19	384190	812.8	3886	3658	194	711	4.5	1.0	6.0	4	284	203.2	0.72	421	703	101.6	101.6	9	129.0	406.4	0.16	448	705	24.0	11.4	16.3	18.4	23.0	0.78
	32	UT-W-20	565222	812.8	3886	3658	194	711	4.5	1.0	6.0	4	129	203.2	0.33	448	705	101.6	101.6	9	129.0	406.4	0.16	448	705	24.0	11.4	16.3	18.4	23.0	0.87
Kapoi (2012)	33	WSU-Wall C1	11150	1016	2032	1829	194	914	1.8	1.0	2.5	5	129	203.2	0.33	450	720	101.6	101.6	9	129.0	203.2	0.3278	450	720	23.9	11.4	16.2	16.8	21.0	0.07
	34	WSU-Wall C2	269416	1016	2032	1829	194	914	1.8	1.0	2.5	5	129	203.2	0.33	455	728	101.6	101.6	9	129.0	203.2	0.3278	455	728	23.9	11.4	16.2	16.8	21.0	0.24
	35	WSU-Wall C3	204235	1016	2032	1829	194	914	1.8	1.0	2.5	3	387	406.4	0.59	455	728	101.6	101.6	9	129.0	203.2	0.3278	455	728	23.9	11.4	16.2	12.6	15.7	0.24
	36	WSU-Wall C4	362720	1829	1422	1219	194	1727	0.7	1.0	1.0	5	387	406.4	0.55	455	728	101.6	101.6	12	129.0	203.2	0.6556	455	728	23.9	11.4	16.2	12.6	15.7	0.10
	37	WSU-Wall C5	365824	1829	1829	1626	194	1727	0.9	1.0	1.3	5	387	406.4	0.55	455	728	101.6	101.6	16	129.0	203.2	0.6556	455	728	23.9	11.4	16.2	12.6	15.7	0.14
	38	WSU-Wall C6	21548	1422	2845	2642	194	1321																							

### 5.3.2 Wall Classification According to CSA S304-14 and TMS 402/602-16

The CSA S304 (2014) divides RMSWs into four categories (conventional, moderately ductile, moderately ductile squat, and ductile walls). Several requirements must be satisfied, including limitations on axial loads, aspect ratio, detailing as well as the distribution of vertical and horizontal reinforcement. In addition, to ensure adequate wall rotational capabilities within the plastic hinge zone, the inelastic rotational capacity of the wall,  $\theta_{ic}$ , should be higher than the inelastic rotational demand of the wall,  $\theta_{id}$  in moderately ductile and ductile shear walls. The TMS 402/602 (2016) divides RMSWs into three categories (ordinary, intermediate, and special). Prescriptive reinforcement requirements in terms of the amount of reinforcement and spacing must be satisfied according to each wall category specification. In addition, the maximum flexural reinforcement provisions shall be satisfied. Walls with large amounts of reinforcement may result in crushing of masonry before adequate development of tensile reinforcement strain and thus limits ductility. Therefore, strain values in the extreme tensile reinforcement and the compressive masonry were examined. If the strain in the extreme tensile reinforcement at the time of masonry failure did not meet or exceed the provisions set, then the wall was downgraded to a lower wall type. The strain in the extreme tensile reinforcement had to be equal to or exceed four times its yield strain for special, three times the yield strain for intermediate, and 1.5 times the yield strain for ordinary shear walls.

Classification of the walls in this study was based on the category description of RMSWs according to CSA S304 (2014), and TMS 402/602 (2016) standards summarized in Appendix C (Table C1, and Table C2). All 43 fully grouted RMSWs from the previous experimental studies were classified according to the shear wall types defined in Canadian and US codes (see Table A3). The majority of the walls were classified as special walls, twelve walls as ordinary walls, and eleven walls as intermediate walls, according to TMS 402/602 (2016). However, the majority of the walls were classified as conventional walls, and four walls were classified as moderately ductile walls, according to CSA S304 (2014). Most of the walls taken under consideration in this study were classified as conventional walls as their inelastic rotational capacity was not sufficient and did not meet the standard limit for the inelastic rotational demand of moderately ductile and ductile walls. It was observed that the calculation for the inelastic rotation capacity according to CSA S304 (2014) is conservative since it assumes a maximum ultimate strain of 0.0025, uses

lower values for  $f'_m$  from Table 4 [CSA S304 (2014)], and a plastic hinge length,  $L_p$  equal to the wall length. In addition, for the inelastic rotation demands,  $L_p$  is assumed to be equal to the wall length. This observation was also valid when reduced values of the lateral displacement at the top,  $\Delta_{fl}$ , were used to compute the inelastic rotational demand. As a result, some of the walls that seem to be ductile are not considered ductile as per CSA S304 (2014) requirements.

### 5.3.3 Load- displacement idealization

As shown in Figure 5.3, for each RMSW, the envelope of the load-displacement hysteretic curves was generated. The displacement ductility value of the walls,  $\mu_{\Delta}$ , is defined as the ratio of the maximum wall displacement to the corresponding experimental yield displacement (see Figure 5.3). The load-displacement envelope curve was subsequently idealized to bilinear elastic-perfect plastic, according to Tomažević (1999). As such, the elastic line intersects the ascending curve in the experimental yield point. Then the perfect plastic line was adjusted such that the area under the idealized bilinear curve equals the area under the experimental load-displacement envelope up to the failure point. The ultimate displacement,  $\Delta_u$ , was identified as the failure point based on [Priestley et al. (1986); Priestley et al. (2007)] recommendation at 20% strength degradation on the post-peak descending curve.

The idealized wall capacity,  $Q_u^{id}$ , idealized yield displacement,  $\Delta_y^{id}$ , idealized stiffness,  $k_y^{id}$ , and ultimate displacement,  $\Delta_u$  are presented in Table 5.6 for both loading directions. The idealized stiffness,  $k_y^{id}$ , is calculated as the ratio between the idealized wall capacity,  $Q_u^{id}$ , and the idealized yield displacement,  $\Delta_y^{id}$ . The idealized bilinear curve was generated to compute the FBD parameters. The following section is focusing on comparing the experimentally computed values with the calculated values based on CSA S304 (2014) and TMS 402/602 (2016) masonry standards procedures.

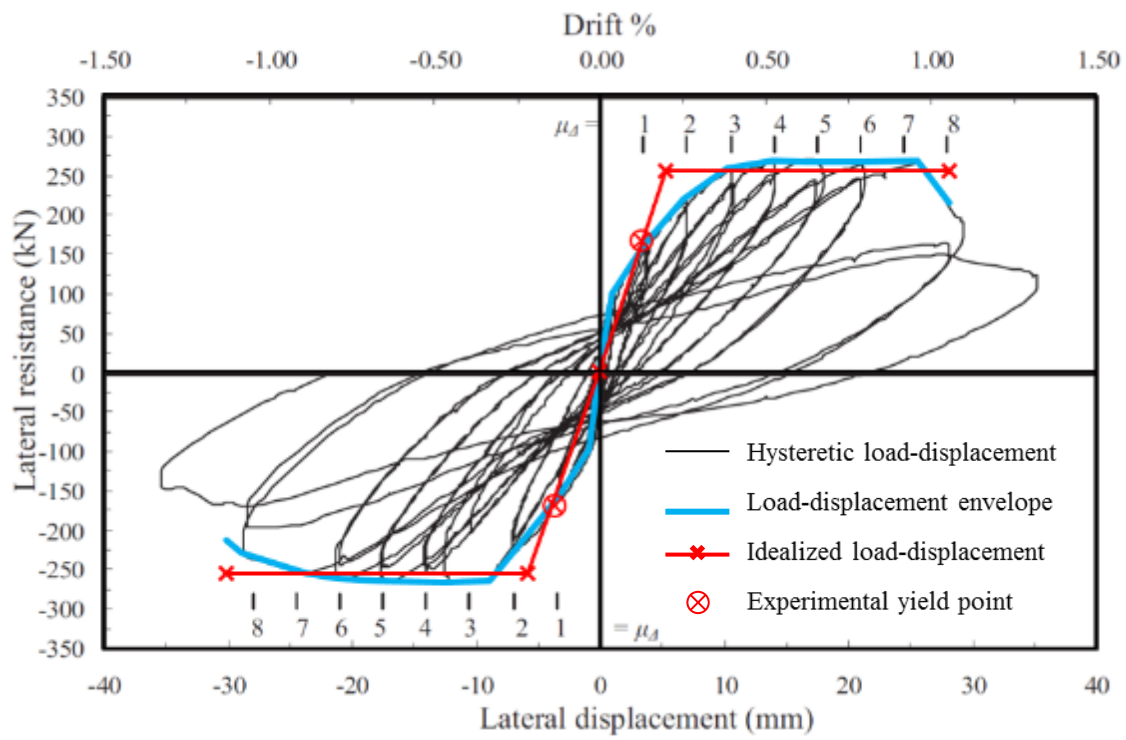


**Figure 5.3** Sample of the experimental load-displacement curve bilinear idealization. (Modified from Shedid et al. (2008))

**Table 5.6** Elastic perfectly plastic idealized loads, displacements, and stiffness

Wall ID#	Specimen label in reference	Reference	Idealized response									
			$Q_u^{id}$		$\Delta_y^{id}$		$\Delta_u$		$k_{eff}$			
			+ve	-ve	+ve	-ve	+ve	-ve	+ve	-ve	Average	
			kN		mm		mm		kN/mm			
W1	Wall 1	Priestley & Elder (1982)	305.0	-286.8	24.3	-22.9	59.9	-58.7	12.5	12.5	12.5	
W2	Wall 3		250.9	-238.0	23.8	-22.5	107.3	-88.4	10.6	10.6	10.6	
W3	Wall 1	Eikanas (2003)	209.4	-195.3	4.7	-4.1	29.2	-29.3	44.7	47.6	46.2	
W4	Wall 2		114.7	-162.6	9.7	-17.8	50.8	-40.7	11.9	9.1	10.5	
W5	Wall 4		259.0	-208.9	6.6	-5.3	19.4	-24.3	39.2	39.2	39.2	
W6	Wall 5		156.2	-189.7	9.6	-14.1	40.0	-46.1	16.3	13.4	14.9	
W7	Wall 6		105.3	-106.0	9.9	-10.2	56.9	-57.1	10.6	10.4	10.5	
W8	Wall 7		243.7	-252.6	4.0	-2.5	25.4	-25.4	60.7	100.0	80.3	
W9	Wall 2		360.1	-367.6	18.2	-18.9	59.0	-53.0	19.7	19.5	19.6	
W10	Wall 3	Shedid (2006)	224.3	-231.5	14.2	-17.1	66.0	-44.0	15.8	13.6	14.7	
W11	Wall 4		251.0	-238.2	14.9	-14.4	66.8	-68.0	16.8	16.5	16.7	
W12	Wall 5		134.0	-117.9	9.9	-10.7	77.5	-74.7	13.6	11.1	12.3	
W13	Wall 6		379.6	-411.5	19.5	-20.8	44.8	-45.7	19.4	19.8	19.6	
W14	Wall 7		557.5	-575.7	21.1	-22.8	51.4	-58.8	26.5	25.3	25.9	
W15	Wall 1		Shedid (2009)	165.3	-167.5	13.5	-13.3	45.2	-49.0	12.2	12.6	12.4
W16	Wall 4			252.9	-255.9	5.3	-5.8	28.1	-30.0	47.6	44.4	46.0
W17	WSU-Wall 1A	Sherman (2011)	172.7	-166.1	11.1	-9.7	49.8	-66.2	15.6	17.1	16.3	
W18	WSU-Wall 1B		197.8	-179.9	10.0	-8.2	40.1	-59.2	19.7	22.0	20.9	
W19	WSU-Wall 2A		160.7	-152.9	7.1	-6.4	39.3	-44.1	22.6	23.9	23.3	
W20	WSU-Wall 2B		161.8	-151.2	7.5	-5.2	37.3	-37.7	21.6	29.0	25.3	
W21	WSU-Wall 3		237.0	-235.4	4.4	-3.7	16.3	-17.4	53.8	63.4	58.6	
W22	WSU-Wall 4		385.7	-407.4	3.5	-3.5	21.2	-20.7	110.0	117.5	113.8	
W23	WSU-Wall 5		285.9	-320.1	2.6	-3.4	16.9	-23.1	111.2	95.4	103.3	
W24	WSU-Wall 6		476.7	-509.1	2.7	-2.9	16.6	-28.2	174.3	176.4	175.3	
W25	UT-W-13		Ahmadi (2012)	124.3	-131.3	12.4	-14.3	67.6	-70.2	10.1	9.2	9.6
W26	UT-W-14	101.8		-102.8	16.4	-18.1	96.7	-90.8	6.2	5.7	5.9	
W27	UT-W-15	137.4		-156.5	21.2	-23.2	74.3	-81.2	6.5	6.8	6.6	
W28	UT-W-16	104.2		-118.1	14.2	-12.6	70.6	-83.1	7.3	9.4	8.3	
W29	UT-W-17	59.8		-60.7	27.1	-27.4	173.4	-169.0	2.2	2.2	2.2	
W30	UT-W-18	39.9		-38.7	14.6	-12.0	95.9	-132.4	2.7	3.2	3.0	
W31	UT-W-19	77.2		-58.5	34.9	-20.3	115.7	-128.5	2.2	2.9	2.5	
W32	UT-W-20	57.5		-58.2	19.5	-18.9	101.7	-106.2	2.9	3.1	3.0	
W33	WSU-Wall C1	Kapoi (2012)		74.4	-74.1	7.9	-7.4	43.8	-58.5	9.4	10.0	9.7
W34	WSU-Wall C2		132.6	-124.5	7.6	-6.0	47.3	-47.3	17.5	20.9	19.2	
W35	WSU-Wall C3		170.4	-147.5	12.0	-9.7	47.6	-59.0	14.2	15.2	14.7	
W36	WSU-Wall C4		573.3	-581.4	3.7	-4.3	19.9	-20.2	155.0	134.6	144.8	
W37	WSU-Wall C5		514.2	-536.6	6.4	-6.7	25.9	-25.9	80.3	80.3	80.3	
W38	WSU-Wall C6		187.1	-193.3	14.0	-15.1	70.1	-69.8	13.4	12.8	13.1	
W39	WSU-Wall C7		240.0	-247.4	13.5	-20.5	79.4	-79.0	17.7	12.0	14.9	
W40	WSU-Wall C8		295.0	-302.5	14.7	-14.0	69.2	-82.5	20.0	21.5	20.8	
W41	Wall 1		Siyam (2015)	86.5	-76.1	7.9	-7.2	33.5	-29.1	11.0	10.6	10.8
W42	Wall 5	13.8		-12.8	13.2	-15.1	53.6	-56.3	1.0	0.9	0.9	
W43	Wall 6	8.5		-8.4	17.2	-17.0	73.8	-79.1	0.5	0.5	0.5	

**5.3.4 Effective stiffness**

The effective stiffness,  $k_e$  of reinforced masonry shear walls (RMSW), is one of the most crucial FBD parameters.  $k_e$  may be used in computing the natural period and thus the elastic forces, and essential also in computing the displacements corresponding to the seismic design forces. To account for the nonlinear behaviour of reinforced masonry (RM) structures, the seismic design forces and deformations are calculated based on reduced section properties. The effective stiffness,  $k_e$  defined in Eq. (5.5) considering both flexure and shear deformations can be determined according to Priestley and Hart (1989), where  $E_m$  is the modulus of elasticity ( $E_m = 850f'_m$ , and  $900f'_m$  following CSA S304 (2014) and TMS 402/602 (2016), respectively),  $G_m$  is the shear modulus taken as  $0.4E_m$  for Poisson's ratio,  $\nu = 0.25$ ),  $h_w$ , is the wall height,  $k$  is the shear shape factor taken as 1.2 for rectangular walls.  $I_e$  is the effective moment of inertia,  $A_e$  is the effective cross-sectional area.  $I_e$  and  $A_e$  are both calculated by multiplying the gross properties,  $I_g$  and  $A_g$ , with a reduction factor  $\alpha_w$ .

$$k_e = 1 / \left( \frac{h_w^3}{3E_m I_e} + \frac{kh_w}{G_m A_e} \right) \quad \text{Eq. (5.5)}$$

According to the US standard TMS 402/602 (2016), the effective stiffness,  $k_e$  can be calculated using  $\alpha_{w(TMS)}$  equal to 0.5. However, the current Canadian standard CSA S304 (2014) allows the use of a reduction factor,  $\alpha_{w(CSA)}$ , as shown in Eq. (5.6), where  $P$  is the factored axial dead and live loads determined at the base of the wall for the seismic load combinations, and  $f'_m$  is the masonry compressive strength in MPa.

$$\alpha_{w(CSA)} = 0.3 + \frac{P}{A_g f'_m} \quad \text{Eq. (5.6)}$$

Figure 5.4 shows a comparison between the idealized yield stiffness,  $k_y^{id}$ , and the effective stiffness,  $k_e$  for the forty-three RMSWs according to the Canadian standard CSA S304 (2014) and the US standard TMS 402/602 (2016), respectively. As it can be observed in Figure 5.4, the CSA reduction factor  $\alpha_{w(CSA)}$  gives a better prediction of the walls' effective stiffness in comparison to the TMS reduction factor  $\alpha_{w(TMS)}$ .

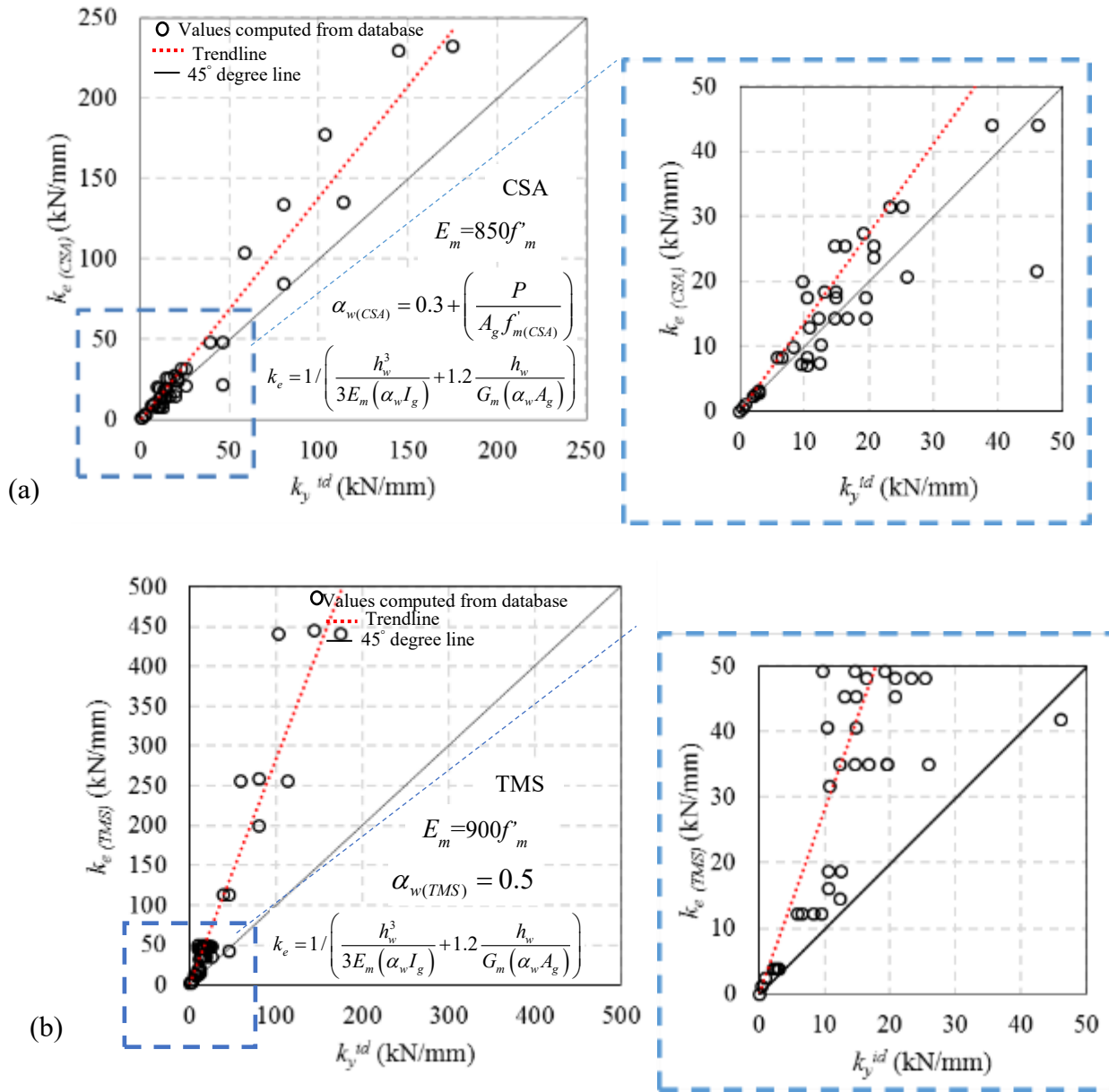


**Figure 5.4** Comparison between idealized yield stiffness and effective stiffness computed using: (a) Canadian standards [CSA S304 (2014)], (b) US standards [TMS 402/602 (2016)]

This is mainly due to the higher values of  $f'_m$  obtained using two masonry blocks high, and young's modulus  $E_m = 900f'_m$  according to TMS 402/602 (2016) in comparison to  $f'_m$  obtained using four masonry blocks high, and young's modulus  $E_m = 850f'_m$  according to CSA S304 (2014) instead. In addition,  $\alpha_w(TMS)$  is taken as 0.5 in TMS 402/602 (2016), which is more than the reduction factor recommended by CSA S304 (2014). Therefore, enhancing the prediction of the RMSW effective

stiffness can provide a better prediction of the SFRS natural frequency and thus the associated seismic forces, in addition, it will provide realistic deformation associated with the seismic demand. Although using the section reduction values will result in a stiffer wall that leads to more conservative seismic design loads, it will underestimate the elastic deformations associated with the seismic design force

#### 5.3.4.1 Effect of design parameters

The normalized stiffness was used to assess the wall's stiffness variation with different design parameters, including aspect ratio, axial stress, vertical and horizontal reinforcement ratio. Figure 5.5 presents the relationship of the normalized stiffness ( $k_y^{id}/k_g$ ) defined as the ratio between the idealized yield stiffness,  $k_y^{id}$ , and the theoretical gross stiffness,  $k_g$  using uncracked cross-sectional properties with different design variables ( $AR, P/f_m', A_g, \rho_v, \rho_h$ ). In general, as shown in Figure 5.5, the stiffness degradation is influenced by the aspect ratio, axial stress, vertical reinforcement ratio, and horizontal reinforcement ratio. For example, in Figure 5.5 (a), at an aspect ratio of 2, the stiffness ratio  $k_y^{id}/k_g$  varied from 0.15 to 0.4, since different design parameters changed simultaneously such as axial stress from 0.06 MPa to 2.21 MPa,  $\rho_v$  from 0.29% to 0.82%, and  $\rho_h$  from 0.16% to 0.33%, in addition to material and construction variability.

Similarly, in Figure 5.5 (c), at  $\rho_v=0.75\%$ , the stiffness ratio  $k_y^{id}/k_g$  varied from 0.2 to 0.6, this is mainly due to the variability of the design parameters of the walls such as axial stress from 0.09 MPa to 2.44 MPa, aspect ratio from 1.8 to 4.5, and  $\rho_h$  from 0.16% to 0.36%. Consequently, the stiffness reduction factor shall account for these parameters to result in a more realistic estimate of the effective stiffness. It is noteworthy to highlight that the wall, W14 from Shedid (2006), had an exceptionally high stiffness ratio  $k_y^{id}/k_g$  equal to 0.8 because of the high yield strength of 629 MPa for the used vertical rebars and the high vertical reinforcement ratio of 1.32% compared to other walls. It is also important to note that the design parameters for RMSWs were not fixed, and the effect of changing a specific parameter is not being studied solely since the results are based on a limited number of previously tested walls from available studies in the literature.

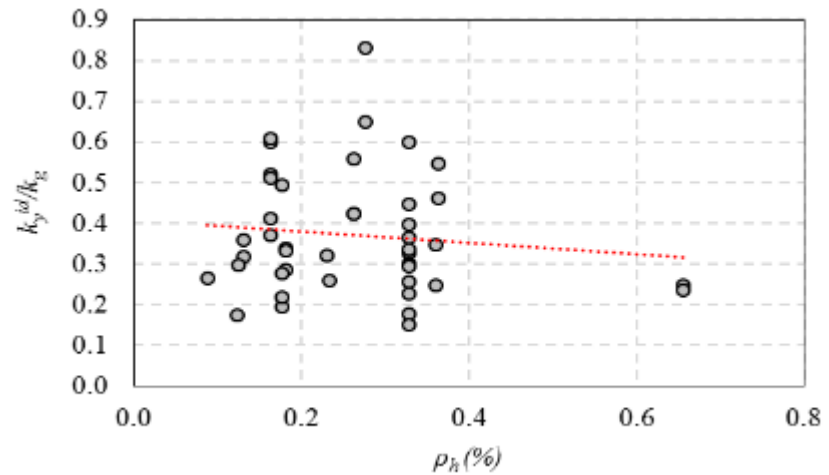
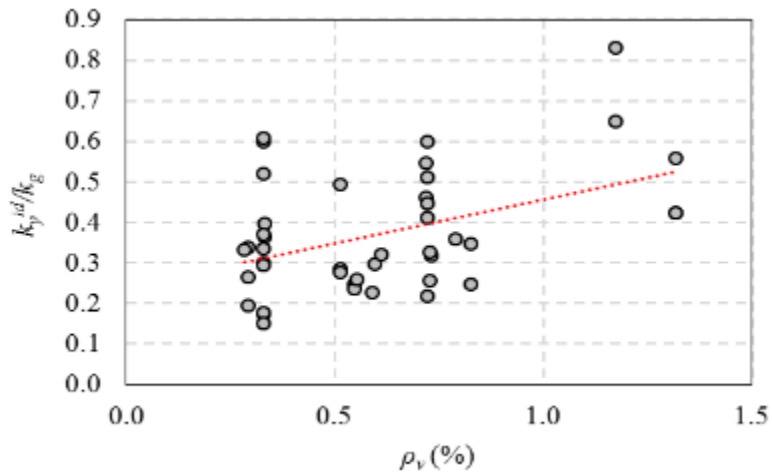
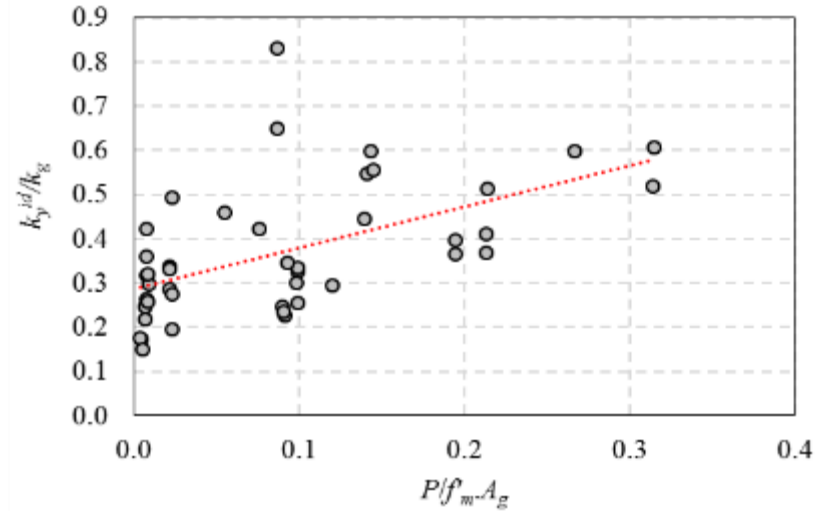
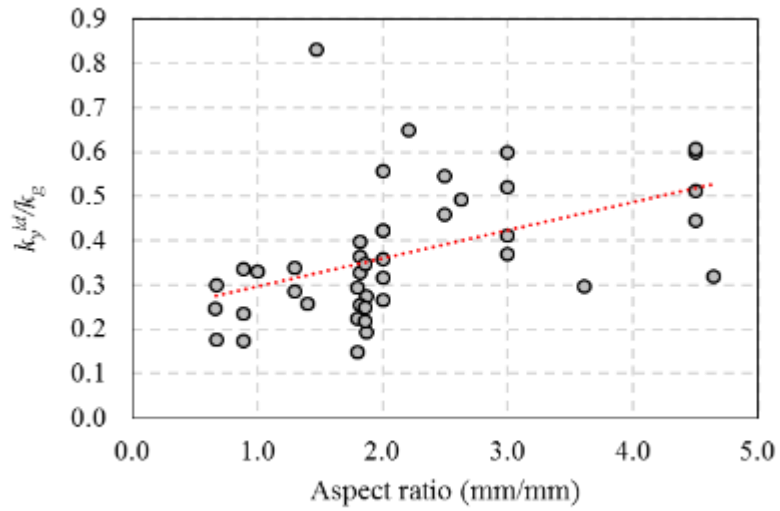


**Figure 5.5** Relationship between idealized yield stiffness gross stiffness ratio and design parameters: (a) aspect ratio, (b) normalized axial stress, (c) vertical reinforcement ratio, (d) horizontal reinforcement ratio

### 5.3.4.2 Proposed stiffness reduction factor $\alpha_w^{proposed}$

A modified section reduction factor,  $\alpha_w^{proposed}$ , is proposed in the current study for determining elastic deformations associated with the seismic design force.  $\alpha_w^{proposed}$  was computed using linear regression that considers the effect of different design parameters: axial stress, vertical reinforcement ratio, and horizontal reinforcement ratio, according to Eq. (5.7) and Eq. (5.8) based on CSA and TMS code procedures, respectively.

$$\alpha_w = 0.18 + 1.07 \left( \frac{P}{A_g f'_{m(CSA)}} \right) + 0.25(\rho_v - \rho_h) \quad \text{Eq. (5.7)}$$

$$\alpha_w = 0.12 + \left( \frac{P}{A_g f'_{m(TMS)}} \right) + 0.17(\rho_v - \rho_h) \quad \text{Eq. (5.8)}$$

Where  $P$  is the axial load,  $A_g$  is the total area of the section,  $\rho_v$  is the vertical reinforcement ratio, and  $\rho_h$  is the horizontal reinforcement ratio. Figure 5.6 shows a comparison between the idealized yield stiffness,  $k_y^{id}$  from experimental results, and the effective stiffness,  $k_e$  using  $\alpha_w^{proposed}$  according to Canadian and US standards, respectively. It can be seen that the proposed equation fits the data well, and there is no overestimation or underestimation.

### 5.3.5 Seismic Response Modification Factors

In North American codes, seismic force-resisting systems (SFRS) for RM are classified based on their expected level of ductility under seismic loading. Several requirements must be met, including limitations on aspect ratios, dimensions, and detailing of reinforcement for the classification of shear walls. Specific  $R_d$  and  $R$  values corresponding to each wall category are set in CSA S304 (2014) and TMS 402-602 (2016), respectively. The current National Building Code of Canada [NBCC (2015)] assigns two seismic force modification factors by which the elastic seismic force can be reduced: the first is related to the ductility,  $R_d$ , and the second is based on the ratio of anticipated over-strength,  $R_o$ . The American code ASCE-7 (2016) defines an overall seismic force reduction factor,  $R$  instead, and a structural over-strength factor,  $\Omega_o$ , to determine the seismic design forces and the corresponding displacements.

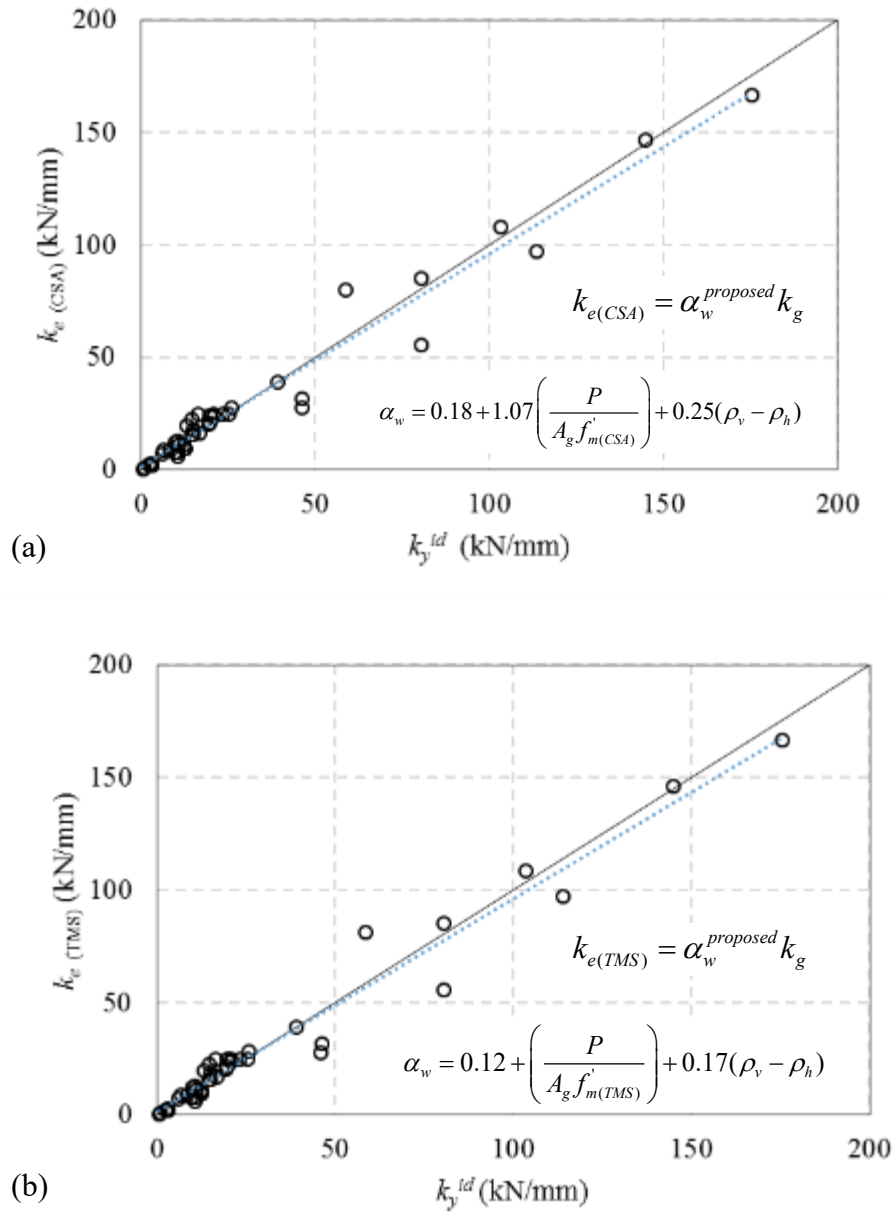


**Figure 5.6** Effective stiffness computed according to CSA and TMS procedure using a new proposed section reduction factor and compared to the experimental idealized yield stiffness

### 5.3.5.1 Seismic force modification factor

Having a reliable estimation of the  $R_d$  factor by defining its relation to the wall displacement ductility is an important factor for efficient seismic design. According to Newmark and Hall (1982)], the  $R_d$  factor can be defined based on either equal energy or equal displacement approach

depending on the period of vibration of the structure. The equal displacement approach is more suitable for structural systems having a long period of vibration ( $T_n \geq 0.5$ s) with frequencies up to 2Hz. However, the equal energy approach is more accurate for structures with short vibration periods ( $T_n < 0.5$ s) and frequencies less than 2 Hz. In the equal displacement approach, both the elastic and the elastic-plastic curves have the same initial stiffness and ultimate displacement ( $\Delta_u = \Delta_e$ ). On the other hand, in the equal energy approach, the elastic load-displacement response is assumed to have the same initial effective stiffness as the elastic-plastic response, where the total area under both load-displacement curves is equal.

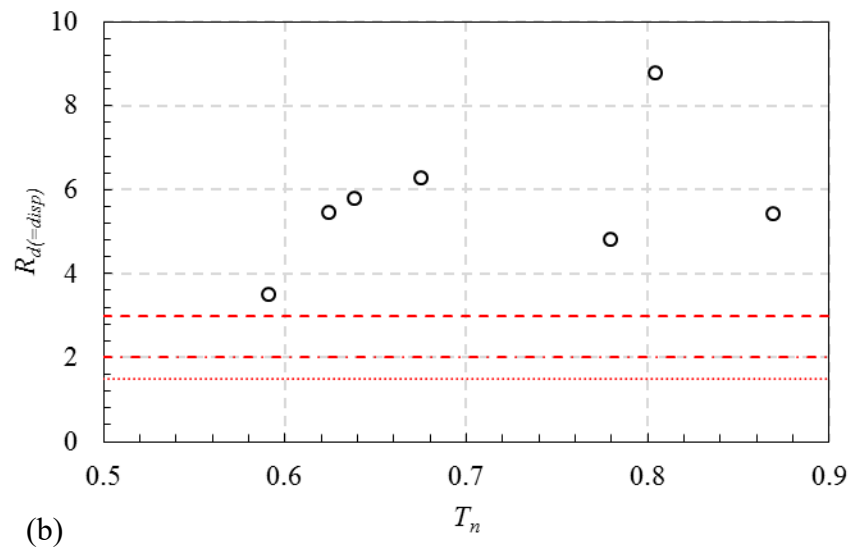
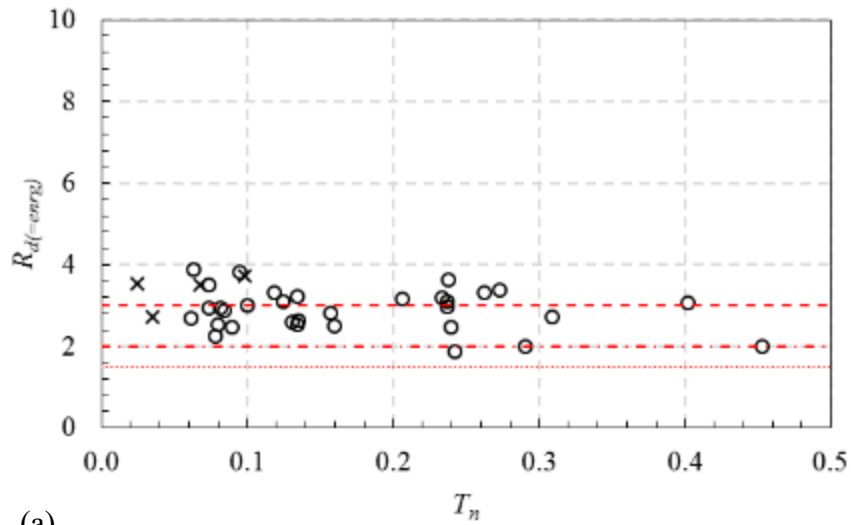
Figure 5.7(a) and (b) show  $R_d$  values computed from quasi-static experimental results of 43 RMSWs. According to the SFRS classification in CSA S304 (2014),  $R_d$  for ductile shear walls, moderately ductile shear walls, and conventional construction shear walls are 3, 2, and 1.5, respectively. Based on quasi-static experimental results, the average, 5<sup>th</sup> percentile, and 95<sup>th</sup> percentile values for  $R_d$  are 4.9, 2.5, and 7.1, respectively, for walls that have  $T_n < 0.5$ s.  $T_n$  for walls was determined according to Eq. (5.9):

$$T_n = 2\pi \sqrt{\frac{m}{k}} \quad \text{Eq. (5.9)}$$

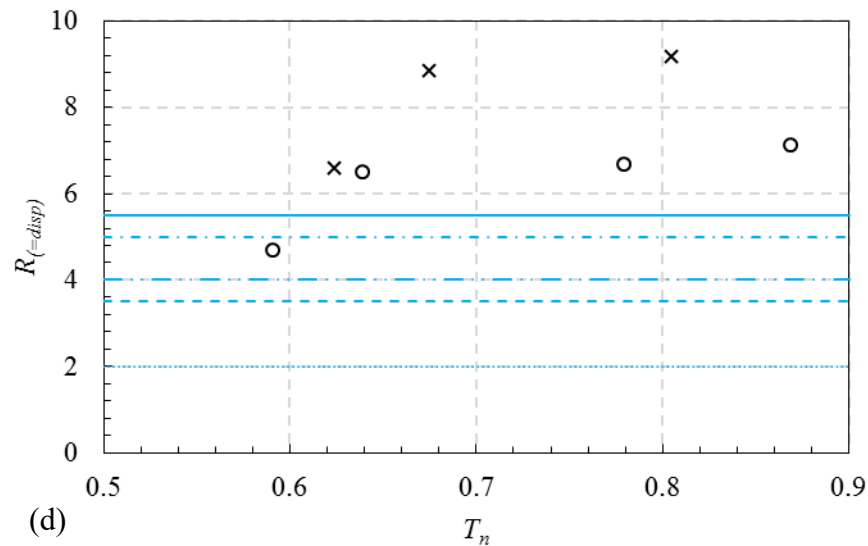
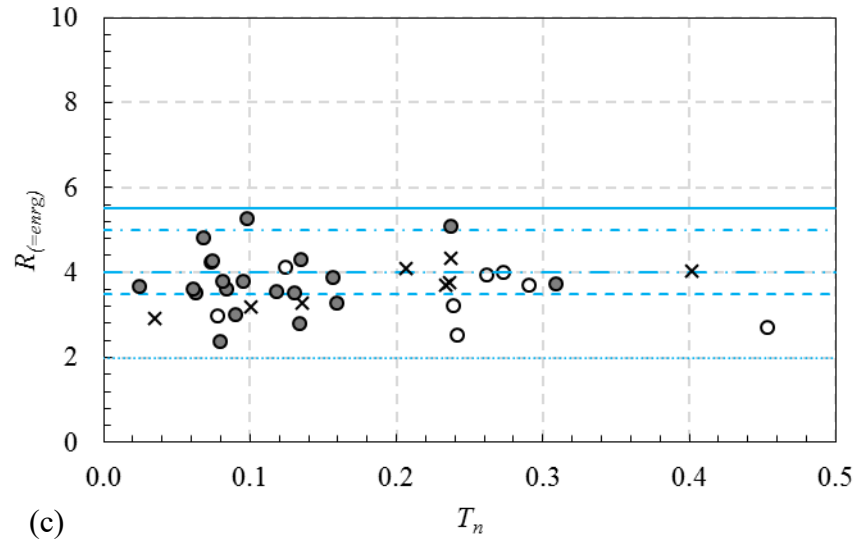
Where  $m$  is the ratio of the axial load on the wall and the gravitational acceleration,  $g$ ,  $k$  is the idealized yield stiffness of the wall. In addition, the average, 5<sup>th</sup> percentile, and 95<sup>th</sup> percentile values for  $R_d$  are 5.7, 3.5, and 8.8, respectively, for walls that have  $T_n \geq 0.5$ s. The 5<sup>th</sup> percentile for  $R_d$  in walls that have  $T_n < 0.5$ s and walls that have  $T_n \geq 0.5$ s is 2.5 and 3.5, respectively, which are both higher than the code limit of  $R_d$  for conventional shear walls of 1.5. It worth noting that  $R_d$  values for  $T_n < 0.5$ s were computed based on an equal energy approach. However,  $R_d$  values for walls having  $T_n \geq 0.5$ s were computed based on an equal displacement approach.

Figure 5.7 (c) and (d) show  $R$  values computed from quasi-static experimental results of 43 RMSWs. According to the SFRS classification in MSJC-17 (2017),  $R$  for special reinforced masonry shear walls (non-bearing), special reinforced masonry shear walls (bearing), intermediate reinforced masonry shear walls (non-bearing), intermediate reinforced masonry shear walls (bearing), and ordinary reinforced masonry shear walls (bearing and non-bearing) are 5.5, 5, 4, 3.5, and 2, respectively. Based on quasi-static experimental results, the average, 5<sup>th</sup> percentile, and

95<sup>th</sup> percentile values for  $R$  are 3.6, 2.5, and 4.3, respectively, for walls that have  $T_n < 0.5$ s. In addition, the average, 5<sup>th</sup> percentile, and 95<sup>th</sup> percentile values for  $R$  are 7.1, 4.7, and 9.2, respectively, for walls that have  $T_n \geq 0.5$ s. The 5<sup>th</sup> percentile value for  $R$  in walls that have  $T_n < 0.5$ s and walls that have  $T_n \geq 0.5$ s is 2.5 and 4.7, respectively, which are both higher than the code limit value of  $R$  for ordinary shear walls of 2.



- × Moderately ductile shear walls
- Conventional Shear walls
- - - NBCC-15 Ductile shear walls
- · - NBCC-15 Moderately ductile shear walls
- · · NBCC-15 Conventional construction shear walls



- Special shear wall
- × Intermediate shear wall
- Ordinary shear wall
- ASCE 7-16 Special reinforced masonry shear walls (non-bearing)
- - - ASCE 7-16 Special reinforced masonry shear walls (bearing)
- · - ASCE 7-16 Intermediate reinforced masonry shear walls (non-bearing)
- · - ASCE 7-16 Intermediate reinforced masonry shear walls (bearing)
- ⋯ ASCE 7-16 Ordinary reinforced masonry shear walls (bearing and non-bearing)

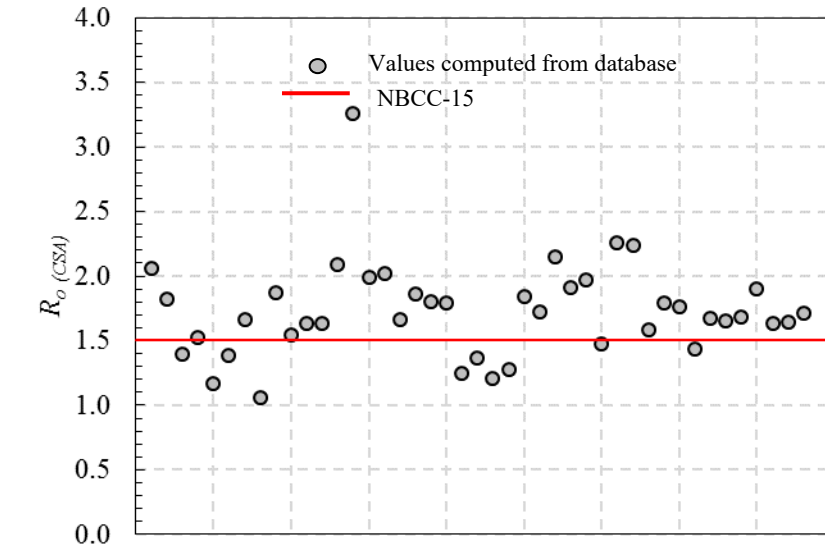
**Figure 5.7** Quasi-static experimental results ( $R_d$  and  $R$  values computed from database): (a)  $R_d$  values for walls with  $T_n < 0.5s$ , (b)  $R_d$  values for walls with  $T_n > 0.5s$ , (c)  $R$  values for walls with  $T_n < 0.5s$ , (d)  $R$  values for walls with  $T_n > 0.5s$

### 5.3.5.2 Overstrength related force modification factor

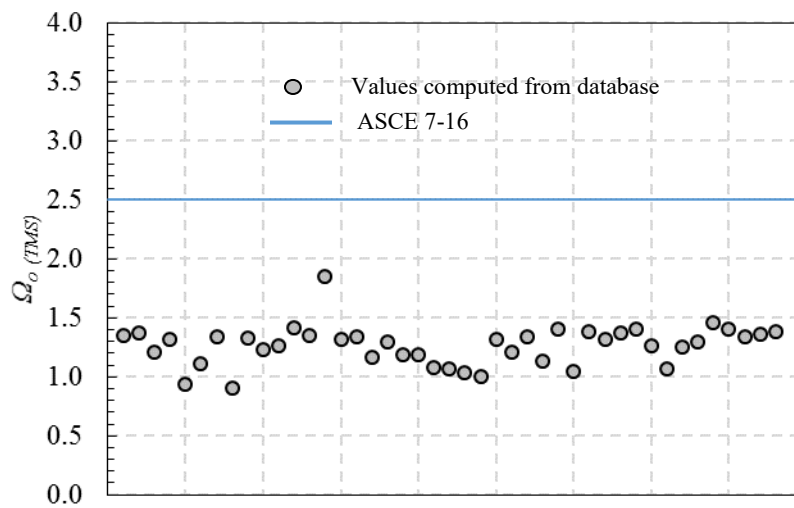
Figure 5.8 (a) shows a comparison between the  $R_o$  factor from quasi-static experimental results of forty-three rectangular RMSWs and the Canadian code.  $R_o$  was computed where the design capacity,  $Q_d$  was determined ignoring the contribution of compression reinforcement and using material resistance factors for masonry ( $\phi_m = 0.6$ ) and steel ( $\phi_s = 0.85$ ),  $E_m$  was taken as  $850f'_m$  where  $f'_m$  is the masonry compressive strength following the guidelines of CSA S304 (2014). According to NBCC-15 (2015),  $R_o = 1.5$  for masonry shear walls. It should be noted that W14 (Shedid (2006)) did not follow the same trend due to the high vertical reinforcement yield strength of 629 MPa compared to other shear walls. From quasi-static experimental results, the average, 95<sup>th</sup> percentile, and 5<sup>th</sup> percentile values for  $R_o$  are 1.7, 2.2, and 1.2, respectively. Recommendations for the overstrength factor were not suggested due to the limitation that only fully grouted individual walls were considered in this study and were built in the lab under idealized conditions. In addition, various components contribute to the overstrength related force modification factor,  $R_o/\Omega_o$  such as system effects, size, and tolerances as suggested by Mitchell et al. (2005), according to the following Eq. (5.10): Where  $R_{size}$  accounts for choices for sizes of members and elements,  $R_\phi$  accounts for the difference between nominal and factored resistance,  $R_{yield}$  is the ratio of actual yield strength to minimum specified material strength,  $R_{sh}$  accounts for the development of strain hardening,  $R_{mech}$  accounts for the additional resistance developed before the formation of collapse mechanism.

$$R_o = R_{size} R_\phi R_{yield} R_{sh} R_{mech} \quad \text{Eq. (5.10)}$$

A comparison between the  $\Omega_o$  factors determined from quasi-static experimental results of forty-three rectangular RMSWs and the US code limit is presented in Figure 5.8 (b). Herein, the design capacity,  $Q_d$ , was determined using material resistance factors for masonry ( $\phi_m = 0.9$ ) and steel ( $\phi_s = 0.9$ ),  $E_m$  was taken as  $900f'_m$  where  $f'_m$  is masonry compressive strength corresponding to the block strength as listed in TMS402/602 (2016). According to ASCE-7 (2016),  $\Omega_o = 2.5$  for shear walls. It can be seen in Figure 5.8 (b) that the scatter of the data from experimental results is less, hence indicating that the predictions are better. From quasi-static experimental results, the average, 95<sup>th</sup> percentile, and 5<sup>th</sup> percentile values for  $\Omega_o$  are 1.3, 1.4, and 0.9, respectively.



(a)



(b)

**Figure 5.8** Comparison of  $R_o$  values computed from quasi-static experimental results and code limits

### 5.3.5.3 Deflection amplification factor

The deflection amplification factor,  $C_d$ , is used to estimate the maximum inelastic displacement by amplifying the elastic design displacement induced by the seismic design forces to account for inelastic deformations, as suggested by Uang (1991). According to NBCC (2015),  $C_d$  referred to as  $R_d \times R_o$  for ductile shear walls, moderately ductile shear walls, and conventional construction shear walls are 4.5, 3, and 2.25, respectively. Figure 5.9 (a) shows a comparison of  $C_d$  values computed for quasi-static experimental results of forty-three rectangular RMSWs and the Canadian code limits.  $C_d$  values were calculated from the database as the ratio between  $\Delta_{max}$ , the wall displacement corresponding to the peak load from the idealized load-displacement envelope, and  $\Delta_y$ , the idealized yield displacement from the bilinear load-displacement curve. It can be seen from Figure 5.9 (a) that for values obtained from the database, the majority of the walls have  $C_d$  values higher than the NBCC (2015) designation for ductile shear walls ( $C_d = 4.5$ ). The average, 95<sup>th</sup> percentile and 5<sup>th</sup> percentile values for  $C_d$  are 5.2, 9.3, and 2.7, respectively.

According to ASCE-7 (2016),  $C_d$  for special and intermediate reinforced masonry shear walls (non-bearing), special reinforced masonry shear walls (bearing), intermediate reinforced masonry shear walls (bearing), ordinary reinforced masonry shear walls (non-bearing), and ordinary reinforced masonry shear walls (bearing) are 4, 3.5, 2.25, 2, and 1.75, respectively. Figure 5.9 (b) shows a comparison of  $C_d$  values computed from quasi-static experimental results of forty-three rectangular RMSWs and the US code limits. The average, 95<sup>th</sup> percentile and 5<sup>th</sup> percentile values for  $C_d$  are 3.8, 7.7, and 2.0, respectively.

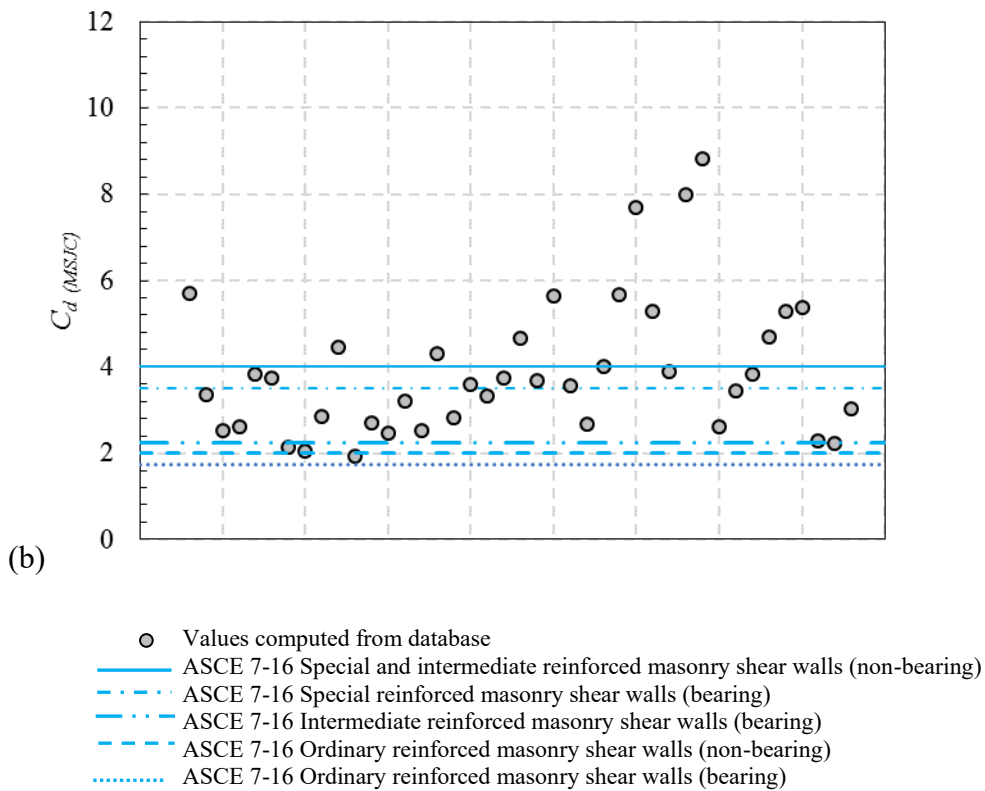
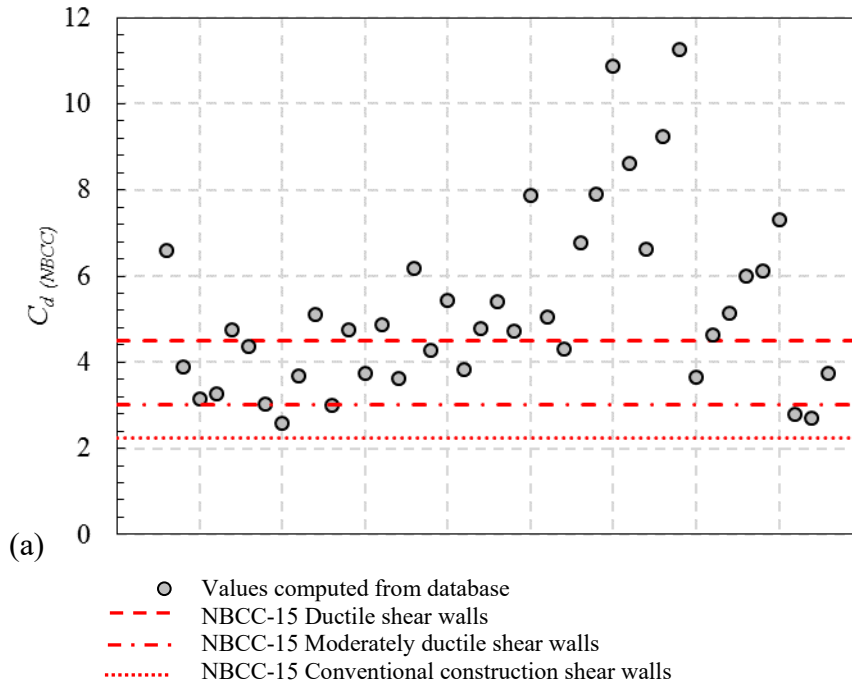


**Figure 5.9** Comparison of  $C_d$  values computed from quasi-static experimental results and code limits

## 5.4 Force-based Design Parameters for RMSW+BEs

### 5.4.1 Ductility Related Modification Factor

Estimating the ductility related modification factor,  $R_d$  accurately by defining its relation to the wall displacement ductility, is essential for an efficient seismic design.  $R_d$  factor can be defined depending on the period of vibration of the structure based on either equal energy or equal displacement principle, according to Newmark and Hall (1982). For structural systems having long vibration periods ( $T_n \geq 0.5s$ ) with frequencies up to 2Hz, the equal displacement approach is considered to be more suitable, However, For structures with short vibration periods ( $T_n < 0.5s$ ), and frequencies less than 2Hz, the equal energy approach is considered more reliable.

In the equal displacement approximation, both the elastic and the elastic-plastic curves are assumed to have the same initial stiffness and ultimate displacement ( $\Delta_u = \Delta_e$ ), thus  $R_d = \mu_\Delta$ . On the other hand, in equal energy approximation, the elastic load-displacement response is assumed to have the same initial effective stiffness as the elastic-plastic response, where the total area under both load-displacement curves are equal, thus  $R_d = \sqrt{2\mu_\Delta - 1}$ . As shown in Table 5.7,  $R_d$  computed using equal energy approximation ranged from 3.8 to 5.5, with an average of 4.7. However, using equal displacement approximation resulted in  $R_d$  from 7.7 to 15.4, with an average of 11.6. Based on Canadian standards CSA S304 (2014), the  $R_d$  factor is specified as  $R_d = 3$  for ductile shear walls. Results show that higher  $R_d$  factors could be suggested for steel-reinforced RMSW+BEs, which could significantly reduce the seismic demand on masonry buildings.

**Table 5.7** Displacement ductility and  $R_d$  for steel-reinforced walls

Wall ID.	$\mu_d$			$R_d$	
	(+ve)	(-ve)	Average	=enrg	=disp
S12S4-60	11.0	11.9	11.5	4.68	11.45
S15S4-60	9.5	10.8	10.1	4.39	10.15
S18S4-60	9.3	9.6	9.5	4.23	9.45
S12S8-60	13.5	13.4	13.5	5.09	13.45
S15S8-60	11.0	11.1	11.0	4.59	11.05
S18S8-60	9.1	9.9	9.5	4.24	9.50
S12S4-120	9.9	9.9	9.9	4.34	9.90
S15S4-120	8.3	8.7	8.5	4.00	8.50
S18S4-120	7.7	7.7	7.7	3.79	7.70
S12S8-120	10.7	10.5	10.6	4.49	10.60
S15S8-120	8.6	8.4	8.5	4.00	8.50
S18S8-120	8.0	8.9	8.5	4.00	8.50
R12S4-60	15.7	15.1	15.4	5.46	15.41
R15S4-60	10.9	11.1	11.0	4.59	11.04
R18S4-60	9.1	10.2	9.6	4.27	9.6
R12S8-60	12.1	12.4	12.3	4.85	12.25
R12S8-60	10.7	10.5	10.6	4.49	10.58
R15S8-60	9.6	9.5	9.6	4.26	9.57
R12S4-120	10.7	10.7	10.7	4.51	10.68
R15S4-120	8.2	8.6	8.4	3.97	8.38
R18S4-120	8.2	8.0	8.1	3.90	8.1
R12S8-120	10.6	10.2	10.4	4.46	10.43
R15S8-120	8.5	8.8	8.7	4.04	8.65
R18S8-120	8.1	7.9	8.0	3.88	8.03

In order to estimate  $R_d$  for GFRP-reinforced walls, the load-displacement response was idealized with the linearly elastic-perfectly plastic curve using the equivalent energy elastic-plastic (EEEP) method. According to current design codes, the elastic-plastic transition point represents the design capacity equal to or exceeding the required factored code-specified seismic force  $P_1$ , which is the maximum load, as shown in Figure 5.10.  $P_2$  is the seismic design force due to an earthquake of intensity as specified in the given seismic map area but corresponding to full elastic structural response. The value of  $P_2$  was obtained using an equal-energy principle (see Figure 5.10).  $R_d$  is defined as the ratio between the lateral elastic load,  $P_2$ , and the idealized wall capacity,  $P_1$ . As listed in Table 5.8, the GFRP-reinforced masonry shear walls had  $R_d$  values ranging from 1.8 to 4.6. Based on the estimated values, the lower bound value of  $R_d = 1.5$  is recommended for the studied walls.

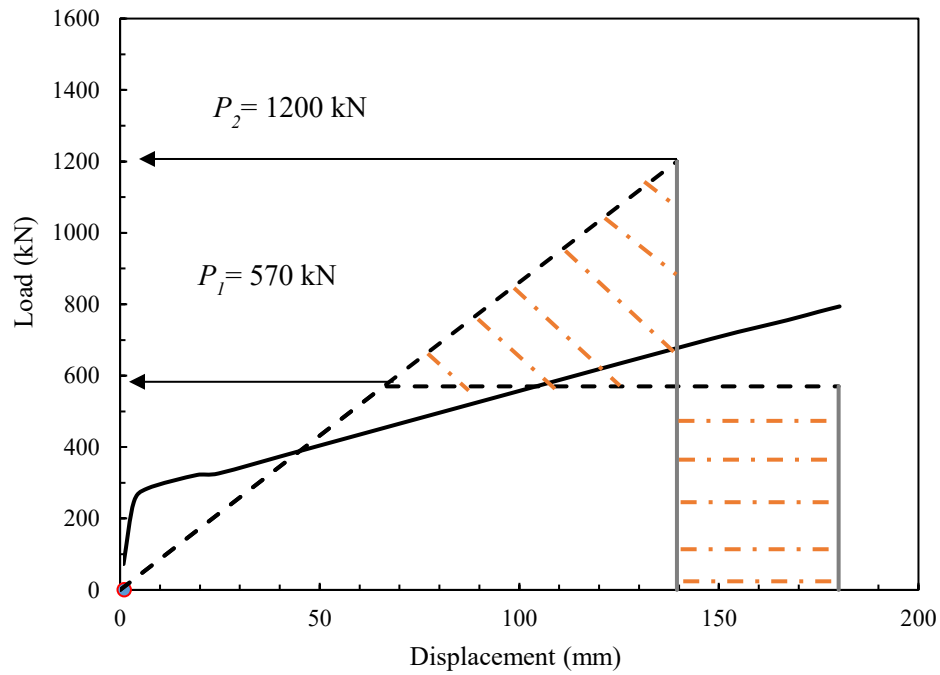


**Figure 5.10** Determination of the equivalent linear elastic response for wall S12G4-60

**Table 5.8**  $R_d$  for GFRP-reinforced walls

Wall ID.	$P_1$ (kN)	$P_2$ (kN)	$R_d = P_2/P_1$
S12G4-60	570	1321	2.3
S15G4-60	395	1375	3.5
S18G4-60	305	1406	4.6
S12G8-60	825	1677	2.0
S12G4-120	555	1235	2.2
S12G8-120	720	1538	2.1
R12G4-60	773	1568	2.0
R12G8-60	1210	2314	1.9
R12G4-120	780	1604	2.1
R12G8-120	1325	2369	1.8

#### 5.4.2 Effective Stiffness for RMSW+BEs

The design seismic forces and deformations may be calculated based on reduced section properties to account for the nonlinear behaviour of RM structures. As described earlier in section 5.3.4, the reduction factor,  $\alpha_w$  taking into account the cracked section of the wall, is used for calculating the wall's effective moment of inertia, and the effective cross-sectional area. The effective stiffness,  $k_e$ , was determined for the studied thirty-four RMSW+BEs, according to Eq. (5.5). As discussed earlier, allows the use of a reduction factor,  $\alpha_{w(CSA)}$ , is suggested by the current Canadian standard CSA S304 (2014), as shown in Eq. (5.6).

Table 5.9 shows the effective stiffness of the studied walls. The walls with square-shaped BEs, had  $k_e$  of 24.6, 12.9, and 7.7 kN/mm for walls with  $AR= 2.4, 3,$  and  $3.5,$  respectively. On the other hand, walls with rectangular-shaped BEs, had  $k_e$  of 25.3, 13.3, and 7.9 kN/mm for walls with  $AR= 2.4, 3,$  and  $3.5,$  respectively. The walls with rectangular shaped BEs have a slightly higher effective stiffness from those with square-shaped BEs due to the increase in the cross-sectional area,  $A_g,$  and the applied axial load,  $P.$

**Table 5.9** Effective stiffness

Wall ID.	$P$ (kN)	$A_g$ (mm <sup>2</sup> )	$I_g$ (mm <sup>4</sup> )	$\alpha$	$A_e$ (mm <sup>2</sup> )	$I_e$ (mm <sup>4</sup> )	$k_e$ kN/mm	$k_g$ kN/mm
S12S4-60	671.6	1119300	2919631747500	0.335	375295	978935350632	24.6	73.2
S15S4-60	839.5	1119300	2919631747500	0.344	385171	1004696807227	12.9	37.5
S18S4-60	1007.4	1119300	2919631747500	0.353	395047	1030458263823	7.7	21.7
S12S8-60	671.6	1119300	2919631747500	0.335	375295	978935350632	24.6	73.2
S15S8-60	839.5	1119300	2919631747500	0.344	385171	1004696807227	12.9	37.5
S18S8-60	1007.4	1119300	2919631747500	0.353	395047	1030458263823	7.7	21.7
S12S4-120	671.6	1119300	2919631747500	0.335	375295	978935350632	24.6	73.2
S15S4-120	839.5	1119300	2919631747500	0.344	385171	1004696807227	12.9	37.5
S18S4-120	1007.4	1119300	2919631747500	0.353	395047	1030458263823	7.7	21.7
S12S8-120	671.6	1119300	2919631747500	0.335	375295	978935350632	24.6	73.2
S15S8-120	839.5	1119300	2919631747500	0.344	385171	1004696807227	12.9	37.5
S18S8-120	1007.4	1119300	2919631747500	0.353	395047	1030458263823	7.7	21.7
R12S4-60	765.2	1275300	3005842027500	0.335	427602	1007843923301	25.3	75.4
R15S4-60	956.5	1275300	3005842027500	0.344	438855	1034366752064	13.3	38.6
R18S4-60	1147.8	1275300	3005842027500	0.353	450108	1060889580826	7.9	22.3
R12S8-60	765.2	1275300	3005842027500	0.335	427602	1007843923301	25.3	75.4
R12S8-60	956.5	1275300	3005842027500	0.344	438855	1034366752064	13.3	38.6
R15S8-60	1147.8	1275300	3005842027500	0.353	450108	1060889580826	7.9	22.3
R12S4-120	765.2	1275300	3005842027500	0.335	427602	1007843923301	25.3	75.4
R15S4-120	956.5	1275300	3005842027500	0.344	438855	1034366752064	13.3	38.6
R18S4-120	1147.8	1275300	3005842027500	0.353	450108	1060889580826	7.9	22.3
R12S8-120	765.2	1275300	3005842027500	0.335	427602	1007843923301	25.3	75.4
R15S4-120	956.5	1275300	3005842027500	0.344	438855	1034366752064	13.3	38.6
R18S8-120	1147.8	1275300	3005842027500	0.353	450108	1060889580826	7.9	22.3
S12G4-60	671.6	1119300	2919631747500	0.335	375295	978935350632	24.6	73.2
S15G4-60	839.5	1119300	2919631747500	0.344	385171	1004696807227	12.9	37.5
S18G4-60	1007.4	1119300	2919631747500	0.353	395047	1030458263823	7.7	21.7
S12G8-60	671.6	1119300	2919631747500	0.335	375295	978935350632	24.6	73.2
S12G4-120	671.6	1119300	2919631747500	0.335	375295	978935350632	24.6	73.2
S12G8-120	671.6	1119300	2919631747500	0.335	375295	978935350632	24.6	73.2
R12G4-60	671.6	1275300	3005842027500	0.335	427602	1007843923301	25.3	75.4
R12G8-60	671.6	1275300	3005842027500	0.335	427602	1007843923301	25.3	75.4
R12G4-120	671.6	1275300	3005842027500	0.335	427602	1007843923301	25.3	75.4
R12G8-120	671.6	1275300	3005842027500	0.335	427602	1007843923301	25.3	75.4

### 5.4.3 Stiffness degradation

Stiffness degradation is an indicator within the scope of evaluating the seismic performance of the walls. Stiffness degradation usually occurs when the walls are subjected to an in-plane reversed cyclic load. The secant stiffness,  $k_{sc,i}$  of each cycle is calculated to evaluate the evolution of the damage caused by the stiffness degradation. The secant stiffness at any loading cycle is defined as the ratio between the peak lateral load,  $Q_i$ , and the corresponding top lateral displacement,  $\Delta_i$ . The secant stiffness was calculated for each cycle in both loading directions and normalized to the gross stiffness,  $k_g$  of the wall.

Figure 5.11 presents the  $k_{sc,i}$  normalized to  $k_g$  for steel-reinforced walls plotted against the top drift based on load-displacement envelopes of the walls. The gross stiffness of the walls was calculated using a transformed moment of inertia  $I_g$ , and the gross area of the wall section,  $A_g$ . The values of  $k_g$  for walls with square-shaped BE were 73.2, 37.5, 21.7 kN/mm for walls with  $AR = 2.4, 3,$  and  $3.5,$  respectively. However, for walls with rectangular-shaped BE, the values for  $k_g$  were 75.4, 38.6, and 22.3 kN/mm for walls with  $AR = 2.4, 3,$  and  $3.5,$  respectively. Based on the results obtained, the trend of stiffness degradation was similar for all walls, but with variation in the level of degradation. It can be seen that there is a rapid reduction in the secant stiffness to about 60% of the gross stiffness at the top drift of 0.5%, followed by a relatively gradual degradation in the stiffness as the level of deformation increased. Figure 5.12 shows the secant stiffness degradation for the GFRP-reinforced walls. The overall stiffness degradation of GFRP-reinforced walls is more rapid compared to steel reinforced walls due to the elastic nature of GFRP reinforcement. However, the stiffness ratio continues almost linear after this initial degradation.

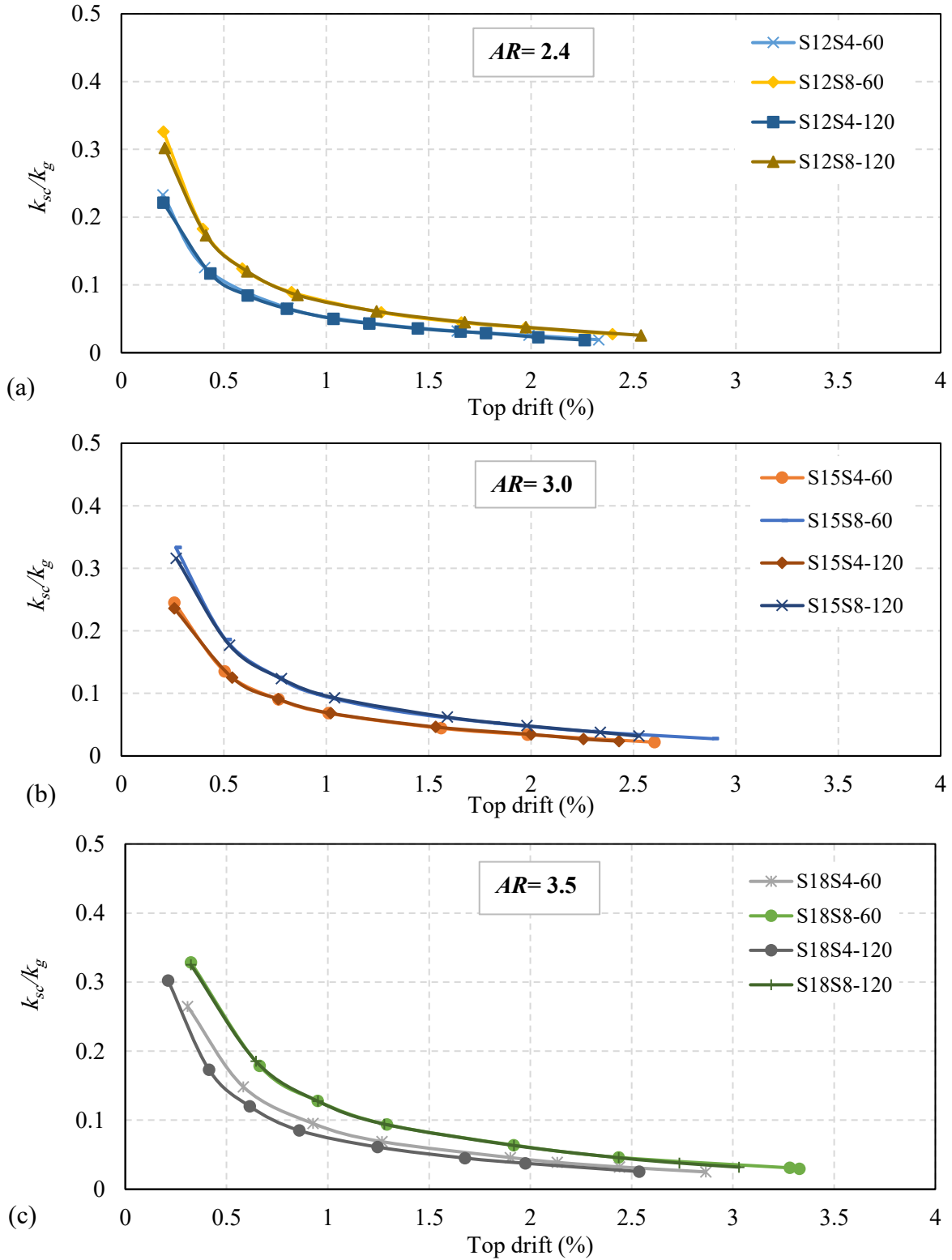


**Figure 5.11** Secant stiffness degradation for steel-reinforced walls.

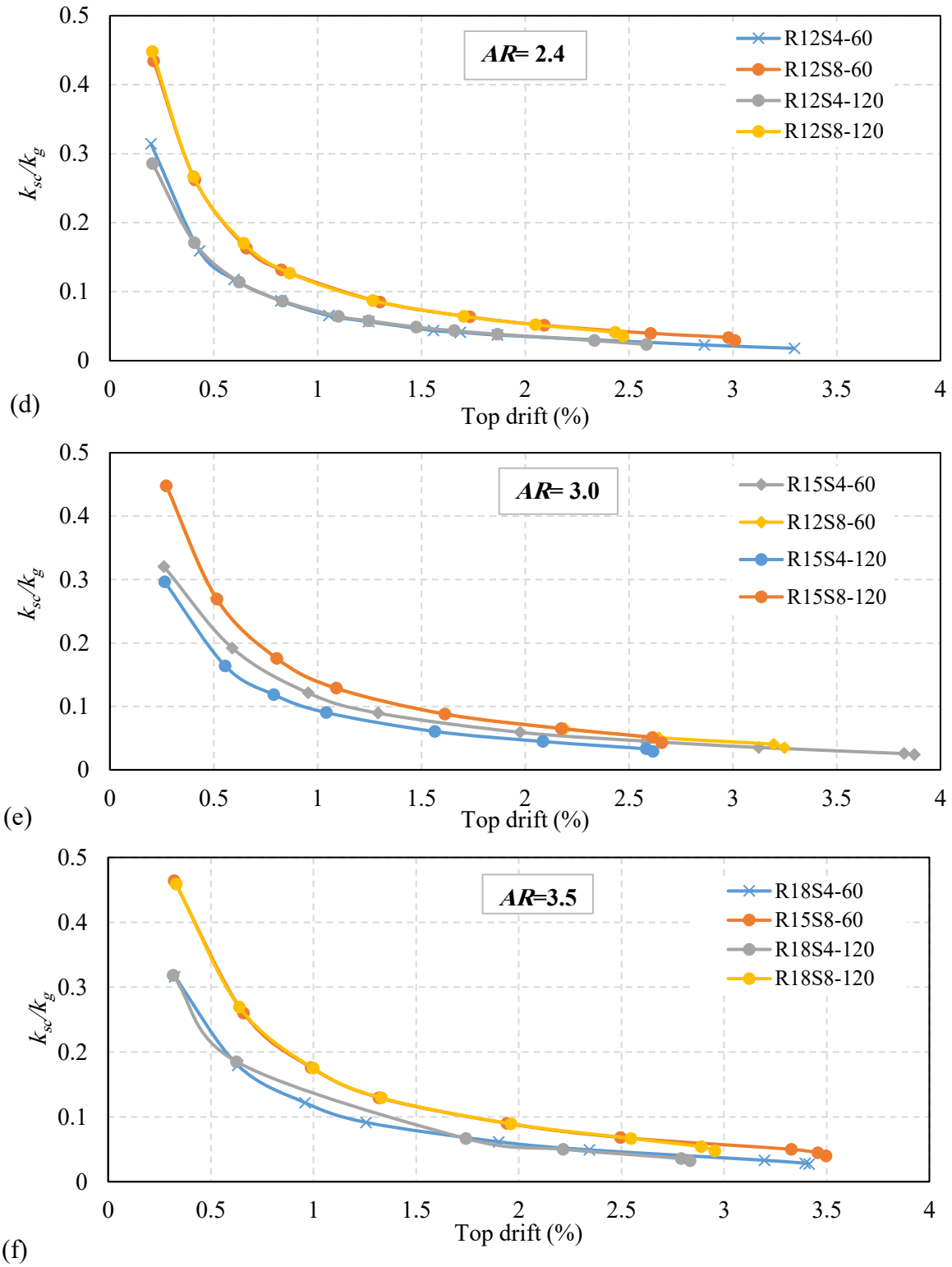
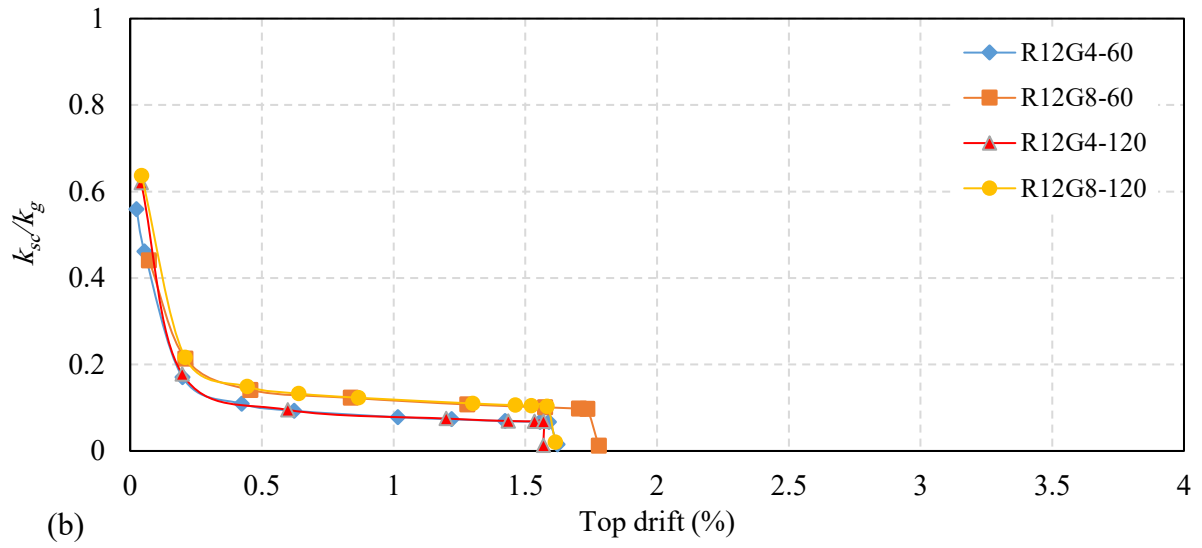
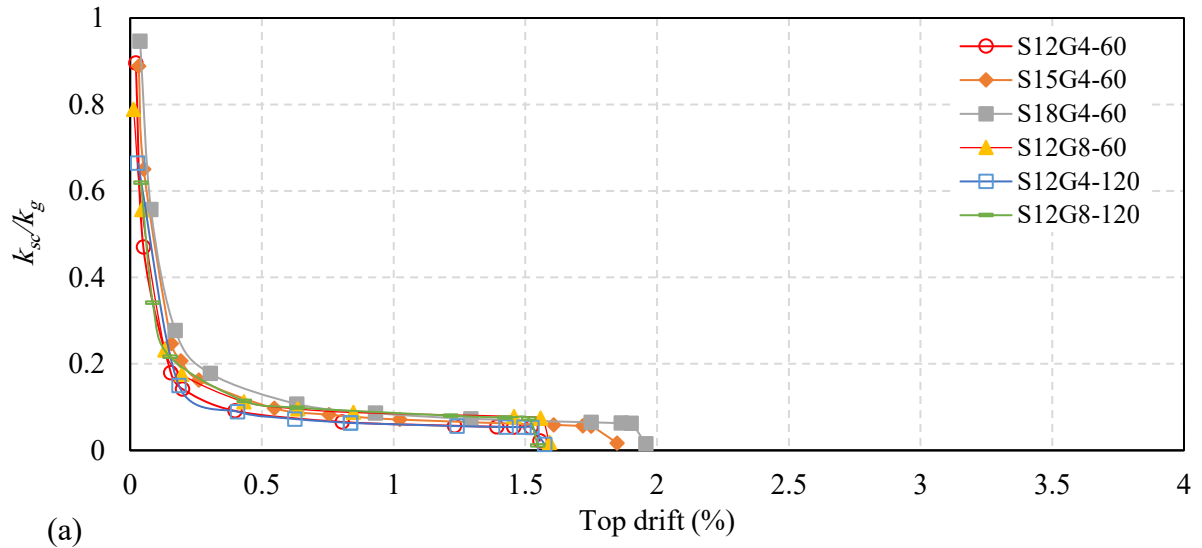


Figure 5.12 Secant stiffness degradation for steel-reinforced walls. (continued)



**Figure 5.13** Secant stiffness degradation for GFRP-reinforced walls.

## 5.5 Conclusions

Based on the need to develop next generation of performance based seismic design codes, results from the numerical models of thirty-six fully grouted walls (Phase I) described in Chapter 4 were used to generate fragility curves in order to assess the damageability of RMSW+BEs subjected to simulated seismic loads. In this chapter, fragility curves were generated for 36 RMSW+BEs utilizing a simplified 2D numerical macro-model in *SeismoStruct*, using fibre based beam column elements approach. The fragility curves for the studied walls were developed according to the methodology set by FEMA P-58-1 (2018) guidelines. Fragility functions for 36 RMSW+BEs were developed for three damage states associated with flexural failure mode: DS1 (slight damage), DS2 (moderate damage), and DS3 (severe damage). Fragility functions relate the probability of exceedance of a damage state to the top drift ratio. Fragility curves for distinct key design parameters ( $\rho_{v(BE)}$ ,  $H_w/L_w$ , and axial stress) were also investigated. Within the design parameters considered in this study, DS1 was mostly influenced by altering the aspect ratio rather than altering the vertical reinforcement ratio in BE or axial stress. Moreover, DS2 was more sensitive to the axial stress and aspect ratio rather than vertical reinforcement in the BE. This was not the case for DS3, which had a noticeable effect on all design parameters considered in this study. The fragility functions were quantified as high quality functions according to Lilliefors test. Therefore, the fragility functions developed in this study can be adopted in future performance based seismic design framework. It also supports the inclusion of Special RM shear walls with confined boundary elements within future masonry design codes.

This study also analyzed the experimental results of previously tested forty-three fully grouted flexure-dominated rectangular RMSWs under quasi-static cyclic loading. An equation for the modified section reduction factor,  $\alpha_w^{proposed}$  for the effective stiffness for both the Canadian and the American masonry standards was proposed using linear regression taking into consideration the effect of axial stress, vertical reinforcement and horizontal reinforcement ratio. The force-based design parameters in terms of seismic force response modification factor, and deflection amplification factor were quantified for the considered 43 RMSWs. The computed  $R_d$  and  $R$  values for the studied RMSWs were found to be high compared to the current factors assigned in the Canadian and US codes. According to Canadian standards, the 5<sup>th</sup> percentile for  $R_d$  in walls that have  $T_n < 0.5s$  and walls that have  $T_n \geq 0.5s$  is 2.5 and 3.5, respectively which are both higher than

the code limit of  $R_d$  for conventional shear walls of 1.5. According to US standards, the 5<sup>th</sup> percentile value for  $R$  in walls that have  $T_n < 0.5$ s and walls that have  $T_n \geq 0.5$ s is 2.5 and 4.7, respectively which are both higher than the code limit value of  $R$  for ordinary shear walls of 2. Moreover, the average values for over-strength modification factor  $R_o/\Omega_o$  were 1.7 and 1.3 according to Canadian and US standards. Results showed that the average values for deflection amplification factor,  $C_d$  were 5.8 and 3.8 according to Canadian and US standards. The  $C_d$  values obtained from database analysis were higher than  $C_d$  for ductile shear walls ( $C_d=4.5$ ) designated in NBCC (2015), and  $C_d$  for special reinforced masonry shear walls ( $C_d=3.5$ ) assigned in ASCE7 (2016). It is noteworthy that the conclusions in this study are based on the assumption that response of individual wall components is representing the overall building response. This limitation needs further investigation in future work, where the system level effects on the seismic response modification factors needs further investigation.

Numerical models using *OpenSees* of thirty-four flexure-dominated fully grouted shear walls (Phase II) described in Chapter 4 were used to evaluate the influence of different design parameters on the hysteretic response, stiffness degradation, effective stiffness, and ductility related response modification factor. Results showed that the GFRP-reinforced walls reached the ultimate design strength through a typical linear envelope curve with no strength degradation. The elasticity of the GFRP reinforcement and the absence of yielding phenomena caused an increase in strength up to failure. In addition, GFRP-reinforced shear walls behaved elastically up to near failure with much higher strength capacity compared to steel. The hysteretic response of the GFRP-walls is pinched with minimal residual strength and much lower energy dissipation capacity. Therefore, GFRP-walls can be used in low to mid seismic zones where the seismic demand can be resisted by the elastic response limited to the permissible limits of GFRP bars.

The effective stiffness,  $k_e$ , was determined for RMSW+BEs following the Canadian standard CSA S304 (2014). For square-shaped BEs walls with  $AR= 2.4, 3, \text{ and } 3.5$ ,  $k_e$  was 24.6, 12.9, and 7.7 kN/mm, respectively. On the other hand, for rectangular-shaped BEs walls,  $k_e$  was 25.3, 13.3, and 7.9 kN/mm for  $AR= 2.4, 3, \text{ and } 3.5$ , respectively. Moreover, the secant stiffness of the walls at each cycle was normalized to the corresponding initial gross stiffness to evaluate the extent of damage for the studied walls. The stiffness degradation relationships showed a similar decreasing trend for all the walls. For steel-reinforced walls, results showed that there is a rapid reduction in

the secant stiffness to about 60% of  $k_g$  at top drift of 0.5% followed by a gradual degradation in the stiffness at higher top drifts. In addition, GFRP-reinforced walls had more rapid degradation due to the elastic characteristics of GFRP bars. There was a significant reduction in the stiffness of each of the walls relative to increased levels of top displacements. In addition, the value of the seismic force modification factor,  $R_d$ , for steel-reinforced walls computed in this study ranged from 3.8 to 5.5 and ranged from 7.7 to 15.4 using equal energy and equal displacement principle, respectively. The value ( $R_d=3$ ) for ductile walls specified by the Canadian standard CSA S304 (2014) seems to be conservative if adopted for this wall type. Therefore, higher  $R_d$  values could be suggested for steel-reinforced walls that could reduce the seismic demand on masonry buildings. In addition, the  $R_d$  value for GFRP-reinforced walls was found to range from 1.8 to 4.6. A conservative value of ( $R_d=1.5$ ) is recommended for GFRP-reinforced walls.

## Chapter 6

### Summary, Conclusions, Recommendations for Future Research

#### 6.1 Summary

This thesis includes numerical research work aiming to enhance the structural performance and competitiveness of reinforced masonry buildings. The main objective was to recommend enhancement features to improve the overall seismic response of reinforced masonry shear walls. This study investigates the response of full-scale fully grouted flexure-dominated RM shear walls with varying design and detailing of C-shaped boundary elements (RMSW+BE) on enhancing the seismic performance of such walls. To the best of the author's knowledge, other researchers have not previously addressed the effects of GFRP reinforcement on the structural performance of RMSW+BEs. This research enriches the knowledge in this area, utilizing nonlinear numerical macro-models to simulate and evaluate the structural response of RMSW+BEs. Findings in this thesis support that RM shear walls with C-shaped boundary elements offer a practical and competitive seismic force-resisting system.

A total of seventy full-scale, fully grouted walls were used for the assessment of different parameters on the in-plane load-displacement response of RMSW+BEs using numerical macro-models. Thirty-six walls were modelled using a simplified macro-modelling approach in *SeismoStruct* (Seismosoft, 2016), and thirty-four walls were modelled using *OpenSees* (McKenna et al. 2013), taking into consideration the bond-slip and shear deformation effects to increase the accuracy of the simulated response. The walls were designed according to the CSA S304 (2014) requirements. The walls considered in this study were designed with a shear span-to-depth ratio greater than or equal to 1.5, and an adequate amount of reinforcement and axial force to be flexure-dominated according to CSA S304 (2014) standard with a safe margin for the shear capacity to avoid undesirable shear failure. The walls were subjected to displacement controlled quasi-static cyclic loading to simulate seismic loads. The utilized numerical macro-model was validated using experimental results available in literature. The models were capable of simulating the nonlinear response of RM shear walls with reasonable accuracy. The numerical investigation results were used to quantify the influence of key design detailing parameters, namely, vertical reinforcement ratio in the boundary element, confinement ratio of transverse reinforcement, length of boundary element, type of vertical reinforcement (Steel / GFRP), the level of axial compressive stress, and

aspect ratio on the inelastic behaviour and ductility of RMSW+BEs. This research contributed to enriching the numerical database of walls with boundary elements having different design parameters to facilitate a better understanding of their behaviour under seismic loads.

This study highlighted the improvement of adding boundary elements to the inelastic behaviour of RMSWs by suggesting design and detailing recommendations to be used by engineers and designers were given to enhance the performance of RMSW+BEs. Moreover, the wall's overall load-displacement response, ductility, effective stiffness, and stiffness degradation were investigated to evaluate the enhancement in the seismic performance of RMSW+BEs. In addition, results showed that there is a possibility of increasing the response modification factors of RMSW+BEs in the next editions of the masonry design codes and standards. Furthermore, fragility curves were also developed to assess the damageability of RMSW+BEs subjected to simulated seismic loads based on the need to develop next-generation of performance-based seismic design codes. Fragility functions for RMSW+BEs were generated for three damage states (DS1, DS2, DS3) that correspond to flexure dominated failure modes according to FEMA P-58-1 (2018) guidelines. Results obtained from the fragility assessment support the inclusion of Special RM shear walls with confined boundary elements and can be used to facilitate decision-making procedure within future masonry design performance-based seismic design codes.

The wall effective elastic stiffness, displacement ductility and seismic force modification factors, are important force based seismic design (FBD) parameters for reinforced masonry (RM) shear walls. The effective stiffness,  $k_e$  of RM shear walls is crucial in computing the natural period and thus the elastic forces, and essential also in computing the displacements corresponding to the design seismic forces. Previously reported test results of forty-three flexure-dominated fully grouted rectangular RMSWs subjected to quasi-static cyclic load were analyzed to evaluate the FBD parameters adopted by Canadian and American standards. Based on the experimental results of forty-three tested walls, a new stiffness reduction factor for stiffness degradation, was proposed for determining elastic deformations associated with the seismic design force using linear regression considering the effect of axial stress, vertical reinforcement ratio, and horizontal reinforcement ratio. Additionally, the seismic force modification factors were compared to the Canadian and US codes. The results demonstrated that ductility-related reduction factors should

be dependent on the wall's natural frequency and the current proposed code values could be more relaxed.

## **6.2 Conclusions**

### **6.2.1 Model validation**

The following points were drawn from the numerical modelling and validation of RM shear walls with BEs:

- The utilized macro-modelling approach proved to be capable of accurately simulating the behaviour of RM shear walls with C-shaped boundary elements cyclic loading, with a reasonable error in predictions.
- Inelastic displacement-based beam column elements were used to model the RMSW+BEs that is capable of capturing the material inelasticity.
- The proposed nonlinear modelling approach, along with the calibrated material modelling parameters were validated against existing experimental test results of RM shear walls.
- Walls with different configurations, aspect ratios, and axial stress levels were used to validate the numerical models; and to ensure accuracy, reliability, and robustness of the utilized modelling approach.
- The proposed nonlinear models were capable of predicting the hysteretic response and capturing the loading and unloading branches as well as the post-peak response.

### **6.2.2 Effect of design parameters**

The following points were concluded for the effect of design parameters on the seismic response of RM shear walls with BEs:

- The use of the C-shaped boundary elements permitted providing sufficient detailing, vertical, and transverse reinforcement in the compression zones. Therefore, an overall enhanced post-peak response was demonstrated in the studied walls.
- The steel-reinforced walls displayed a ductile behaviour, which approximately had a linear elastic response until the onset of the first yield in the outermost vertical reinforcement accompanied by thin hysteresis loops signifying a low level of energy dissipation; then, wider hysteresis loops signifying the increase in the energy dissipated by the walls were

observed as the response of the walls started to become nonlinear at higher lateral displacements.

- The GFRP-reinforced walls reached the ultimate design strength through a typical linear envelope curve with no strength degradation. The elasticity of the GFRP reinforcement and the absence of yielding phenomena caused an increase in strength up to failure.
- GFRP-reinforced shear walls behave elastically up to near failure with much higher strength capacity compared to steel. The hysteretic response of the GFRP-walls is pinched with minimal residual strength and much lower energy dissipation capacity. Therefore, GFRP-walls can be used in low to mid seismic zones where the seismic demand can be resisted by the elastic response limited to the permissible limits of GFRP bars.
- Results on the effect of varying the aspect ratio ( $H_w/L_w = 1.5, 2.25, 3,$  and  $3.75$ ) showed that the maximum lateral resistance of the walls increased as the height to length ratio decreased. Results indicated that walls with lower aspect ratios developed higher displacement ductility than those with higher aspect ratios. As  $H_w/L_w$  increased from 1.5 to 3.75,  $\mu_{\Delta 0.8u}$  dropped by 37%, 39%, and 55% for walls with zero, low, and high axial stress, respectively. The inversely proportional aspect ratio-ductility relationship is due to the increase in the yield displacement as the aspect ratio increases, which was not offset by the increase in the displacement at maximum loads.
- Increasing the level of axial stress from zero to high (0.3 MPa per story) resulted in increasing  $Q_{u(num)}$  by 26% for walls with ( $H_w/L_w = 1.5$ ), 42% for walls with ( $H_w/L_w = 2.25$ ), 48% for walls with ( $H_w/L_w = 3$ ), and 53% for walls with ( $H_w/L_w = 3.75$ ). However, the displacement ductility tended to decrease with increasing axial stress, which is mainly attributed to an increase in yield displacement with increased axial stress. It was found that there was a decrease in  $\mu_{\Delta 0.8u}$  by 15% for walls with ( $H_w/L_w = 1.5$ ), 20% for walls with ( $H_w/L_w = 2.25$ ), 23% for walls with ( $H_w/L_w = 3$ ), and 40% for walls with ( $H_w/L_w = 3.75$ ).
- The variation of vertical reinforcement in the boundary element had a noticeable effect on the RMSW+BEs peak strength. Results show that walls with a higher vertical reinforcement ratio in the boundary element ( $\rho_{v(BE)} = 1.58\%$ ) achieved a higher peak strength than those with lower vertical reinforcement ratios in the boundary element ( $\rho_{v(BE)} = 0.79\%$ ). In this respect, as  $\rho_{v(BE)}$  increased from 0.79% to 1.58%,  $Q_{u(num)}$

increased by 60%, 47%, 38% for walls with zero, low, and high axial stress, respectively. However, it caused a drop in  $\mu_{\Delta 0.8u}$  by 15%, 17%, 20% for walls having zero, low, and high axial stress, respectively. This was explained based on the fact that the yield displacement of walls was highly dependent on the amount of vertical reinforcement, whereas the displacement at maximum loads for all walls was almost similar.

- Decreasing the transverse hoop spacing from 120 mm to 60 mm significantly enhanced the lateral strength and displacement of steel-reinforced and GFRP-reinforced walls. This indicates the effectiveness of confining the masonry core by decreasing the hoop spacing in delaying failure.
- An increase in the vertical reinforcement ratio in the boundary element resulted in an increase in the yield and ultimate strength of the walls with square-shaped and rectangular-shaped BEs. Moreover, increasing the vertical reinforcement in boundary elements increased the lateral strength, and the yield and ultimate displacement, but it had a minor effect on the ductility.
- Increasing the length of boundary element from 390 mm to 780 mm resulted in a slight improvement in the ultimate displacement of steel-reinforced and GFRP-reinforced walls. However, a significant increase in the lateral load around 50% was observed for walls with rectangular-shaped BEs. It also resulted in higher ductility, yield and ultimate displacement of the wall.
- Steel-reinforced and GFRP-reinforced walls with lower  $AR$  experienced more rapid strength degradation than did walls with higher  $AR$ , and the displacement at ultimate loads increased as the  $AR$  increased.
- Having higher confinement in the boundary element by decreasing the spacing between hoops had a noticeable effect on the displacement ductility for both walls with square-shaped and rectangular-shaped BEs.
- A high level of displacement ductility was achieved for the studied walls, reflecting the benefit of adding boundary elements to RM shear walls. This result indicates a significant effect on the seismic performance that should influence the seismic response modification factor of RMSW+BEs.

### 6.2.3 Fragility and stiffness assessment

The following points were concluded for the fragility and stiffness assessment of RM shear walls with BEs:

- A series of fragility curves were generated to assess the damageability of RMSW+BEs subjected to simulated seismic loads using FEMA P-58-1 (2018) guidelines and checked using the Lilliefors test (Lilliefors 1967) for confidence. Fragility functions relate the probability of exceedance of a damaged state to the story drift ratio,  $\Delta_i$ . Three damage states associated with flexure failure modes were considered: slight (DS1), moderate (DS2), and severe (DS3).
- Results obtained from the fragility assessment indicate that the developed set of fragility functions for the in-plane response of RMSW+BEs were considered high quality functions which can be adopted in the performance-based seismic design framework.
- Fragility curves for distinct key design parameters ( $\rho_{v(BE)}$ ,  $H_w/L_w$ , and axial stress) were investigated. Within the design parameters considered in this study, DS1 was mostly influenced by altering the aspect ratio rather than altering the vertical reinforcement ratio in BE or axial stress. Moreover, DS2 was more sensitive to the axial stress and aspect ratio rather than vertical reinforcement in the BE. This was not the case for DS3 that had a noticeable effect on all design parameters considered in this study.
- The effective stiffness,  $k_e$ , was determined for RMSW+BEs following CSA S304 (2014). For square-shaped BEs walls with  $AR= 2.4, 3,$  and  $3.5$ ,  $k_e$  was 24.6, 12.9, and 7.7 kN/mm, respectively. On the other hand, for rectangular-shaped BEs walls,  $k_e$  was 25.3, 13.3, and 7.9 kN/mm for  $AR= 2.4, 3,$  and  $3.5$ , respectively.
- The secant stiffness of the walls at each cycle was normalized to the corresponding initial gross stiffness of the wall. The stiffness degradation relationships show a similar decreasing trend for all the walls. There was a significant reduction in the stiffness of each of the walls relative to increased levels of top displacements.
- The value of the seismic force modification factor,  $R_d$ , for steel-reinforced walls is sensitive to the approach followed by either equal energy or equal displacement. The values for  $R_d$  computed using equal energy principle range from 3.8 to 5.5. However, using equal displacement principle results in  $R_d$  values ranging from 7.7 to 15.4. The value ( $R_d=3$ ) for ductile walls specified by the Canadian code CSA S304 (2014) seems to be conservative

if adopted for this wall type. Accordingly, the results emphasize the possibility of increasing the response modification factors of RM shear walls with boundary elements in the future editions of the masonry design standards and codes, NBCC, CSA S304, ASCE7, and TMS 402/602.

- The  $R_d$  value for GFRP-reinforced walls was evaluated based on the idealized curve and found to range from 1.8 to 4.6. A conservative value of  $R_d=1.5$  is recommended.
- An equation for the modified section reduction factor,  $\alpha_w^{proposed}$  for stiffness degradation, is proposed for determining elastic deformations associated with the seismic design force using linear regression. The effect of different design parameters: axial stress, vertical reinforcement ratio, and horizontal reinforcement ratio were considered based on CSA S304 (2014) and TMS 402/602 (2016) code procedures, respectively.
- The force-based design parameters in terms of seismic force response modification factor, and deflection amplification factor were quantified for the considered 43 rectangular RMSWs. The computed  $R_d$  and  $R$  values for the studied walls were found to be acceptable compared to the current factors assigned in the Canadian and US codes.
- For the considered forty-three rectangular RMSWs available in the literature, the analysis of results has shown that  $T_n$  has a direct impact on the ductility-related seismic force modification factor,  $R_d$  and response modification factor,  $R$ . According to Canadian standards, the 5<sup>th</sup> percentile for  $R_d$  in walls that have  $T_n < 0.5s$  and walls that have  $T_n \geq 0.5s$  is 2.5 and 3.5, respectively which are both higher than the code limit of  $R_d$  for conventional shear walls of 1.5. According to US standards, the 5<sup>th</sup> percentile value for  $R$  in walls that have  $T_n < 0.5s$  and walls that have  $T_n \geq 0.5s$  is 2.5 and 4.7, respectively, which are both higher than the code limit value of  $R$  for ordinary shear walls of 2. Therefore, the  $R_d$  and  $R$ -values are high compared to the current factors assigned in the codes.
- The average values for over-strength modification factor  $R_o/\Omega_o$  were 1.7 and 1.3 according to Canadian and US standards. Results showed that the average values for deflection amplification factor,  $C_d$  were 5.8 and 3.8 according to Canadian and US standards. The  $C_d$  values obtained from database analysis were higher than  $C_d$  for ductile shear walls ( $C_d=4.5$ ) designated in NBCC (2015), and  $C_d$  for special reinforced masonry shear walls ( $C_d=3.5$ ) assigned in ASCE7 (2016).

It is noteworthy that the reported conclusions are based on the assumption that the response of individual wall components is representing the overall building response. This limitation needs further investigation in future work, where the system-level effects on the seismic response modification factors need further investigation.

### **6.3 Recommendations for Future Research**

The conclusions of the current study were limited to the parameters that were being modelled and analyzed. However, to further expand the knowledge in this field, other parameters may be considered. Hence, some recommendations for future research works are listed as follows:

- 1- Enhancing the accuracy of the numerical modelling of RM shear walls by overcoming the highlighted limitations. This can be achieved by developing a material (stress-strain) model that is specific to grouted masonry instead of utilizing the available concrete material models.
- 2- Extending the numerical methodology developed in this study to investigate the effect of design variables, such as the compressive strength of masonry.
- 3- All the studied walls were subjected to in-plane quasi-static fully reversed cyclic loading. Therefore, the responses of RM shear walls with boundary elements subjected to dynamic loading (i.e., shake table tests) still need to be investigated.
- 4- Performing an experimental and numerical investigation for RM shear walls with openings and coupled wall systems.
- 5- Conducting an economic analysis comparing the RC shear walls to RM shear walls with boundary elements to judge the commercialization and future development of this wall type.

## References

- Abdel-Latif, A., Okail, H., Shedid, M., and Abdelrahman, A. (2015). Modelling of reinforced masonry structural walls under lateral loads. In *12th North American Masonry Conference*. Denver, Colorado, United States of America.
- Abo El Ezz A, Eldin H, Galal K. (2015). Influence of confinement reinforcement on the compression stress–strain of grouted reinforced concrete block masonry boundary elements. *Structures Journal*, Vol. 2, 32-43.
- Abrams, D. P. (1986). Lateral resistance of a two-story block building. *Proc., Advances in Analysis of Structural Masonry*, ASCE, Reston, VA, 41–57.
- Ahmadi, F. (2012). Displacement-based seismic design and tools for reinforced masonry shear wall structures. PhD thesis, University of Texas at Austin, 2012.
- Ahmadi, F., Hernandez, J.S., Kapoi, C. (2014). Seismic performance of cantilever-reinforced concrete masonry shear walls. *Journal of Structural Engineering*, 140(9).
- AlAjarmeh, O.S., Manalo, A.C., Benmokrane, B., Vijay, P.V., Ferdous, W., Mendis, P. (2019), Novel testing and characterization of GFRP bars in compression. *Journal of Construction and Building Materials*, 225 (2019) 1112–1126.
- Aly, N., and Galal, K. (2019). Seismic performance and height limits of ductile reinforced masonry shear wall buildings with boundary elements. *Journal of Engineering Structures*, 190 (19), 171-188.
- Aly, N., and Galal, K. (2020). Effect of ductile shear wall ratio and cross-section configuration on the seismic behavior of reinforced concrete masonry shear wall buildings. *ASCE Journal of Structural Engineering*, 146(4).
- American Society for Testing and Materials (ASTM). (2012). *Standard Test Methods for Cyclic (Reversed) Load Test for Shear Resistance of Vertical Elements of the Lateral Force Resisting Systems for Buildings*, E2126-12. West Conshohocken, PA, United States of America.
- American Society of Civil Engineers/Structural Engineering Institute (ASCE/SEI). (2016). *Minimum design loads for buildings and other structures (ASCE7-16)*, Reston, Virginia, United States of America.
- Amir Z. Fam and Sami H. Rizkalla (2001), “Behavior of axially loaded concrete-filled circular fiber reinforced polymer tubes.” *ACI Materials Journal*, May-June, 280-289.

- ATC (Applied Technology Council), (2006). FEMA 445, Next-Generation Performance-Based Seismic Design Guidelines Program Plan for New and Existing Buildings. Applied Technology Council, Redwood City, California, United States of America.
- ATC (Applied Technology Council), (2007). FEMA 461, Interim testing protocols for determining the seismic performance characteristics of structural and nonstructural components. Applied Technology Council, Redwood City, California, United States of America.
- ATC (Applied Technology Council), (2018). FEMA P-58-1, Background document: Damage states and fragility curves for reinforced masonry shear walls. Applied Technology Council, Redwood City, California, United States of America.
- ATC (Applied Technology Council), (2009). FEMA P695, Quantification of building seismic performance factors, Applied Technology Council, Redwood City, California, United States of America.
- Banting B, El-Dakhakhni W. (2012). Force-and displacement-based seismic performance parameters for reinforced masonry structural walls with boundary elements. *Journal of Structural Engineering*, Vol. 138, No. 12, 1477-1491.
- Banting, B. R. (2013). Seismic performance quantification of concrete block masonry structural walls with confined boundary elements and development of the normal strain-adjusted shear strength expression (NSSSE). Ph.D. Thesis, McMaster University, Hamilton, Canada.
- Banting, B., and El-Dakhakhni, W. (2014). Seismic performance quantification of reinforced masonry structural walls with boundary elements. *Journal of Structural Engineering*, 140(5), 04014001.
- Bohl, A., and Adebar, P. (2011). Plastic hinge lengths in high-rise concrete shear walls. *ACI Structural Journal*, 108(2), 148-157.
- Boulanger, B., Paultre, P., and Lamarche, C. (2013). Analysis of a damaged 12-storey frame-wall concrete building during the 2010 Haiti earthquake — Part II: Nonlinear numerical simulations<sup>1</sup>. *Canadian Journal of Civil Engineering*, 40(8), 803-814.
- Calabrese, A., Almeida, J., and Pinho, R. (2010). Numerical issues in distributed inelasticity modelling of RC frame elements for seismic analysis. *Journal of Earthquake Engineering*, 14(sup1), 38-68.
- Carvalho, G., Bento, R., and Bhatt, C. (2013). Nonlinear static and dynamic analyses of reinforced concrete buildings - comparison of different modelling approaches. *Earthquakes and Structures*, 4(5), 451–470.

- Chang, G. A., and Mander, J. B. (1994). Seismic energy based fatigue damage analysis of bridge columns: Part I—Evaluation of seismic capacity. *NCEER Technical Report No. NCEER-94-0006*, State University of New York, Buffalo, NY, 222
- Correa, M. R. S. (2016). A 20-storey high masonry building in Brazil — design problems and adopted strategies. In *16th International Brick and Block Masonry Conference* (pp. 623–628). Padova, Italy.
- CSA (Canadian Standards Association). (2014). *Design of Masonry Structures*. CSA S304.14. Mississauga, Ontario, Canada.
- De Luca, A., Matta, F., and Nanni, A. (2009). Behavior of full-scale concrete columns internally reinforced with glass FRP bars under pure axial load. *COMPOSITES & POLYCON 2009, American Composites Manufacturers Association*, January 15-17, Tampa, FL USA, 1-10.
- Deitz, D. H., Harik, I. E., and Gesund H. (2003). Physical properties of glass fiber reinforced polymer rebars in compression. *Journal of Composite Construction*, 7(4), 363-366.
- Dhanasekar M, Shrive NG. (2002). Strength and deformation of confined and unconfined grouted concrete masonry. *American Concrete Institute (ACI) Journal*, Vol. 99, No. 6, pp. 819–26.
- Drysdale, R.G. and Hamid A.A. (1979). Behaviour of concrete block masonry under axial compression. *ACI Journal*, 707-721.
- Drysdale, R. G., and Khattab, M. M. (1995). In-plane behavior of grouted concrete masonry under biaxial tension-compression. *ACI Structural Journal*, 92(6), 653–664.
- Drysdale, R.G., and Hamid, A. (2005). *Masonry structures-behaviour and design*. 3 ed., Canada Masonry Design Centre, Mississauga, Canada.
- Eikanas, K., I. (2003). Behavior of concrete masonry shear walls with varying aspect ratio and flexural reinforcement. Ph.D. thesis, Department of civil engineering, Washington State University, US.
- Ezzeldin, M., Wiebe, L., Shedid, M., and El-Dakhakhni, W. (2014). Numerical modelling of reinforced concrete block structural walls under seismic loading. *9th International masonry conference*, Guimarães, Portugal.
- Ezzeldin, M., Wiebe, L., and El-Dakhakhni, W. (2015). Seismic performance assessment of reinforced masonry walls with and without boundary elements using the FEMA P695 methodology. *12th North American masonry conference*, Denver, USA.
- Ezzeldin, M., Wiebe, L., and El-Dakhakhni, W. (2016). Seismic Collapse Risk Assessment of Reinforced Masonry Walls with Boundary Elements Using the FEMA P695 Methodology. *Journal of Structural Engineering*, 142(11), 04016108.

- Filippou F.C., Popov E.P., and Bertero VV. (1983). Modelling of R/C joints under cyclic excitations. *Journal of Structural Engineering*, 109: 2666–2684.
- Hart, G.C., Noland, J.L., Kingsley, G.R., Englekirk, R.E., and Sajjad, N.A. (1988). The use of confinement steel to increase the ductility in reinforced concrete masonry shear walls. *The Masonry Society Journal*, 7(2), 19-42.
- Hart, G. C., Sajjad, N., Kingsley, G. R., and Noland, J. L. (1989). Analytical stress-strain curves for grouted concrete masonry. *The Masonry Society Journal*, 8(1), 21-34.
- Hassanein, A., Mohamed, N., Farghaly A. S., and Benmokrane, B., (2019a). Experimental investigation: new ductility-based force modification factor recommended for concrete shear polymer bars. *ACI Structural Journal*, 116(1), 213-224.
- Hassanein, A., Mohamed, N., Farghaly, A., and Benmokrane, B. (2019b). Modeling of Hysteretic Response for GFRP-Reinforced Concrete Walls. *ACI Structural Journal*, 116-S122.
- Ibrahim, K., and Suter, G. (1999). Ductility of concrete masonry shear walls subjected to cyclic loading. *8th North American Masonry Conference*, June 6-9, USA.
- International Code Council, Inc. (ICC). (2000), 2000 International Building Code (IBC), Ch.21, Falls Church, Virginia.
- Kapoi, C., M. (2012). Experimental performance of concrete masonry shear walls under in-plane loading. Master Thesis, Washington University, Washington University Press, Washington.
- Karsan, A. I., and Jirsa, J. O. (1969). Behavior of concrete under compressive loadings. *Journal of the Structural Division*, ASCE, Vol. 95, pp. 2535-2563.
- King, J. (1946). The effect of lateral reinforcement in reinforced concrete columns. *ASCE Journal of Structural Engineering*, (24)7, 355-38.
- Kolozvari, K., Orakcal, K., and Wallace, J. W. (2015a). Modeling of cyclic shear-flexure interaction in reinforced concrete structural walls. I: theory. *Journal of Structural Engineering*, 141(5).
- Kowalsky, M. J., Priestley, M. J. N., and Seible, F. (1999). Shear and flexure behavior of lightweight concrete bridge columns in seismic regions. *ACI Structure Journal*, 96(1), 136–148.
- Lam, L., and Teng, J. (2003). Design-oriented stress-strain model for FRP-confined concrete in rectangular columns. *Journal of Reinforced Plastics and Composites*, 22(3), 1149-1186.
- Légeron F, Paultre P, Mazars J. (2005). Damage mechanics modeling of nonlinear seismic behavior of concrete structures. *Journal of Structural Engineering*; 131:946–55.

- Lilliefors, H. (1967). On the Kolmogorov-Smirnov test for normality with mean and variance unknown. *Journal of the American Statistical Association*, 62(318), 399.
- Lourenço, P.B.; Rots, J.G.; Blaauwendraad, J. (1998). Continuum model for masonry: Parameter estimation and validation. *Journal of Structural Engineering*, 124(6), 642-652.
- Lowes, L., Lehman, D., Kuchma, D., Mock, A., and Behrouzi, A. (2013). Large scale tests of C-shaped reinforced concrete walls. (<https://nees.org/warehouse/project/104>).
- Mallick, P.K. (2008). *Fiber- Reinforced Composites: Materials, Manufacturing, and Design*. Third Edition, International Slandered Book Number-13: 978-0-8493-4205-9.
- Malmquist, K.J. (2004). Influence of confinement reinforcement on the compressive behavior of concrete block masonry and clay brick masonry prisms. M.S. Thesis, Washington State University, Washington, U.S.A.
- Mander, J. B., Priestley, M.J.N., and Park, R. (1988). Theoretical stress-strain model for confined concrete. *Journal of Structural Engineering*, 114:8(1804), 1804-1826.
- Martínez-Rueda, J., and Elnashai, A. (1997). Confined concrete model under cyclic load. *Materials and Structures*, 30(3), 139-147.
- Masonry Standards Joint Committee of the American Concrete Institute, American Society of Civil Engineers, and The Masonry Society (MSJC). (2017). *Building Code Requirements for Masonry Structures*. TMS 402-17/ASCE 5-17/ACI 530-17, Detroit, MI, New York, and Boulder, CO.
- Massone, L. M., and Wallace, J. W. (2004). Load-deformation responses of slender reinforced concrete walls. *ACI Structural Journal*, 101:1, 103-113.
- McKenna, F., Fenves, G. L., Scott, M. H., and Jeremic, B., (2013). Open system for earthquake engineering simulation (*OpenSees*). Pacific Earthquake Engineering Research Center, University of California, Berkeley.
- Menegotto, M., and Pinto, P.E. (1973). Method of analysis for cyclically loaded R.C. plane frames including changes in geometry and non-elastic behavior of elements under combined normal force and bending. *Proceedings, IABSE Symposium on Resistance and Ultimate Deformability of Structures Acted on by Well Defined Repeated Loads*, Lisbon, Portugal, 15-22.
- Mitchell, D., Tremblay, R., Karacabeyli, E., Paultre, P., Saatcioglu, M, and Anderson, D. (2005). Seismic force modification factor for the proposed 2005 edition of the National Building Code of Canada. *Canadian Journal of Civil Engineering*; 30: 308-327.
- Mohammed, N., Farghaly, A. S., Benmokrane, B., and Neale K.W. (2014). Experimental

- investigation of concrete shear walls reinforced with glass fiber-reinforced bars under lateral cyclic loading. *Journal of Composites for Construction*, ASCE, 18(3), 04014001.
- Masonry Standards Joint Committee (MSJC-11). (2011). *Building Code Requirements for Masonry Structures*. ACI 530/ASCE 5, TMS 402, ASCE, Reston, VA, United States of America.
- National Building Code of Canada (NBCC). (2015). National Building Code of Canada 2015. NRCC-15, Ottawa, Canada.
- Newmark N.M., and Hall W.J. (1982). Earthquake spectra and design. *Earthquake Engineering Research Institute*, Berkeley, C.A.
- NIST. (2010). Evaluation of the FEMA P695 methodology for quantification of building seismic performance factors. NIST GCR 10-917-8, Gaithersburg, MD.
- Obaidat, A., Abo El Ezz, A., and Galal, K. (2017a). Compression behaviour of confined concrete masonry boundary elements. *Engineering Structures*, 132, 562-575.
- Obaidat, A., Ashour, A., and Galal, K. (2018). Stress-strain behaviour of C-Shape confined concrete masonry boundary elements of RM shear walls. *ASCE Journal of structural engineering*, 144 (8):1804-26.
- Orakcal, K., Wallace, J., and Conte, J. P. (2004). Flexural modeling of reinforced concrete walls-model attributes. *ACI Structural Journal*, 101.5.
- Park, R., and Paulay, T. (1975). *Reinforced concrete structures*. John Wiley and Sons, New York.
- Paulay, T., and Priestley, M. J. N. (1992). *Seismic design of reinforced concrete and masonry buildings*. John Wiley and Sons, New York.
- Priestley M.J.N. and Bridgeman, D.O. (1974). Seismic resistance of brick masonry walls. *Bulletin of the New Zealand National Society for Earthquake Engineering*, 7(4), pp.167-187.
- Priestley, M. J. N., and Elder, D. M. (1982). Seismic behavior of slender concrete masonry shear walls. *Research report*, University of Canterbury, Christchurch, New Zealand.
- Priestley MJN, Elder DM. (1983). Stress–strain curves for unconfined and confined concrete masonry. *American Concrete Institute (ACI) Journal*, Vol. 80, No. 3, 192–201.
- Priestley, M. (1986), Seismic design of concrete masonry shear walls. *ACI Structural Journal*, (83)1, 58-68.
- Priestley, M. J. N., Robinson, L.M. (1986). Discussion: Seismic behaviour of unreinforced masonry walls. *Bulletin of the New Zealand National Society for Earthquake Engineering*, vol. 19, no. 1, pp. 65-75.

- Priestley, M., and Hart, G. (1989). Design recommendations for the period of vibration of masonry wall buildings. *Structural Systems Research Project, Report No. SSRP 89/05*, University of California at San Diego.
- Priestley, N., Calvi, G., and Kowalsky, M. (2007). *Displacement-based seismic design of structures*. Istituto Universitario di Studi Superiori (IUSS), Pavia, Italy.
- Rodrigues, H., Varum, H., Arêde, A., and Costa, A. (2012). Comparative efficiency analysis of different nonlinear modelling strategies to simulate the biaxial response of RC columns. *Earthquake Engineering and Engineering Vibration*, 11(4), 553-566.
- Sajjad, N.A. (1990). Confinement of Concrete Masonry. Ph.D. Thesis, University of California, Los Angeles, USA.
- Seible, F., Priestley, M.J.N., Kingsley, G.T., and Kurkchubasche, A.G. (1994b). Seismic response of a five-story full-scale RM research building. *ASCE Journal of Structural Engineering*, Vol. 120, No. 3.
- Seismosoft (2014). SeismoStruct 2014 – A computer program for static and dynamic nonlinear analysis of framed structures. Available from <http://www.seismosoft.com>.
- Shedid, M. (2006). Ductility of reinforced concrete masonry shear walls. M.A. Sc. Thesis, Department of Civil Engineering, McMaster University, Ontario, Canada.
- Shedid, M., Drysdale, R., and El-Dakhakhni, W. (2008). Behavior of fully grouted reinforced concrete masonry shear walls failing in flexure: Experimental results. *Journal of Structural Engineering*, 134(11), 1754-1767.
- Shedid, M.T. (2009). Strategies to enhance seismic performance of reinforced masonry shear walls. Ph.D. Thesis, McMaster University, Hamilton, Canada.
- Shedid, M., El-Dakhakhni, W., and Drysdale, R. (2010b). Characteristics of confined and unconfined masonry prisms for seismic performance enhancement of structural walls. *Masonry Int.*, 23(2), pp.69–78.
- Shedid, M., El-Dakhakhni, W., and Drysdale, R. (2010a). Alternative strategies to enhance the seismic performance of reinforced concrete-block shear wall systems. *Journal of Structural Engineering*, 136(6), 676-689.
- Sherman, J., D. (2011). Effects of key parameters on the performance of concrete masonry shear walls under in-plane loading. PhD thesis. Washington State University.
- Shing, P. B., Schuller, M., and Hoskere, V. S. (1990). In-plane resistance of reinforced masonry shear walls. *Journal of Structural Engineering (ASCE)*, Vol. 116, No. 3, 619-640.

- Siyam, M., El-Dakhakhni, W., Shedid, M., and Drysdale, R. (2015a). Seismic response evaluation of ductile reinforced concrete block structural walls. I: experimental results and force-based design parameters. *Journal of Performance of Constructed Facilities.*, 10.1061/ (ASCE) CF 1943-5509.0000794, 04015066.
- Taucer, F.F., Spacone, E., Filippou, F.C. (1991). Fiber beam column element for seismic response analysis of reinforced concrete structures. Report No. UCB/EERC-91/17 to the National Science Foundation and the California Department of Transportation, Earthquake Engineering Research Center, University of California, Berkeley.
- The Masonry Society (TMS). (2016). *Building Code Requirements and Specification for Masonry Structures*, TMS 402/602-16. Longmont, Colorado, United States of America.
- Tomažević, M. (1999). *Earthquake resistant design of masonry buildings*. Imperial College Press, London, ISBN: 1-86094-066-8.
- Uang, C. (1991). Establishing  $R$  (or  $R_w$ ) and  $C_d$  factors for building seismic provisions. *Journal of Structural Engineering*; 117(1): p.19-28.
- Voon, K., and Ingham, J. (2006). Experimental in-plane shear strength investigation of reinforced concrete masonry walls. *ASCE Journal of Structural Engineering*, (132)3, 400-408.
- Waugh, J. D., and Sritharan, S. (2010). Lessons learned from seismic analysis of a seven-story concrete test building. *Journal of Earthquake Engineering*, 14: 3, 448 — 469.
- Zhao, J., and Sritharan, S. (2007). Modeling of strain penetration effects in fiber-based analysis of reinforced concrete structures. *ACI Structures Journal*, 104 (2), 133–141.

## Appendix A

### Supplemental Information for the Numerical Investigation

This Appendix presents additional information to the numerical research presented in Chapter 3.

#### A1. Sensitivity of the numerical model

The element's size and number of fibres of the utilized numerical models were presented in Chapter 3. In this section, the results of the sensitivity analysis on the choice of number of fibres and element's length are assessed and presented for walls modelled in *SeismoStruct* and *OpenSees*. Wall W2 from Banting and El-Dakhakhni (2014) (see Table 3.7) is selected to investigate the optimum number of fibres and element's length needed to accurately simulate the lateral load-displacement response of the wall. A study is performed for number of fibres ranging from 50 to 350 fibres, at an increment of 50. The lateral force-displacement responses for the different section fibres are shown in Figure A.1. It can be seen from the results that there are no significant changes in the overall response of the walls as the number of fibres increased. However, in some cases the post-peak response is not fully captured when a lower number of fibres are used. It should be noted that the use of higher number of fibres did not yield any major increase in the processing time of the model, but it ensured the post-peak response of the walls is well captured. As a result, 300 fibres are used in the developed *SeismoStruct* model to ensure the accurate simulation of the wall response.

Wall W2 from Banting and El-Dakhakhni (2014) (see Table 3.7) is selected to verify the validity of the proposed element distribution and length for the wall models. Figure A.2 shows the hysteresis loops using a variety of number of elements as well as first element's length and compares it against experimental results. It is observed that having the first element's length equal to twice the plastic hinge length,  $2L_p$  resulted in the best agreement with the experimental results. Figure A.2 (a) compares the numerical and the experimental hysteresis loops of the wall with varying the length of the first element with 4 elements. It can be seen from Figure A.2 (a) that using the plastic hinge length,  $L_p$  as the first element length results in underestimation of the wall's strength and stiffness. In addition, numerical models with the first element's length larger than  $L_p$  overestimate the strength and do not capture the stiffness degradation. Figure A.2 (b) shows the numerical hysteresis response using first element's length of  $2L_p$  and varying the total number of

elements (4 elements, 6 elements, and 8 elements). It can be observed that for the proposed model, varying the number of elements from 4 to 8 elements did not result in any effect on the simulated numerical hysteresis response. However, it was observed that when using a DB element formulation, the capacity of the wall is underestimated with increasing the number of elements, resulting in a sharp degradation using this regularization technique (i.e. first element length equal to  $2L_p$ ). On the other hand, the capacity of the wall is overestimated resulting in almost no post-peak degradation when utilizing smaller number of elements. Therefore, the proposed geometrical model for RM shear walls using the suggested regularization technique is proven to be non-sensitive to the number of utilized elements.

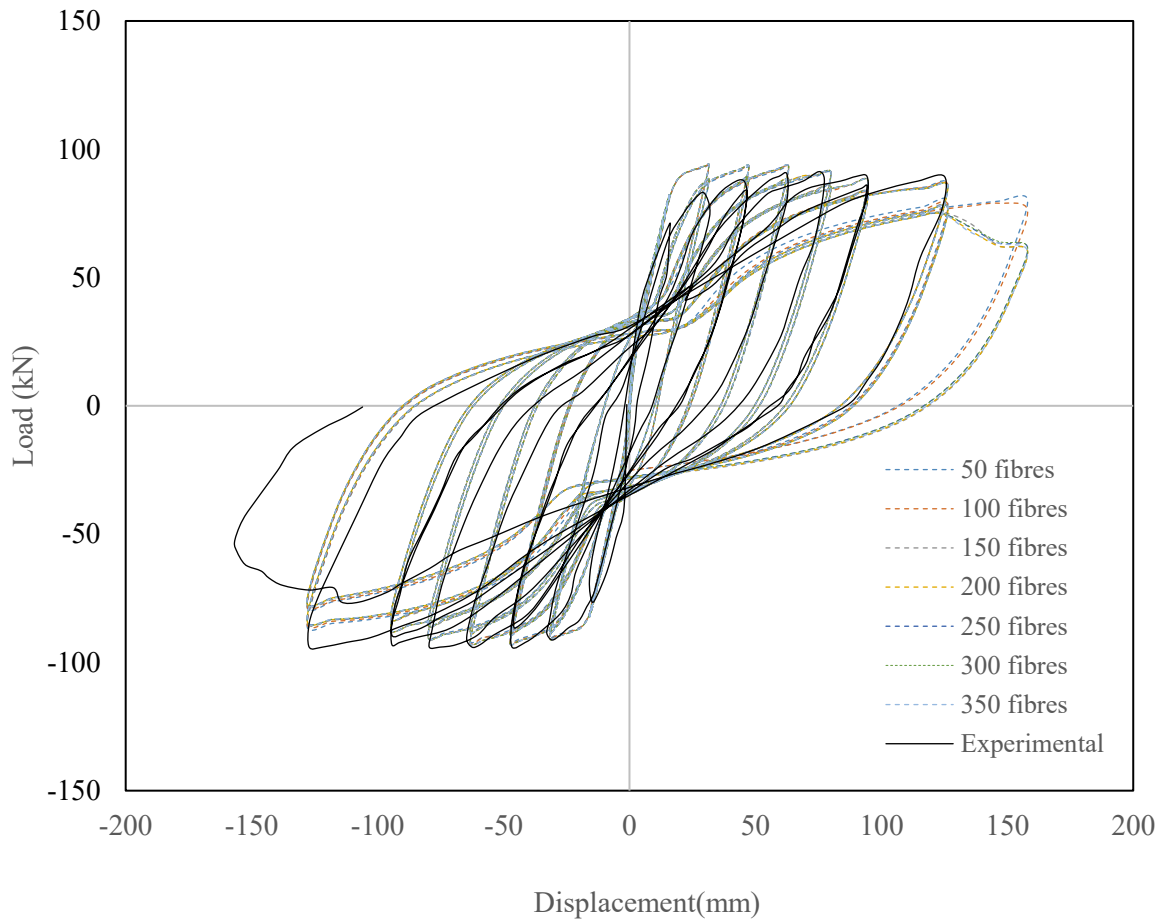


**Figure A.1** Experimental and numerical hysteresis loops for wall W2 (Banting and El-Dakhkhni 2014) with varying number of fibres

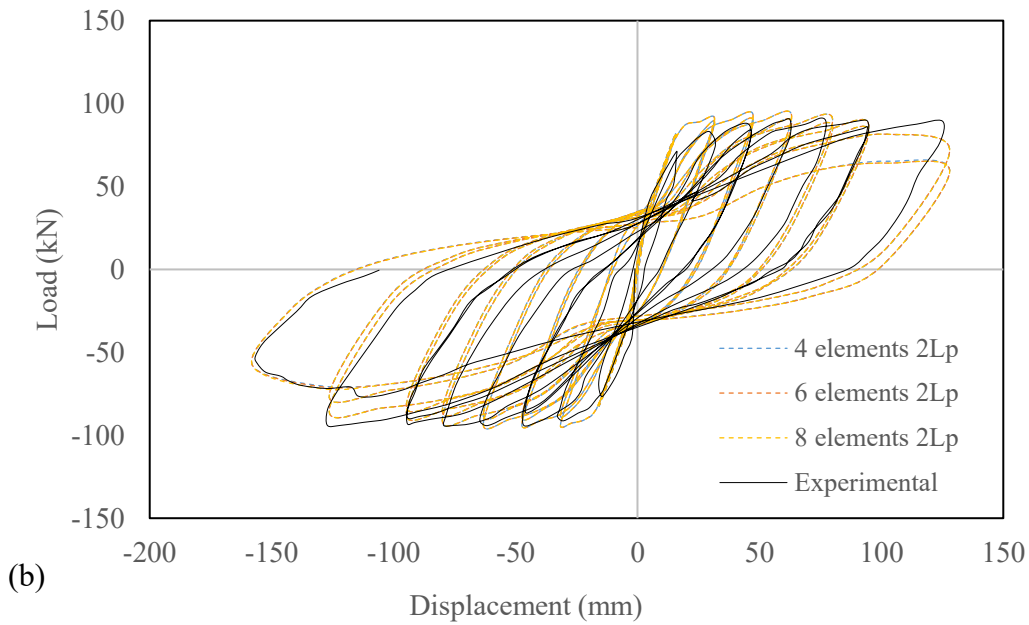
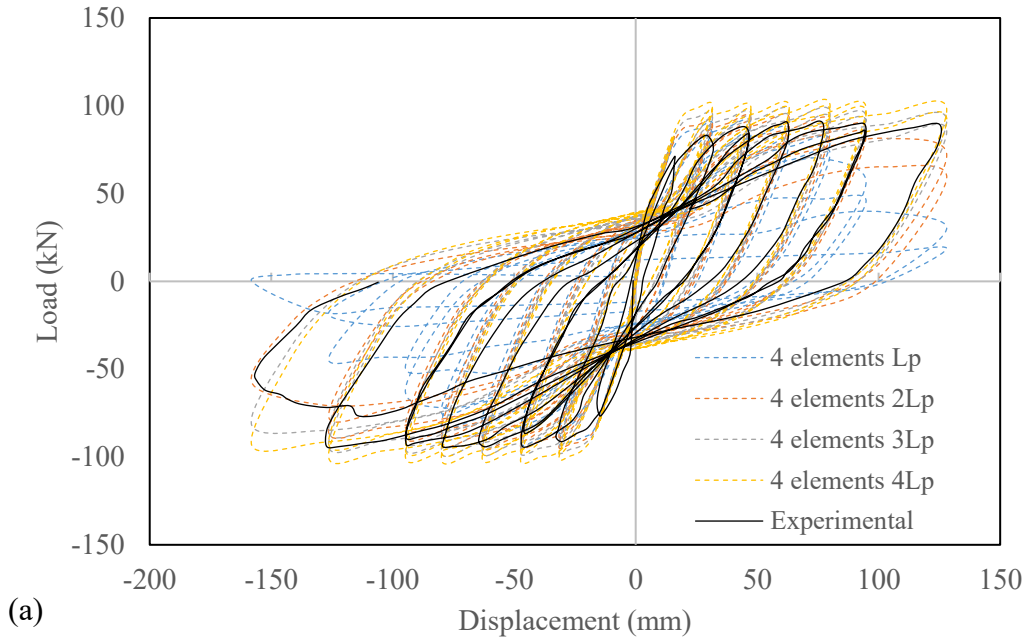


**Figure A.2** Experimental and numerical hysteresis loops for wall W2 (Banting and El-Dakhkhni 2014) with: (a) 4 elements and varying first element length; (b) varying number of elements and first element length= $2L_p$

Similarly, the sensitivity of the utilized response regularization technique was assessed for RM shear walls modelled in *OpensSees*. Figure A.3 presents the load-displacement response of wall W3 from (Shedid et al. 2010), details in Table 3.8, with varying the number of elements and using the first element length equal to twice the plastic hinge length. It was observed that the overall simulated hysteresis response was not affected by the choice of the total number of elements. Thus, this regularization technique (i.e., first element length equal to  $2L_p$ ), was proven to reduce the dependency of the hysteresis response results on the number of utilized elements; hence, increasing the objectivity of the response predictions and scatter of results.

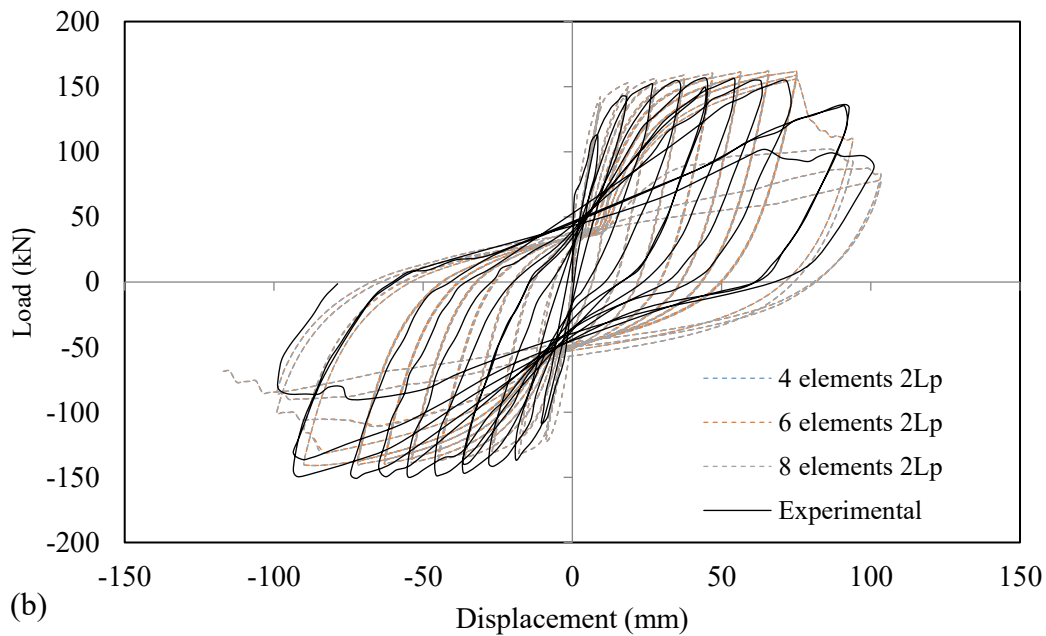
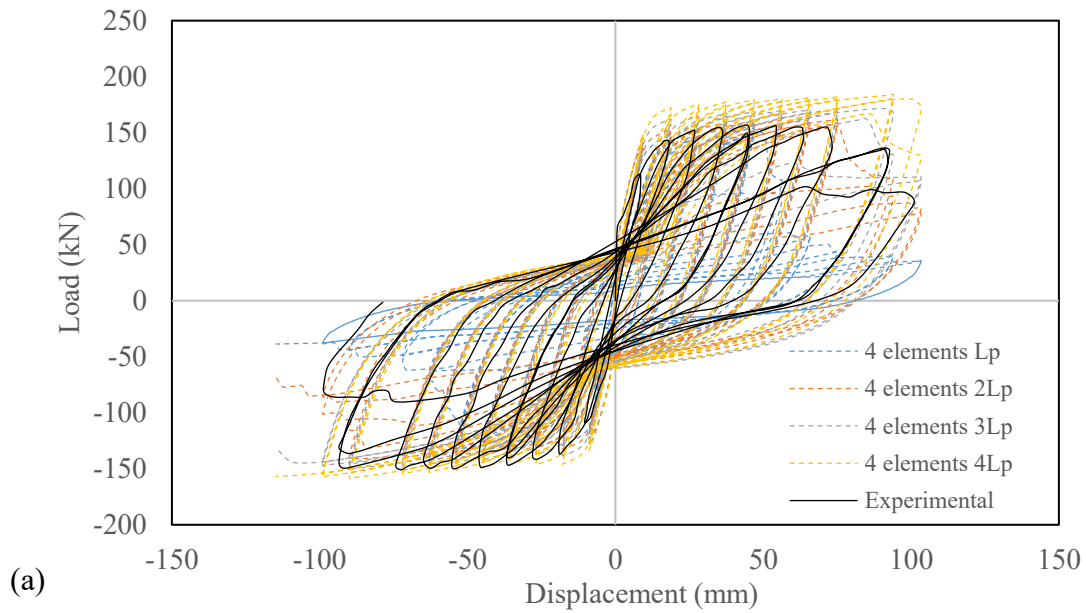


**Figure A.3** Experimental and numerical hysteresis loops for wall W3 (Shedid et al. 2010) with:  
 (a) 4 elements and varying first element length; (b) varying number of elements and first element  
 length= $2L_p$

In addition, different material and modelling parameters were assessed for the sensitivity of the models. The model developed in *SeismoStruct* and utilized in Phase I of the research is found to be mostly suitable for flexure-dominated walls since it does not take into consideration shear effects. The nonlinear modelling parameters of the reinforcement were more influential than the masonry modelling parameters, especially in terms of the initial shape factor,  $R$ , and the calibrating coefficients ( $A1$  and  $A2$ ) of the transition curve. Figure A.4 compares the experimental and numerical hysteresis response of wall W2 (Banting and El-Dakhakhni 2014), details in Table 3.7, with varying initial shape factor,  $R$  ranging from 18.4 to 19. It can be seen from Figure A.4 that using  $R$  higher than 18.8, results in overestimation of the strength and a more pinched hysteresis response. Moreover, it was observed that when lower values of  $R$  were used, the stiffness degradation was not well captured and the strength of the wall was underestimated. Figure A.5 presents the comparison of the experimental and numerical hysteresis response with varying the calibrating coefficients ( $A1$  and  $A2$ ) of the transition curve from elastic to plastic zone. It is clear from Figure A.5 that the post-peak degradation was not well captured when  $A1$  was defined lower than 18.5. However, the strength and the stiffness degradation of the wall were underestimated when a higher  $A1$  was used. In addition, defining  $A2$  a value higher than 0.3 resulted in overestimation of the stiffness degradation and capacity of the wall.

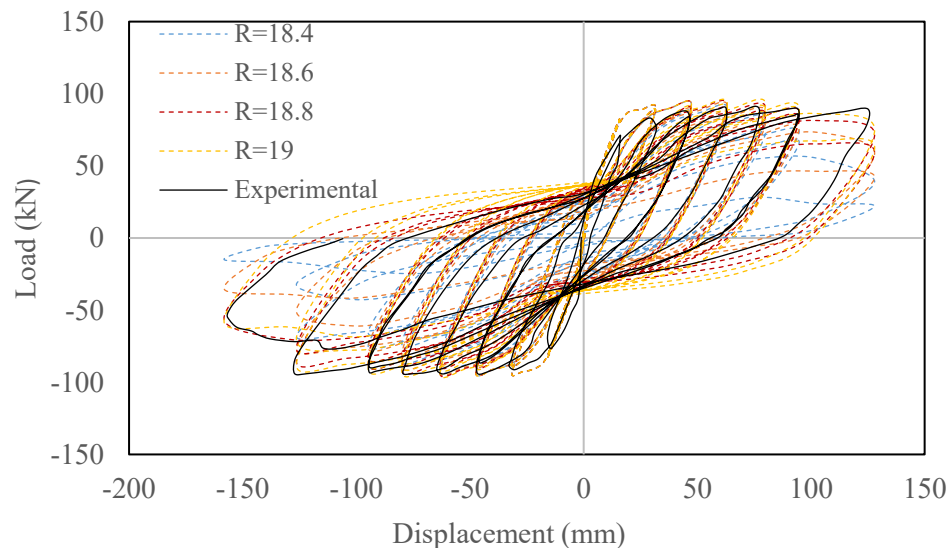


**Figure A.4** Experimental and numerical hysteresis loops with varying initial shape factor of the transition curve,  $R$

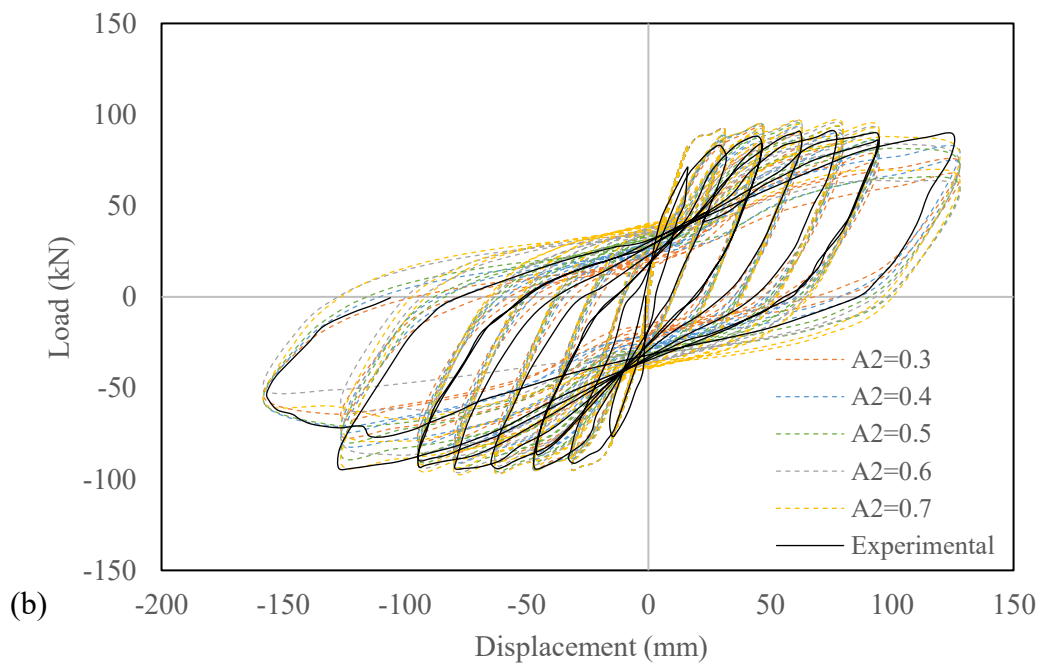
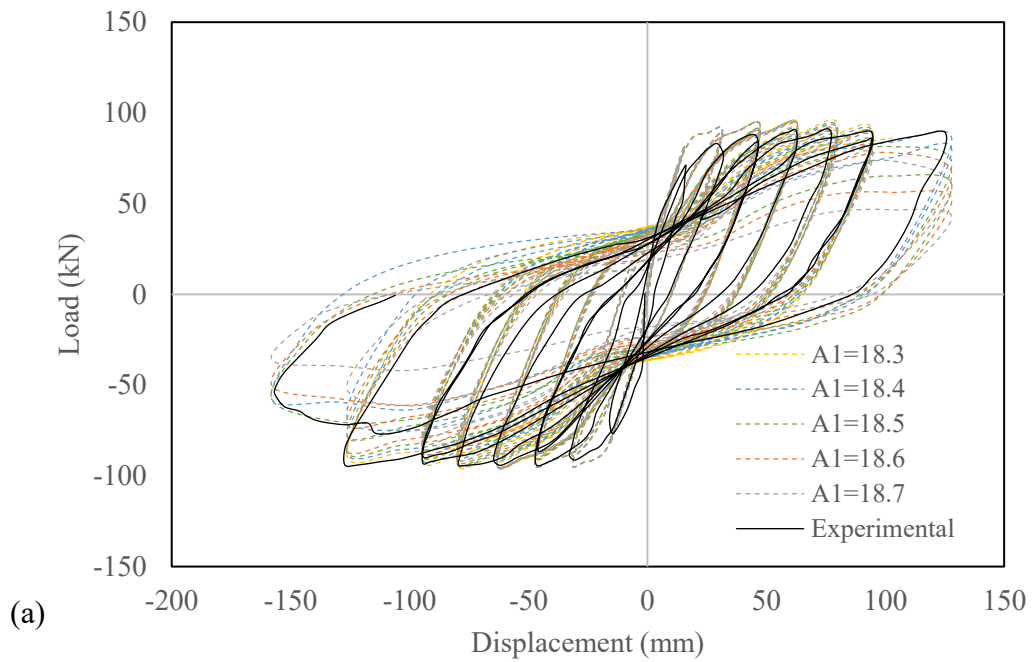


**Figure A.5** Experimental and numerical hysteresis loops with varying calibrating coefficients ( $A1$  and  $A2$ ) of transition curve

Similarly, the modelling parameters of the reinforcing steel were also the most influential on the simulated response for walls in Phase II that were modelled using *OpenSees* program. The nonlinear modelling parameters of the reinforcement were more influential than the masonry modelling parameters, in particular in terms of the initial curvature parameter,  $R_0$ , and the curvature degradation parameters ( $CR1$  and  $CR2$ ) of the transition curve. Figure A.6 displays the experimental and numerical hysteresis response of wall W3 (Shedid et al. 2010), details in Table 3.8, with varying initial curvature parameter,  $R$  ranging from 10 to 20. It can be seen from Figure A.6 that when  $R$  higher than 10 is used, the hysteresis response of the wall does not capture the post-peak response accurately. Figure A.7 shows the numerical against experimental hysteresis response with varying the curvature degradation parameters ( $CR1$  and  $CR2$ ) of the transition curve from elastic to plastic zone. It was observed from Figure A.7 that the stiffness degradation is underestimated and not well captured in the lateral load-displacement response when  $CR1$  values lower than 0.95 are used. In addition, the strength and the stiffness degradation of the wall were underestimated when  $CR2$  lower than 1.1 was used.

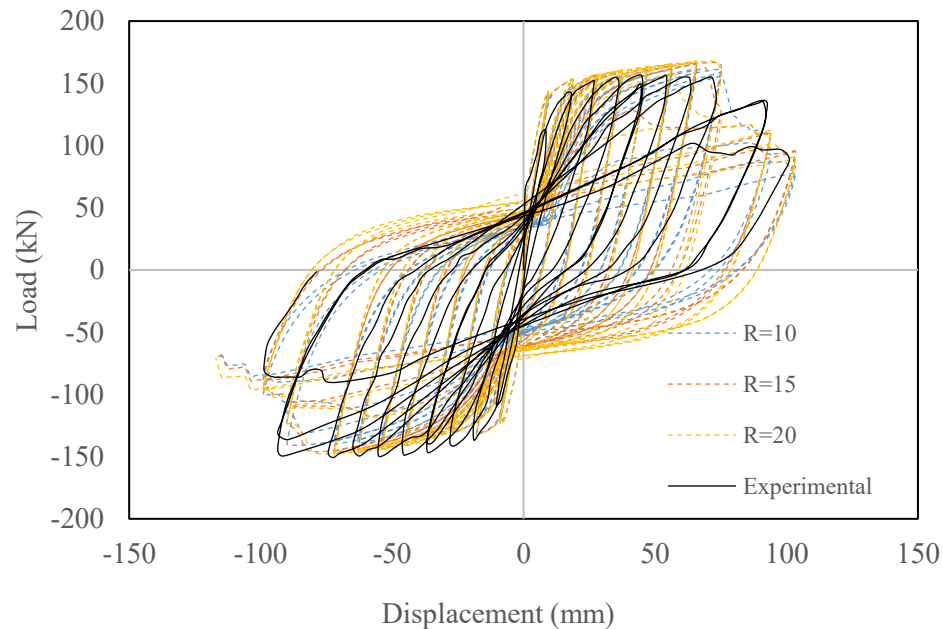


**Figure A.6** Experimental and numerical hysteresis loops for wall W3 (Shedid et al. 2010) with varying initial curvature parameter,  $R_0$

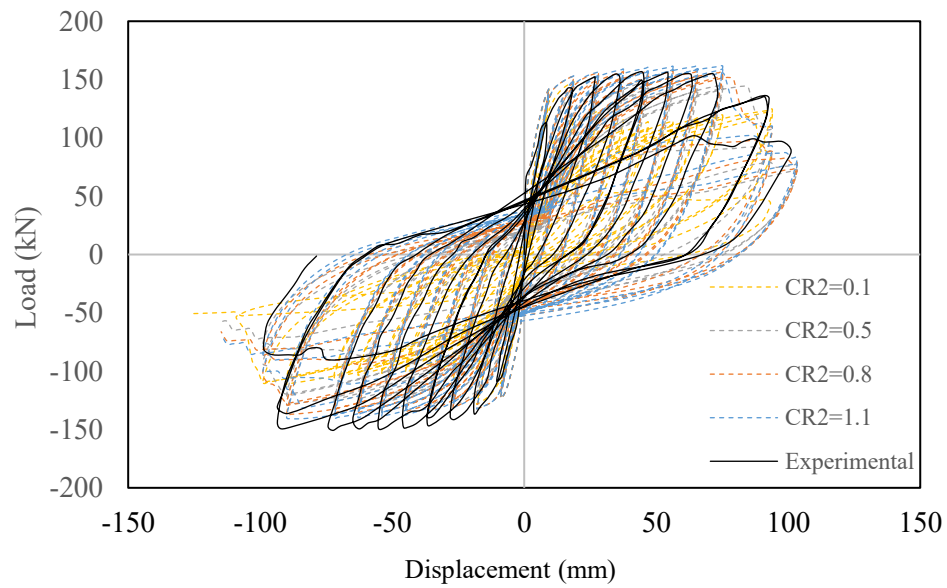
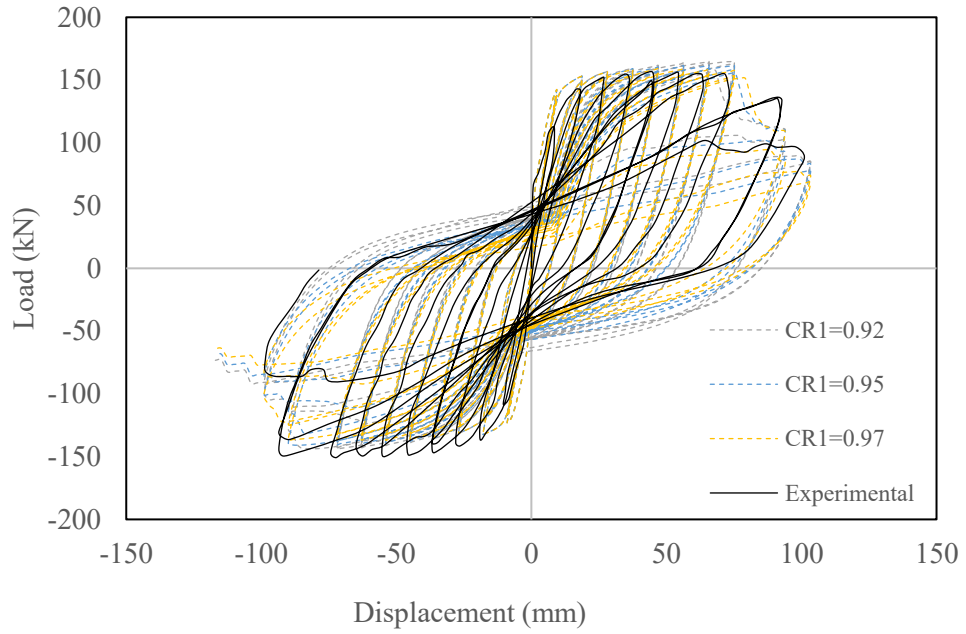


**Figure A.7** Experimental and numerical hysteresis loops for wall W3 (Shedid et al. 2010) with varying curvature degradation parameters ( $CR1$  and  $CR2$ )

## **A2. Limitations of the numerical model**

This section highlights the limitations in the utilized numerical models and the performed analyses. These limitations can be addressed in future studies based on the findings of this research.

The limitations of the developed numerical models are as follows:

- The developed numerical models in *SeismoStruct* and *OpenSees* were two-dimensional; therefore, the out-of-plane loading effect on the in-plane failure mode was neglected.
- The nonlinear cyclic response of masonry was modelled using the uniaxial concrete models since there are no pre-defined constitutive material models developed for the simulation of the response of grouted concrete masonry.
- More research is required considering wider ranges of design material parameters (e.g., different strengths for the blocks and grout) in order to further enhance the modelling accuracy.
- The local failure modes such as shear failure along the web and the boundary element interface were not captured by the models.
- The modelling approaches assumed that only the local failure modes seen in the experimental testing would occur. This is mainly because the simulated response in the model was extrapolated from the considered validation parameters (i.e., available specimens' sizes and material characteristics).

## **A3. Analytical failure modes**

Despite the several failure criteria adapted for the material behaviour in the model, some failure modes cannot be captured in the numerical model during the analysis. Therefore, the failure criteria were captured after post processing of the obtained output results. The following failure modes of the walls were assessed and monitored:

- **Concrete crushing:** Masonry crushing will occur when 25% of the cross-section reaches the end of the softening branch of the masonry stress-strain curve (i.e. crushing strain). For the unconfined masonry areas, the crushing strain is considered to be 0.01, which represents the strain at the end of the descending branch of the masonry stress-strain curve. As for the confined regions, crushing strain is considered to correspond to the strain at the end of the descending branch of the confined masonry stress-strain curve according to Mander et al. (1988).

- Steel buckling/fracture: Fracture of reinforcement was defined when 25% of the bars in the cross-section lose their tensile strength due to rupture or reach their compressive strength due to buckling. Fracture of the reinforcement was taken as 0.05 and 0.1 for unconfined and confined bars, respectively (NIST 2010).

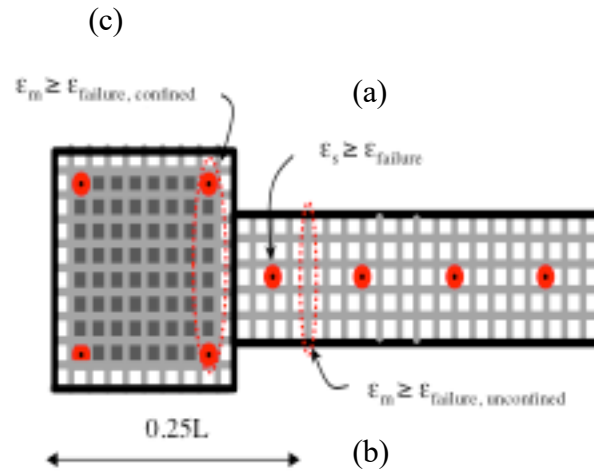
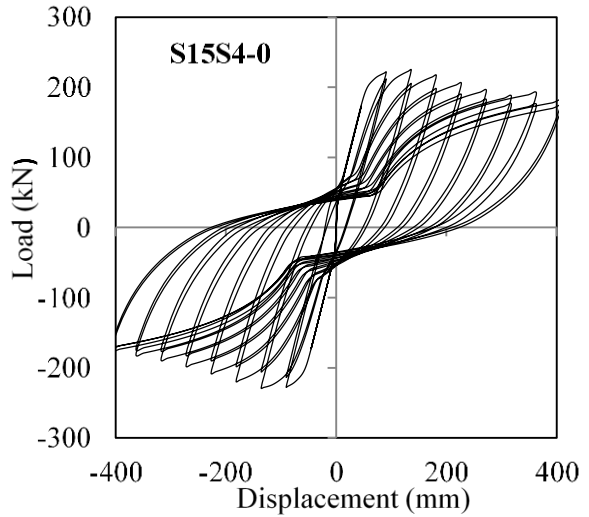
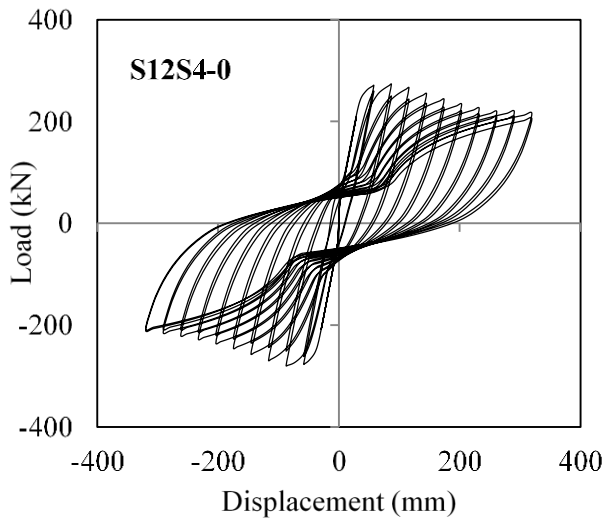
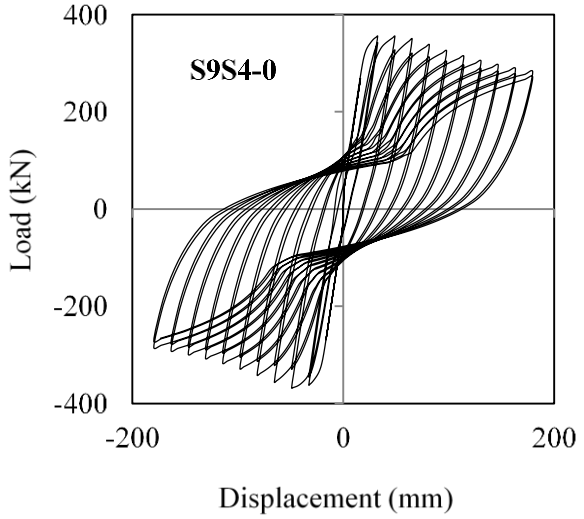
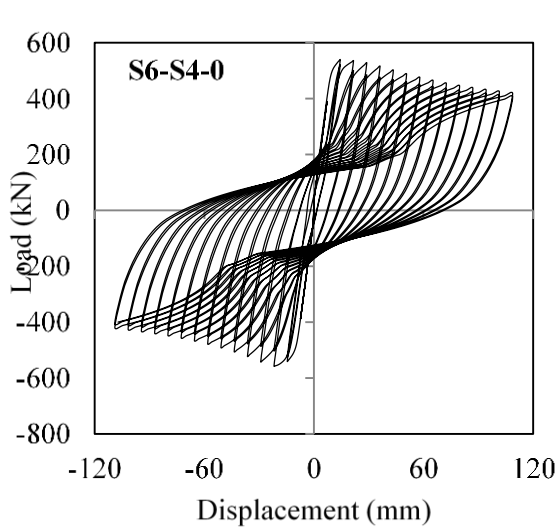


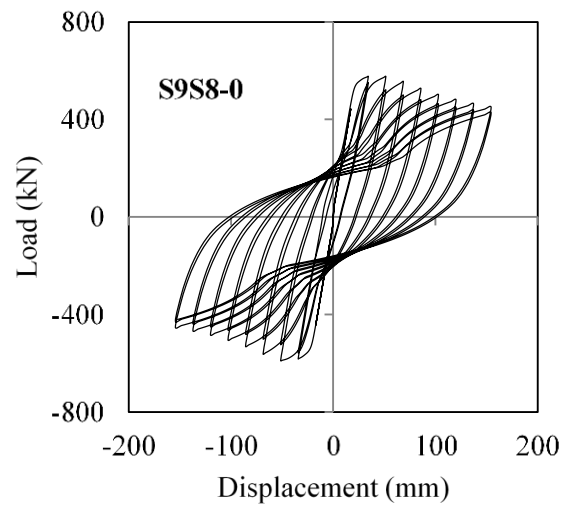
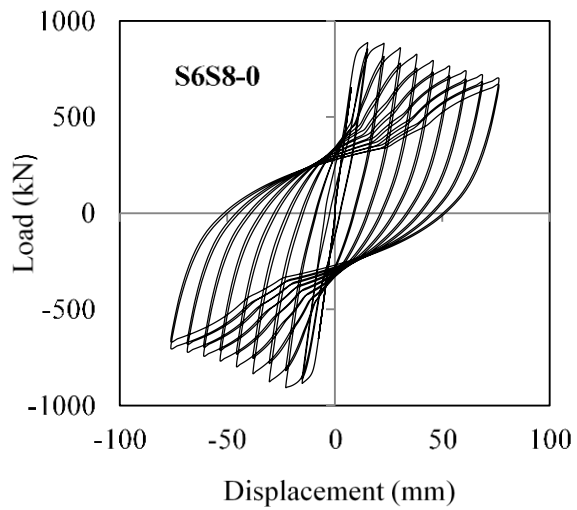
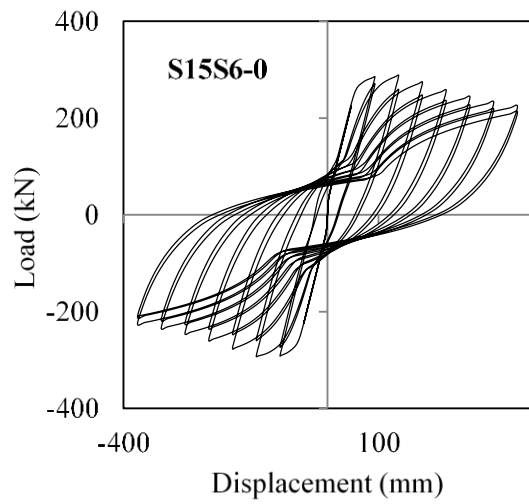
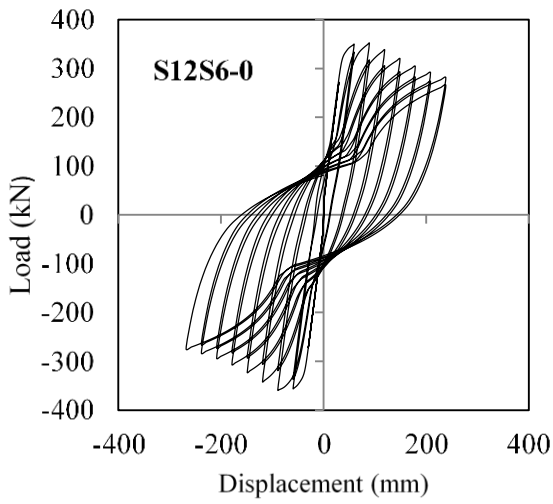
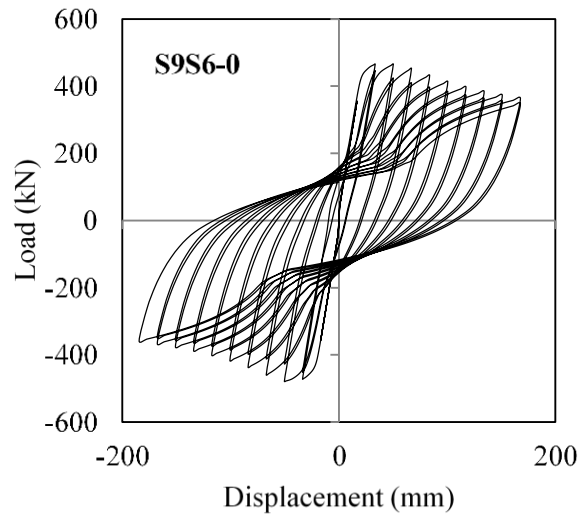
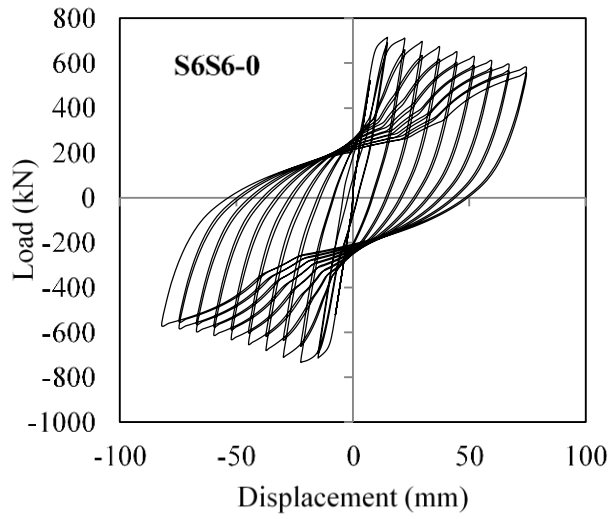
**Figure A.8** Reinforcing steel and masonry failure mode criteria: (a) steel rebar failure; (b) masonry crushing in confined region; (c) masonry crushing in unconfined region

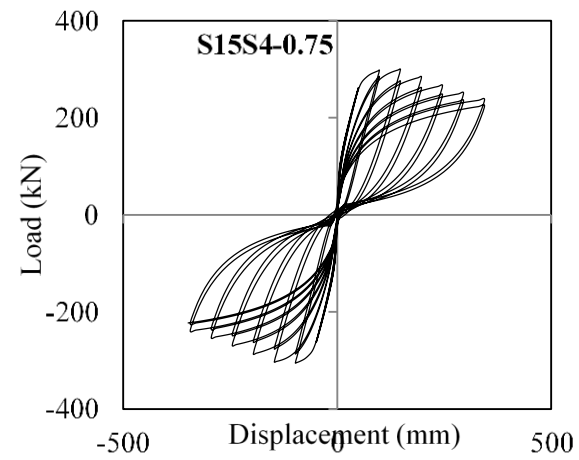
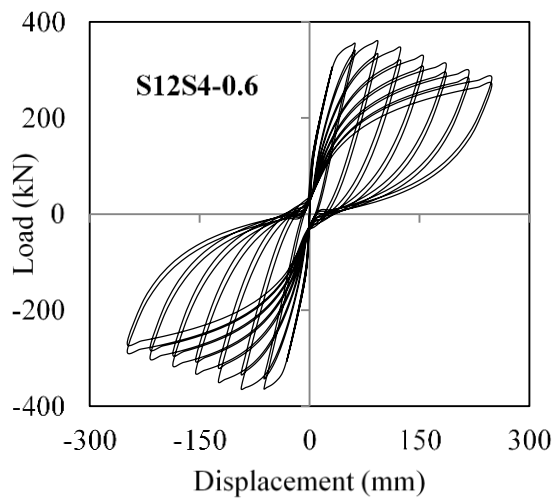
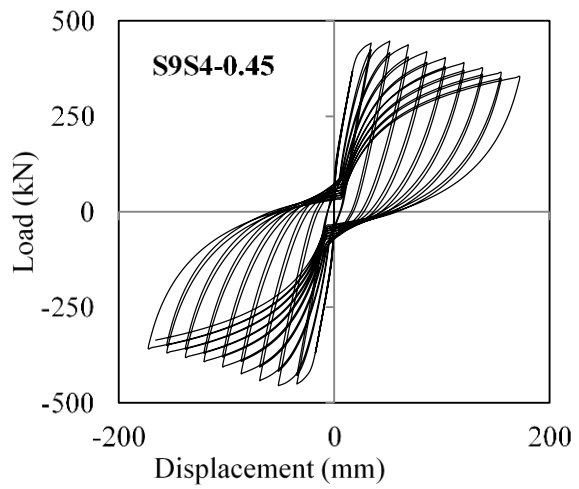
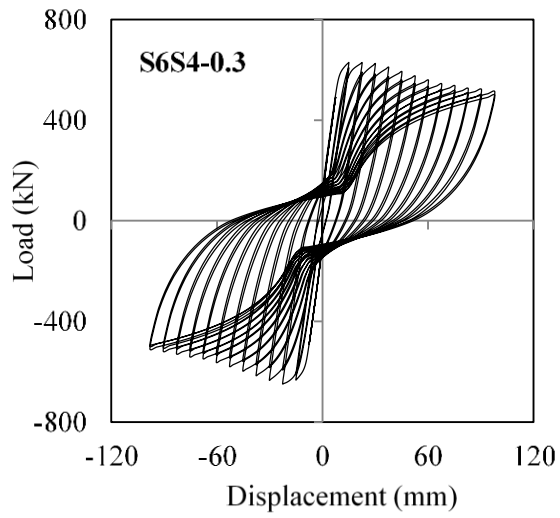
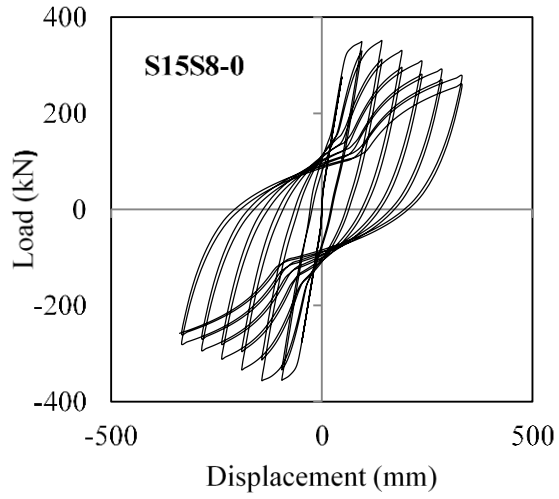
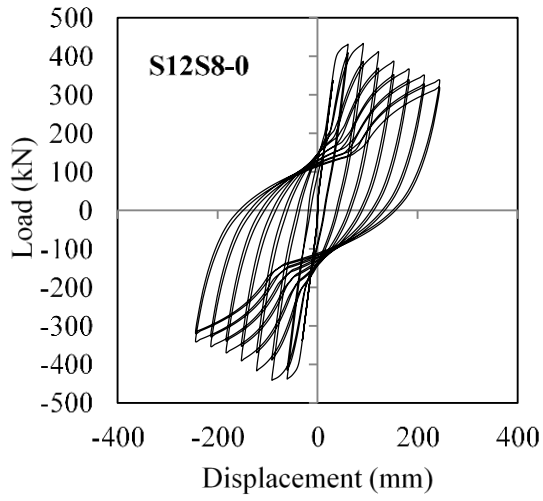
## Appendix B

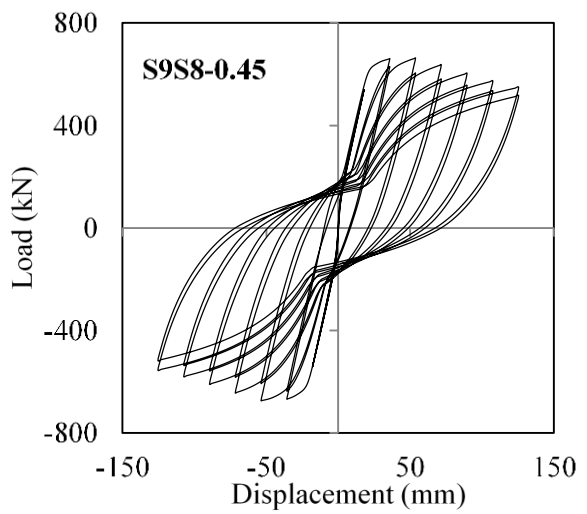
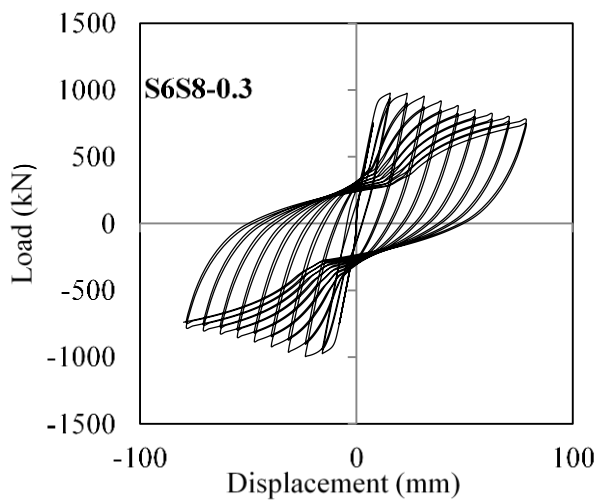
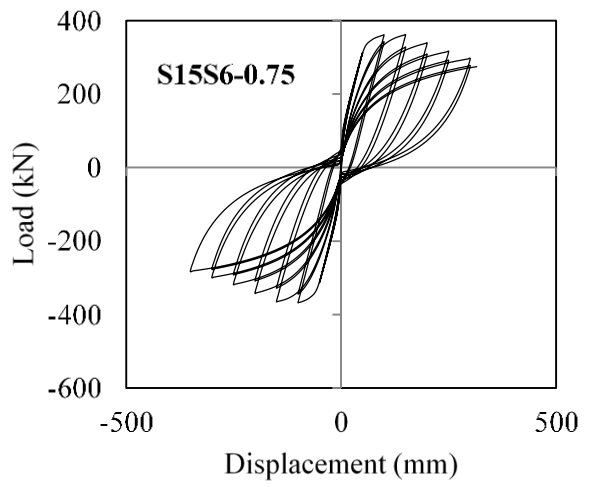
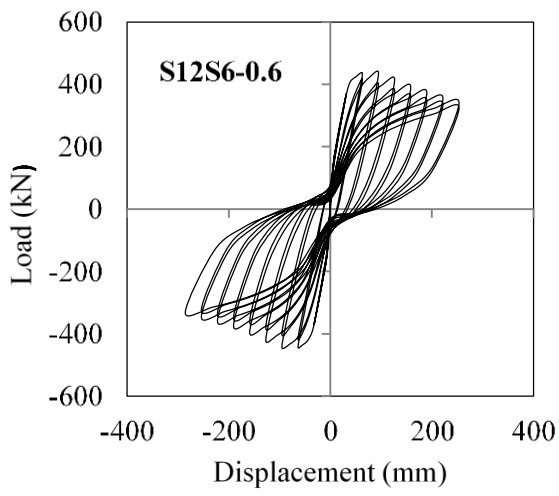
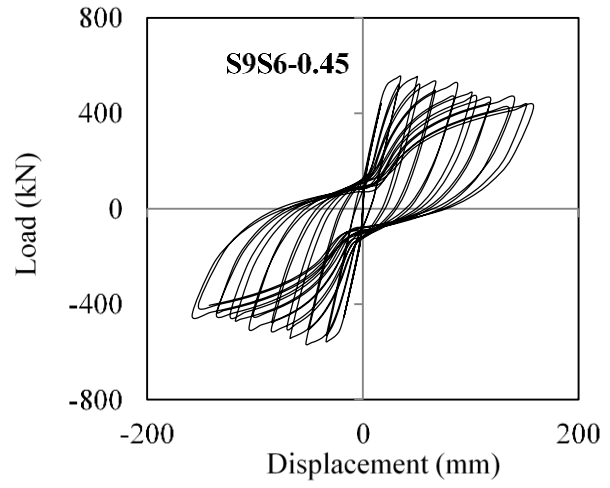
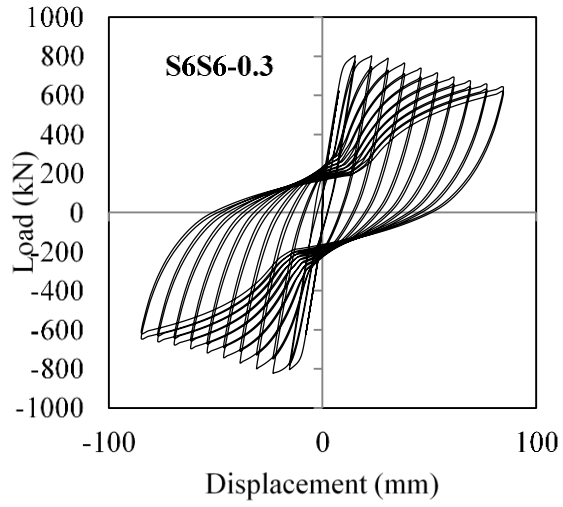
### Hysteresis Load-displacement Response for 70 Modelled Walls

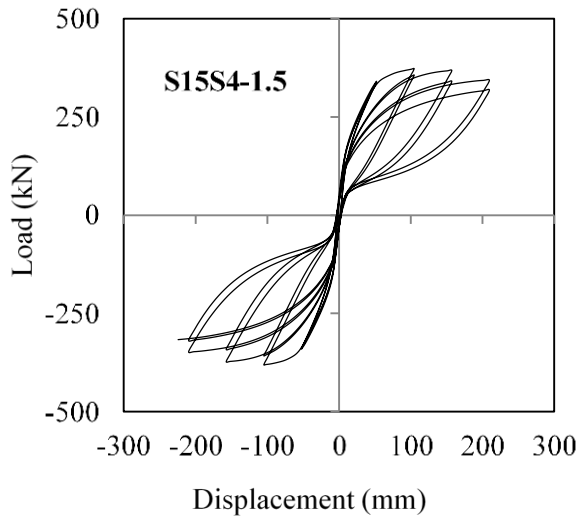
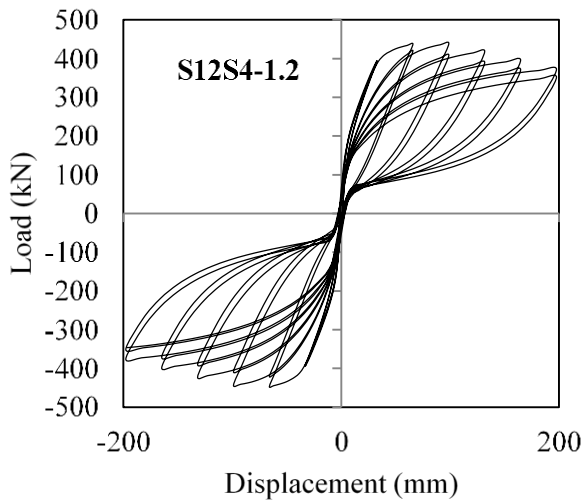
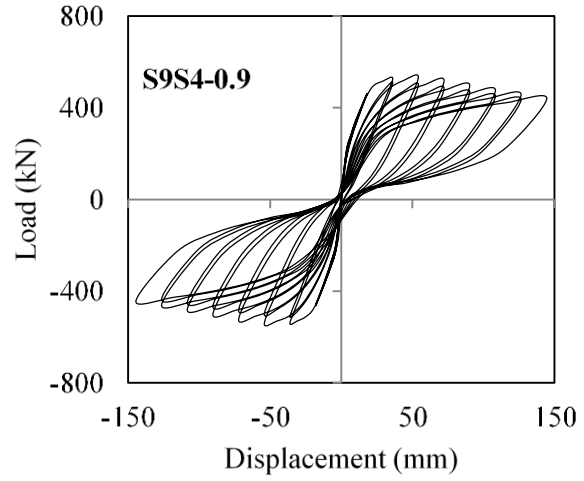
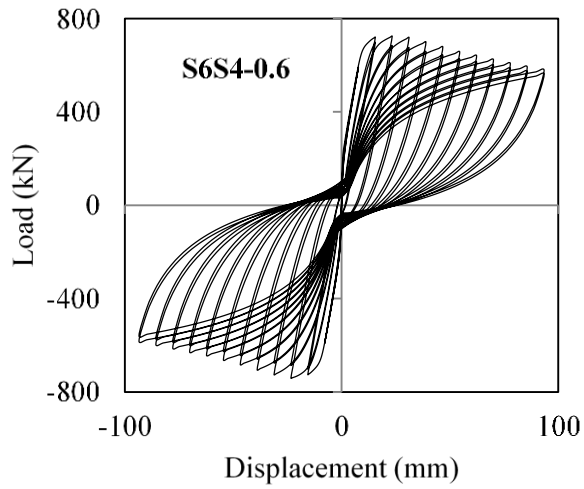
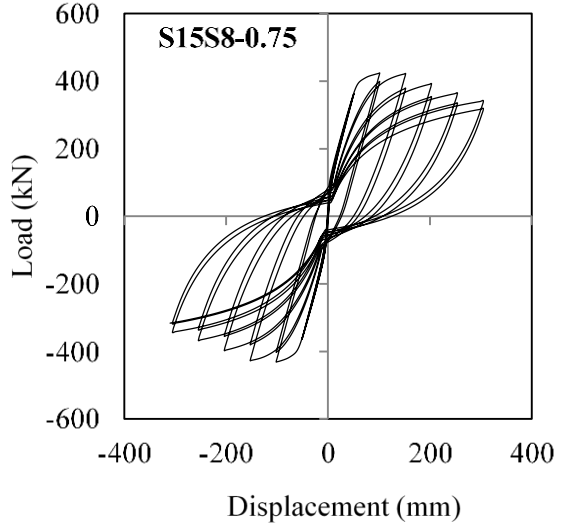
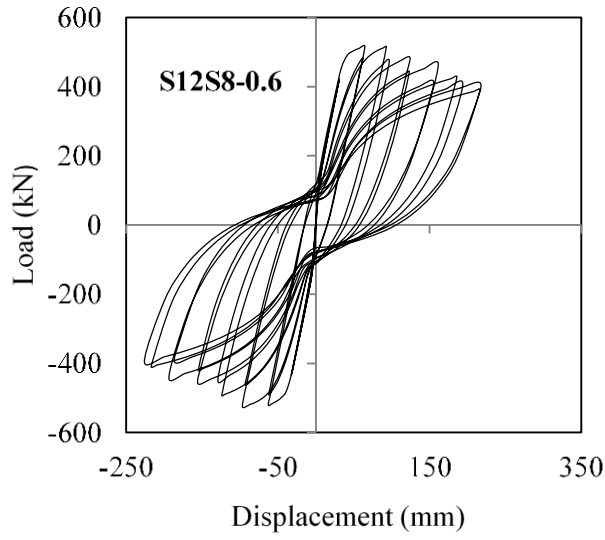
This Appendix presents additional information to the numerical investigation presented in Chapter 4.

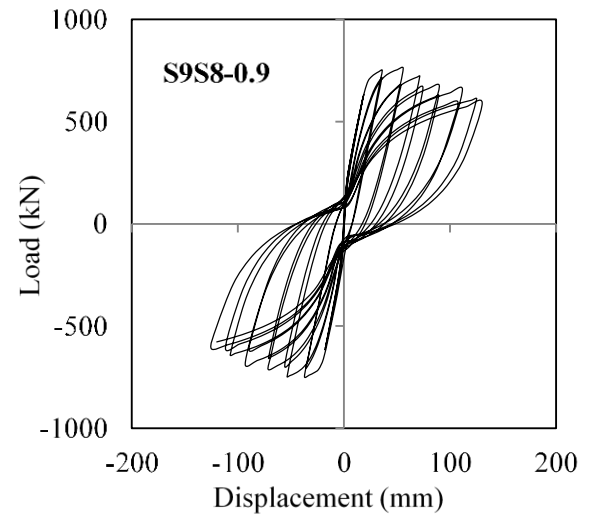
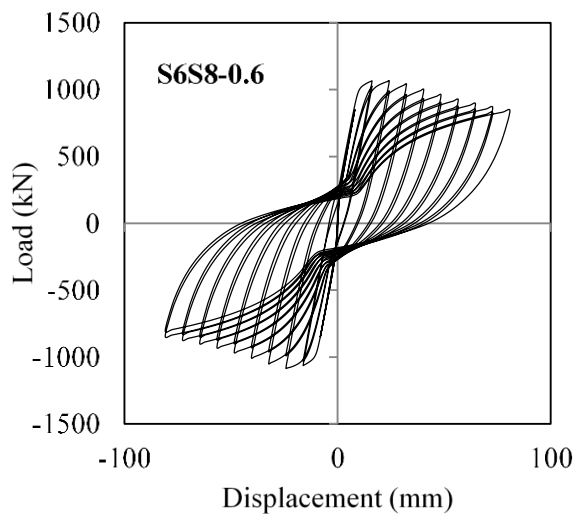
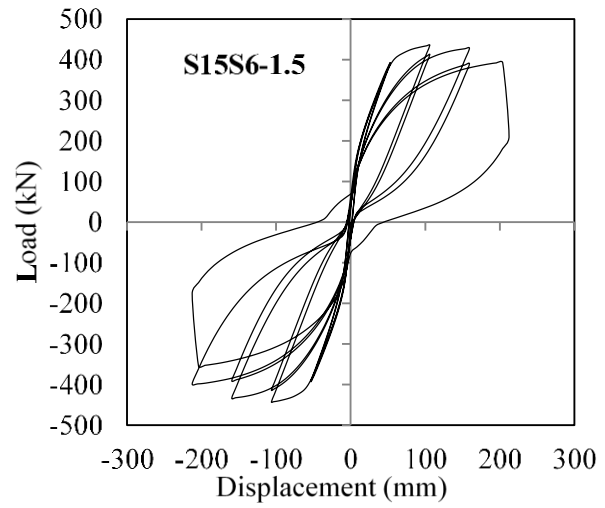
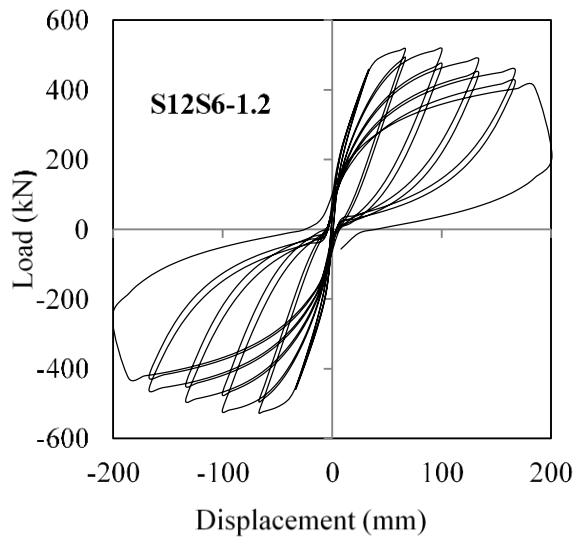
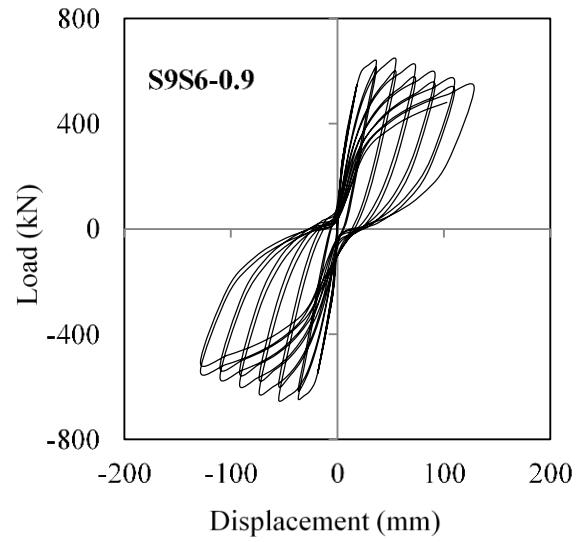
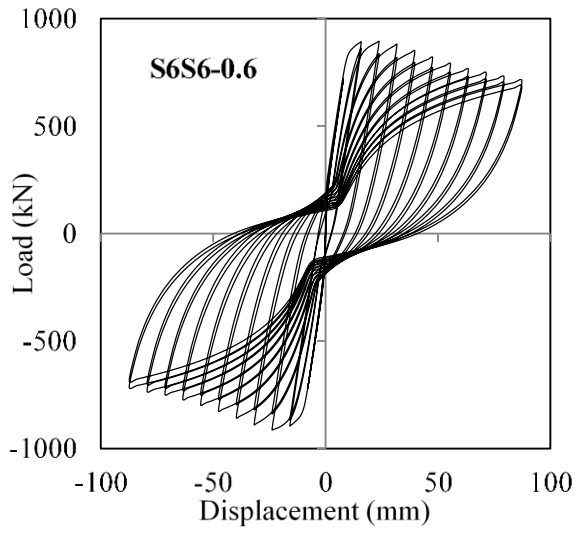


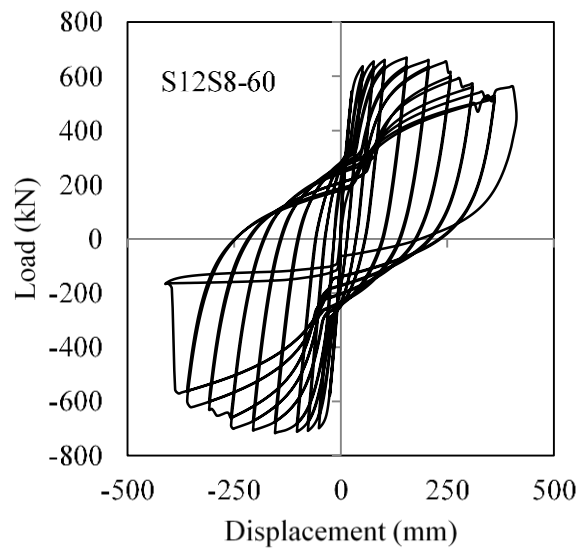
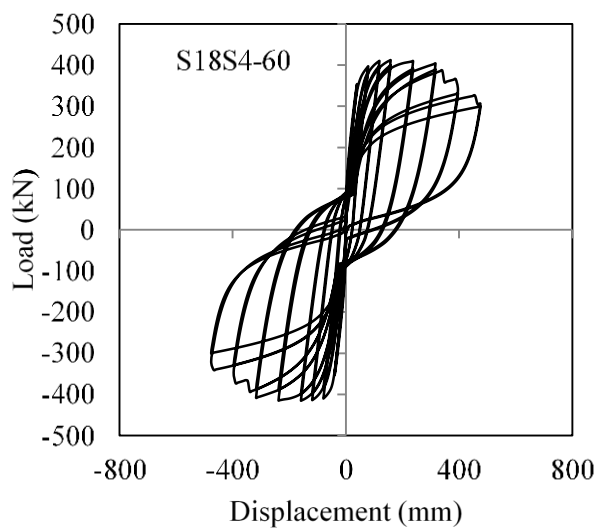
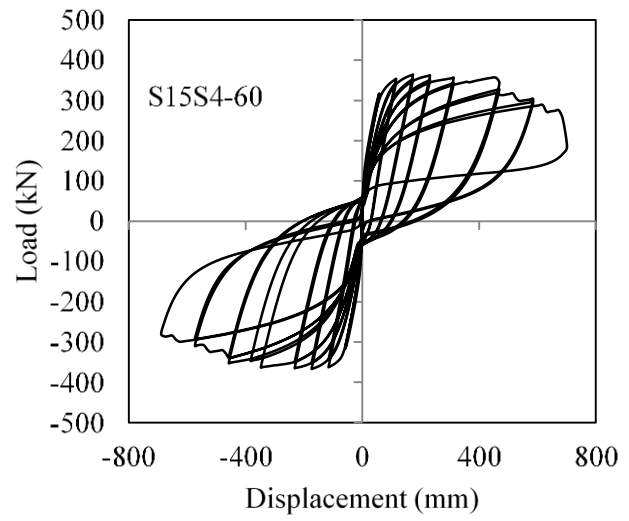
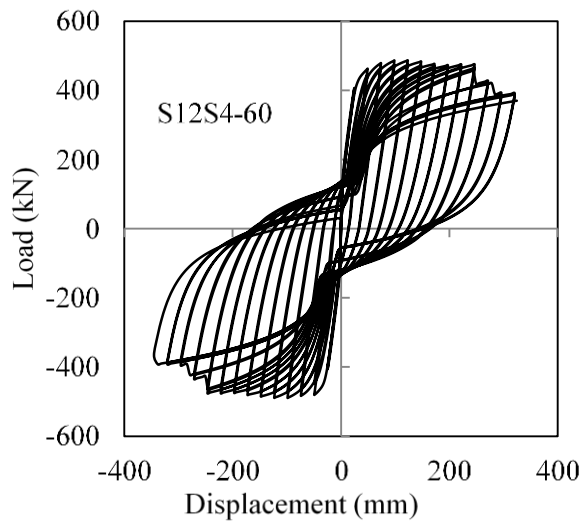
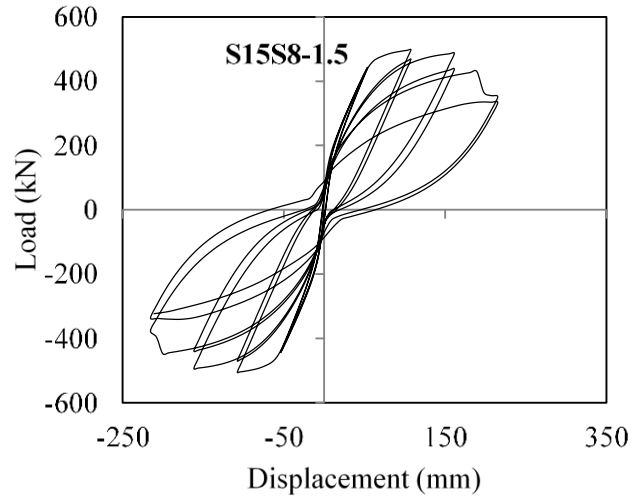
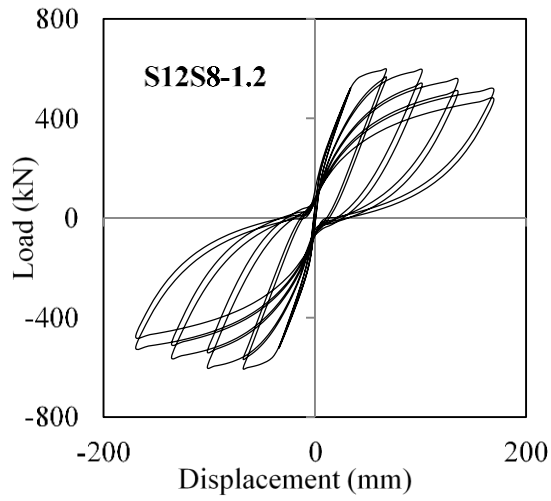


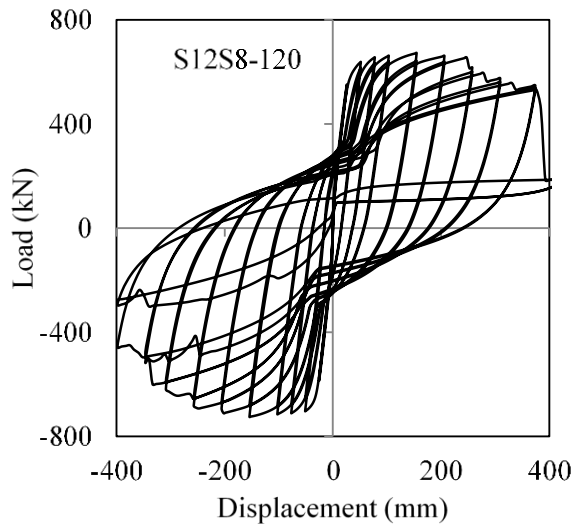
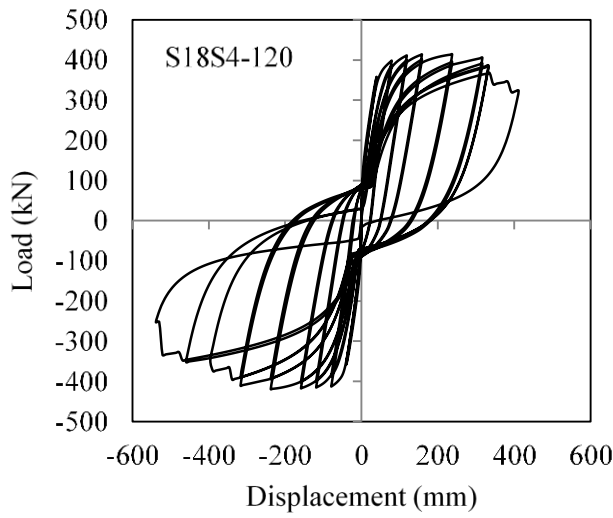
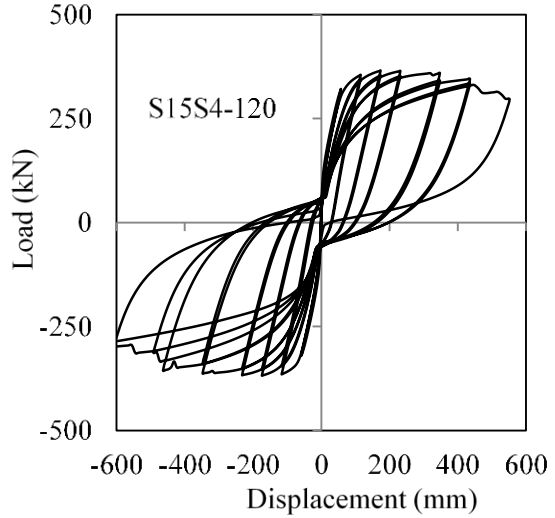
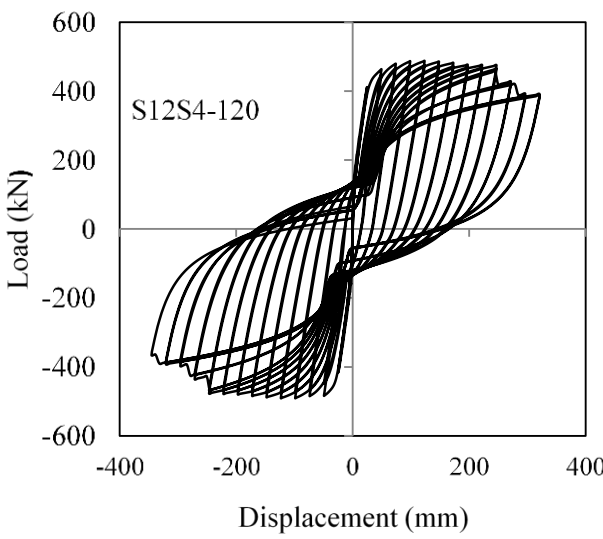
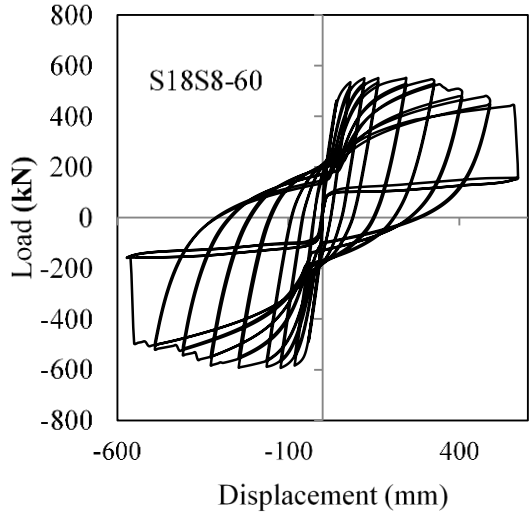
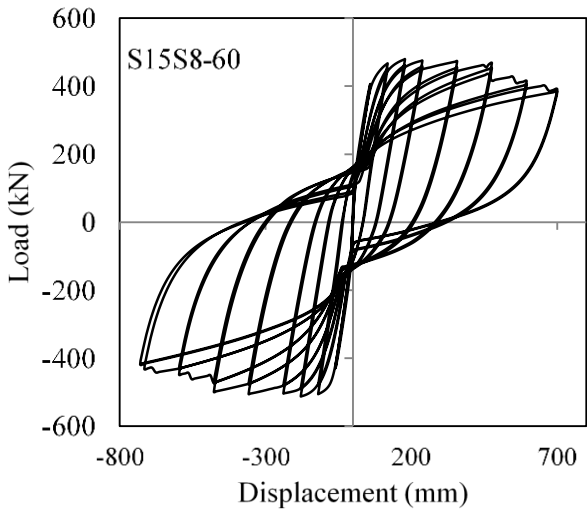


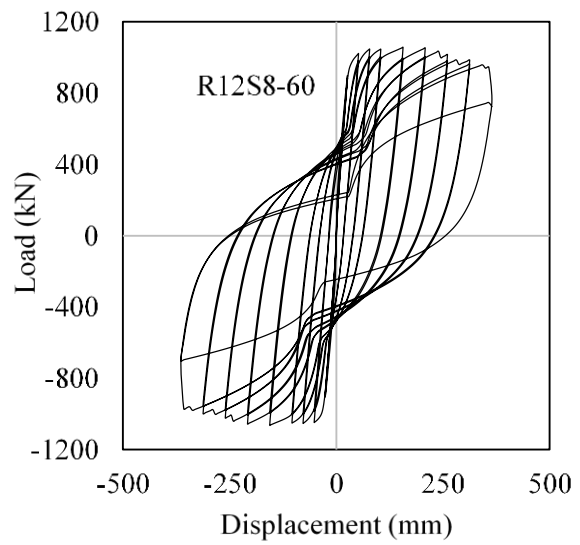
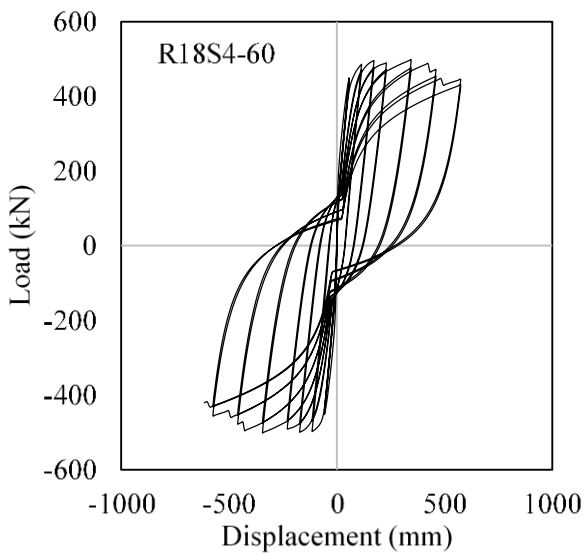
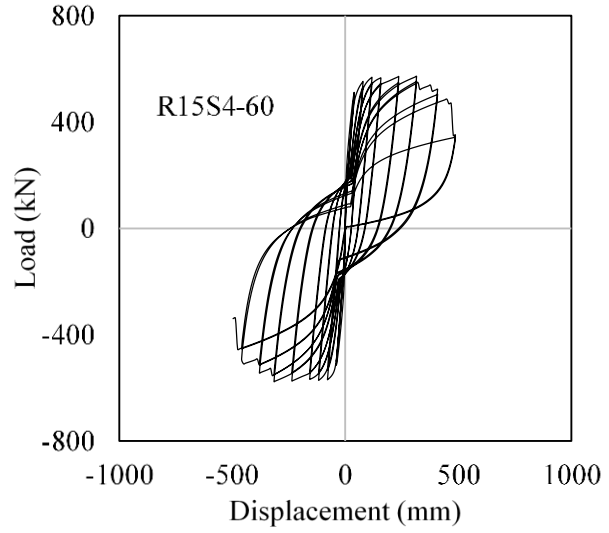
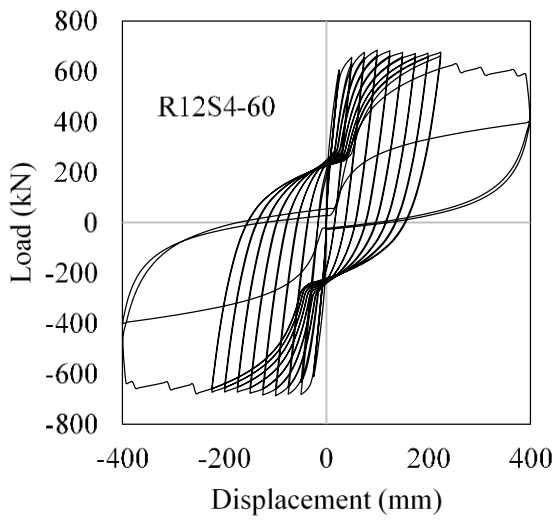
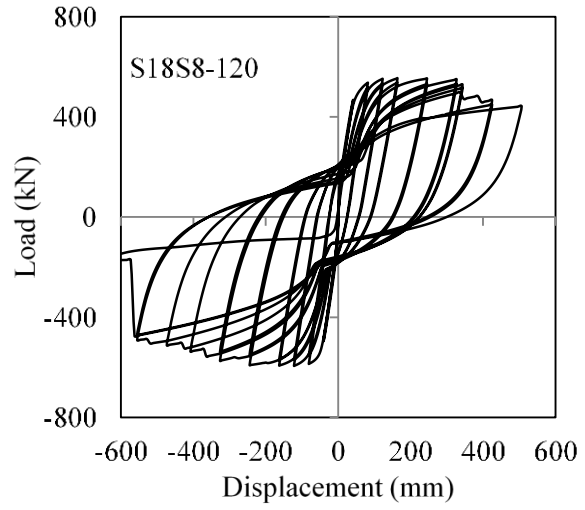
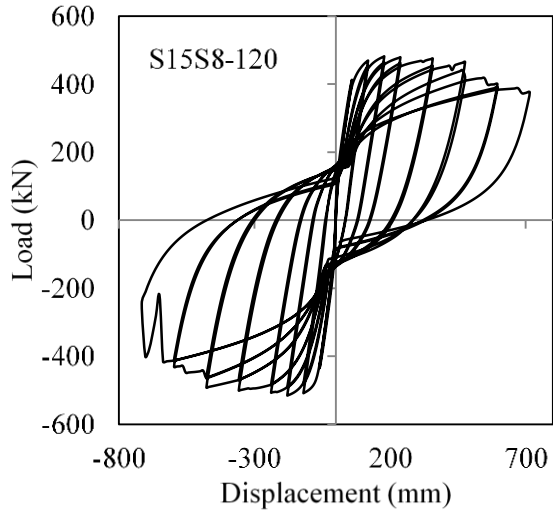


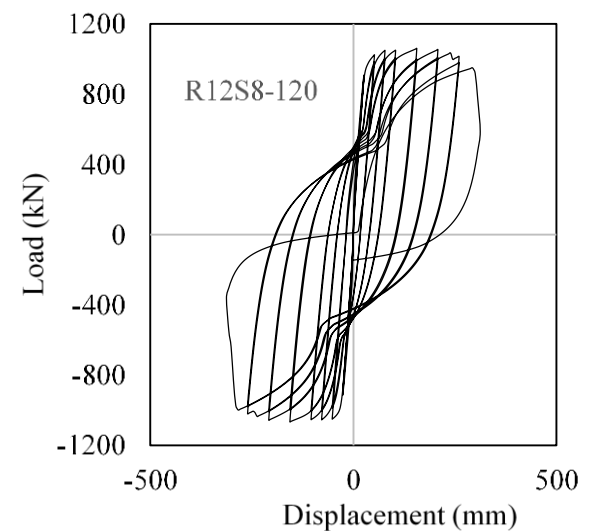
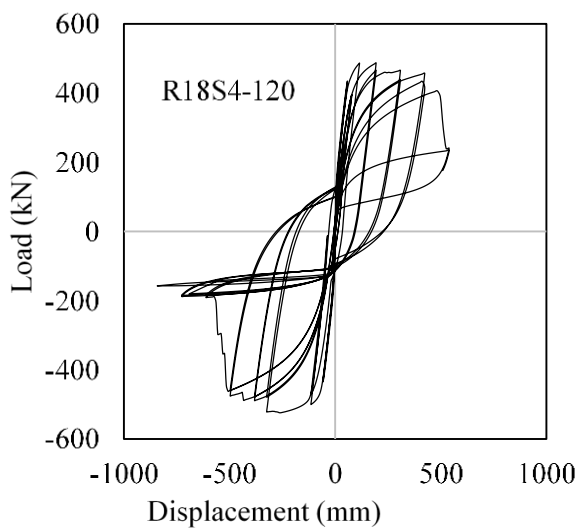
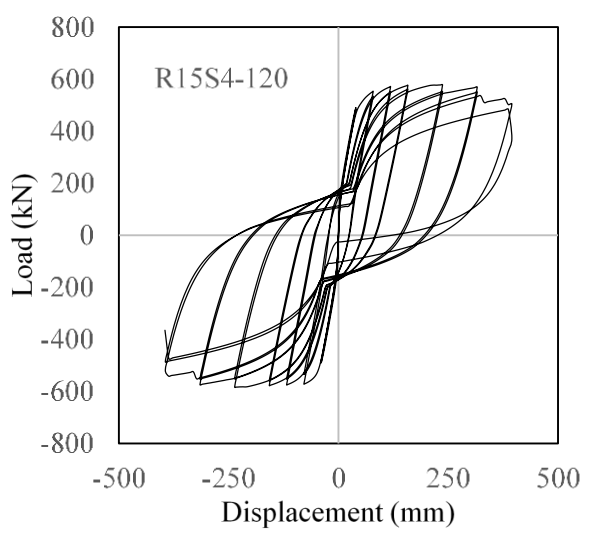
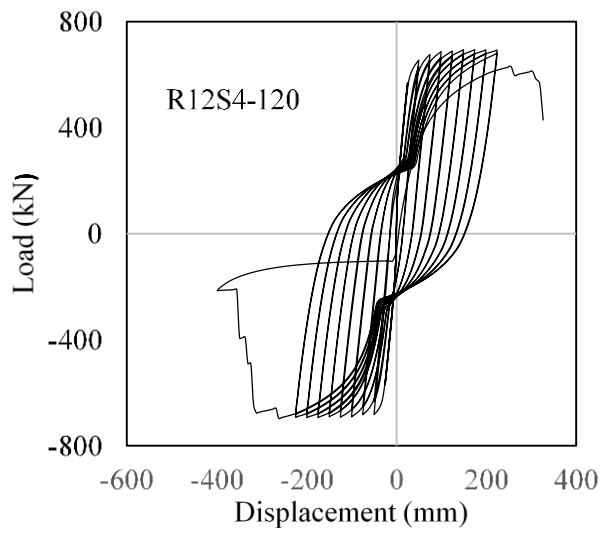
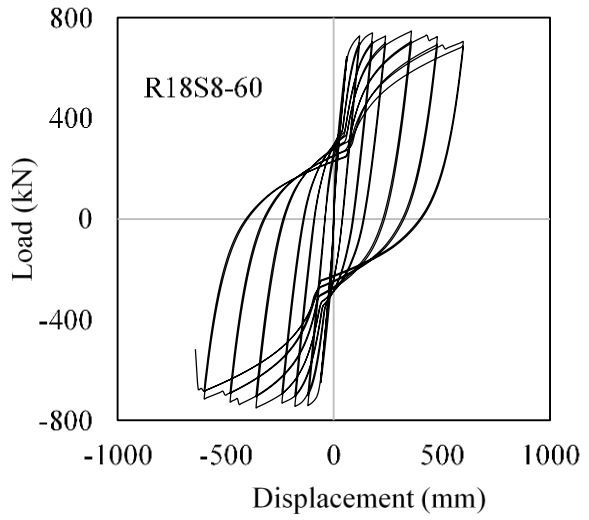
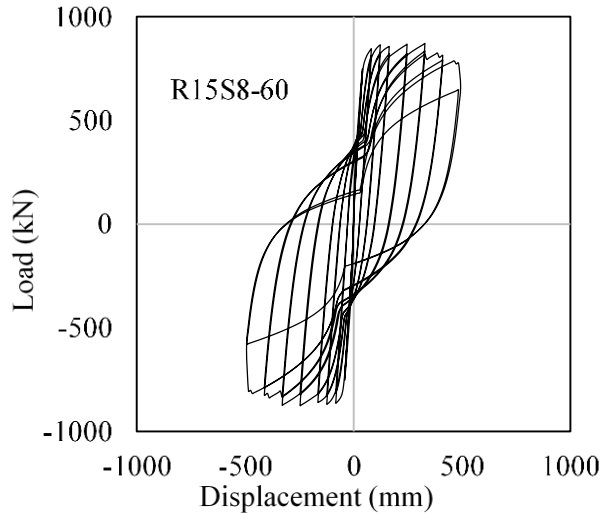


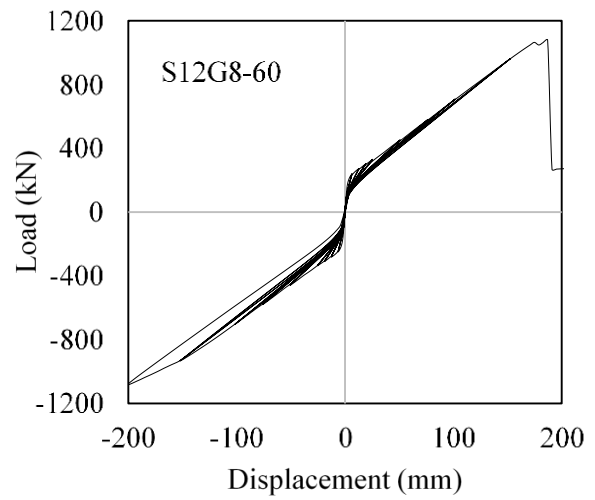
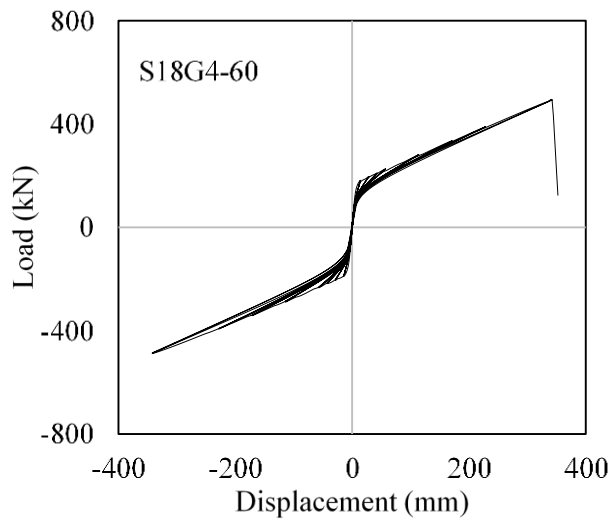
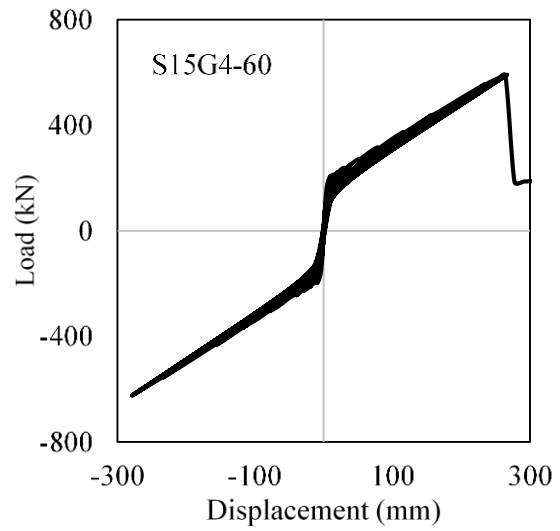
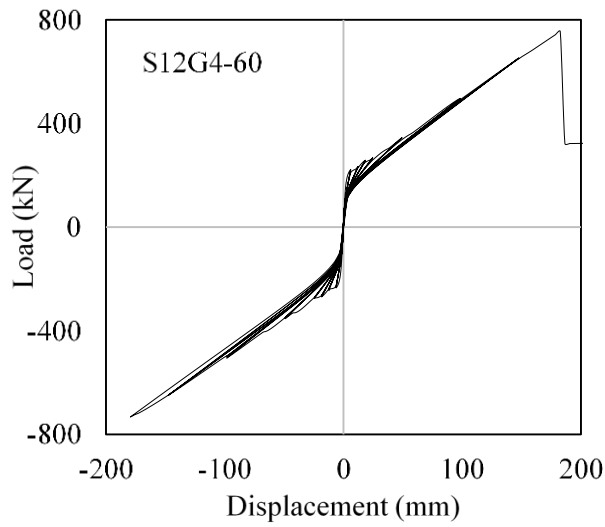
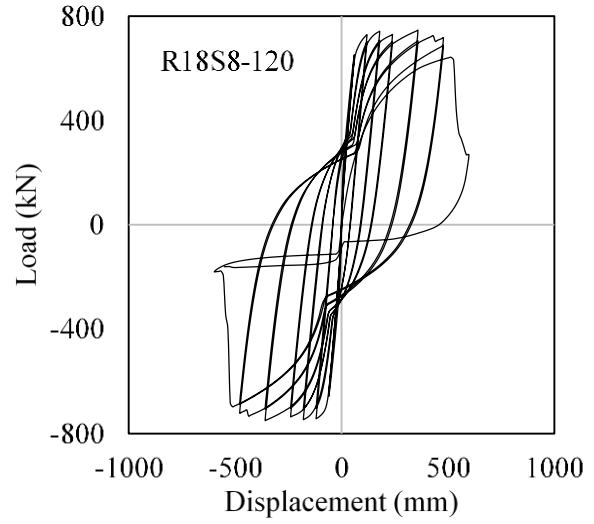
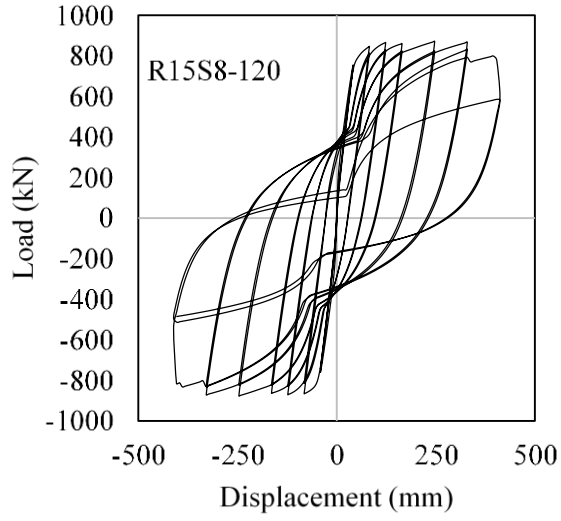












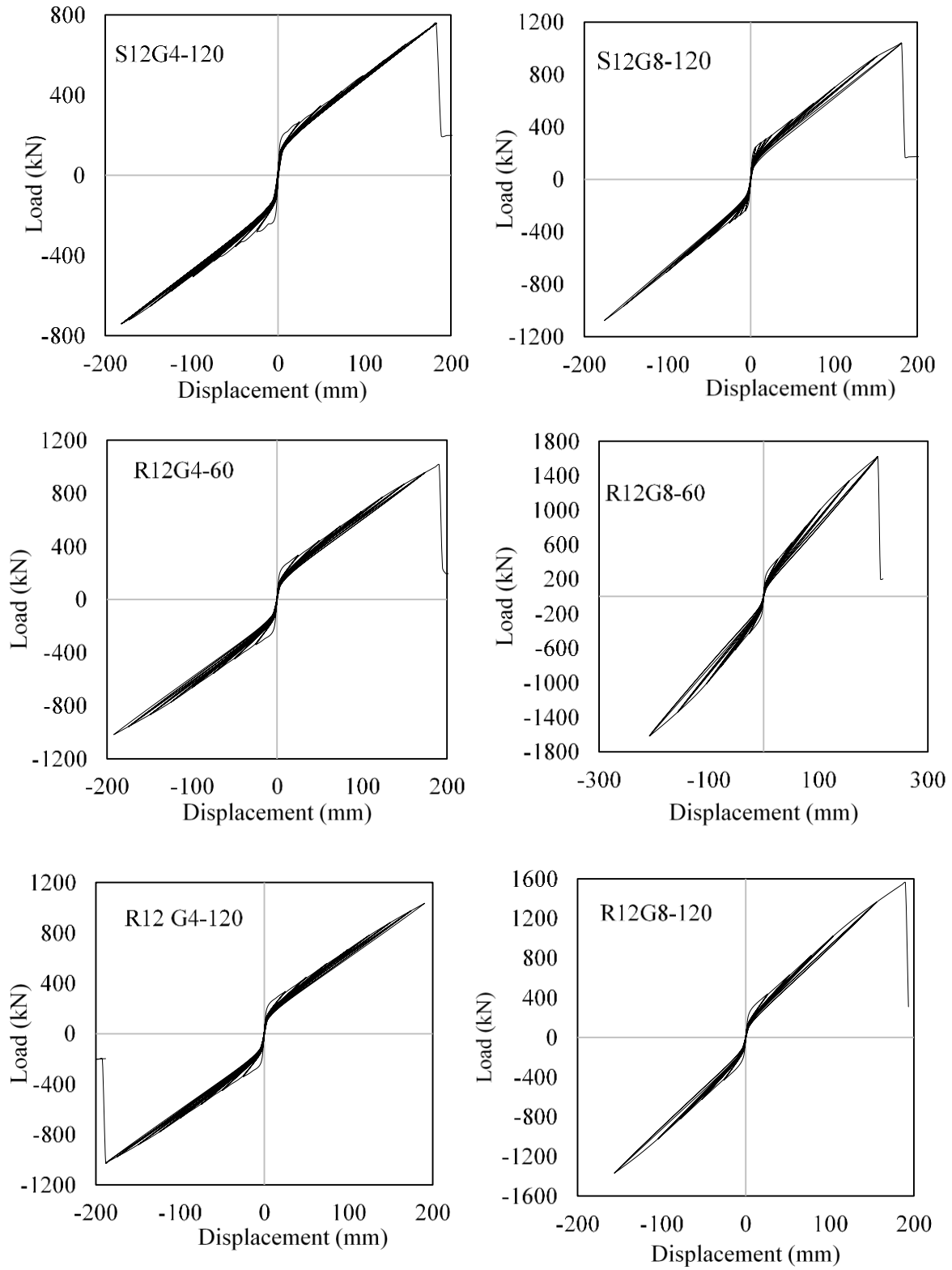


**Figure B. 1** Load-displacement hysteresis loops for 70 walls

## Appendix C

### RMSWs Category Description and Classification.

This Appendix presents additional information for the analytical work presented in Chapter 5.

**Table C.1** RMSW category description according to TMS 402/602 and ASCE-7 (2016)

TMS 402/602	RM shear walls SFRS Category				
	Ordinary shear walls	Intermediate shear walls	Special shear walls		
Response modification factor ( $R$ )	$R=2$ ASCE7 Table 12.2-1	$R=3.5$ ASCE7 Table 12.2-1	$R=5$ ASCE7 Table 12.2-1		
Seismic design Category	A, B, C Table CC-7.3.2-1	A, B, C Table CC-7.3.2-1	Any		
Masonry blocks Pattern	Not specified		Masonry not laid in running bond shall be fully grouted and constructed of hollow open-end units or two wythes of solid units Cl.7.3.2.6		
Vertical extent of BE	Not specified		Max of: $l_w$ or $M_u/4V_u$ Cl.9.3.6.6.3		
Minimum reinforcement ratio	$A_v \geq 129 \text{ mm}^2$ in bond beam or 2 W1.7 wires as joint reinforcement Cl.7.3.2.3.1		<table style="width: 100%; border: none;"> <tr> <td style="width: 50%; border: none;">Masonry not laid in running bond: <math>\rho_v \geq 0.07\%</math> <math>\rho_h \geq 0.15\%</math> <math>\rho_v + \rho_h \geq 0.2\%</math> Cl.7.3.2.6</td> <td style="width: 50%; border: none;">Masonry laid in running bond: <math>\rho_v \geq 0.07\%</math> <math>\rho_h \geq 0.07\%</math> <math>\rho_v + \rho_h \geq 0.2\%</math> Cl.7.3.2.6</td> </tr> </table>	Masonry not laid in running bond: $\rho_v \geq 0.07\%$ $\rho_h \geq 0.15\%$ $\rho_v + \rho_h \geq 0.2\%$ Cl.7.3.2.6	Masonry laid in running bond: $\rho_v \geq 0.07\%$ $\rho_h \geq 0.07\%$ $\rho_v + \rho_h \geq 0.2\%$ Cl.7.3.2.6
Masonry not laid in running bond: $\rho_v \geq 0.07\%$ $\rho_h \geq 0.15\%$ $\rho_v + \rho_h \geq 0.2\%$ Cl.7.3.2.6	Masonry laid in running bond: $\rho_v \geq 0.07\%$ $\rho_h \geq 0.07\%$ $\rho_v + \rho_h \geq 0.2\%$ Cl.7.3.2.6				
Maximum vertical reinforcement spacing ( $S_v$ )	$S_v \leq 203 \text{ mm}$ (Ends of wall) $S_v \leq 203 \text{ mm}$ (Each side of movement joints) $S_v \leq 406 \text{ mm}$ (Each side of openings) $S_v \leq 3048 \text{ mm}$ (on center) Cl.7.3.2.1	$S_v \leq 203 \text{ mm}$ (Ends of wall) $S_v \leq 203 \text{ mm}$ (Each side of movement joints) $S_v \leq 406 \text{ mm}$ (Each side of openings) $S_v \leq 1219 \text{ mm}$ (on center) Cl.7.3.2.5	$S_v$ min [ $1/3 l_w$ , $1/3 h_w$ , 1219 mm for masonry laid in running bond, 610 mm for masonry not laid in running bond Cl.7.3.2.6		
Maximum horizontal reinforcement spacing ( $S_h$ )	Joint reinforcement only: $S_h \leq 406 \text{ mm}$ Bond beam only: $S_h \leq 3048 \text{ mm}$ At the top and bottom of wall openings: $40d_b \leq S_h \leq 610 \text{ mm}$ , At the top of the wall: $S_h \leq 406 \text{ mm}$ Cl.7.3.2.1		$S_h$ min [ $1/3 l_w$ , $1/3 h_w$ , 1219 mm for masonry laid in running bond, 610 mm for masonry not laid in running bond] Cl.7.3.2.6		
Maximum area of flexural tensile reinforcement	For $M_u/V_u d_v \geq 1$ , Cross-sectional area of flexural tensile reinforcement < Area required to maintain axial equilibrium				
	A strain gradient shall be assumed corresponding to a strain in the extreme tensile reinforcement equal to 1.5 multiplied by the yield strain. Cl.9.3.3.2.1	A strain gradient shall be assumed corresponding to a strain in the extreme tensile reinforcement equal to 3 multiplied by the yield strain. Cl.9.3.3.5.2	A strain gradient shall be assumed corresponding to a strain in the extreme tensile reinforcement equal to 4 multiplied by the yield strain. Cl.9.3.3.5.3		
Anchorage of horizontal reinforcement	Not specified		Horizontal reinforcing bars shall be anchored around vertical reinforcement with a standard hook Cl.7.3.2.6		

**Table C.2 RMSW category description according to CSA S304 (2014)**

CSA S304-14 (2014) limits	RM shear walls SFRS Category			
	Conventional construction shear walls	Moderately ductile squat shear walls	Moderately ductile shear walls	Ductile shear walls
Ductility related force modification factor ( $R_d$ )	$R_d=1.5$ Cl. 16.5	$R_d=2.0$ Cl.16.7	$R_d=2.0$ Cl.16.8	$R_d=3.0$ Cl.16.9
Masonry blocks pattern	Shear walls shall be constructed in 50% running bond Cl.16.1.2			
Wall height to length ratio ( $h_w/l_w$ )	No limit	$h_w/l_w < 1.0$ Cl.16.7.2	$h_w/l_w \geq 1.0$ Cl.16.8.2	$h_w/l_w \geq 1.0$ Cl.16.9.2
Plastic hinge length ( $L_p$ )	Not specified	Not specified	$L_p = \max [0.5l_w, 0.167h_w]$ but $\leq 1.5l_w$ Cl.16.8.4	$L_p = \max [0.5l_w + 0.1h_w, 0.8l_w]$ but $\leq 1.5l_w$ Cl.16.9.4
Check inelastic rotational capacity	Not required	Not required	$\theta_{ic} \geq \theta_{id}$ Cl.16.8.8.1 Cl.16.9.7	
Minimum reinforcement ratio	Loadbearing walls: $I_E F_a S_a (0.2) \geq 0.35$ $\rho_v \geq 0.067\% (L_w \times b_w)$ $\rho_h \geq 0.067\% (h_w \times b_w)$ $\rho_v + \rho_h \geq 0.2\%$ Cl.16.4.5.1		Nonloadbearing walls: $0.35 \leq I_E F_a S_a (0.2) < 0.75$ $\rho_v \geq 0.05\% (L_w \times b_w)$ $\rho_h \geq 0.05\% (h_w \times b_w)$ Cl.16.4.5.2	
	Not specified	$\rho_h \geq V_f / (\phi_s b_w h_w f_y)$ $\rho_v \geq \rho_h - P_s / (\phi_s b_w h_w f_y)$ Cl.16.7.5	Not specified	Not specified
Maximum vertical reinforcement spacing ( $S_v$ )	$I_E F_a S_a (0.2) < 0.75$ : $S_v = \min [2400 \text{ mm}, 12(t+10)]$	$S_v = \min [1200 \text{ mm}, 6(t+10)]$ Cl.16.4.5.3	$S_v = \min [1200 \text{ mm}, 6(t+10)]$ Cl.16.4.5.3	
	$I_E F_a S_a (0.2) \geq 0.75$ : $S_v = \min [1200 \text{ mm}, 6(t+10)]$ Cl.16.5.2		$S_{v(lp)} = \min [6(t+10), 1200 \text{ mm}, 0.25 l_w]$ but $\geq (600 \text{ mm unless required for wall strength})$ Cl.16.8.5.3	$S_{v(lp)} = \min [6(t+10), 1200 \text{ mm}, 0.25 l_w]$ but $\geq (400 \text{ mm unless required for wall strength})$ Cl.16.9.5.3
Maximum horizontal reinforcement spacing ( $S_h$ )	Joint reinforcement only: $S_h \leq 400 \text{ mm}$ Bond beam only: $S_h \leq 1200 \text{ mm}$ Joint reinforcement and bond beam: $S_h \leq 2400 \text{ mm}$ (bond beam), $S_h \leq 400 \text{ mm}$ (joint reinforcement) Cl. 16.4.5.4			
	Not specified		$S_{h(lp)} = \min [1200 \text{ mm}, 0.5l_w]$ Cl.16.8.5.4	$S_{h(lp)} = \min [600 \text{ mm}, 0.5l_w]$ Cl.16.9.5.4
Edge distance after which lap splice is allowed in horizontal reinforcement ( $l_{edge}$ )	Not specified	Cl.16.7.6	$l_{edge} = \max [600 \text{ mm}, 0.2 l_w]$ Cl.16.8.5.4	Cl.16.9.5.4
Anchorage of horizontal reinforcement	Not specified	Horizontal reinforcing bars shall have 90° or more standard hooks Cl.16.7.6 and Cl.16.8.5.4		Horizontal reinforcing bars shall have 180° standard hooks Cl.16.9.5.4
Limitation on axial loads	$I_E F_a S_a (0.2) \geq 0.35$ : Axial compressive stress $\leq 0.1 f'_m$ Cl.16.5.3	No limit		
Wall unsupported height	Not specified	$h_w/(t+10) < 20$ Cl.16.7.4	$h_w/(t+10) < 20$ $h_w/(t+10) \leq 30$ (if satisfying Cl.16.8.3.3) Cl.16.8.3.1	$h_w/(t+10) < 12$ $h_w/(t+10) \leq 16$ (if satisfying Cl.16.9.3.3) Cl.16.9.3.1

**Table C.3** RMSW’s classifications according to CSA S304 (2014) and TMS 402/602 (2016)

Ref.	Wall ID#	Specimen label in the reference	RMSW SFRS Categories	
			CSA S304-14	TMS 402/602-16
Priestley & Elder (1982)	1	Wall 1	Conventional shear wall	Ordinary shear wall
	2	Wall 3	Conventional shear wall	Special shear wall
Eikanas (2003)	3	Wall 1	Conventional shear wall	Special shear wall
	4	Wall 2	Conventional shear wall	Special shear wall
	5	Wall 4	Conventional shear wall	Special shear wall
	6	Wall 5	Conventional shear wall	Special shear wall
	7	Wall 6	Conventional shear wall	Special shear wall
	8	Wall 7	Conventional shear wall	Special shear wall
Shedid (2006)	9	Wall 2	Conventional shear wall	Ordinary shear wall
	10	Wall 3	Conventional shear wall	Special shear wall
	11	Wall 4	Conventional shear wall	Special shear wall
	12	Wall 5	Moderately ductile shear wall	Special shear wall
	13	Wall 6	Conventional shear wall	Ordinary shear wall
Shedid et al. (2008)	14	Wall 7	Conventional shear wall	Ordinary shear wall
	15	Wall 1	Conventional shear wall	Ordinary shear wall
Sherman (2011)	16	Wall 4	Conventional shear wall	Ordinary shear wall
	17	WSU-Wall 1A	Conventional shear wall	Intermediate shear wall
	18	WSU-Wall 1B	Conventional shear wall	Intermediate shear wall
	19	WSU-Wall 2A	Conventional shear wall	Ordinary shear wall
	20	WSU-Wall 2B	Conventional shear wall	Ordinary shear wall
	21	WSU-Wall 3	Moderately ductile shear wall	Intermediate shear wall
	22	WSU-Wall 4	Conventional shear wall	Special shear wall
	23	WSU-Wall 5	Conventional shear wall	Special shear wall
Ahmadi (2012)	24	WSU-Wall 6	Conventional shear wall	Special shear wall
	25	UT-W-13	Conventional shear wall	Intermediate shear wall
	26	UT-W-14	Conventional shear wall	Intermediate shear wall
	27	UT-W-15	Conventional shear wall	Ordinary shear wall
	28	UT-W-16	Conventional shear wall	Ordinary shear wall
	29	UT-W-17	Conventional shear wall	Intermediate shear wall
	30	UT-W-18	Conventional shear wall	Intermediate shear wall
	31	UT-W-19	Moderately ductile shear wall	Ordinary shear wall
Kapoi (2012)	32	UT-W-20	Conventional shear wall	Ordinary shear wall
	33	WSU-Wall C1	Conventional shear wall	Special shear wall
	34	WSU-Wall C2	Conventional shear wall	Special shear wall
	35	WSU-Wall C3	Conventional shear wall	Intermediate shear wall
	36	WSU-Wall C4	Conventional shear wall	Intermediate shear wall
	37	WSU-Wall C5	Conventional shear wall	Intermediate shear wall
	38	WSU-Wall C6	Conventional shear wall	Special shear wall
	39	WSU-Wall C7	Conventional shear wall	Special shear wall
Siyam et al. (2015a)	40	WSU-Wall C8	Conventional shear wall	Intermediate shear wall
	41	Wall 1(5)	Moderately ductile shear wall	Special shear wall
	42	Wall 5(1,2)	Conventional shear wall	Special shear wall
	43	Wall 6(out)	Conventional shear wall	Special shear wall